# Propulsion System Control of Ships Sailing in Waves

## Refinement of Diesel Engine's Dynamic Response by Means of Optimal Governor Gains Scheduling


by

**Nikolaos Makrygiannis**

Faculty of Mechanical, Maritime & Materials Engineering,
Delft University of Technology, Delft, the Netherlands

TU Delft Delft University of Technology

DAMEN

# Propulsion System Control of Ships Sailing in Waves

## Refinement of Diesel Engine's Dynamic Response by Means of Optimal Governor Gains Scheduling

**Thesis**

to obtain the degree of Master of Science
at the Delft University of Technology.

by


**Nikolaos Makrygiannis**

Faculty of Mechanical, Maritime & Materials Engineering,
Delft University of Technology, Delft, the Netherlands


| | | |
|---|---|---|
| Student number: | 4522567 | |
| Thesis Number: | SDPO.18.044.m | |
| Project duration: | January 1, 2017 – September 4, 2018 | |
| Thesis committee: | Prof. Dr. Ir. K. Visser, | TU Delft |
| | Dr. Ir. A. Vrijdag, | TU Delft, supervisor |
| | Ir. E.J. Boonen, | Damen Shipyards Group |


An electronic version of this thesis is available at http://repository.tudelft.nl/.

# Contents

**Summary** **ix**

**1 Introduction** **1**
1.1 The Need for Improved Design and Advanced Control of Marine Propulsion Systems . . . 1
1.2 Motivation . . . 3
1.3 Research Scope . . . 7
1.4 Research Objectives . . . 8
1.5 Approach . . . 8
1.6 Thesis Outline . . . 9

**2 Ship Propulsion System Model: An Overview** **11**
2.1 Propulsion Topologies . . . 11
2.1.1 Mechanical Propulsion . . . 11
2.1.2 Electrical Propulsion . . . 13
2.1.3 Hybrid Propulsion . . . 14
2.2 Ship Propulsion System Modelling . . . 15
2.2.1 General Considerations . . . 15
2.2.2 Non-linear Ship Propulsion System Model . . . 15
2.2.3 Linearised Ship Propulsion System Model . . . 18
2.3 Propulsion Control Strategies . . . 21
2.3.1 Ideas On Propulsion Control . . . 21
2.4 Wave Disturbance Rejection Techniques on Diesel Engines . . . 24
2.5 Ship Propulsion System Model Disturbances . . . 27
2.5.1 Wake Field Disturbance Due To Waves . . . 27
2.5.2 Added Resistance in Waves . . . 33
2.6 Conclusions . . . 41
2.6.1 Propulsion System and Propulsion Control Model . . . 41
2.6.2 Disturbances Modelling . . . 42

**3 Ship Simulation Model** **45**
3.1 General Ideas on the Simulation Model Approach . . . 45
3.2 Reference Vessel . . . 47
3.3 Simulation System Models . . . 48
3.3.1 Propeller . . . 50
3.3.2 Controlled Diesel Engine Model . . . 52
3.3.3 Gearbox Model and Rotor Dynamics . . . 56
3.3.4 Ship's Hull Model . . . 58

3.4 Tuning of the Controller of Simulation Model . . . . . 62
3.4.1 Values of Governor Gains and System Variables Examined . . . . . 63
3.4.2 Results of Two-Step Engine Speed Increase . . . . . 64
3.5 Simulation Model Validation . . . . . 69
3.6 Conclusions . . . . . 71

**4 Linearisation of Ship Simulation Model 73**
4.1 Introduction and General Considerations . . . . . 73
4.2 Linearisation Process . . . . . 75
4.3 Core Propulsion System . . . . . 81
4.4 Uncontrolled system with actuators . . . . . 85
4.5 Controlled System . . . . . 89
4.6 Conclusions . . . . . 95

**5 Load Variations: Ship Direction, System Operating Point and Sea State 97**
5.1 Introduction . . . . . 97
5.2 General Considerations . . . . . 98
5.2.1 Ellipse Geometric Properties . . . . . 99
5.3 Ship Direction . . . . . 102
5.4 Operating Point . . . . . 116
5.5 Sea State . . . . . 127
5.6 Conclusions . . . . . 131

**6 Governor Gain Scheduling: Refinement of Diesel Engine's Dynamic Behaviour 133**
6.1 Introduction & General Considerations . . . . . 133
6.2 Problem Formulation . . . . . 135
6.2.1 Angle of Rotation . . . . . 136
6.2.2 Area of Ellipse . . . . . 138
6.2.3 Shortest Distance Between an Ellipse and a Straight Line . . . . . 139
6.2.4 Infeasible Solutions . . . . . 143
6.3 Contour Plots . . . . . 144
6.4 Governor Gains Scheduling Algorithm . . . . . 153
6.4.1 Regular Waves . . . . . 156
6.4.2 Irregular Waves . . . . . 161
6.5 Conclusions . . . . . 167

**7 Conclusions & Recommendations 169**
7.1 Conclusions . . . . . 169
7.2 Recommendations for Future Work . . . . . 173

**A Wake Disturbance Modelling 179**
A.1 Introduction . . . . . 179
A.2 Standard Wave Spectra . . . . . 179
A.3 Wake Disturbance Due to Wave Orbital Motion . . . . . 182
A.4 Wake Disturbance in Irregular Waves . . . . . 186

**B Shortest Distance Between an Ellipse & a Straight Line** **189**
B.1 Introduction . . . . . . . . . . . . . . . . . . . . . . . . . . . . . . . . 189
B.2 Calculation Process . . . . . . . . . . . . . . . . . . . . . . . . . . . . 189
B.3 Special Case: Ellipse - Line Intersection . . . . . . . . . . . . . . . . 194

**C Metaheuristics for Hard Optimisation: Simulated Annealing** **201**
C.1 Introduction . . . . . . . . . . . . . . . . . . . . . . . . . . . . . . . . 201
C.2 Simulated Annealing Algorithm . . . . . . . . . . . . . . . . . . . . . 204

**References** **213**

# SUMMARY

The need for advanced control strategies of marine propulsion systems is constantly increasing. Trying to list the reasons for which more advanced marine propulsion control systems are demanded, the necessity of every new-built vessel to demonstrate its ability for high performance has to be stressed out. Sea trials and particularly speed trials are considered for shipyards as a specific situation during which a new-built vessel has to showcase its performance by successfully attaining the contractually agreed maximum average speed. Nevertheless, speed trials may take place under non ideal environmental conditions such as waves, which affect the dynamic response of the main engine. In case of vessels with Controllable Pitch Propellers and Diesel engine as prime mover, the action of the controller of the Diesel engine, which tries to counteract the impact of the wave induced disturbances, causes fluctuations of the engine operating point in the engine operating envelope in terms of engine speed and torque. When these fluctuations reach the limits of the engine operating envelope the propeller pitch controller is activated, reducing the propeller pitch in order to effectively protect the engine from overloading. This pitch reduction leads to reduction of maximum average delivered power and generated thrust and thus to reduction of the maximum average ship speed.

Trying to deal with the above mentioned negative effects of propeller pitch controller activation, the possibility of influencing the dynamic response of the engine operating point in the operating envelope is investigated, attempting to keep the engine's operating point fluctuations away from the operating envelope limits and thus, the pitch control deactivated. This investigation, which is the main research objective of this thesis, is addressed by means of gain scheduling the existing Diesel engine speed governor.

Using as a starting point and essential tool the linearised ship propulsion system model, the impact of different factors on the dynamic response of the Diesel engine operating point is investigated. More specifically, the impact of the direction of the ship with respect to the waves, the impact of the system operating point and the impact of the Sea State on the dynamic behaviour of the Diesel engine operating point are examined. The outcome of this examination leads to the conclusion that it would make sense to improve the classical Diesel engine speed governor, which uses constant values for its gains, by making the values of the controller parameters dynamically adaptive and dependent on the ship direction with respect to the waves, on the system operating point and on the Sea State.

In order to achieve this, the linear model is again employed as the fundamental tool providing a mathematical framework to the engineering problem. As a first step, a static solution is proposed by deriving contour plots. These contour plots provide combinations of governor gains, $K_p$&$K_i$, which ensure that the fluctuations of Diesel engine's operating point lie as far away as possible from the limits of the engine operating envelope. In that way, the propeller pitch controller remains deactivated and the resulting negative effects avoided. This solution proves the potential of improvement, regarding the dynamic response of the Diesel engine, allowing at the same time a manual scheduling of the governor gains according to the wave induced disturbance. As a second step, a dynamic solution is suggested in order to reach the goal of keeping the propeller pitch controller deactivated when the ship sails in waves. This solution consists of the development of Gains Scheduling Algorithm, which is able to automatically adjust the governor settings according to the wave induced disturbance. The developed algorithm employs the derived linear model of the propulsion system combined with an optimisation algorithm. The selected optimisation algorithm, which is called Simulated Annealing, is a metaheuristic method well-known for effectively solving difficult optimisation problems by determining the global optimum of their objective function.

The developed algorithm is integrated in the non-linear simulation model of the ship propulsion system. Simulations are run in case of both regular and irregular waves. In that way the developed algorithm is tested and evaluated with respect to its effectiveness in terms of dynamically adjusting the engine controller settings, according to the wave disturbance acting on the model and preventing the activation of propeller pitch controller. Simulation results demonstrate that the proposed refinement of the Diesel engine speed governor, with the integrated Gains Scheduling Algorithm, achieves the ultimate goal of re-sizing and re-orientating the fluctuations of the Diesel engine operating point, avoiding any contact with the limits of the engine operating envelope, preventing in any case the activation of the propeller pitch controller and thus, maintaining the maximum average ship speed.

# 1
# INTRODUCTION

*The purpose of this chapter is to explain the reasoning behind the initiative, which led to this research. The problem is described and the challenges that it poses are clearly defined. Additionally, the limits of the work are presented along with the research objectives. Finally, the method which will be followed in the direction of answering the research questions is clearly stated, as well as a general overview of the whole project.*

## 1.1. THE NEED FOR IMPROVED DESIGN AND ADVANCED CONTROL OF MARINE PROPULSION SYSTEMS

It goes without saying, that design and optimisation of marine propulsion plants are essential parts of modern ship design procedures. As a matter of fact, the behaviour of the propulsion plant affects, crucially, the global behaviour of a vessel. Marine propulsion plants are requested to operate efficiently and safely under a wide range of operational profiles, dependent on the particular type of the ship. In other words, besides steady state conditions, transient conditions have to be taken into consideration, too. Under these operational conditions, the dynamic behaviour of every single component, which constitutes the total propulsion plant, influences substantially the global performance of the vessel's propulsion plant. A wide range of operational speeds, acceleration, deceleration, crash stop, heavy manoeuvring and faults are a sample of transient conditions, which a marine propulsion plant will have to cope with, maintaining the required level of the vessel's safety and reliability.

Furthermore, the shipping industry, like many other kinds of industry, is obliged to decrease its environmental impact and comply with the strict regulations about the engine emissions, imposed by the International Maritime Organisation, [IMO, 2014]. What is more, at the same time that the pressure for fuel consumption reduction is constantly increasing, the operating profile of modern ships is increasingly varying; offshore vessels carrying out heavy lifts, transit operations, dynamic positioning, naval ships executing patrol operations in open sea, as well as being engaged in coastal operations, tug boats demanding high amount of bollard pull during towing and significantly lower

1

power during transit. For that reason, the power and propulsion plant of a vessel has to perform adequately on many performance aspects. The above-mentioned variety of operational profiles leads to many difficulties regarding the optimisation of the propulsion plant for one operating point at the early stage of designing a vessel. In addition, the need for both efficiency and adaptability to different operating profiles resulted in a growing variety of power and propulsion configurations. The increasing complexity of propulsion configuration combined with traditional control do not remarkably reduce fuel consumption and emissions. According to the research done, advanced propulsion architecture require fresh and smart control strategies regarding the prime mover, in the direction of achieving significant decrease of fuel consumption and emissions, while the system complexity is increasing.

As far as the maintenance costs of the prime mover are concerned and more specifically the maintenance costs of the Diesel engine used a the prime mover of a vessel, they are considered to be remarkably high [Van Spronsen and Tousain, 2001]. Thus, researchers thoroughly investigated the medium speed Diesel engines and particularly the wakefield disturbances due to waves, which act on the propeller causing continuous variations of the engine and shaft speed. The governor of the Diesel engine applies an intense control effort, trying to counteract these fluctuations and keep the engine speed constant, aiming to protect the engine. Therefore, the governor continuously adjusts the amount of the fuel injected in the engine, in order to control the engine speed. As a consequence, the engine, quite often, ends up operating outside the preferred region of the operating envelope. This preferred operating region of the Diesel engine is determined by a reduced time between overhaul (RTBO) line, which is usually defined by the manufacturer. A relation between the engine speed and the fuel rack position is described by this line. As a result, this also defines a relation between the amount of fuel that is injected in the cylinders of the engine and the engine speed, as well as a relation between the engine revolutions and the torque generated by the Diesel engine, since fuel rack position and engine torque are proportional, at least for static conditions.

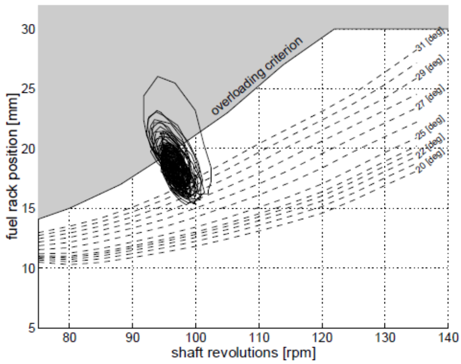


Figure 1.1: The overloading criterion and a typical violation of the constraints measured in real life. Grey area defines the region of operating points for which RTBO holds[Van Spronsen and Tousain, 2001].

The violation of the RTBO line, as it is depicted in Figure 1.1, is called overloading of marine Diesel engines and is caused by Sea States, intense accelerations and decelerations or strong manoeuvring. As long as the system operates below the RTBO line, the engine is not overloaded and the maintenance costs will not be exceeded. Investigating the solutions for the diesel engine overloading problem from a control system point of view, smarter control strategies, regarding the diesel engine, like an advanced controller for the fuel rack position could eliminate the violation of the engine's envelope limits. Reduced control effort or influencing the shape of the disturbance in the operating envelope could be beneficial towards the direction of establishing advanced control strategies of the diesel engine. Introducing a second control variable could be profitable for the problem of the diesel engine overloading, too.

## 1.2. MOTIVATION

Trying to enrich the list with the reasons for which an improved design and advanced control of marine propulsion systems are demanded, the necessity of every new-built vessel to demonstrate its ability for high performance, during the sea trials should also be pointed out. There is no doubt that especially new-built vessels, as it was referred before, as well as overhauled and maintained vessels, undergo intense sea trials before they are delivered to their owner.

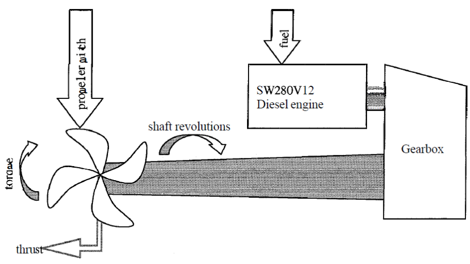


Figure 1.2: Fuel energy transformation into thrust power throughout the propulsion system.

In that way, shipyards prepare the ships for operations, ensuring high product quality, increased vessel uptime and compliance with performance criteria. That is the reason that sea trials are always considered important for shipyards. One of the most important tests that are carried out during the sea trials, in order to measure the ship's general performance are the *speed trials*. During *the speed trials*, the satisfactory attainment of the contractually agreed maximum speed is to be verified. In order to obtain the maximum ship speed, it is necessary that the maximum engine brake power, $P_B$ is continuously delivered to the vessel's propellers. Subsequently, the delivered amount of power, $P_D$ has to be efficiently transformed into thrust power, $P_T$, as shown in Figure 1.2. Nevertheless, it is inevitable that speed trials often take place under non-ideal environmental conditions caused by wind and waves.

The fact that the vessel operates in off-design conditions, such as wind-generated waves, is translated into two main disturbances acting on the ship propulsion system and affecting the dynamic behaviour of the engine operating point in the operating envelope of the Diesel engine, [Stapersma and de Heer, 2000]. These disturbances can be attributed to two main causes. The first disturbance is the unsteady wake velocities due to waves, which cause fluctuations of the advance velocity $V_A$ and consequently variations of the angle of attack of the water flow with respect to the propeller blade. The second disturbance is the added resistance due to the motions of the ship advancing in waves, which causes fluctuations of the total ship resistance.

The attempt of the propulsion control system to counteract the above mentioned disturbances gives the shape of an elliptic trajectory to the engine operating points in the operating envelope of the Diesel engine, as it can be noticed in Figure 1.3. The interaction between rough environmental conditions, the ship, the ship's propulsion plant and propulsion control system leads to fluctuations of the delivered brake engine power, $P_B$, the propeller pitch, $P/D$ and the engine speed, $n_e$ as the plots of Figure 1.4 show respectively.

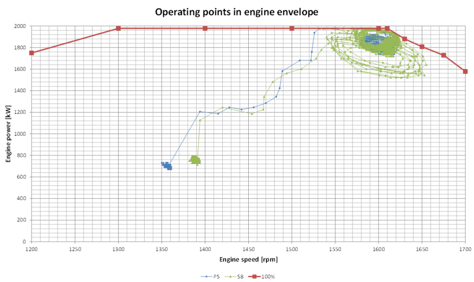


Figure 1.3: Operating cloud touching the Diesel engine operating envelope limits. Data from ship sea trials measurements, provided by Damen Shipyards Group.

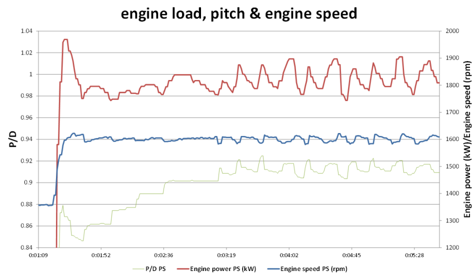


Figure 1.4: Engine brake power, propeller pitch and engine speed variations due to pitch control activation. Data from ship sea trials measurements, provided by Damen Shipyards Group.

For a Controllable Pitch Propeller (CPP) driven vessel, the propeller pitch control is activated as soon as the elliptic trajectory of the engine operating point touches the limits of the operating envelope of the Diesel engine. In that case, the propeller pitch control actuator applies a temporary pitch reduction, in order to directly compensate any occurring overload of the engine, effectively avoiding its negative effects. This process is depicted in Figure 1.5, in which the continuous red line depicts the engine brake power $P_B$ and the horizontal red dashed line is the limit of the power of the engine. The yellow line shows the normalised pitch angle of the propeller, $P/D$ and the blue one the engine speed, $n_e$. Finally, the green line is the vessel's speed $v_s$. As it is clearly illustrated, every time the continuous red line (engine power) touches the engine's limits (horizontal dashed line), a cut-off of the crest of the engine power occurs, followed by a significant drop of the value of the engine power. This problem arises due to the fact that the propeller pitch control reduces the propeller pitch (yellow line), whenever the value of the engine power reaches the power limit line of the Diesel engine. Subsequently, the ship speed is, considerably, decreased. The foregoing can be clearly noticed by following the sequence of the incidents starting, for instance, at the moment 05:02:10 in Figure 1.5. There is no doubt that the performance of the vessel will be, significantly, influenced and an undesirable drop in the average maximum ship speed $v_{smax}$, which has to be attained, will be noticed. Moreover, a general overview of the problem definition is given in Figure 1.6, clearly documenting the order of the facts which cause the problem.

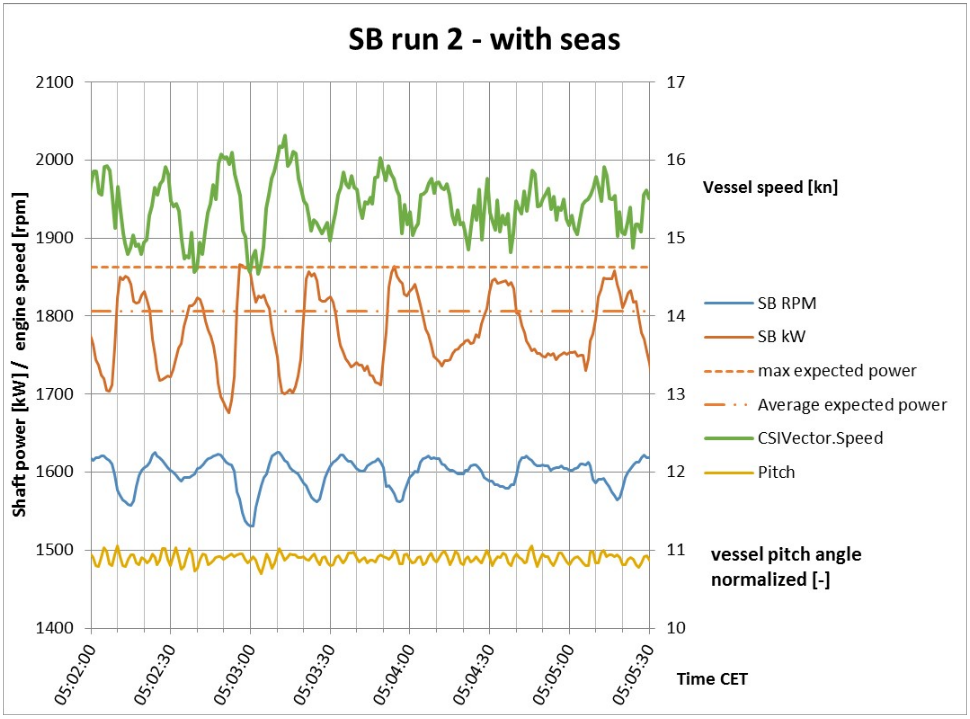


Figure 1.5: Cut-offs of power crests and vessel speed fluctuations due to propeller pitch control activation. Data obtained from ship sea trials measurements of Damen Shipyards Group.

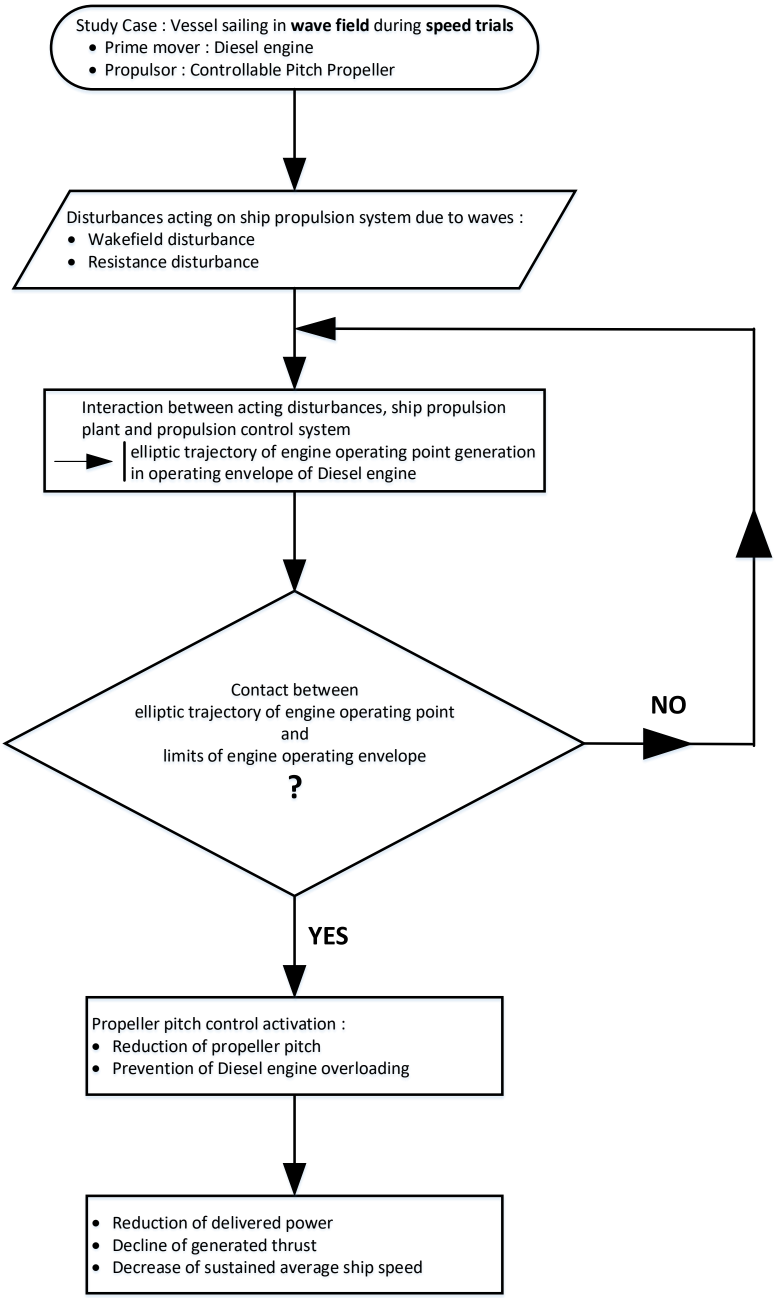


Figure 1.6: Project motivation flow chart.

Given the above-mentioned negative impact of the propeller pitch control activation, two main actions can be considered:

1. Attempt to influence the size and the orientation of the elliptic trajectory of the engine operating points in the operating envelope of the Diesel engine, aiming at keeping the propeller pitch control deactivated.

2. Optimise the behaviour of the propeller pitch control algorithm.

At this point, it has to be mentioned that this master thesis focuses **on the investigation of the possibility to re-size and re-orientate the elliptic trajectory of the engine operating points, without engaging the use of the propeller pitch control, when the vessel sails in waves**. In that way, the achieved average maximum speed of a vessel during the procedure of ship speed trials is maintained, avoiding the activation of the propeller pitch control, which results in reduction of the delivered power, the generated thrust and consequently in drop of the attained ship speed, in order to protect the Diesel engine from thermal overloading.

Furthermore,the two above-mentioned points should be examined by the point of view of the operator of the vessel after the shipyard's speed trials procedure. It goes without saying that less frequent activation of the propeller pitch control will be beneficial for the operator of the ship, since the propulsion system of the vessel will be capable of maintaining the maximum average ship speed without the unfavourable effect of the propeller pitch reduction. In addition, the operator will have the benefit of less maintenance costs of the Diesel engine due to the prevention of thermal overloading of the engine, by ensuring that the operating ellipse (or cloud) lies as far as possible from the limits of the engine envelope, [Grimmelius and Stapersma, 2001, Van Spronsen and Tousain, 2001]. On the other hand, the maintenance costs of the controllable pitch propeller and its hydraulic actuating system will be reduced, since the aim of this research project is less activation of the propeller pitch control.

## 1.3. Research Scope

As far as the limits and the context of this research are concerned, the following points are going to be examined:

- Vessels using Diesel engines as prime movers and Controllable Pitch Propeller.
- The effect of different Sea States.
- The effect of two sailing directions of the vessel with respect to the waves:
  - head waves
  - following waves
- The effect of system operating point.

On the other hand, this graduation project will **not** investigate the behaviour of the ship propulsion plant:

- During manoeuvring.
- During acceleration and deceleration.

1

## 1.4. RESEARCH OBJECTIVES

Summarising all the above-mentioned,the objectives and the related research questions that this master thesis will examine and try to answer are:

- Is it possible to maintain the maximum average ship speed during speed trials by means of tuning governor gains?
- With respect to the diesel engine load fluctuations in a seaway:
    - What is the impact of the different sea states?
    - What is the impact of head and stern waves?
    - What is the impact of the propulsion system operating point?
- Is it possible to influence the size and the orientation of the diesel engine operating ellipse, by trying to refine the existing propulsion control system and making the gain scheduling of the governor dependent on the system operating point, on the sea state and/or on the heading of the vessel regarding the waves?

## 1.5. APPROACH

Regarding the approach to answer the aforementioned research objectives, the steps, which are presented below, will be followed:

- **Obtain the non-linear simulation model of the propulsion system of a reference vessel.**
  The attempt to answer the above-mentioned research questions will be based on the employment of non-linear simulation model of the ship's propulsion system. Therefore, the simulation model of a reference vessel propulsion system will be used. The reason for this is that the utilisation of simulated models is quite common for controller development or controller refinement purposes, due to the benefits that they can provide in terms of testing cost and time. What is more, the non-linear model will be validated with existing data from the reference vessel's sea trials, provided by Damen Shipyards Group.
- **Linearisation of the non-linear reference vessel propulsion system model.**
  Linear models are often more simple and require less parameter and system knowledge when compared to non linear models. Furthermore, the derived linear model can be employed to predict the system behaviour in the frequency domain. Consequently, it can be used for analysis of propulsion system behaviour in waves and for controller design and tuning. Nevertheless, the linearised ship propulsion system model should not be considered as a replacement of the non-linear model, but rather as an easy-to-handle, additional tool.
- **Investigation of Diesel engine dynamic behaviour, based on linear reference vessel propulsion system model.** The impact of the propulsion system operating point, the Sea State and the direction of the vessel with respect to the waves on the dynamic response of the Diesel engine in the engine operating envelope will

be examined by employing the linear propulsion system model of the reference vessel.

- **Governor gains scheduling.** Governor gains scheduling will be attempted, aiming at re-sizing and re-orientating the elliptic trajectory of the engine operating point in the engine operating envelope. A gains scheduling algorithm will be developed based on the implementation of the linear ship propulsion system model. The gains scheduling algorithm will be evaluated by implementing it in the non-linear propulsion system model in case of both regular and irregular waves.

## 1.6. THESIS OUTLINE

The dissertation is structured into 6 chapters.

- In chapter 2 relevant literature is reviewed.
- In chapter 3, the propulsion system of the reference vessel along with its dynamic environment are described and transformed into a simulation model. The mathematical formulas of each component are presented. Moreover, the non-linear simulation model is validated with data obtained during the vessel's sea trials.
- In chapter 4, the non-linear propulsion system model is linearised and verified in steps. The verification is carried out by means of comparison between the Bode plots of the non-linear and linear model. The verification will prove that the linear model is derived correctly from the non-linear model and that can be, rightfully, used for the controller design.
- In Chapter 5, the linearised ship propulsion system model is employed for the investigation of the impact of the system operating point, the Sea State and the direction of the ship with respect to the waves on the dynamic response of the elliptic trajectory of the engine operating point in the Diesel engine operating envelope.
- In Chapter 6, the existing Diesel engine speed governor is attempted to be refined. The refinement is addressed by means of developing a gains scheduling algorithm which employs the already derived linear propulsion system model and a metaheuristic algorithm. The developed gains scheduling algorithm is implemented in the non-linear ship propulsion system model and the achieved results in regular and irregular waves are evaluated.
- In Chapter 7, the conclusions of this thesis are drawn and recommendations for further research are provided.

# 2

# Ship Propulsion System Model: An Overview

*In this chapter the main propulsion architectures applied on ships are presented. Additionally an overview of the modelling techniques of marine propulsion systems is documented, along with the most common propulsion system control strategies and their alternatives. Besides this, linearisation methods of non-linear ship propulsion models are described. Furthermore, an analysis is given regarding the disturbances that act on a ship propulsion system model, when the vessel sails in a wind generated wave field. Finally, some techniques for wave disturbance rejection in Diesel engines are described.*

## 2.1. Propulsion Topologies

Diverse operating profiles force vessel's power and propulsion plants to perform adequately on many performance criteria, such as fuel consumption, emissions, manoeuvrability, maintenance costs and minimisation in noise and vibration. Due to the increasing diversity in operational profiles, it is considered quite difficult to optimise the power and propulsion plant for a specific operating point as it is commonly done during the design procedure of a ship. As a result there is a trade-off between efficiency and adaptability to diverse operating profiles. This fact led to an increasing variety of power and propulsion architectures. As far as the development and implementation of propulsion architectures is concerned, the propulsion topology categorised into:

- mechanical propulsion
- electrical propulsion
- hybrid propulsion

### 2.1.1. Mechanical Propulsion

Mechanical propulsion systems have been employed on ships since the 19th century. A typical layout of this propulsion system is illustrated in Figure 2.1. A propulsion machine, which is usually a Diesel engine or a gas turbine, drives the propulsor, which is usually a propeller. This is achieved either directly or through a gearbox. Additionally, in such a propulsion plant some Diesel generators and an electrical AC network is required to generate the electric power needed for the auxiliary loads like for instance heating ventilation and air-conditioning or other auxiliary systems. Low speed Diesel engines do not require a gearbox. On the other hand, medium- and high-speed Diesel engines do require a gearbox. As far as the propellers are concerned, in mechanical propulsion system both fixed pitch and controllable pitch propellers are used with the latter one offer an extra degree of control. Apart from these two kind of propellers other propulsors like water jets, surface piercing propellers, cycloidal propellers or paddle wheels can also be applied.

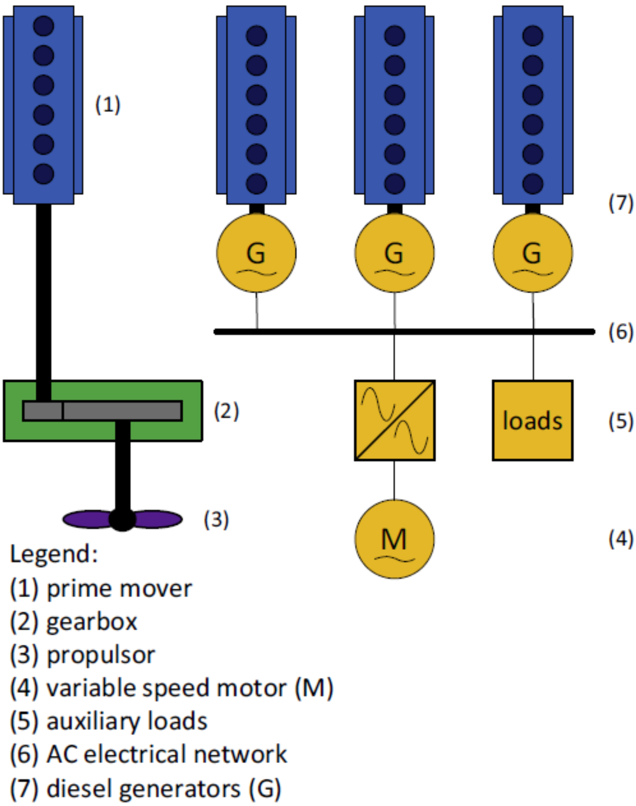


Figure 2.1: Typical mechanical propulsion system layout, [Geertsma et al., 2017a]

Regarding the advantages of the mechanical propulsion systems, the main benefit is their high efficiency when operating at design speed, which is between 80% and 100% of maximum speed. Furthermore, mechanical propulsion systems consist of only three power conversion stages, the main engine, the gearbox and the propeller a fact that leads to low conversion losses. Additionally, mechanical propulsion systems are not complex and their simplicity leads to low purchase cost. On the other hand, some of the major disadvantages of mechanical propulsion systems are the increased maintenance costs when the main engine is overloaded, the low fuel efficiency and high emissions when the engine runs in off-design operating points and the low availability since failure of any of the components of the drive train leads to loss of propulsion.



### 2.1.2. ELECTRICAL PROPULSION

The architecture of electrical propulsion, which has been applied since 1990s, is demonstrated in Figure 2.2, where its typical layout can be noticed. Diesel generator sets feed a fixed frequency high voltage electrical bus which in turn feeds the electrical propulsion motor drive through a transformer. High fuel efficiency especially in cases that the hotel load is a significant part of the total load of the vessel, low $NO_x$ emissions, reduced maintenance costs and high flexibility in terms of the arrangement of the engine room on the vessel due to the absence of shaft line are some of the advantages that the electrical propulsion offers. On the other hand, the main disadvantage of the electrical propulsion is the fact that additional conversion stages in power converters and electric motors are introduced to the propulsion plant causing at the same time increased losses and increased specific fuel consumption.

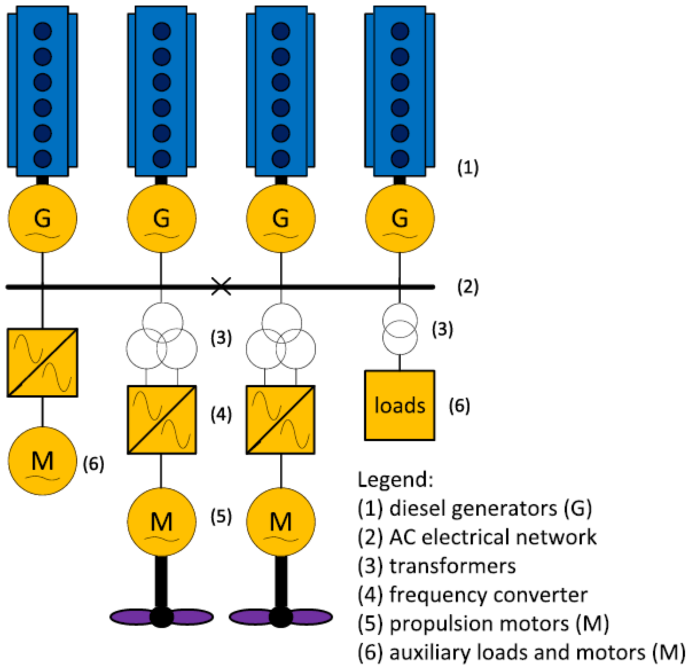


Figure 2.2: Typical electrical propulsion system layout, [Geertsma et al., 2017a]

### 2.1.3. Hybrid Propulsion

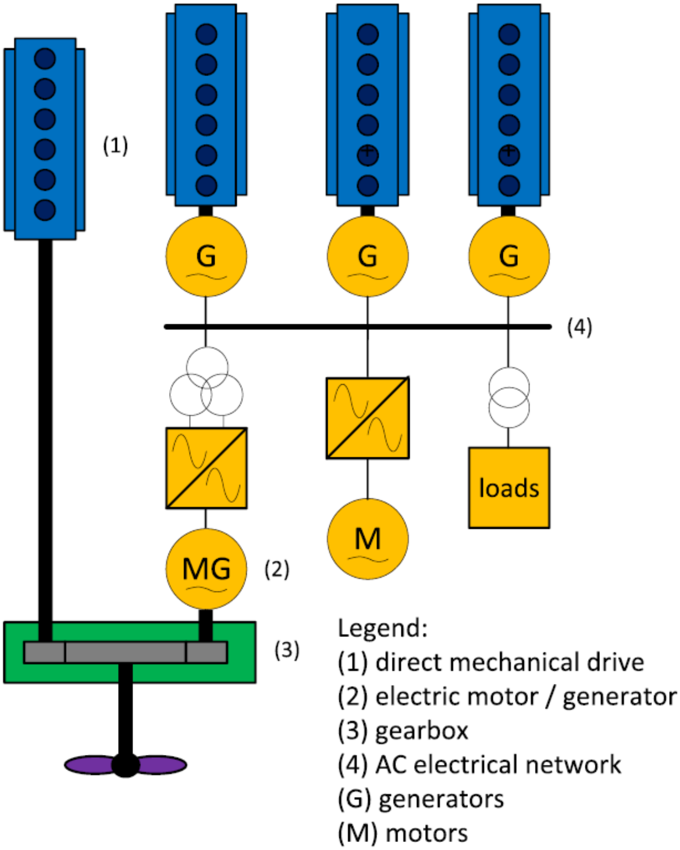


Figure 2.3: Typical hybrid propulsion system layout, [Geertsma et al., 2017a]

The typical layout of a hybrid propulsion system can be observed in Figure 2.3. A hybrid propulsion system usually consists of a direct mechanical drive providing propulsion in high speeds with high efficiency and of an electric motor coupled to the same shaft through a gearbox or directly to the shaft driving the propeller. This electric motor usually provides propulsion for low speeds preventing the insufficient use of the main engine in part load operation. Additionally, the electric motor can provide power as a generator for the vessel's electrical loads. Since a hybrid propulsion plant combines the features of a mechanical and electrical propulsion it can benefit from advantages of both previously discussed systems. However, a trade-off between the use of mechanical and electrical propulsion has to be made in order to achieve highest performance and efficiency. This trade-off is usually made by the control system of the propulsion plant which should be designed in such a way that could ensure that the propulsion plant takes advantage of both propulsion systems. The interested reader can have a better insight of a variety of propulsion and power systems as well as their control strategies in [Geertsma et al., 2017a].

## 2.2. SHIP PROPULSION SYSTEM MODELLING

### 2.2.1. GENERAL CONSIDERATIONS

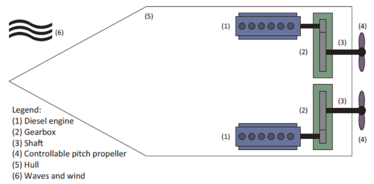


Figure 2.4: Typical mechanical propulsion layout of a vessel, [Geertsma et al., 2017b].

In this section modelling approaches for ship propulsion systems, which are suitable for propulsion control system design and propulsion control system tuning, are documented. Non linear models are preferred in case of propulsion controller design and tuning since non-linear time domain simulations are able to mathematically describe the ship propulsion system and adequately capture the intricacies of the propulsion plant under consideration. On the other hand, linear models offer the opportunity to simplify complicated non linear simulation models of dynamic systems. The derived linear model can then be used to predict system's behaviour in frequency domain, avoiding time consuming time domain simulations. Regarding the preliminary design of controllers, based on linear models, the effect of a controller on the dynamic behaviour of ship propulsion system model can be examined and evaluated.

### 2.2.2. NON-LINEAR SHIP PROPULSION SYSTEM MODEL

General non-linear ship propulsion model is presented in block diagram in [Stapersma and de Heer, 2000] where the non-linear dynamics of the ship propulsion plant are modelled including also the environment induced dynamic disturbances, for instance due to waves, as it is illustrated in Figure 2.5 and 2.4. An attempt to describe mathematically the physical ship propulsion plant is demonstrated in [Van Spronsen and Tousain, 2001], where the non-linear simulation model of the ship propulsion system is derived.

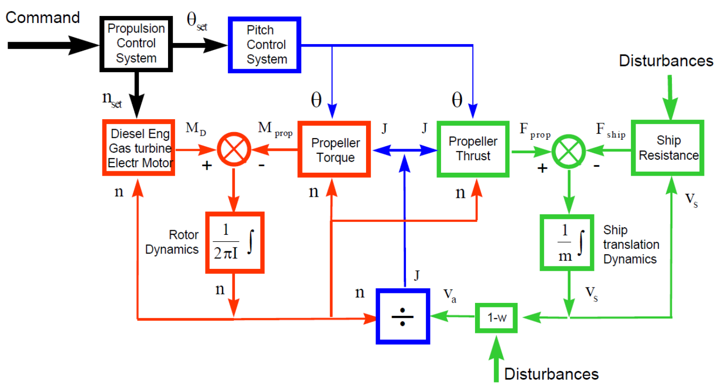


Figure 2.5: General ship propulsion block diagram, [Stapersma and de Heer, 2000]

More precisely, according [Stapersma and de Heer, 2000], the ship dynamic block diagram includes blocks representing the propulsion control system, the propulsion machine, the propulsor and the vessel's hull. At this point it should be mentioned that regarding the general ship propulsion diagram suggested by [Stapersma and de Heer, 2000], the gear box is not included for for clarity reasons. Moreover, it can be noticed that for the propulsion machine dynamic block diagram is general leaving to the user the option of selecting a Diesel engine, a gas turbine, an electric motor or any other device the user desires as the prime mover of the vessel's propulsion plant.

Closer observation of the structure of the ship dynamic block diagram could lead to the conclusion that the ship dynamic model can be divided in three main parts:

**Right Hand Side**

On the right hand side of the ship dynamic model, the hull of the ship is mathematically described by the resistance curve which is non linearly dependent on ship speed:

$$R = a \cdot v_s^2 \quad \text{with} \quad a = f(v_s)$$

On this side, the ship translation dynamics are included based on the force balance between propeller thrust and ship resistance. With those two forces being out of balance, a net force will result in an acceleration which can be integrated to calculate the ship speed:

$$\frac{d(m_{ship} \cdot v_s)}{dt} = F_{prop} - F_{ship}$$

where $m_{ship}$ is the total ship mass including the added water mass.

**Left Hand Side**

On the left hand side of the ship dynamic model, the rotational dynamics are included describing the balance between the propeller and shaft torque. Imbalance between these two torques results in a net torque which causes an angular acceleration. By integrating this angular acceleration, the shaft speed can be obtained:

$$2\pi \frac{d(I_p \cdot n)}{dt} = M_s - M_{prop}$$

where $I_p$ is the total polar moment of inertia of the rotating shaft system, including engine, gearbox, propeller and entrained water.

At this point it has to be stressed out that according to [Stapersma and de Heer, 2000] the type of propulsion machine is not selected in first place. However, later on in this paper a turbocharged Diesel engine is selected as the propulsion machine and the corresponding block diagram is shown which includes the cylinder model and the turbocharger dynamics. The cylinder model consists of two distinct parts; the cylinder flow model and the work and heat model. For the work and heat model a 6-point Seilinger is employed in order to obtain the work by calculating the mean effective pressure and thus the engine torque. The employment of Seilinger diagram requires the determination of trapped conditions by using the gas exchange model. Both models, work and heat model using the Seilinger diagram and gas exchange model are described in details, thermodynamic cycle and mass flows during positive scavenging for a four stroke Diesel engine [Grimmelius and Stapersma, 2000] and [Grimmelius and Stapersma, 2001].

Furthermore, [Kidd et al., 1985] and [Smith, 1988] describe ship propulsion plants which use gas turbines as propulsion machines. More specifically, propulsion plant and simulation model schematics are presented with [Kidd et al., 1985] documenting the mathematical equations describing the ship and propulsion machinery simulation model. The non-linear hull resistance characteristics and the non-linear propeller torque and thrust characteristics are described by linear functions which include steady state data. Additionally, the generated torque by the gas turbine is determined by a linear empirical equation, with the dynamics of the turbine torque being represented by a fixed first-order lag.

Besides the rotational dynamics and the propulsion machine, the left hand side of the ship dynamic model includes the propulsion control system. Depending on the variable that is selected to be the controlled variable, the propulsion control system has to be fed by the value of the corresponding output of the ship dynamic model. Furthermore, in order to control the chosen variable, the propulsion control system has to adjust a controlling variable. This controlling variable is either the fuel flow to the engine or the propeller pitch in case of controllable pitch propeller. A short discussion on different control strategies with respect to the chosen controlled and controlling variables and possible combinations of them is presented in following Section.

**Middle of the block diagram**

In the middle of the ship dynamic model, the propeller of the vessel is modelled. The physical lay-out and the block diagram of the ship's propeller is illustrated in Figure 2.6.

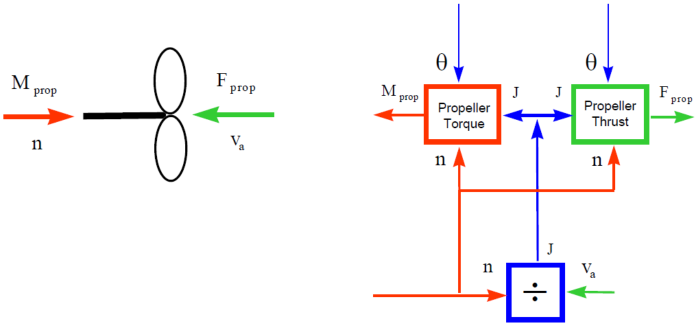


Figure 2.6: Physical lay-out (left) and block diagram of ship's propeller (right), [Stapersma and de Heer, 2000].

The required outputs of the propeller's block diagram are the propeller thrust T and torque Q:

$$T = \rho \cdot n^2 \cdot D^4 \cdot K_T(J, \theta)$$

$$Q = \rho \cdot n^2 \cdot D^5 \cdot K_Q(J, \theta)$$

$$J = \frac{v_a}{n \cdot D}$$

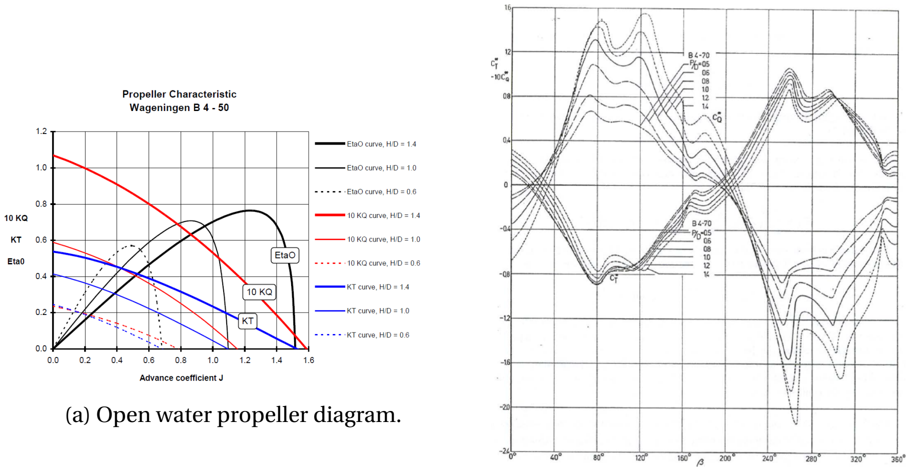


(a) Open water propeller diagram.

(b) Four quadrants diagram.

Figure 2.7: Propeller characteristics.

Propeller thrust and torque can be modelled based on the open water diagram for which thrust, $K_T$ and torque, $K_Q$ coefficient are dependent on the advance ratio, $J$ and on propeller pitch $\theta$, in case of controllable pitch propeller. What is more, the the propeller can be modelled based on the four quadrant diagram for which thrust, $C_T$ and torque, $C_Q$ coefficient are dependent on the hydrodynamic pitch angle $\beta$ and on propeller pitch $\theta$, in case of controllable pitch propeller. It has to be stressed out that in case of both diagrams the propeller block is considered to be a completely static element. As far as other propulsors are concerned, the performance like a Voith Schneider propeller or a water jet can be modelled by using $K_T - J$ and $K_Q - J$ non dimensional diagrams.

### 2.2.3. LINEARISED SHIP PROPULSION SYSTEM MODEL

The understanding and analysis of the behaviour of a non-linear ship propulsion plant contributes significantly to selection of the control strategy to be applied as well as to the design and tuning of the control system under consideration. Additionally, linear models are usually more simple and require less parameter and system knowledge compared to non-linear models. For that reason, linearised models derived from non-linear time domain simulation models are employed as valuable, additional tools for the analysis of the dynamic behaviour of ship propulsion plants. However, linearisation of non-linear system models comes at a cost; linear models can be considered valid only in the specific equilibrium point that the system model has been linearised for or in case of small perturbations around this specific equilibrium point. In this section, some techniques for the linearisation of ship propulsion plants are highlighted.

A complete linearisation process is documented in [Stapersma and Vrijdag, 2017]. In this work, the linear model of the non-linear uncontrolled, core ship propulsion system, which is illustrated in Figure 2.8 is derived.

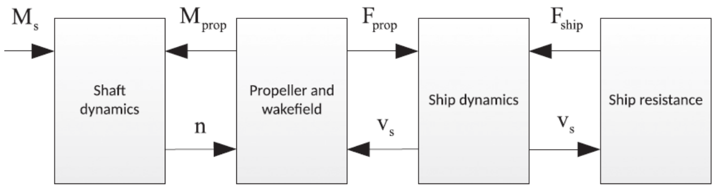


Figure 2.8: Core ship propulsion block diagram, [Stapersma and Vrijdag, 2017].



Additionally, the authors call attention to the fact that during the linearisation process some non-linearities are neglected, introducing in that way considerable limitations for the linearised ship propulsion system model. The non-linearities which are neglected can be summarised in the following three categories:

- Non-linearity due to curvature in the characteristics of component models, for instance the curvature of the propeller characteristics.
- Non-linearity due to multiplication, division and general power operations like for instance: $T = \rho \cdot n^2 \cdot D^4 \cdot K_T(J,\theta)$, $J = \frac{v_a}{n \cdot D}$ and $R = a \cdot v_s^e$.
- Non-linearity due to hard limits of the non-linear simulation model. Mechanical end-stop of fuel rack and minimum and maximum pitch of a hydraulic controllable pitch propeller can be considered as such hard limits. What is more, limits applied in the engine governor in order to protect the engine are also neglected.

Besides the limitations which are introduced by neglecting important non-linearities during the linearisation process, [Stapersma and Vrijdag, 2017] extensively presents the necessary mathematical background on the normalisation and linearisation process. Giving a summary of the procedure that is documented there, a variable that is the product of powers of other variables:

$$Z = c \cdot Y^e \cdot X$$

can be linearised and normalised. By using the shorthand notation for differential increment given by:

$$\delta Z^* \equiv \frac{\delta Z}{Z_0}, \delta Y^* \equiv \frac{\delta Y}{Y_0}, \delta X^* \equiv \frac{\delta X}{X_0}$$

the product of powers can be approximated by:

$$\delta Z^* = \delta X^* + e \cdot \delta Y^*$$

What is achieved in that way is that the relative change in output Z is related to the relative change in inputs X and Y with the exponent e in the original equation being changed to a constant multiplication factor. On the other hand the multiplication of X and Y in the original equation has been transformed into a summation of their relative changes.

Apart from the linearisation of the system following the above mentioned process, [Stapersma and Vrijdag, 2017] derives the transfer functions of the linearised system by making use of the Laplace transform. Moreover, the stability of the derived linear model is investigated by determining the location of the poles of the system in the complex plane.

In [Vrijdag and Stapersma, 2017] which is directly related to [Stapersma and Vrijdag, 2017], the authors extend the core ship propulsion system model which is linearised. The derived linear model is verified and applied to examine the dynamic behaviour of the elliptic trajectory of the engine operating point in the engine operating envelope in case of regular waves. Following the same mathematical technique for the normalisation and linearisation as [Stapersma and Vrijdag, 2017], the non-linear ship propulsion system model which now includes the propulsion machine, the propeller pitch actuator and the propulsion system controller is linearised. The derivation of the linear system model takes place in steps by starting with core ship propulsion system, then adding the diesel engine and finally linearising the controlled propulsion system which includes the Diesel engine controller. This procedure is shown in Figure 2.9.

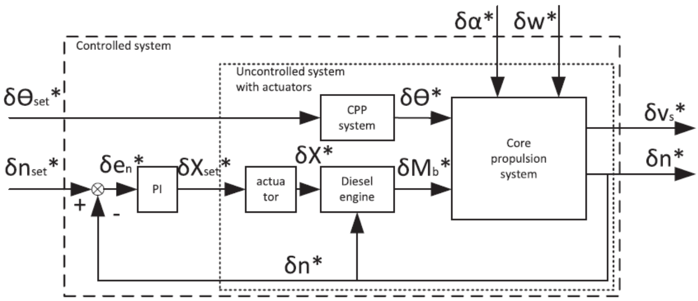


Figure 2.9: Block diagram showing the linearisation in three steps, [Vrijdag and Stapersma, 2017].

In this work the authors decides to focus on a Diesel engine regarding the propulsion machine, which is modelled by using a map of the engine which relates the inputs which are the engine speed $n_e$ and the fuel rack setpoint $X_{set}$ with the output which is the brake engine torque $M_b$. In addition to the Diesel engine and the propeller pitch actuator, the propulsion controller which is included to the model is a classic engine speed governor with a PID controller.

As it was previously mentioned, the linearisation of the ship propulsion system model takes place so as to examine the dynamic behaviour of the ship propulsion system in the frequency domain. In order to achieve that, [Stapersma and Vrijdag, 2017] derived the transfer functions by using the Laplace transform of the mathematical equations describing the linear system. On the other hand, [Vrijdag and Stapersma, 2017] suggests the State-Space notation in order to obtain the dynamic response of the linear system in the frequency domain. The State-Space method is less laborious compared to the derivation of transfer functions. On top of that it can be easily implemented and analysed by using software tools from the field of Systems and Controls. The State-Space form that is used is given by:

$$\dot{\mathbf{x}} = A\mathbf{x} + B\mathbf{u} + G\mathbf{w}$$

$$\mathbf{y} = C\mathbf{x} + D\mathbf{u} + \mathbf{v}$$

The first equation is called the state equation and the second one is called is called the output equation. With respect to the variables, variable A is the system matrix, B is the input matrix, G is the gain matrix for disturbances, C is the output matrix and D is the direct coupling matrix between input and output. As far as **x**, **u**, **y** and **v** are concerned, they are respectively the state vector, input vector, output vector and sensor noise vector with the latter not being considered. After that the derived linear ship propulsion system model is verified by means of step responses. This means that the step responses of the outputs of the propulsion system model caused by step disturbances of different amplitude of the system inputs are compared between the non-linear and the linear model. The verification process gives a sense of whether the derived linear model can rightfully be applied in order to investigate the dynamic behaviour of the system in case of realistic disturbances around the equilibrium point. Finally, by making use of the derived Bode plots of the linear propulsion system model, [Vrijdag and Stapersma, 2017] examines the dynamic response of the elliptic trajectory of the engine operating point in the engine operating envelope for different frequencies of regular waves and different combinations of settings of the Diesel engine governor. Similarly, the dynamic behaviour of the engine operating point is investigated in case of irregular waves for head and following direction of the vessel with respect to the waves.

Besides ship propulsion plants that use Diesel engine as propulsion machines [Smith, 1988] and [Kidd et al., 1985] describe the linearisation of ship propulsion system models that employ gas turbines as propulsion machines. More specifically, [Smith, 1988] the linear model of the ship propulsion system including the gas turbine by making use of the State-Space notation. The derived linear model is then validated by means of comparison between the step response of outputs of the non-linear and linear model testing their level of agreement. On the other hand [Kidd et al., 1985] linearises the ship propulsion system which includes a gas turbine as propulsion machine by making use of the Laplace transform in order to derive the required transfer-function matrix which describes mathematically the linear system.

## 2.3. PROPULSION CONTROL STRATEGIES

In the current section an overview of different control strategies of ship propulsion plants is given. The most common propulsion control architectures are presented together with alternative control strategies.

### 2.3.1. IDEAS ON PROPULSION CONTROL

**No Feedback Control**

Following [Stapersma et al., 2004] and [Stapersma and Grimmelius, 2009], a ship propulsion plant has two controlling variables, the fuel rack and the propeller pitch. Combination of these two variables in a single lever command results in the most simple propulsion control, which is called “no control”or more precisely “no feedback control”, as shown in Figure 2.10.

2

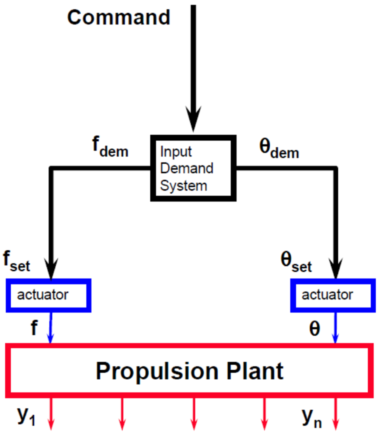


Figure 2.10: Propulsion control without feedback, [Stapersma and Grimmelius, 2009].

#### Single Output Control

A ship propulsion plant has many outputs which can be employed as controlled variables; engine speed, torque, thrust, ship speed. In the control strategy of single output control, a single output variable of the propulsion system is selected as controlled variable. The actual measured variable is compared to the demand value as determined by the ship operator is fed to the controller. This controller can be placed in front of one of the two controlling variables; either the fuel rack or the propeller pitch. The most common propulsion control architecture is the one that employs the engine speed as the controlled variable and the fuel rack as the controlling variable, with the pitch remaining constant.

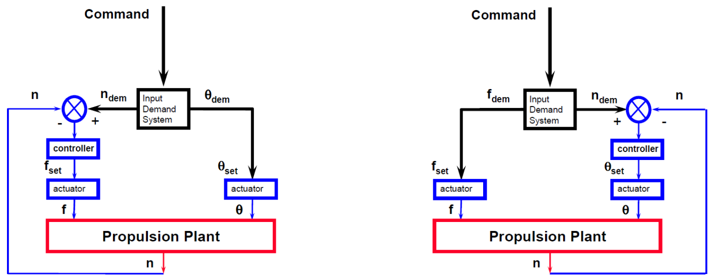


Figure 2.11: Engine speed control by fuel rack on the left or by propeller pitch on the right, [Stapersma and Grimmelius, 2009].

Given that the ship propulsion system has two controlling variables, an alternative to the above mentioned most common control practice is the use of propeller pitch setting as the controlling variable with the engine speed being the controlled variable. The layout of such propulsion control is shown in Figure 2.11.

#### Control of Two Outputs

Apart from the control strategy of using only one output of the vessel propulsion system as controlled variable with the engine speed being the most common controlled variable, the use of two controlled variables is also applied in modern propulsion control systems.

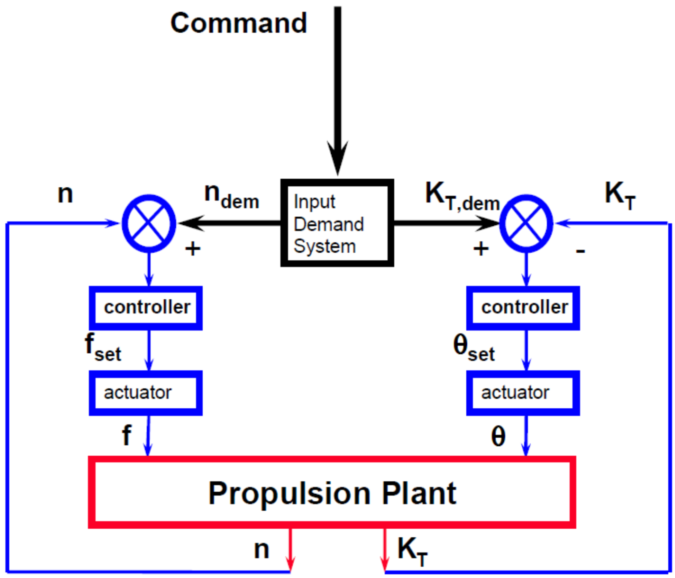


Figure 2.12: Propulsion control with two controlling variables and two controlled variables, [Stapersma and Grimmelius, 2009].

The design and implementation of propulsion control systems with two controlled variables requires two controlling parameters which already exist for ships with controllable pitch propellers. As a result the most common layout of control systems controlling two outputs of the ship's propulsion system is the one shown in Figure 2.12, where the engine speed is controlled by adjusting the fuel rack. In Figure 2.12 the second variable which is controlled by the propeller pitch is the non-dimensional thrust coefficient, $K_T$, since it is preferred one of the two controlled variables to be a "commanding"variable, that means monotonically proportional but not necessarily linearly proportional to the ultimate objective which is the ship speed. Additionally, there is the option to change sides and make the engine speed controlled by the propeller pitch and the non-dimensional thrust coefficient, $K_T$, controlled by the fuel rack position.

Moreover, according to [Stapersma et al., 2004] in case of control of two outputs, except for the non-dimensional thrust coefficient $K_T$, there are more outputs of the ship propulsion system which can be considered as controlled variables. Provided that the controlling variables are two:

- fuel rack
- propeller pitch

the list with candidates as controlled variables could include:

- engine speed, $n_e$
- ship speed, $v_s$

- torque, $Q$
- thrust, $T$
- non-dimensional torque coefficient, $K_Q$
- non-dimensional thrust coefficient, $K_T$
- advance coefficient, $J$
- exhaust temperature, $T_{exh}$
- thermal wear parameter diesel engine
- mechanical wear parameter diesel engine

As it can be seen in Figure 2.12 both controllers act in parallel. Besides this, a layout with the two controllers acting in series either on the side of fuel rack or on the side of propeller pitch can also be implemented.

A better insight on the advantages and disadvantages of different combinations of the above mentioned controlled and controlling variables is given in [Stapersma et al., 2004] and [Stapersma and Grimmelius, 2009]. Different controlled variables can generate multiple propulsion control designs with the optimal selection being dependent on the operating profile of the vessel and the ultimate objective of the propulsion control which could be for instance command of ship speed, manoeuvrability or cavitation-free operation of the vessel. At this point it should be mentioned that for the scope of this thesis, the possibilities of refinement of the already existing propulsion control are examined. This means that since the propulsion controller of the examined reference vessel is a classic engine speed governor, only the single output control architecture will be investigated and more specifically the case that the engine speed is controlled by changing the fuel rack.

## 2.4. WAVE DISTURBANCE REJECTION TECHNIQUES ON DIESEL ENGINES

In this Section a short overview of techniques used to reject the wave disturbances acting on Diesel engines and causing overloading or other negative impacts.

[Jiang, 1994] develops a generalised gain scheduling control mechanism for Diesel engines based on offline optimisation techniques. More specifically, the linear model of Diesel engines are derived for specific operating points. Then the optimal values of the settings of a PID controller are determined by making use of off-line numerical optimisation aiming at minimising the integral squared error (ISE) of the engine speed deviation when applying a step speed change command:

$$j\left(K_p, K_i.K_d\right) = \min \int_0^{\infty} [e(t)]^2 \, dt$$

The numerical optimisation that is employed is sequential quadratic programming. The derived gain scheduling control scheme is evaluated on a real engine under multiple tests. The outcome of the tests is that the performance of the engine with the designed control scheme is better compared to the existing engine governor. What is more, the connection between of the controller settings and the engine fuel efficiency is investigated with the drawn conclusions stressing out that the developed gain scheduling controller has better fuel efficiency.

[Pan et al., 2010] attempts to change the classic PID algorithm that is commonly applied in engine speed governors in order to reject disturbances acting on marine Diesel engines. Given that the control process of a marine Diesel engine speed is highly nonlinear and time varying due to the dynamic environment it is considered extremely difficult to achieve optimal control system behaviour in terms of robustness to the nonlinear characteristic of the ship and the disturbances acting on the system.

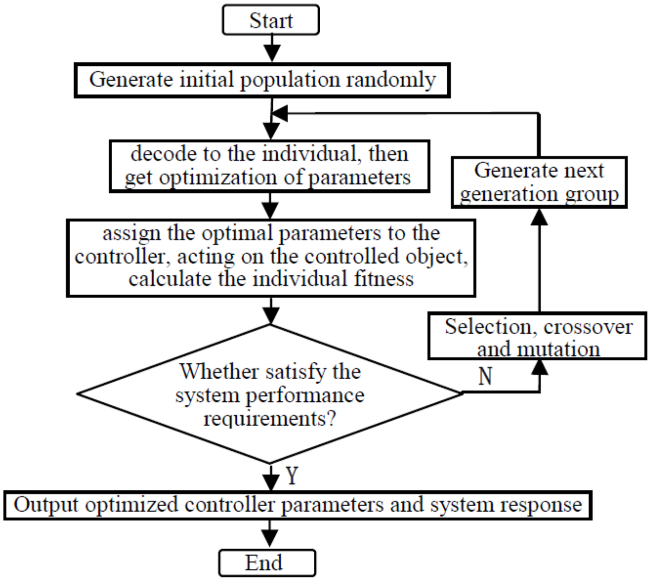


Figure 2.13: Flow chart of genetic algorithm optimisation process, [Pan et al., 2010].

For that reason, [Pan et al., 2010] develops an Active Disturbance Rejection Controller (ADRC) in order to improve the disadvantages of the classic PID controller. In this work the dependence of the performance of an ADRC on its large number of parameters is pointed out. Some of these parameters need to be adjusted on-line during the operation of the ship. In order to deal with this challenge, a genetic algorithm is applied for the online optimal selection of values of the ADRC parameters when this is required always depending on the disturbance acting on the engine. After executing some simulation tests with the developed ADRC being applied on a marine Diesel engine the results regarding the performance of the controller are quite promising; speed response of optimal ADRC controller is faster and smoother compared to the classic PID controller. Additionally, the speed response seems to be quite smooth and accurate in case of load changes due to disturbances.

An attempt for disturbance rejection is made by [Van Spronsen and Tousain, 2001] who suggests the investigation of control strategies based on $H_\infty$ control, aiming to prevent the overloading of marine Diesel engines when vessel sails in waves. More precisely, in this work the goal is to avoid the violation of the reduced time between overhaul (RTBO) line, which is defined by the engine manufacturer and can be noticed in Figure 2.14. [Van Spronsen and Tousain, 2001] attempts to achieve that by optimising existing control architectures and by introducing more control variables.

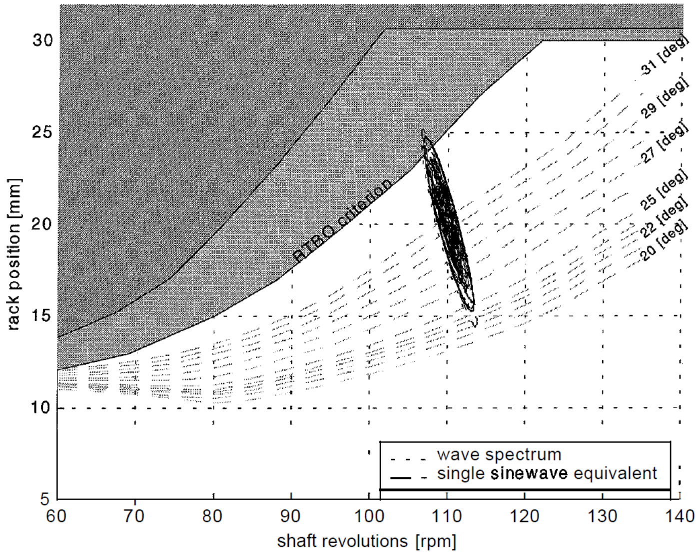


Figure 2.14: Violation of RTBO line due to wave disturbance.

As a first step, [Van Spronsen and Tousain, 2001] tries to improve the existing controller by reducing the control effort and thus the response and sensitivity of the fuel rack position. The second choice is an attempt to give to the disturbance the desired shape in the engine operating envelope. This does not mean that the control effort is again reduced but rather shifted to a more favourable location in the engine operating envelope like for instance a dynamic response whose orientation is parallel to the RTBO line.

Another attempt of [Van Spronsen and Tousain, 2001] to prevent marine Diesel engine's overloading involves the introduction of another controlling variable. This controlling variable is the propeller pitch whose variations are able to effectively counteract the impact of the Sea State on the Diesel engine in terms of causing fluctuations to the propeller torque. Finally, [Van Spronsen and Tousain, 2001] integrates both fuel rack control and propeller pitch control by introducing a Multiple Input Multiple Output control concept. The tracking performance of this control concept is optimised by optimising the weightings of the controller which weigh the sensitivity of the response of the controlling variables with respect to the disturbance input always aiming for disturbance rejection and prevention of Diesel engine overloading. According to [Van Spronsen and Tousain, 2001] conclusions the implementation of Single Input (fuel rack position) Single Output (shaft speed) does not give satisfactory results in terms of waves disturbance rejection. On the other hand, the employment of a more complex Multiple Input Multiple Output controller including time optimal response solutions at the same time ends up with more promising results regarding disturbance rejection and prevention of marine Diesel engine overloading.

Similarly to [Van Spronsen and Tousain, 2001], [Xiros, 2004] makes use of the linear model of ship propulsion system which is mathematically described by a reduced second-order transfer function in order to design a typical PID Diesel engine speed governor based on sensitivity $H_\infty$-norm specification. [Xiros, 2004] aims at improving the governor's performance in case of counteracting severe load fluctuations caused by heavy weather.

## 2.5. Ship Propulsion System Model Disturbances

This section contains a presentation of the disturbance inputs that act on the ship propulsion system model. These two disturbance inputs, which act on ship resistance and on wakefield, can be attributed to a variety of reasons. However, as far as this thesis is concerned, they are both due to waves interacting with the vessel. Furthermore, some information, regarding the approaches used in order to calculate these two disturbances is given in the following subsections. A detailed insight can be found in the suggested literature.

### 2.5.1. Wake Field Disturbance Due To Waves

The first of the main disturbances acting on the propulsion system, that will have to be modelled in this thesis, is the wake field disturbance. With respect to the ship propulsion system model, the wake field disturbance can be located at some point after the ship's translation integrator in the simulated propulsion model as in can be noticed in Figure 2.5. Caused by wave fields and the waves induced ship's motions, the wake field disturbance leads to variations of the wake speed seen by the propeller, which in turn affects the propeller torque and dynamic behaviour of the prime mover.

A significant amount of research has been conducted by [Aalbers and van Gent, 1984, van Terwisga et al., August 8-13 2004, Taskar et al., 2016, Ueno et al., 2013], aiming to model the wake fluctuations, which is necessary for the analysis of the prime mover-propeller interaction in case of sailing in waves.

A thorough study existing in literature and gives a clear picture for the case of a ship moving in waves, regarding the unsteady wake velocities is [Aalbers and van Gent, 1984]. In this work, an effort is addressed to define the factors contributing to the unsteady wake field. According to the linear wave theory, the total wake field is assumed to be a linear superposition of the contribution of the steady wake field, which is the wake field developed when the ship sails in calm water and the unsteady seakeeping components, in other words the contributions of waves and ship motions to the wake field. Attempting to validate the theory of linear superposition, in [Aalbers and van Gent, 1984] some tests were performed, during which, the unsteady velocities in the wake of frigate type ship model were both measured and calculated. During these tests, two scenarios were investigated:

- a model towed in head waves, being restrained at static equilibrium draught and trim
- a model towed in head waves, being completely free in its six-degrees of freedom

The validity of the linear superposition theory is examined by comparing the average value of the advance speed in waves with the advance speed in calm water that was measured during both test series that were carried out. The drawn conclusion is that the results from the calculation of the linear superposition following the theory agree in sufficient level with the measurements done in the tests. Consequently, the linear superposition theory is considered to be valid.

Following the same theory in [van Terwisga et al., August 8-13 2004], a simulation tool is applied to a naval ship and its propeller, in order to demonstrate the effect of sea state, heading and propeller control strategy on the cavitation inception speed. For the development of the simulation tool, the total wake field is modelled, following the same decomposition of the components contributing to the total wake field, as in [Aalbers and van Gent, 1984]. This results in the following mathematical approach of the total wake field:

$$\begin{aligned}\overline{V}^{eff}_{total} &= \overline{V}^{eff}_{calmwater} + \overline{V}_{waves} \\ &= \overline{V}^{n}_{cw} + \overline{V}^{int}_{cw} + \overline{V}^{i}_{wi} + \overline{V}^{d}_{wi} + \overline{V}^{r}_{wi} + \overline{V}^{t}_{sm}\end{aligned} \tag{2.1}$$

According to the approach presented in [van Terwisga et al., August 8-13 2004], the total calm water (cw) wake field, $\overline{V}^{tot}_{cw}$ consists of:

- the nominal wake field, $\overline{V}^{n}_{cw}$, which is caused by the hull of the vessel and its appendages when the propeller is not implemented on the vessel yet
- the propeller induced wake field, $\overline{V}^{i}_{cw}$, which is attributed to the propeller action in an already existing wake field
- the propeller-wake interaction wake field, $\overline{V}^{int}_{cw}$, which includes the effect of the propeller suction on the incoming hull flow and on the vorticity distribution

Since, usually the total, $\overline{V}^{tot}_{cw}$ and the induced, $\overline{V}^{i}_{cw}$, wake field are not available, the effective, $\overline{V}^{eff}_{cw}$ wake field in calm water is used, which can be decomposed in the following components:

$$\overline{V}^{eff}_{cw} = \overline{V}^{tot}_{cw} - \overline{V}^{i}_{cw} = \overline{V}^{n}_{cw} + \overline{V}^{int}_{cw} \tag{2.2}$$

As far as the unsteady wake field is concerned, this is composed of:

- the undisturbed incoming waves orbital velocity, $\overline{V}^{i}_{wi}$
- the wave system velocity which is partly reflected on the hull, resulting in a diffracted wave system, $\overline{V}^{d}_{wi}$

- the wave system velocity which is radiated by the hull due to ship motions, $\overline{V}^{r}_{wi}$
- the velocities introduced to the propeller plane because of the ship motions, $\overline{V}_{sm}$. The corresponding wake field experienced by the propeller is $\overline{V}^{t}_{sm} = -\overline{V}_{sm}$



Another example, regarding the effort done to describe mathematically the wake velocities, is [Ueno et al., 2013]. In this work, measurements take place in order to estimate the inflow velocity in real time, based on thrust and torque variations in unsteady conditions. Furthermore, it is claimed that the results, with regard to the fluctuating wake velocities, are dominated by the wave induced particle motion and surge motion of the ship, whereas the effect of oscillation of the propeller position, in other words the effect of heave and pitch motion is negligible. Thus, the following formula is derived, regarding the estimation of the inflow velocity:

$$\begin{aligned} V_{fluctuating} =& (1-w)\{U - \omega_e \xi_a \sin(\omega_e t - \epsilon_\xi)\} \\ & + \alpha \omega h_a \exp(-k z_P) \cos\chi \cos(\omega_e t - k x_P \cos\chi) \end{aligned} \tag{2.3}$$

where

| | |
|---|---|
| $h_a$ | :amplitude of incoming regular wave |
| $k$ | :incoming regular wave number |
| $\omega$ | :incoming regular wave circular frequency |
| $\omega_e$ | :wave encounter circular frequency |
| $U$ | :average ship speed |
| $\xi_a$ | :surge motion amplitude |
| $\epsilon_\xi$ | :surge motion phase delay |
| $(x_P, 0, z_P)$ | :propeller co-ordinates |
| $t$ | :time |

Eq. (2.3) describes the wake flow including the surge oscillation effect and the orbital motion of water particles in an attenuated wave at the stern. The effect of the interaction of the wave with the hull, until it reaches the propeller, is included in coefficient $\alpha$, which also takes also, into consideration the impact of the encounter angle $\chi$:

$$\alpha = \begin{cases} 0.2\left(\frac{\lambda}{L|\cos\chi|}\right) + 0.5, & \text{for } \frac{\lambda}{L|\cos\chi|} \leq 2.5 \\ 1, & \text{for } 2.5 \leq \frac{\lambda}{L|\cos\chi|} \end{cases} \tag{2.4}$$

Differences for some wave encounter angles comparing test results and theoretical calculations in [Ueno et al., 2013] are attributed to the poor estimation of wave amplitude attenuation, calculated in Eq. (2.4).

Following the same approach, concerning the wake field model, in [Taskar et al., 2016] the impact of a range of waves (head, bow-quartering, following and stern-quartering) on the propulsion efficiency has been studied. Effects of events like propeller emergence and propeller operation near the free surface are taken into account. The thrust and torque losses for the former phenomenon are assumed proportional to the out of the water area of the propeller. The effect of the latter phenomenon is calculated by using a thrust and propeller torque reduction factor. As for the wake velocities, the contribution of wave induced orbital motion and surge ship motion are modelled as in [Ueno et al., 2013]. Additionally, the ship's pitch motion contribution was taken into consideration, by the following term:

$$V_{mean} = \sqrt{\left(1 - \frac{\Delta\overline{p}}{0.5\rho U^2}\right)} \tag{2.5}$$

This term is added to Eq. (2.3), resulting in the following equation, which contains the wave induced orbital motion, as well as the surge and pitch ship motion contributions:

$$\begin{aligned} V_{fluctuating} &= (1-w)\{U - \omega_e \xi_a \sin(\omega_e t - \epsilon_\xi)\} \\ &+ \alpha\omega h_a \exp(-k z_P) \cos\chi \cos(\omega_e t - k x_P \cos\chi) \cdot \sqrt{\left(1 - \frac{\Delta\overline{p}}{0.5\rho U^2}\right)} \end{aligned} \tag{2.6}$$

In Eq. (2.6), $\Delta\overline{p}$ stands for the pressure gradient below the bottom of the vessel due to pitch motion estimated by:

$$\Delta\overline{p} \sim -\frac{\rho}{4}\omega_e^2 |\eta_5|^2 x^2 \tag{2.7}$$

where:

| | |
|---|---|
| $\eta_5$ | :pitch motion amplitude |
| $x$ | :longitudinal distance of the propeller from the centre of gravity of the ship |

Time varying wake velocities calculated based on Eq. (2.6) were compared to wake data in waves. Sufficient matching between the two, led to the decision of using Eq. (2.6) to obtain wake variations in different wake conditions.

## WAVE INDUCED PARTICLE MOTIONS

As it was mentioned before, part of the contributions to the unsteady wake velocities for a vessel sailing in wave field, is the undisturbed incoming waves. In other words, this is referred to the undisturbed wave orbital velocity. In this thesis, this component of the breakdown of the total wake field, as it was presented in [Aalbers and van Gent, 1984, van Terwisga et al., August 8-13 2004], is the only one extensively presented. The reason for that is that it is the only component, which will be taken into account for the generation of wake disturbance time signals.

What is meant by *undisturbed wave orbital velocity*, is the orbital motion of the water particles under a harmonic wave, usually observed in a two-dimension wake field. Additionally, there is a velocity, called *orbital velocity*, corresponding to motion of particles in closed, circular or elliptical orbits. This kind of motions and velocities, due to harmonic oceanic waves are documented in [Holthuijsen, 2007, Journée and Massie, 2000, Krogstad and Arntsen, 2000].

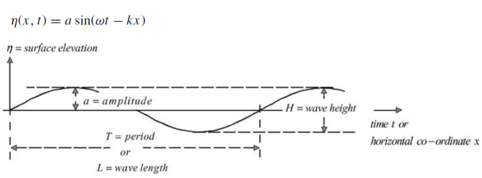


Figure 2.15: A propagating harmonic wave, [Holthuijsen, 2007].

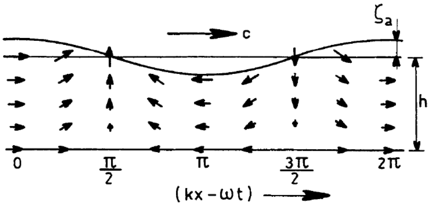


(a) Shallow Water Wave

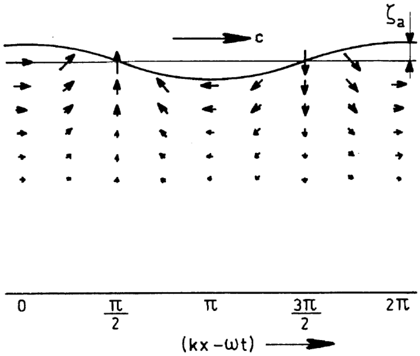


(b) Deep Water Wave

Figure 2.16: Velocity fields in waves, [Journée and Massie, 2000].

According to the aforementioned literature, the water particle velocities can be obtained from the spatial derivatives of the velocity potential $\phi$, $\frac{\partial \phi}{\partial x} = u_x$ and $\frac{\partial \phi}{\partial z} = u_z$. This results in:

$$u_x = \hat{u}_x \sin(\omega t - kx) \qquad \text{with} \qquad \hat{u}_x = \omega \alpha \frac{\cosh[k(d+z)]}{\sinh(kd)} \tag{2.8}$$

$$u_z = \hat{u}_z \cos(\omega t - kx) \qquad \text{with} \qquad \hat{u}_z = \omega \alpha \frac{\sinh[k(d+z)]}{\sinh(kd)} \tag{2.9}$$

where:

| | |
|---|---|
| $\alpha$ | :wave amplitude |
| $k$ | :wave number |
| $d$ | :water depth |
| $\omega$ | :harmonic wave frequency |
| $z$ | :vertical co-ordinate |
| $x$ | :horizontal co-ordinate |
| $t$ | :time |

In case of *deep* water, when $kd \to \infty$ the expressions for the amplitudes of the velocity components $\hat{u}_x$ and $\hat{u}_z$ become:

$$\hat{u}_x = \omega \alpha e^{kz} \qquad \text{and} \qquad \hat{u}_z = \omega \alpha e^{kz} \tag{2.10}$$

From these expressions, one can easily extract the conclusion that in deep water, the wave induced velocities decrease exponentially with the distance to the surface, given that $z < 0$ below the still-water surface. On the other hand, in case of *very shallow* water, when $kd \to 0$, the expressions for the amplitudes of the velocities become:

$$\hat{u}_x = \frac{\omega \alpha}{kd} \qquad \text{and} \qquad \hat{u}_z = \omega \alpha \left(1 + \frac{z}{d}\right) \tag{2.11}$$

The conclusion drawn by Eq. (2.11) is that for very shallow water, the amplitude of the horizontal velocity is independent of the depth of the observed water particle with respect to the still-water surface. On the contrary, the amplitude of the vertical velocity is linearly dependent on the depth of the water particle under consideration, with respect to the still-water surface. Regarding the path of a water particle, is obtained by integrating the corresponding velocity in time. Assuming a particle located at an arbitrarily chosen point with co-ordinates $\overline{x}$, $\overline{z}$, the local co-ordinates will be defined as $x'$ and $z'$, always centred on $\overline{x}$, $\overline{z}$. The integration of velocity equations, Eq. (2.8) and (2.9), will lead to:

$$x' = -\alpha \frac{\cosh\left[k(d+\overline{z})\right]}{\sinh(kd)} \cos(\omega t - k\overline{x}) \tag{2.12}$$

$$z' = \alpha \frac{\sinh\left[k(d+\overline{z})\right]}{\sinh(kd)} \sin(\omega t - k\overline{x}) \tag{2.13}$$

The horizontal, $x'$ and vertical position, $z'$, are formulas of cosine and sine in time, respectively. Therefore, each water particle's trajectory can be represented as an ellipse equation:

$$\frac{x'^2}{A^2} + \frac{z'^2}{B^2} = 1 \tag{2.14}$$

Consequently, the horizontal and vertical semi-main axes are respectively:

$$A = \alpha \frac{\cosh\left[k(d+\overline{z})\right]}{\sinh(kd)} \tag{2.15}$$

$$B = \alpha \frac{\sinh\left[k(d+\overline{z})\right]}{\sinh(kd)} \tag{2.16}$$

In case of deep water, when $kd \to \infty$, the values of the length of the two above mentioned axes become equal, $A = B$.

$$r = \alpha e^{kz} \tag{2.17}$$

According to Eq. (2.17), the water particles move in circles with the radius being reduced exponentially with the distance to the surface, since $z < 0$ below the still-water surface, as shown in Fig. 2.17.

In case of very shallow water, when $kd \to 0$, the lengths of the axes are $A = \frac{\alpha}{(kd)}$ and $B = \alpha(1 + \frac{z}{d})$. As a result, water particles trajectory is an ellipse which becomes flatter as the water particle approaches the bottom. With the vertical axis being dependent on the distance from the still-water surface, it is obvious that $B \to 0$ as $z \to -d$, while the horizontal axis remains constant, as it is independent of the distance from the still-water surface, $A = \frac{\alpha}{(kd)}$. As far as the bottom position is concerned, $z = -d$, the ellipse is degenerated to a straight, horizontal line, as it is depicted in Fig. 2.17.

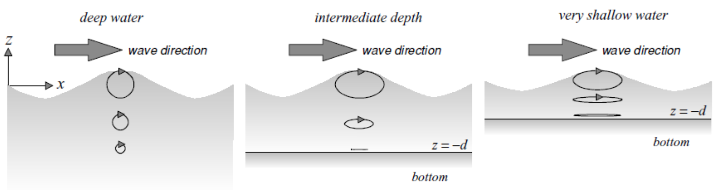


Figure 2.17: The orbital motion of water particle in deep, intermediate-depth and very shallow water respectively, [Holthuijsen, 2007].



### 2.5.2. ADDED RESISTANCE IN WAVES

The second one of the two main disturbances acting on the propulsion system, is the ship resistance disturbance. With regard to the propulsion system model, as it can be seen in Figure 2.5, the resistance disturbance is located at the Ship Resistance block. *Resistance disturbance* is caused by additions to the nominal ship resistance. These additions can be attributed to degradation of performance in time, because of hull fouling and to operational conditions, like displacement variations, sea state and water depth under the keel [Woud and Stapersma, 2002]. As far as this thesis is concerned, resistance disturbance on the propulsion system model is considered to be the result of sea state.

The resistance disturbance concerned in this thesis, as the result of sea state, is called added resistance in waves. In particular, when a vessel sails in a wave field, two kinds of waves are generated:

- Waves related to the forward speed in still water
- Waves related to the vessel's vertical relative motion response to incident waves

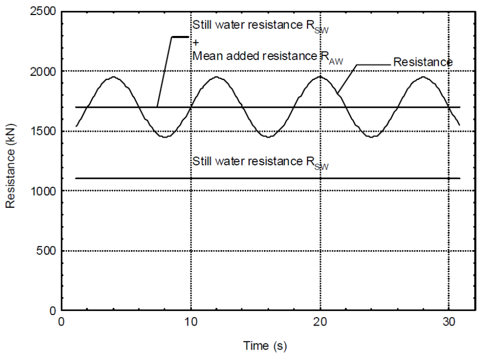


Figure 2.18: Extra-induced energy loss when sailing in regular waves, [Journée and Massie, 2000].

Both kinds of generated waves dissipate ship energy. For this reason, it is, rightfully, considered that a vessel moving in waves will dissipate more energy than a vessel sailing in calm water. This extra-induced loss of energy is called *added resistance in waves.*

The fact that the added resistance has a significant impact on the vessel's propulsion system design and consequently on its economical exploitation, has spurred a considerable amount of research, in order to examine different methods applied to obtain the added resistance in waves of a ship, trying at the same time to validate their results against sea keeping tests. A valuable overview of this research is well documented in [Journée and Massie, 2000, Arribas, 2007, Alexandersson, 2009, Strom-Tejsen et al., 1973].

One of the conclusions that can be extracted, regarding the calculations for the added resistance, after studying this literature, is that they are based on the prediction of ship motions in a realistic seaway. It has to be pointed out, that the research done takes into account only heave and pitch motions for the performance of the vessel in head seas. The reason for that is that the estimation of the added resistance in case of waves direction other than head seas is considered to be complicated, due to the complexity of the impact of motions of roll, yaw and sway, which has to be taken into account. Additionally, head waves are considered to be the most difficult condition, leading to maximum added resistance for a ship.

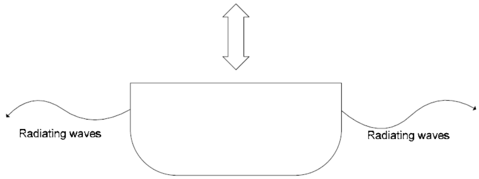


Figure 2.19: Radiating waves due to oscillatory motion, [Alexandersson, 2009].

As far as the analysis of the added resistance due to waves in head seas is concerned, it can be simplified by decomposing it to three separate components:

- A component resulting from interference between incident waves and waves generated by the ship, due to heave and pitch motions. This component is called *drifting force*.
- A component which is related to the damping force of the heave and pitch motions of the ship in waves.
- A component associated to the wave reflection against the ship, called *diffraction effect*.

These three components are related to the energy supplied from the ship to the surrounding water. Apart from a very small part of the energy loss, which can be attributed to the viscous friction, all the rest is considered to be generated by the ship propulsion plant and transmitted to the waves generated by the ship. In other words, hydrodynamic damping of ship motions (heave and pitch) is dominating compared to the viscous damping, which is considered to have minor impact to the added resistance, which consequently can be assumed to be a non-viscous phenomenon. An additional drawn conclusion is that the added resistance can be divided in radiation and diffraction induced resistance. More specifically, the radiation induced resistance is dominating in the region of frequencies around the resonance frequency of heave and pitch motions, with the peak of the added resistance occurring at the frequency that the wavelength is about the same as the vessel's length. This can be attributed to the pitch motion that has also its peak at that frequency. On the other hand, it is reasonable to consider that the diffraction induced resistance is dominating in the region of frequencies where the ship motions are small, that means in the region of high wave frequency. This is illustrated in Figure 2.20.

Regarding the analytical methods that can be used for the calculation of added resistance, a number of general conclusions can be drawn:

- The added resistance is proportional to the square of the wave height.

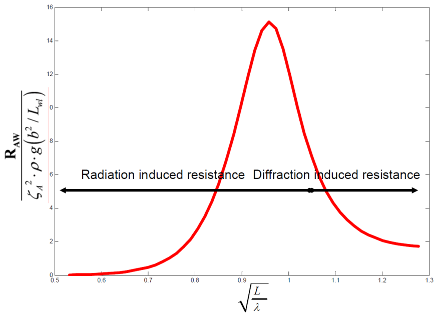


(a) Radiation and diffraction induced resistance for a range of frequencies.

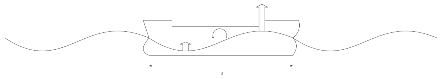

(b) Wavelengths near ship length producing maximum pitch motion and added resistance.

Figure 2.20: Added resistance value behaviour through frequency range, [Alexandersson, 2009].

- The added resistance is independent of the calm water resistance.
- The added resistance is dependent on the motions and their phase relationship to the wave field.

Some of the most well-known analytical methods for the calculation of added resistance are, briefly, presented below:

**Havelock formulation:** One of the first attempts to deal with the problem of calculating the resistance increase in regular waves was the work of [Havelock, 1942], which resulted in an expression as a function of heave, $z_\alpha$ and pitch, $\theta_\alpha$, amplitude described below:

$$R_{AW} = -\frac{k}{2}\left(F_\alpha z_\alpha \sin\epsilon_{zF} + M_\alpha \theta_\alpha \sin\epsilon_{\theta M}\right) \tag{2.18}$$

where:

| | |
|---|---|
| $k$ | :wave number [-] |
| $F_\alpha$ | :exciting force amplitude [N] |
| $M_\alpha$ | :exciting moment amplitude [Nm] |
| $\epsilon_{zF}$ | :phase angle between exciting function and response for heave [-] |
| $\epsilon_{\theta M}$ | :phase angle between exciting function and response for pitch [-] |

Despite the fact that this formulation lacks of accuracy given that it does not take into account the diffraction of waves, viscous damping and pitch and heave coupling, it is considered the first step and a fundamental work, providing a simple way to calculate the added resistance in waves, since there is no need of integration along ship length or other complicated mathematical calculations [Strom-Tejsen et al., 1973, Arribas, 2007].

**Integrated Pressure Method/Boese's Method:** Similarly to Havelock formulation, this method can be considered as a "simple technique", as a consequence of the fact that

2

Boese used as foundation a hydrodynamic approach similar to the one which was followed in the original work performed by Havelock [Strom-Tejsen et al., 1973, Arribas, 2007]. Due to the fact that three-dimensional pressure distribution on a ship hull sailing in waves can not be accurately obtained , Boese proposes the use of *linear strip theory*, aiming to calculate the pressure distribution.

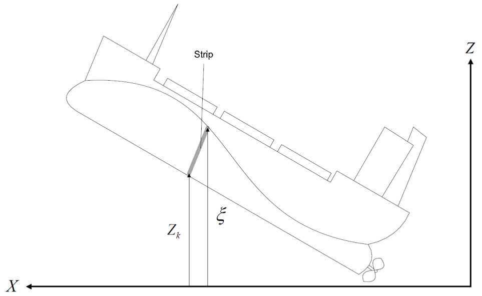


Figure 2.21: Pressure integration on each strip along ship's length, [Alexandersson, 2009].

Additionally, a small contribution of the vertical motions is included, due to the pitch angle that produces a longitudinal component. Boese divided the pressure forces acting on a ship's hull into two components. At this point the difficulty to obtain the longitudinal force directly has to be mentioned, on the grounds that one of the requirements of the strip theory is that interaction effects between the strips have to be neglected. For that reason, Boese had to obtain a mean value for the longitudinal force for a section (strip) at $x_b$ which is derived starting from the pressure of the undisturbed wave with Bernoulli's equation [Journée and Massie, 2000, Alexandersson, 2009]:

$$p + \rho \cdot g \cdot z + \rho \frac{\partial \Phi}{\partial t} + \frac{\rho}{2} \cdot \nabla \Phi \cdot \nabla \Phi = C \tag{2.19}$$

Boese used only the linear part in his method:

$$p = -\rho \cdot g \cdot z - \rho \frac{\partial \Phi}{\partial t} \tag{2.20}$$

The pressure is integrated over the strip, from the bottom of the strip to the wave surface, giving the force per unit length:

$$f(x_b, t) = \int_{Z_k}^{\xi} p \cdot \partial z_b \tag{2.21}$$

where:

$\xi$ :wave surface [m]
$Z_k$ :deepest point of the strip [m]

$$Z_k = D_s - \eta_3 + x_b \cdot \eta_5 \tag{2.22}$$

where:

$D_s$ :water depth [m]
$\eta_3$ :heave [m]
$x_b$ :x coordinate of the strip [m]
$\eta_5$ :pitch [rad]

The mean force per unit length is calculated:

$$\overline{f}(x_b) = \int_0^{T_e} f(x_b, t) \cdot \partial T \tag{2.23}$$

For this mean value of the force per unit length [Arribas, 2007] gives a more detailed formula:

$$f^* = \frac{\rho g \zeta^2}{4}\left(-1 + \frac{z_x^2}{\zeta^2} + \frac{2s\cos\left(-kx_b\cos(\mu) - \epsilon_s\right)}{\zeta}\right) \quad \text{with} \quad z_x = Z_a - x_b\theta_a \tag{2.24}$$

where:

| | |
|---|---|
| $Z_a$ | :heave amplitude [m] |
| $\theta_a$ | :pitch amplitude [rad] |
| $x_b$ | :x coordinate of the strip [m] |
| $s$ | :amplitude of the vertical relative motion [m] |
| $\epsilon_s$ | :phase lag of the vertical relative motion |

The horizontal part of the mean force per unit length as expressed in Eq. (2.23) is calculated by:

$$\overline{f}(x_b)_{\eta_1} = \overline{f}(x_b) \cdot \left(\frac{\partial y_w}{\partial x_b}\right) \tag{2.25}$$

This fluctuating force caused by waves and heave and pitch motion is integrated over a fixed surface, which in case of Boese's Method is the waterline plane, in order to obtain the first component of added resistance:

$$R_{aw1} = 2 \cdot \int_0^L \overline{f}(x_b) \cdot \left(\frac{\partial y_w}{\partial x_b}\right) \cdot \partial x_b \tag{2.26}$$

The contribution of the vertical motions is calculated by:

$$R_{aw2} = \frac{1}{T_e}\int_0^{T_e} \rho \cdot \nabla \cdot \ddot{\eta}_3(t) \cdot \eta_5(t) \cdot \partial t \tag{2.27}$$

which can be re-written as:

$$R_{aw2} = \frac{1}{2} \cdot \rho \cdot \nabla \cdot \omega_e^2 \cdot \eta_3 \cdot \eta_5 \cdot \cos\left(\epsilon_{\eta_3} - \epsilon_{\eta_5}\right) \tag{2.28}$$

where:

| | |
|---|---|
| $\omega_e$ | :encounter frequency [rad/sec] |
| $\eta_3$ | :heave amplitude [m] |
| $\eta_5$ | :pitch amplitude [rad] |
| $\epsilon_{\eta_3}$ | :heave phase lag [-] |
| $\epsilon_{\eta_5}$ | :pitch phase lag [-] |

Consequently, the total added resistance in waves calculated by Boese's Method is given by adding the two aforementioned components $R_{aw} = R_{aw1} + R_{aw2}$.

**Potential Flow Solution/Mauro's Method:** In the analytic method that he developed applying a potential flow solution, Mauro has confirmed that pitching and heaving motions of the ship dominate the effect of surge. Hence, he reasonably neglects the effects of variation in ship speed. As far as Mauro's formula calculating the added resistance is concerned, it consists of six components, with each one referring to a specific component of ship motion or to wave reflection against ship's hull or coupling between them. Therefore, the added resistance in Mauro's formulation is given by:

$$\sigma_{AW} = D_{11} + D_{22} + D_{33} + D_{12} + D_{13} + D_{23} \tag{2.29}$$

where the non dimensional added resistance coefficient is defined by:

$$\sigma_{AW} = \frac{R_{AW}}{\rho g \left(\frac{B^2}{L}\right) \zeta_A^2} \tag{2.30}$$

Regarding the terms of Eq. (2.29), their physical interpretation is:

| | |
|---|---|
| $D_{11}$ | :heaving motion [-] |
| $D_{22}$ | :pitching motion [-] |
| $D_{33}$ | :wave reflection [-] |
| $D_{12}$ | :coupling between heaving and pitching motion [-] |
| $D_{13}$ | :coupling between the heaving motion and the resistance associated with wave reflection[-] |
| $D_{23}$ | :coupling between the pitching motion and the resistance associated with wave reflection |

The analytical formula for the coefficients $D_{mn}$, in integral form is given below:

$$D_{mn} = \frac{1}{\pi}\frac{V^2}{gL}\left(-\int_{-\infty}^{-k^*} + \int_{-\frac{2\pi l}{\lambda}}^{\infty} \frac{\left(\eta+\omega_1\right)^3\left(\eta+\frac{2\pi\lambda}{l}\right)}{\left(\eta+\omega_1\right)^{\frac{1}{2}} - k_0^2\eta^2} C_{mn}(\eta)\,d\eta\right) \tag{2.31}$$

where:

$$\begin{aligned}
k_0 &= gl/V^2 \\
l &= L/2 \\
\omega_1 &= \omega_e l/V \\
k^* &= \tfrac{1}{2}\left[k_0 + 2\omega_1 + \left(k_0 + 4k_0\omega_1\right)^{\frac{1}{2}}\right]
\end{aligned}$$

The functions $C_{mn}(\eta)$ are defined below:

$$\begin{aligned}
C_{11} &= (\omega_1+\eta) z_\alpha^2 G_1^2 \\
C_{22} &= (\omega_1+\eta)(2\pi l/\lambda)^2 \theta_\alpha^2 G_2^2 \\
C_{33} &= (2\pi l/\lambda) k_0 G_3^2/(\omega_1+\eta) \\
C_{12} &= -2(\omega_1+\eta) G_1 G_2 (2\pi l/\lambda) z_\alpha \theta_\alpha \cos\left(\epsilon_z - \epsilon_\theta + \alpha - \beta\right) \\
C_{13} &= -2G_1 G_2 (2\pi l k_0/\lambda)^{\frac{1}{2}} z_\alpha \cos\left(\epsilon_z + \alpha - \gamma\right) \\
C_{23} &= 2G_2 G_3 (2\pi l k_0/\lambda)^{\frac{1}{2}} \theta_\alpha \cos\left(\epsilon_\theta + \beta - \gamma\right)
\end{aligned}$$

where:

| | |
|---|---|
| $G_1, G_2$ and $G_3$ | =magnitudes of the complex functions |
| $\alpha, \beta$ and $\gamma$ | =phase angles of the complex functions |

The interested reader is referred to [Strom-Tejsen et al., 1973] for more details, regarding the six added-resistance components as defined in Mauro's formula.

**Drift Force Approach/Joosen's Method:** Based on the extension of the analysis of aforementioned Maruo's method, Joosen was able to develop another added resistance theory. In his work, Joosen demonstrated that the drift force in the longitudinal direction in head waves is dependent only upon the potential of the radiated waves. More specifically, he drew the conclusion that if the ship motion amplitude is of similar order of magnitude over the whole range of encounter frequencies, the impact of wave diffraction is negligible for the whole range of frequencies, apart from very high frequencies, where it is proved to be dominating. Joosen's final expression for the added resistance is similar to Havelock's formula, apart from the fact that it takes into account wave-motion coupling phenomena:

$$\sigma_{AW} = E_1 + E_2 + E_3 \tag{2.32}$$

where:

$$\begin{aligned}
E_1 &= C_0 B_{33} z_\alpha^2 \\
E_2 &= C_0 \left(2\pi L/\lambda\right)^2 B_{55} \theta_\alpha^2 \\
E_3 &= -2C_0 \left(2\pi L/\lambda\right) B_{3,5} z_\alpha \theta_\alpha \cos\epsilon \\
C_0 &= \frac{1}{16}\frac{L^2}{B^2}\left(\omega_e\sqrt{\frac{L}{g}}\right)^3 \nabla/L^3
\end{aligned}$$

and

$$\epsilon = |\epsilon_z - \epsilon_\theta|$$

A better insight to Joosen's formula is provided in [Strom-Tejsen et al., 1973].

**Radiated Energy Approach/Gerritsma & Bulkerman's Method:** Based on the principle that added resistance can be attributed to the damping waves radiated away from the hull of the ship, Gerritsma and Beukelman achieved to calculate the added resistance as the energy flux radiated away from the hull, which for one wave encounter period is defined below:

$$E = \int_0^{T_e} \int_{x_\alpha}^{x_f} b(x) V_z^2(x,t)\, dx\, dt \tag{2.33}$$

where:

| | |
|---|---|
| $b(x)$ | :damping coefficient of the body at any longitudinal position |
| $V_z(x,t)$ | :vertical velocity of the ship section relative to the disturbed water surface elevation |

Given that the relative vertical velocity $V_z$ can be expressed as $V_z = V_{z\alpha}\cos\left(\omega_e t + \epsilon\right)$, Eq. (2.33) after integration in terms of time gives $E = \frac{\pi}{\omega_e}\int_{x_\alpha}^{x_f} b(x)V_{z\alpha}^2(x)dx$. Furthermore, Gerritsma and Beukelman have confirmed that added resistance is proportional to radiated energy, $E = \lambda R_{AW}$, where $\lambda$ is the wave length. This results in the formula below:

$$R_{AW} = \frac{k}{2\omega_e}\int_{x_\alpha}^{x_f} b(x)V_{z\alpha}^2(x)dx \tag{2.34}$$

In Eq. (2.34) $b(x)$ is the distribution of the sectional added-mass/damping coefficient, which is necessary for the calculation of the added resistance, is described below:

$$b(x) = N(x) - V\left[dm(x)/dx\right] \tag{2.35}$$

where:

$m(x)$ :zero-speed sectional added-mass coefficient
$N(x)$ :zero-speed sectional damping coefficient

The interested reader is referred to [Strom-Tejsen et al., 1973], where quite a bit of information is given, regarding Gerritsma and Beulkerman formula for the added resistance.

**Faltinsen's Asymptotic Method:** This method is only referred to the calculation of the diffraction induced added resistance [Alexandersson, 2009], which is dominating only in the region of high wave frequencies, as graphed in Figure 2.20a. Faltinsen's Method aims to calculate the force that a wave exerts on the ship hull, when it hits the hull and bounces off. The formulation of the method is based on the idea of a wave hitting a vertical wall. The resulting force on the wall in such a case is $\overline{F} = \frac{\rho\cdot g}{2}\cdot\zeta_\alpha^2\cdot L_{wall}$. This force could be integrated over a curved surface, representing the side of a ship hull, $\overline{F} = \frac{\rho\cdot g}{2}\cdot\zeta_\alpha^2\cdot\int_{L_1}\sin\left(\theta+\beta\right)\cdot\overline{n}\cdot\partial l$, where $\overline{n}$ is the normal vector and $L_1$ the length of corresponding hull side. Since these formulas are referred to a wall, with no speed, being hit by a wave, they can be valid for the case of a vessel sailing in a wave field when multiplied with a speed factor. As a result, Faltinsen's method equation for added resistance is given by:

$$R_{AW} = \frac{\rho g}{2}\cdot\zeta_\alpha^2\left(1+\frac{2\cdot\omega\cdot U}{g}\right)\cdot\int_{L_1}\sin\left(\theta+\beta\right)\cdot n_x\cdot\partial l \tag{2.36}$$

At this point, it should be noted that in the literature that is taken under consideration, the analytical methods demonstrated for the calculation of added resistance in waves are validated by means of comparison of the results of implementation of those methods against experimental data. Profound and detailed description, with respect to the results of the validation of each method is offered in [Strom-Tejsen et al., 1973, Arribas, 2007, Alexandersson, 2009].

As far as the added resistance in irregular waves is concerned, using the aforestated analytic methods, in first place the added resistance, $R_{AW}$ is estimated in regular waves for a sufficiently enough range of wave-encounter frequencies $\omega_e$ to obtain an accurate representation of the mean response curve for added resistance as defined below:

$$R(\omega_e) = \frac{R_{AW}}{\zeta_A^2} \tag{2.37}$$

where:

$\zeta_A$ :wave amplitude

Having calculated the mean response curve $R(\omega_e)$ for regular waves, then the average value of the added resistance $\overline{R}_{AW}$ of the ship, sailing at a specific speed in *irregular head waves* can be estimated using the mean response curve $R(\omega_e)$ and the energy spectrum of the sea state under consideration $S_\zeta(\omega_e)$. The procedure of superposition has to be followed, which, in principle is similar to the method used to predict ship motions in wave fields and it is described in the following equation:

$$\overline{R}_{AW} = 2\int_0^\infty R(\omega_e) S_\zeta(\omega_e) d\omega_e \tag{2.38}$$

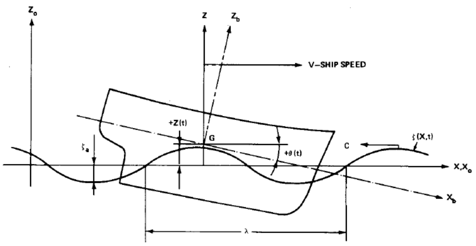


Figure 2.22: Wave and resulting ship motions, [Strom-Tejsen et al., 1973].

According to the above mentioned methods, there is no doubt that a vast amount of information and details, regarding the ship hull under investigation are demanded in order to calculate sectional offset distances or sectional geometric coefficients, depending on the chosen method each time. Similarly, hydrodynamic characteristics, like added mass and damping coefficients for each one of the transverse sections of the hull of the vessel have to be calculated. That makes the process of calculation of added resistance in waves mainly dependent on the ship motions and the accuracy of the outcome directly related to the accuracy of the motion data available.

## 2.6. CONCLUSIONS

### 2.6.1. PROPULSION SYSTEM AND PROPULSION CONTROL MODEL

Regarding the propulsion system that will be examined in this work, it will be a typical mechanical propulsion system which consists of a medium-speed Diesel engine, a gearbox and a Controllable Pitch Propeller. With respect to the propulsion system control that will be examined in this thesis, it will be a traditional Diesel engine speed governor, controlling the engine speed by adjusting the fuel rack position.

As far as the non-linear model of the ship propulsion system is concerned, it will be derived based on the work presented in [Stapersma and de Heer, 2000]. Then, the non-linear model will be linearised following the linearisation method of [Vrijdag and Stapersma, 2017] as it was presented in Section 2.2.3.

### 2.6.2. Disturbances Modelling

As far as the modelling of the disturbances is concerned, it has to be mentioned that only the effect of a varying wakefield will be examined in this thesis. The reasons for that are stated and justified below:

- The more direct impact of the wakefield variations on the behaviour of the rotating shaft system and the engine operating point, which is investigated in this thesis, compared to the ship resistance variations [Stapersma and de Heer, 2000].

- The level of difficulty of the methods used to obtain the resistance variations in waves, compared to those for calculation of the wakefield variations, as it was adequately discussed in Section 2.5.2

As for the first above mentioned reason, following the block diagram of ship propulsion system in Figure 2.5 and as it is argued in [Stapersma and de Heer, 2000], the wakefield disturbance affects directly the entrance velocity at the propeller and finds its way easily to the engine, by causing a change in propeller torque and disturbing the shaft rotational balance, which is translated into a change in shaft speed. This change leads the engine, more particularly the governor, to the adjustment of injected fuel and thus delivered torque, aiming to restore the balance at the rotating shaft. As it can be concluded, only the shaft dynamics lies between the wakefield disturbance and the engine with the former being able to influence directly the dynamic behaviour of the operating point of the latter. On the other hand, it is clearly viewed that for the ship resistance disturbance it is more difficult to find its way to the engine, since its way is, firstly, blocked by an additional integrator, compared to the wakefield disturbance, the ship mass integrator and secondly by the shaft's inertia integrator. Consequently, the impact of the ship resistance disturbance on the dynamic behaviour of the engine operating point is considered to be less direct, compared to the wakefield disturbance. Additionally, shaft dynamics is faster in comparison to ship dynamics [Stapersma and de Heer, 2000]. Hence, the impact of wakefield disturbance will be more significant compared to ship resistance disturbance. Besides this, it has to be mentioned that according to the theory, [Stapersma and de Heer, 2000], the integrator of ship's mass is considered to be a "low pass"filter between the Diesel engine's dynamic response and the resistance disturbance. This means that the block of the integrator, as shown in Figure 2.5, allows only low frequency disturbance signals to pass. On the other hand, the majority of high frequency disturbances are effectively blocked, without affecting the system's dynamic behaviour.

Regarding the second reason for which only the effect of a varying wakefield will be modelled, from the methods presented in Section 2.5.2, it was clearly demonstrated, that the process of obtaining the added resistance in waves requires the accurate determination of hydrodynamic characteristics. Furthermore, the estimation of the added resistance depends upon the use of accurate motion data. Apart from the fact that the calculation of complicated hydrodynamic characteristics and ship motion data lies outside the scope of this thesis, it also renders the objective of obtaining the added resistance in waves significantly laborious.

On the other hand, wakefield variations can be obtained according to the theory presented in Section 2.5.1. Additionally, in this thesis, some assumptions and simplifications will be applied for the calculation of the wakefield disturbance and they are cited below:

- Only the undisturbed incoming waves orbital velocity is modelled. The rest of the components related to radiated and diffracted waves velocities, contributing to the unsteady wakefield are neglected. Additionally, relative water velocity due to ship motions, like surge, heave and pitch, as examined in Section 2.5.1 are not taken into consideration.

- Only the axial component, $u_x$, of the velocity through the propeller disc is considered.

- The distribution of the disturbance over the propeller disc is not taken into account. The wake disturbance is assumed equal to the disturbance at the centre of the propeller hub.

- The speed and heading of the ship are considered constant in the unsteady wakefield model.

Following these assumptions, the calculation and model of the wakefield variations are simple and sufficiently accurate for the objective of this thesis.

# 3

# Ship Simulation Model

*In this chapter, the propulsion plant of a vessel is introduced and explained. Furthermore, the process of obtaining the non-linear model of the propulsion plant, by modelling each one of the components of the propulsion plant with the use of mathematical equations, describing the behaviour of each component, is also included in this chapter. Additionally, the simulation model of the vessel's propulsion system is validated, regarding the static operating points. Finally, the speed governor of the simulation model is tuned by means of evaluation of the dynamic response for specific operating mode.*

## 3.1. General Ideas on the Simulation Model Approach

In order to proceed with the refinement of the already existing control system of the prime mover of a vessel, a valid simulation model of the propulsion plant has to be built. There are quite some reasons that dictate the need for use of a simulation model, when the ultimate goal is the design and development of a controller. Besides the advantages, there are also some drawbacks regarding the use of a simulation model. A brief summary of those will be given in the following paragraph.

One of the most common ways to predict the dynamic behaviour of marine propulsion systems is the use of simulation models. The use of simulated marine propulsion plants ensures the elimination of risk, as well as the prevention of different kinds of limitations. Multiple scenarios, which would not be easy to test in real life due to possible material or human losses, can be simulated. Additionally, by doing simulations, the use of scale models, which are, usually, costly may be avoided. Simulations are also faster than real-time tests. This allows the designer to increase, significantly, the amount of tests that can be carried out, providing valuable results regarding the investigation of the system behaviour, before it is actually built. At this early stage of designing the propulsion system, a sufficient number of simulations give the opportunity to the designer to predict the dynamic behaviour of the vessel's propulsion plant under different operational conditions. Consequently, different system parameters can be chosen optimally (choice of suitable pitch-speed combinator law, engine governor calibration etc.), improving the performance of the designed propulsion system.

However, besides the benefits, the use of simulation models has also drawbacks. The most significant one is that the designer has to fully understand the physical processes, as a first step, and then build the conceptual model in such way that it adequately and accurately represents the reality. This whole process is considered complicated and time consuming.

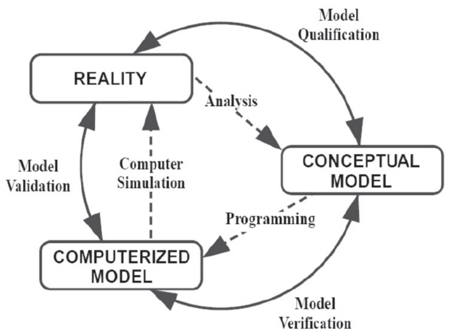


Figure 3.1: Process of deriving a simulation model from reality [Schlesinger, 1979]

As the purpose of this chapter is to extract the simulation model from a real vessel's propulsion plant, an outline of the process followed can be given in Figure 3.1, where the key elements of a credible simulation model are presented, as they were given by [Schlesinger, 1979]. The inside arrows represent the process needed to derive one element from another. The outside arrows represent the process that has to take place in order to evaluate the credibility of the derivation of each element. The process followed in this chapter for the simulation model to be derived is based in the process followed in [Vrijdag et al., 2009], where a systematic approach regarding the derivation, verification and validation of ship propulsion plant simulation model is given.

The first step, before starting deriving a simulation model of a ship propulsion plant is to clearly state the purpose of the derivation of such a simulation model and the objectives that need to be achieved by using it. A short statement of the goals of the model, which will be presented in this chapter, is cited below: The ship propulsion plant simulation presented in this session should be able to represent accurately the physical subsystems of a propulsion drive train, rendering possible the investigation of the impact of different sea states, different heading of the vessel with respect to waves and different operating point on engine's fluctuations. Additionally, the simulation model should provide the tools for the refinement, if it is possible, of an existing Diesel engine controller, aiming at the reduction of the engine load fluctuations. From this non-linear simulation model, a linear one is going to be directly derived. The parameters of this linear model will be used for the optimisation of the propulsion control system.

Besides this first insight, with respect to the models goals, some more specifications can be stated, giving a clear starting point for the model derivation:

- The model should include sub-models of the prime mover (Diesel engine), the transmission system, the propeller and the ship's hull.

- The simulation model should give accurate results, in terms of the dynamic behaviour of the system, when the ship sails in waves. This includes speed (vessel, engine, shaft) and torque (engine, shaft) fluctuations, around static operating points.

- The model should be able to simulate the fluctuating ship resistance and wake-field, due to the seaway.
- With the main idea being to keep the model as simple and easy handled as possible, a main assumption in the model is that the efficiency of different components along the shaft line i.e. gearbox efficiency, shaft line efficiency, are constant, neglecting part load losses.
- The model is not able to simulate manoeuvres, since manoeuvring is out of the scope of this thesis. Moreover, the model is not capable of modelling big accelerations and decelerations, due to the lack of limitations, which are related to the operation of the engine under intense acceleration and/or deceleration. This kind of limitations exist in real propulsion and power plants in order to protect the engine from overloading or operating with very low efficiency i.e. fuel limitation in case of load take-up which will result in limited presence of air and incomplete combustion in the combustion chamber, due to the turbocharger's inertia.



## 3.2. Reference Vessel

The propulsion plant that will be modelled belongs to a ship design called RGS9316. This type of vessel is shown in Figure 3.2. The outline of a Rescue Gear Ship 9316 is given

Figure 3.2: Rescue Gear Ship 9316.

in Figure 3.3. The arrangement of the propulsion plant of such a vessel is depicted in Figure 3.4 and Figure 3.5 and some of the ship's particulars are given in Table 3.1. The overall length of this type of vessel is 93.2 meters with a breadth of 16 meters and has a total displacement of approximately 3483 tons. It is a twin shaft ship, which uses as prime movers two 4-stroke, turbocharged, high-speed Diesel engines, which allow the vessel to sail at a maximum speed of 16 knots in calm water conditions. Two 4-bladed

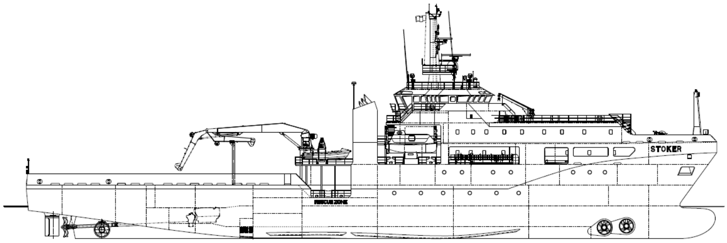


Figure 3.3: Outline of RGS 9316.



Controllable Pitch Propellers (CPP), rotating inward over the top, are used in both shafts.

| Vessel Particulars | |
|---|---|
| Length o.a | 93.20 m |
| Length p.p. | 84.90 m |
| Breadth mld | 16.00 m |
| Depth mld | 7.20 m |
| Design draught | 3.80 m |
| Design deadweight | 850 ton |
| Total displacement | 3483.6 ton, @ design draft |
| Maximum speed | 16 kn |
| Prime mover | 2 3516C HD Diesel engines, 1920 bkW @ 1600 rpm |
| Propeller | 2 4-bladed, CPP, rotating inward over the top, with diameter D=2.7 m |

Table 3.1: General RGS9316 data

## 3.3. SIMULATION SYSTEM MODELS

The conceptual model used in this work is shown schematically in block diagram form in Figure 3.6 and it is almost identical to the general block diagram of a ship propulsion plant, which was described in Figure 2.5 in Section 2.2.2. Taking into account that the actual ship under consideration has the same installation for port and starboard side, only the one side is depicted here. Furthermore, depending on the goals of the use of the propulsion plant model, the complexity of each one of the components constituting the model in total may vary. In this chapter, the main idea is to keep each one of the sub models as simple as possible, maintaining the level of accuracy needed, according to the aforementioned goals. In Figure 3.6 the blocks of the vessel's propulsion plant are presented, as well as the linking variables between the sub-models. As it is shown, the propulsion system model consists of the models for the prime mover, which is a Diesel engine, its control system, which is the governor, the gearbox, which is not depicted separately but it is included in the Diesel engine block, the rotor dynamics loop, the

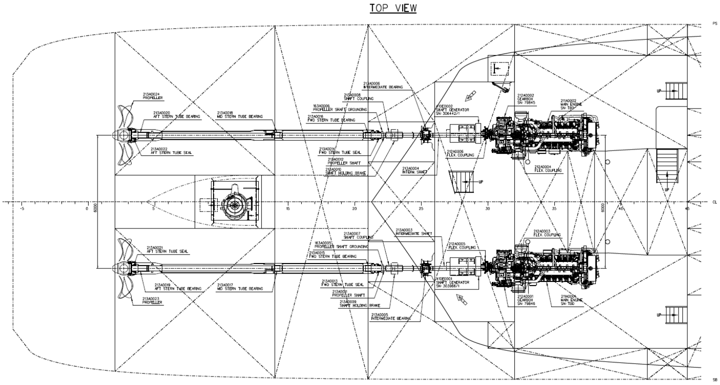


Figure 3.4: Top view of propulsion plant of RGS9316.

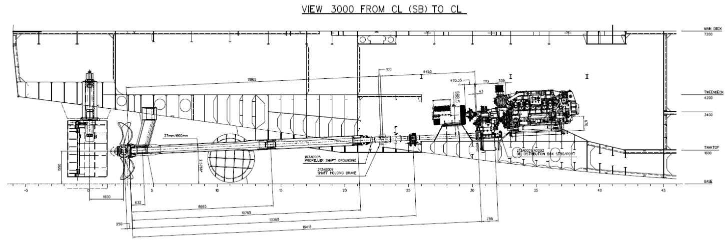


Figure 3.5: Side view of engine room of RGS9316.

propeller, the ship's hull, the ship translation dynamics and the external disturbances, acting upon the wakefield and the total resistance of the vessel.

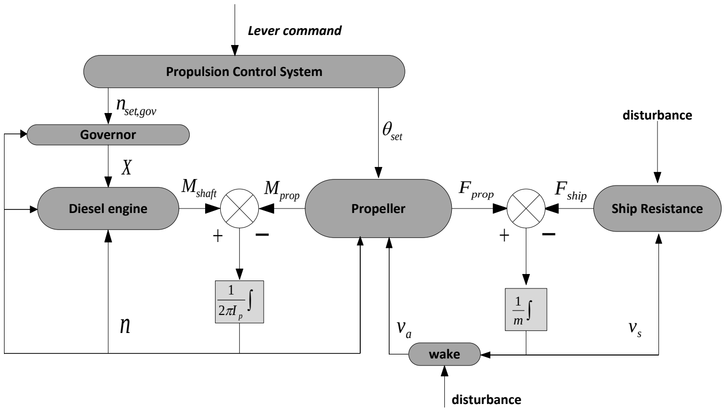


Figure 3.6: RGS9316 modelled propulsion plant.

### 3.3.1. PROPELLER

The propeller of the vessel is the natural link between the machinery installed inside the ship and the fluid, surrounding the hull of the ship. The prime mover is connected with the propeller through a shaft. In that way, the engine brake torque, $M_b$ is delivered to the propeller. This propeller torque, $M_{prop}$ is translated into thrust power, which propels the whole vessel. The ability of the propeller to provide the traction of the ship, can be used for a wide range of combinations of pitch angles $\theta$, since it is a Controllable Pitch Propeller, and advance ratios, $J$. The purpose of this propeller model is to calculate the thrust, which is generated by the propeller and the torque encountered by the propeller, depending on a range of different combinations of pitch angles and advance ratios. For this reason, the propeller model is "built" based on the, relatively simple, open water diagram. The component model chosen for the propeller is the Wageningen B-Series, which is based on the well-known systematic propeller series. The propellers in this series are non-ducted fixed pitch propellers. The series covers a wide range of numbers of blades, of blade area ratios and pitch diameter ratios.

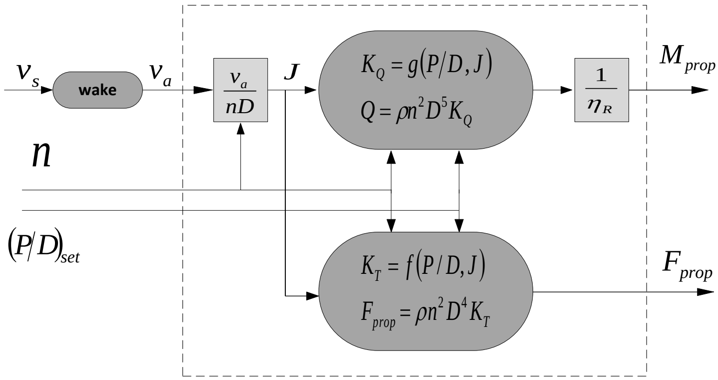


Figure 3.7: Propeller block diagram.

As it is shown in Figure 3.7, the propeller model needs as inputs the shaft speed, $n_s$, the advance velocity, $v_a$ and the pitch diameter ratio of the propeller, $P/D$. The advance ratio is defined as: $J = \frac{v_a}{nD}$, where the advance speed $v_a$ is the incoming velocity, seen by the propeller and is calculated with the use of the vessel's speed, $v_s$ and the wake fraction, $w$, by: $v_a = v_s(1-w)$. Using two polynomials provided by Oosterveld and van Oossanen the values of the two dimensionless coefficients, $K_Q$ and $K_T$, are calculated for different combinations of the values of the advance ratio, $J$ and the actual pitch diameter ratio, $P/D$. The values of the rest of the unknown coefficients, $C_n$, $S_n$, $t_n$, $u_n$, $v_n$ are given in tables.

$$K_Q = \sum_{n=1}^{47} C_n J^{S_n} (P/D)^{t_n} (A_E/A_o)^{u_n} (Z)^{v_n} \tag{3.1}$$

$$K_T = \sum_{n=1}^{39} C_n J^{S_n} (P/D)^{t_n} (A_E/A_o)^{u_n} (Z)^{v_n} \tag{3.2}$$

With the values of those two coefficients, $K_Q$, $K_T$, determined, the open water thrust and torque are also calculated by:

$$F_{prop} = K_T \rho n^2 D^4 \tag{3.3}$$



$$Q = K_Q \rho n^2 D^5 \tag{3.4}$$

The propeller torque, $Q$ is, to some extend, changed, because of the propeller-wake interaction effects. Rotating in behind conditions, the propeller torque is adjusted by a relative rotative efficiency, $n_r$, which is defined as: $M_{prop} = \frac{Q}{n_r}$.

At this point, the absence of the Controllable Pitch Propeller hydraulic actuating system and the propeller pitch controller has to be pointed out. The hydraulic actuating model and the propeller pitch controller, are closely related to the propeller model and according to the block diagram presented in Figure 3.7, they will be absent in the simulation model used in this thesis. The reason for this is that, as it was referred in Section 1.2, this master thesis focuses on the investigation of the possibility to influence the geometrical properties (size, orientation etc.) of the elliptic trajectory of the operating point in the engine operating envelope, without engaging the use of the propeller pitch control. According to this, it is clear that the propeller pitch controller and the behaviour of the Controllable Pitch Propeller actuating system will not be studied. Furthermore, it has to be considered that the simplicity of the model is always an objective. This fact leads to the decision of neglecting the use of a model of the hydraulic system, which is a complex, non-linear, time-variant system with several modelling challenges, which will increase the complexity of the model as a total.

Consequently and according to the propulsion plant model graphed in Figure 3.6, the input to the propeller model is the pitch diameter ratio setpoint, $P/D_{set}$, as it is defined by the lever command and the combinator curve, since there is no propeller pitch control and actuating system, intervening between the lever command and the propeller model

As far as the main disturbances acting on the propulsion system model are concerned, as it was mentioned in Section 2.5, they are attributed to the wave field. According to the theory presented in Section 2.5.1, the wakefield disturbance due to the waves can be linearly superimposed to the advance speed, $v_a$, in calm water. There are various ways to simulate these wakefield disturbances. As for this simulation model, the wake field disturbance, regarding the simulation of regular waves, is implemented as a sinusoidal disturbance of certain amplitude and frequency acting on the wake factor of the model, $w$, as shown in Figure 3.8. This kind of disturbance is included in the propeller sub-model.

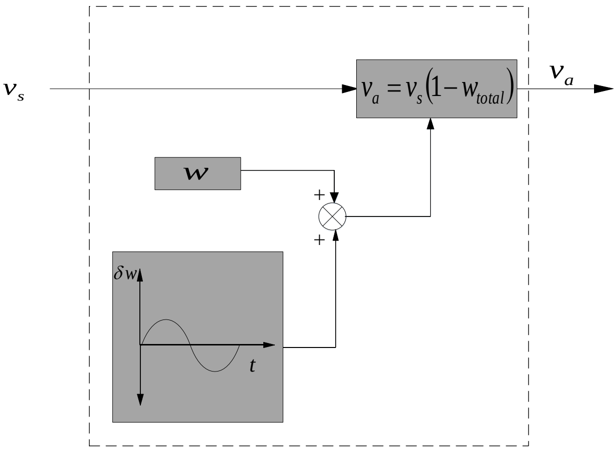


Figure 3.8: Wake field disturbance block diagram.

### 3.3.2. CONTROLLED DIESEL ENGINE MODEL

The controlled system of the Diesel engine, which is used as a prime mover, is shown in Figure 3.9. It consists of the governor, the actuator that actuates the fuel rack, and the Diesel engine itself. In the system depicted in Figure 3.9 the gearbox and the rotating shaft system are also included and presented below.

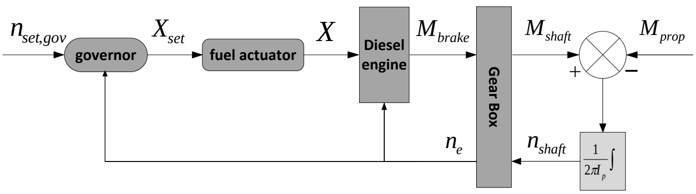


Figure 3.9: Controlled Diesel engine block diagram.

#### GOVERNOR MODEL

In Figure 3.9, the governor block is clearly shown. The input values for the governor are the desired engine speed $n_{set,gov}$, determined by the lever command and the combinator curve, and the actual engine speed $n_e$, as it is calculated by measuring the shaft speed and then multiplied by the reduction ratio of the gear box. The signals of the two input variables, $n_{set,gov}$ and $n_e$ are normalised as they enter the governor's block. More specifically they are translated into a dimensionless number, with the use of a look up table, which assigns every value between zero and maximum engine speed (for both desired engine speed, $n_{set,gov}$ and actual engine speed, $n_e$) to a dimensionless number between zero and one. In this way the engine speed error, $e_n$, in other words the difference between the values of $n_{set,gov}$ and $n_e$, is also calculated as a dimensionless number between zero and one, which is more intuitive and easily handled. Since the error signal, $e_n$,is calculated, it enters the PID controller, which is the "brain" of the feedback loop [Franklin et al., 1994]. The PID controller receives the input signal (error:set engine speed value minus measured engine speed value) and performs three mathematical operations with the calculated error signal, $e_n$. These three mathematical operations can be briefly described below:

- P action:
  The calculated dimensionless error value, $e_n$ is amplified.

- I action:
  The calculated dimensionless error value, $e_n$ is integrated over time from the start of the whole operation.

- D action:
  The calculated dimensionless error value, $e_n$ is differentiated to time.

The three processed values that are obtained after the mathematical operations are then combined in one single output value [Triantafyllou and Hover, 2003]:

$$u(t) = K_p e_n(t) + K_i \int_0^t e_n(t)dt + K_d e_n^{'}(t) \tag{3.5}$$

At this point it has to be mentioned that, in the governor block, besides the look up tables, transforming the desired engine speed, $n_{set,gov}$ and the actual engine speed, $n_e$ into a dimensionless number, another look up table exists, imposing torque limitations during the Diesel engine's operation, preventing its thermal overloading. This look up table assigns each value of actual engine speed, $n_e$, to the torque limits of the Diesel engine, as they are defined by the engine's operating envelope, given by the engine's manufacturer. The value of the torque limit, for each value of the engine speed, is normalised by dividing it with the value of the maximum brake engine torque. The value of the torque limit, which corresponds to the actual engine speed at each moment of the engine's operation is compared to the single output value of the PID controller, whose derivation is described in Eq: (3.5). The minimum of the two output signals, following the idea of prevention of the engine's overloading, will be the input to the following block diagram of the fuel rack actuator and then directly to the Diesel engine model, as the value of the fuel rack position, $X_{set}$, dictating the demanded, by the controller, brake engine torque $M_b$ which has to be offered to the system. The detailed block diagram of the governor, including the look up tables normalising the signals, as they were mentioned before, as well as the PID controller itself, are shown in Figure 3.10.

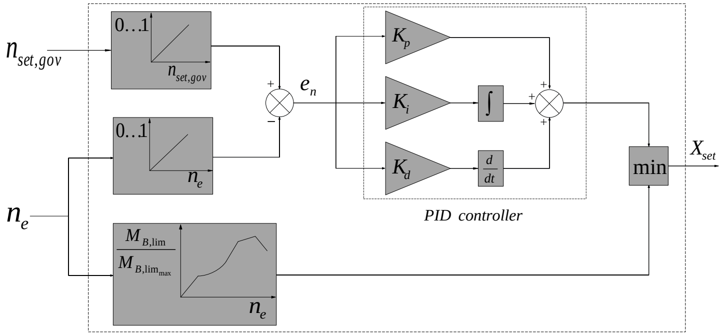


Figure 3.10: Diesel engine's governor block diagram.

## FUEL RACK ACTUATOR MODEL

In the next step, following the process of transmitting the control signal in the controlled Diesel engine model, it can be noticed that the output of the governor is the input for the fuel rack actuator of the model. The fuel rack actuator is represented by a first order system, $\frac{1}{\tau \cdot s+1}$. The value of variable $\tau$ is low, $\tau = 0.02$. This means that the first order system, which counts for the fuel pumps inertia and the ignition delay, has a quite fast response, being able to follow high frequency fluctuations of the system.

## DIESEL ENGINE MODEL

As it was mentioned in Section 1.3, this thesis will focus on vessels that use Diesel engine as a prime mover. Regarding the diesel engine modelling, a variety of models can be found in the literature, ranging from highly complex CFD-based models, able to describe in details the phenomena that take place in the combustion chamber, during the operation of the engine, to relatively simple models, based on look-up tables which need easily accessible look up-data as input.

For the purpose of this thesis, a highly simplified approach for the Diesel engine model will be used, which needs as input the engine speed, $n_e$ and the fuel rack position, $X$, which is an indication of the amount of injected fuel, and gives back, as output, the engine brake torque, $M_b$. The output of such a model is considered sufficient for the goals of this work, as determined in Section 3.1. In Figure 3.11, the simple representation of the Diesel engine model in a block diagram, with the input needed and the output generated are shown. A simple mathematical formula relating the fuel rack position, $X$, the engine speed, $n_e$ and the brake engine torque, $M_b$, can be extracted by a fuel rack map of the diesel engine in use, Figure 3.12, as it is referred in [Vrijdag and Stapersma, 2017]. According to this map, the torque generated by a Diesel engine, $M_b[kNm]$, for a given constant value of the fuel rack position, $X[mm]$ is, to some extend, reduced as the engine speed, $n_e[rpm]$ is increased. This negative slope of the constant fuel rack line, which can be noticed on the map, is due to increased piston friction in the engine and leakage in the fuel pump, as the engine speed increases. Additionally, it should be mentioned that the limits of the Diesel engine operating envelope, which can be clearly distinguished on the map of Figure 3.12, are defined by the engine manufacturer. The

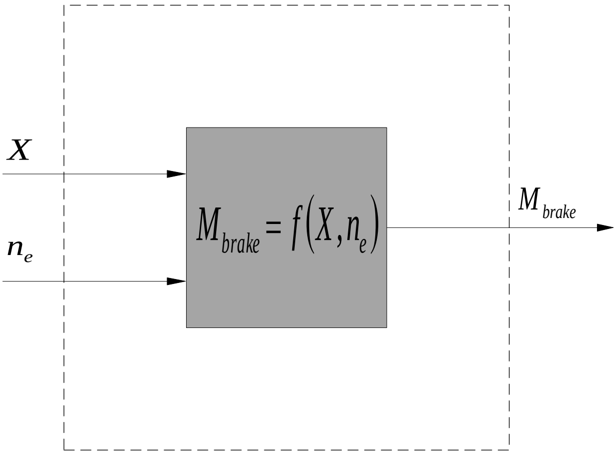


Figure 3.11: Diesel engine block diagram.

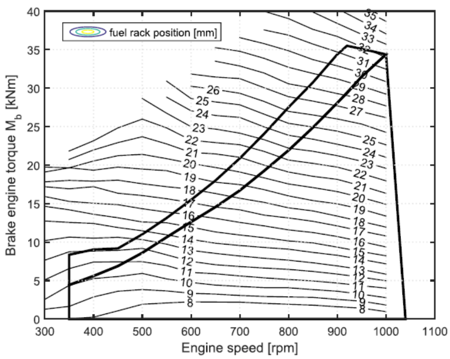


Figure 3.12: Typical fuel rack map of a diesel engine, [Vrijdag and Stapersma, 2017].

mathematical formula describing the fuel rack map is given below:

$$M_b = k \cdot n_e + m \cdot X + M_{b,offset} \tag{3.6}$$

Apart from the diesel engine fuel rack map, Eq. (3.6) can also be derived using the factory acceptance test (FAT) reports. In case of this simulation model of the diesel engine, neither the fuel rack map, nor the factory acceptance test reports are available. For that reason, the common practise of using typical values of the variables $k$ and $m$ is followed. With respect to variable $k$, another assumption was made. According to this assumption, the generated brake engine torque, $M_b$ is considered to be dependent, only, on the fuel rack position, $X$ and not on the engine speed, $n_e$. This assumption leads to the fact that, unlikely the map presented in Figure 3.12, the constant fuel rack lines of the map, considered in this thesis, are absolutely horizontal and parallel to the engine speed axis.

This means that the value of variable $k$ introduced in Eq. (3.6) is zero, $k = 0$. With these assumptions implemented, the diesel engine is modelled as a constant torque machine, as it is ideally considered to be.

### 3.3.3. GEARBOX MODEL AND ROTOR DYNAMICS

Following the general idea of keeping the simulation model as simple as possible, the gearbox of the propulsion plant is modelled based on the idea that the gearbox reduces the power generated by the diesel engine due to power losses that occur in the gearbox and the shaft line, during the power transmission, as shown in the block diagram of the gearbox in Figure 3.13.

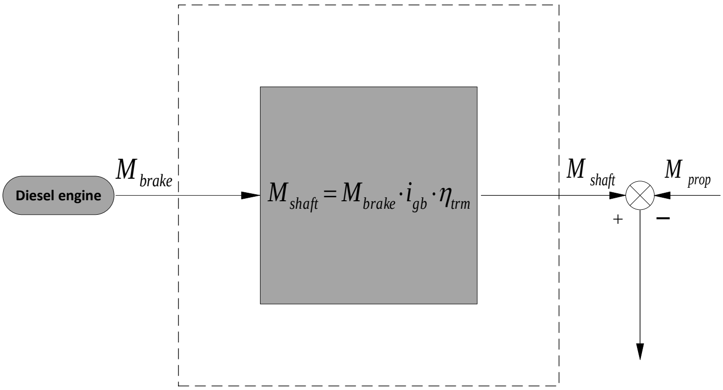


Figure 3.13: Gearbox blockdiagram.

These losses are represented by a constant total transmission efficiency, $\eta_{trm}$ which is calculated by multiplying the gearbox efficiency, $\eta_{gb}$ and the shaft line efficiency, $\eta_s$:

$$\eta_{trm} = \eta_{gb} \cdot \eta_s \tag{3.7}$$

As a result, the power output of the gearbox is:

$$P_{shaft} = P_b \cdot \eta_{trm} \tag{3.8}$$

Using the gearbox reduction ratio $i_{gb} = \frac{n_e}{n_{shaft}}$, the relation between the brake engine torque, $M_b$ and the shaft torque, $M_{shaft}$ is derived:

$$M_{shaft} = M_b \cdot \frac{n_e}{n_{shaft}} \cdot \eta_{trm} \tag{3.9}$$

For this simulation model, the values of the gearbox efficiency, $\eta_{gb}$, the shaft line efficiency, $\eta_s$ and the gearbox reduction ratio, $i_{gb}$ are given in the following table: As far as the rotor dynamics loop of the model is concerned, it is based on Newton's second law of

| | |
|---|---|
| $\eta_{gb}$ | 0.97 |
| $\eta_s$ | 0.98 |
| $\eta_{trm}$ | 0.95 |
| $i_{gb}$ | 7.52 |

Table 3.2: Efficiencies along propulsion chain and gearbox reduction ratio

movement. The shaft rotational dynamics are calculated by using the Newton's second law, regarding the rotational movement, yielding in a differential equation for the shaft rotational speed:

$$M = I \cdot \frac{d\omega}{dt} \Longrightarrow \frac{dn}{dt} = \frac{1}{2\pi} \cdot \frac{d\omega}{dt} = \frac{1}{2\pi} \cdot \frac{M_{in} - M_{out}}{I} \tag{3.10}$$

Taking into consideration Figure 3.14 and Eq. (3.10), in the rotor dynamics loop the

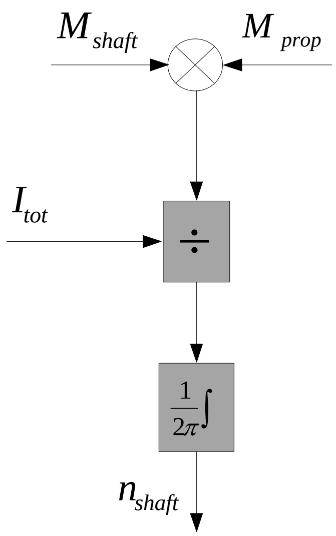


Figure 3.14: Rotational dynamics block diagram.

torque balance between the torque delivered by the prime mover (Diesel engine), after the losses in the shaft line and the gear box have been accounted for, $M_{shaft}$ and the torque required by the propeller, $M_{prop}$ results in a net torque. The division of this net torque by the product of the effective shaft inertia, $I_{tot}$, and $2\pi$, provides the angular acceleration of the shaft. This shaft acceleration can be integrated, in order to derive the shaft rotational speed, $n_{shaft}$, according to Eq. 3.11:

$$n_{shaft} = \frac{1}{2\pi I_{tot}} \int (M_{shaft} - M_{prop}) dt \tag{3.11}$$

The shaft speed calculated after the integrator is multiplied by the gear box reduction ratio and then fed back to the engine block diagram, as the engine torque is, generally, dependent on the engine speed.

Regarding the effective shaft inertia, $I_{tot}$, it has to be mentioned that the whole shaft line is considered as a system consisting of different, discrete components. For each component, the mass moment of inertia, $I$ is calculated, based on the torsional vibration calculation data. The mass moment of inertia of each component depends on its rotational speed, which is different for each component, depending on its location, with respect to the gear box. Using the gear box as the reference point, at which the rotational speed changes along the shaft line, the mass moment of inertia of the components which are located in the engine side (before the gear box), are corrected, due to their different angular speed, by being multiplied by the squared gear ratio.

$$I_{component,cor} = I_{component} \cdot i_{gb}^2 \tag{3.12}$$

### 3.3.4. SHIP'S HULL MODEL

The subsystem representing the ship and its hull is considered valuable, since it determines the interaction of the propulsion plant with the surrounding environment, in other words the water, in which the vessel sails. This subsystem includes the ship's translation dynamics which means that it must contain Newtonian mechanics and hydrodynamic properties, regarding the translation of the vessel. At this point, it has to be mentioned that only the longitudinal direction of motion of the vessel is examined. As a result, the translation mechanics and the hydrodynamic properties, taken into account in the model, are only referred to the longitudinal displacement.

This longitudinal translation of the vessel's hull through water requires a force. This force, which is sufficient to tow the ship at a desired speed, without the use of a propulsor, is called *resistance*. This resistance is meant to be overcome by the thrust generated by the installed propulsion system on a vessel. According to theory [Woud and Stapersma, 2002, Journée and Massie, 2000], the total resistance is composed of three main components:

- *Frictional or viscous resistance*: This component is the result of tangential forces which act on the hull, as the effect of the boundary layer along the hull.
- *Form resistance*: This component of the total resistance is the outcome of the pressure difference in front of and behind a moving vessel. The separation of the boundary layer from the hull at the stern of a vessel, leads to remarkable drop of pressure at the stern of the ship.
- *Wave resistance*: This component of resistance is because of the waves, which are generated by the vessel's motions. Part of the generated energy by the propulsion system of the vessel, which is meant to be used for translation of the vessel, is transmitted to the generated waves.

The component of *air resistance*, which is attributed to the part of the ship, which is above the sea level, is usually neglected. The summation of the above mentioned components of resistance results in the *total hull resistance*, $R_t$. The mathematical formula, which can describe the total hull resistance of a vessel is:

$$R_t = a \cdot v_s^e \tag{3.13}$$

As far as the resistance curve, which is used in the ship's hull model, is concerned, the predicted resistance curve, before the process of sea trials, for the reference vessel of this thesis is given in the Figure below. On the left hand side plot of Figure 3.15, two resistance plots can be seen. The first one with the red dots is the above mentioned predicted resistance curve of the reference vessel, in which an irregularity can be noticed, compared to the expected (it is expected that ship's resistance is roughly proportional to the square of ship speed for relatively low speeds [Woud and Stapersma, 2002]) shape of the curve, at the range of speeds from 4.5 m/s up to 6 m/s. This irregularity of the shape of the predicted resistance led to the derivation of a curve, which fits the data of the predicted resistance given. This curve, which is quadratic, is the second curve with the black tiny squares of the left hand side plot of Figure 3.15. This second resistance curve is the one which is implemented in the ship's hull sub model of the simulation model, as the total resistance of the ship's hull, dependent on the vessel's speed. On the right hand side of Figure 3.15, the difference in percentage between the two resistance curves at each speed is presented.

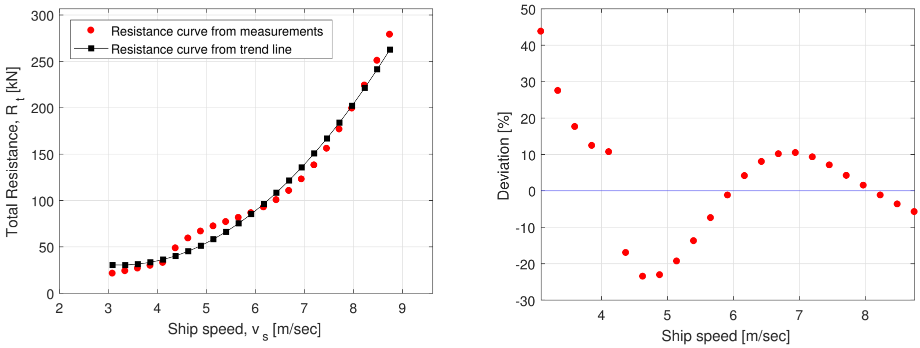


Figure 3.15: LHS: Resistance curve derived from sea trials data and interpolated resistance curve. RHS: Divergence between the two resistance curves.

The ship's hull model can be shown in Figure 3.16. The ship resistance curve is modelled as a look up table. This curve defines the ship's resistance without a propeller for a range of values of static speed.

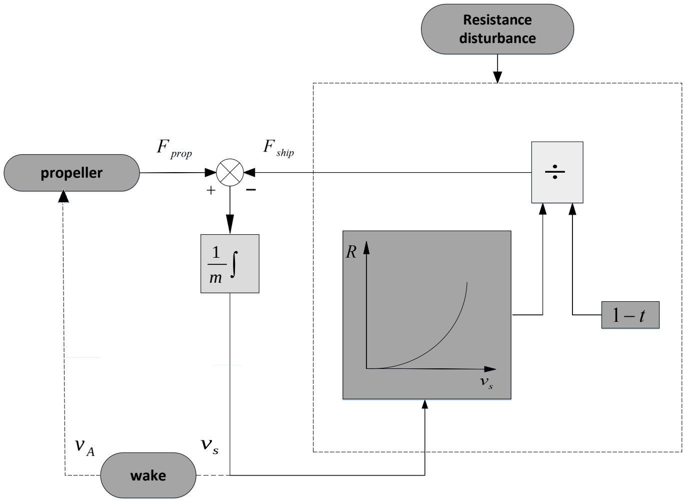


Figure 3.16: Ship's hull block diagram.

As it is, also, depicted in Figure 3.16, for that calm water resistance values, corrections are applied to ensure that the propeller-hull interaction effects are taken into consideration. The effects of the propeller-hull interaction are expressed by the use of the thrust deduction factor, $t$ and the corrected calm water ship resistance, $F_{ship}$ is calculated by:

$$F_{ship} = \frac{R_{ship}}{(1-t)} \tag{3.14}$$

What is more, in Figure 3.16, the component of resistance disturbance is shown. Resistance disturbance represents is used to simulate the resistance variations, due to the fact that the ship moves forward in a wave field as for this thesis. Regarding the regular waves, the effect of such resistance disturbance is modelled with a sinusoidal signal, which represents the added wave resistance as referred in Section 2.5.2. The summation of the oscillating part of resistance, due to the motions of the vessel and the constant part, due to calm water resistance, give the total resistance for a ship sailing in waves [Journée and Massie, 2000]. The introduction of the resistance disturbance in the model is shown in Figure 3.17. Additionally, in Figure 3.16, besides the ship's resistance curve, the ship translation dynamics can be noticed. The expression for the translational movement is based on Newton's law of translation, resulting in a differential equation for longitudinal ship speed:

$$F = m_{ship} \cdot \frac{dv_s}{dt} \implies \frac{dv_s}{dt} = \frac{F_{in} - F_{out}}{m_{ship}} \tag{3.15}$$

Taking into account Eq. 3.15 and Figure 3.18, it can be noticed that in the ship translational dynamics loop, the force balance between ship resistance, $F_{ship}$, and the thrust generated by the propeller, $F_{prop}$ provides a net force. This net force is divided by the

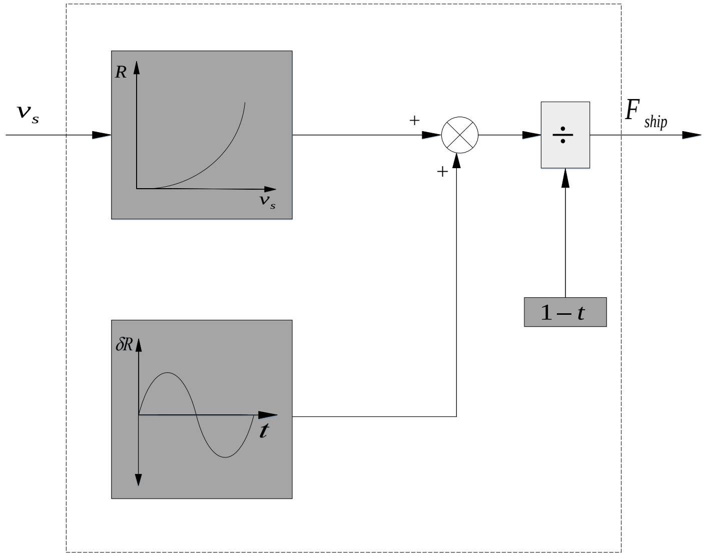


Figure 3.17: Introduction of ship resistance variation for regular wave in ship's hull model.

ship mass, resulting in the longitudinal acceleration of the vessel. By integrating the calculated acceleration, the longitudinal velocity of the ship is obtained as shown in the Eq. 3.16:

$$v_s = \frac{1}{m_{ship}} \int (F_{prop} - F_{ship}) dt \tag{3.16}$$

Since the ship's resistance is non-linearly dependent on ship speed, the calculated ship speed is provided as a feed back to the ship's hull block diagram, after the integrator.

At this point, it should be mentioned, regarding the ship translation dynamics loop, that the ship mass by which the balance between ship resistance and the propeller thrust is divided, is the total mass, $m_t$ of the system. More specifically, this total mass, $m_t$ includes the actual mass of the vessel, $m_s$ as well as the hydrodynamic mass or added mass, $m_a$. In a physical sense, this added mass is the weight added to the system, due to the fact that the accelerating or decelerating vessel must move some volume of surrounding fluid with it as it moves. The added mass, due to the motion of the ship in one direction, in longitudinal direction in this case or as it is widely known *surge motion*, caused by a force applied also in the longitudinal direction, is considered to get a value between 5-8% of the actual mass of the ship, $m_s$, according to the literature [Journée and Massie, 2000]. For the simulation model into consideration, the added mass, $m_a$ is assumed to be 7.5% of the ship mass, $m_s$:

$$m_t = m_s + m_a \implies m_t = m_s + 0.075 \cdot m_s \implies m_t = 1.075 \cdot m_s \tag{3.17}$$

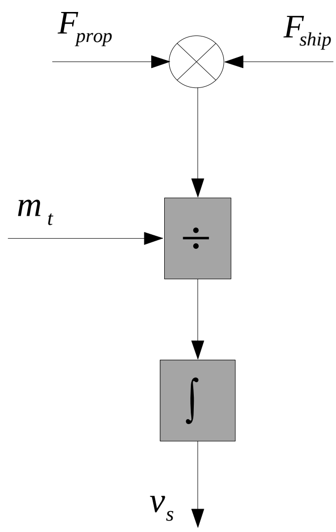


Figure 3.18: Translational dynamics block diagram.

## 3.4. TUNING OF THE CONTROLLER OF SIMULATION MODEL

In this section, the engine speed controller of the simulation model (governor), which was previously described, is tuned. The values of the PI controller, the proportional, $K_p$ and integral, $K_i$, gains of the controller are chosen, by evaluating the dynamic behaviour of the simulation model, during a specific, implemented operating mode. The reason for this process is to obtain reasonable values for the engine governor settings as a starting point in this work.

As far as the way in which the dynamic behaviour of the simulation model is going to be evaluated is concerned, there are four available options. These four ways are related to the four different input variables of the simulation model. The first two of them are the engine speed, $n_e$ and the pitch diameter ratio, $P/D$, which in case of a real propulsion plant are determined by the operator through the lever command. The other two are called disturbance inputs, referring to the hull's resistance and the wakefield. These two, in reality, are determined by the environment. For example, resistance disturbance might be caused by wind, waves, shallow water, hull fouling or changes in ship draft and trim. Wakefield disturbances can be caused by ship motions, orbital water particles motion due to waves or manoeuvres. In Figure 3.19 these four input variables are shown, with the propulsion plant model being a black box.

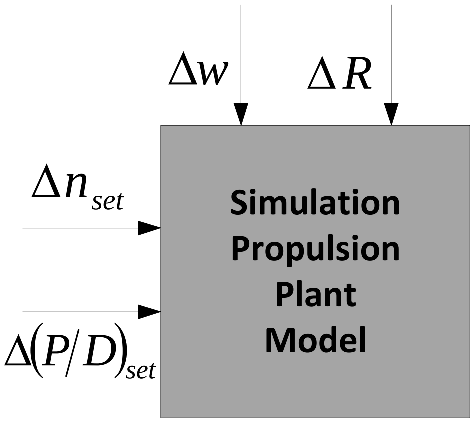


Figure 3.19: Input variables variation.

Moreover, it has to be mentioned that another common method which is followed, in order to tune the governor of the Diesel engine, instead of influencing the aforementioned input variables of the simulation model, is to try and find the suitable settings while sailing on board the vessel. Obviously, in this case this is not possible, with the use of simulation model being the only option.

### 3.4.1. VALUES OF GOVERNOR GAINS AND SYSTEM VARIABLES EXAMINED

As it was mentioned in the previous Section, the evaluation of the dynamic behaviour of the simulation model, in order to tune the governor can be done by influencing four input variables. In this case, the variable that will be influenced is the engine speed. In particular, a specific type of acceleration is going to be implemented, among an infinite number of speed variations. This type of acceleration is a two-step increase of the engine speed. In the first step, the speed is increased from 59% to 78% of the maximum speed of the Diesel engine and in the second step, the engine speed is increased from 78% to 91% of the maximum speed of the Diesel engine. Furthermore, it should be pointed out that, despite the fact that a combinator curve is used in the simulation model, during this transient, it is decided that the pitch diameter ratio will be constant, getting the value of the design point. In this way, the implementation of the two step acceleration will be simpler. The two step acceleration is described in Table 3.3. In Figure 3.20 the combinations of propeller pitch, $P/D$, and engine speed, $n_e$ are depicted.

| Type of acceleration | $P/D$ [-] | Engine Speed Step Increase (% of maximum engine speed) |
|---|---|---|
| Two steps | 1.2 | first step: 59% to 78%<br>second step: 78% to 91% |

Table 3.3: Engine speed increase implementation

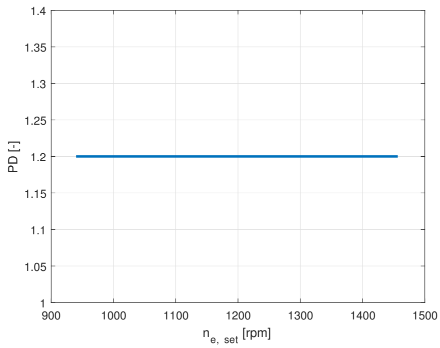


Figure 3.20: Combinator curve for two step engine speed increase.

Given the actual values of the gains of the PI controller of the actual propulsion plant, a range of values for the gains of the governor is implemented, aiming to set the most suitable values, with respect to the step response of certain variables of the propulsion plant to the controllable input of $n_{e,set}$. The system variables, whose the step response is checked are the diesel engine's brake power, $P_B$, the Diesel engine's brake torque, $M_B$, and the engine's speed, $n_e$ compared to the setpoint governor, $n_{e,set}$. Additionally, the behaviour of the propeller demand curve in the Diesel engine envelope, $P_B$-$n_e$, is examined. Given that the values of the gains of the PI controller of the actual propulsion plant are known, a combination of very low and very high values for the proportional, $K_p$ and integral gain, $K_i$ are investigated. The range of values for the gains of the governor, which are examined are shown in Table 3.4.

| Gain Combinations | 1 | 2 | 3 | 4 |
|---|---|---|---|---|
| $K_p$ | 0.5 | 1.5 | 2 | 10 |
| $K_i$ | 5 | 2 | 1.2 | 0.25 |
| $K_p/K_i$ | 0.1 | 0.75 | 1.67 | 40 |

Table 3.4: Values of gains of governor.

### 3.4.2. Results of Two-Step Engine Speed Increase

By implementing the combinations of PI controller gains, which are referred in Table 3.4, the response of the aforementioned system variables to a two-step engine speed increase is investigated. This is shown in Figures 3.21 - 3.23. For each one of the Figures, the first plot is the general picture of the response of the corresponding system variable to the two-step engine speed increase. As far as the second and third plot of each one of the Figures 3.21 - 3.23 are concerned, they both give detailed view of the response of each system variable, regarding each one of the two steps in speed increase.

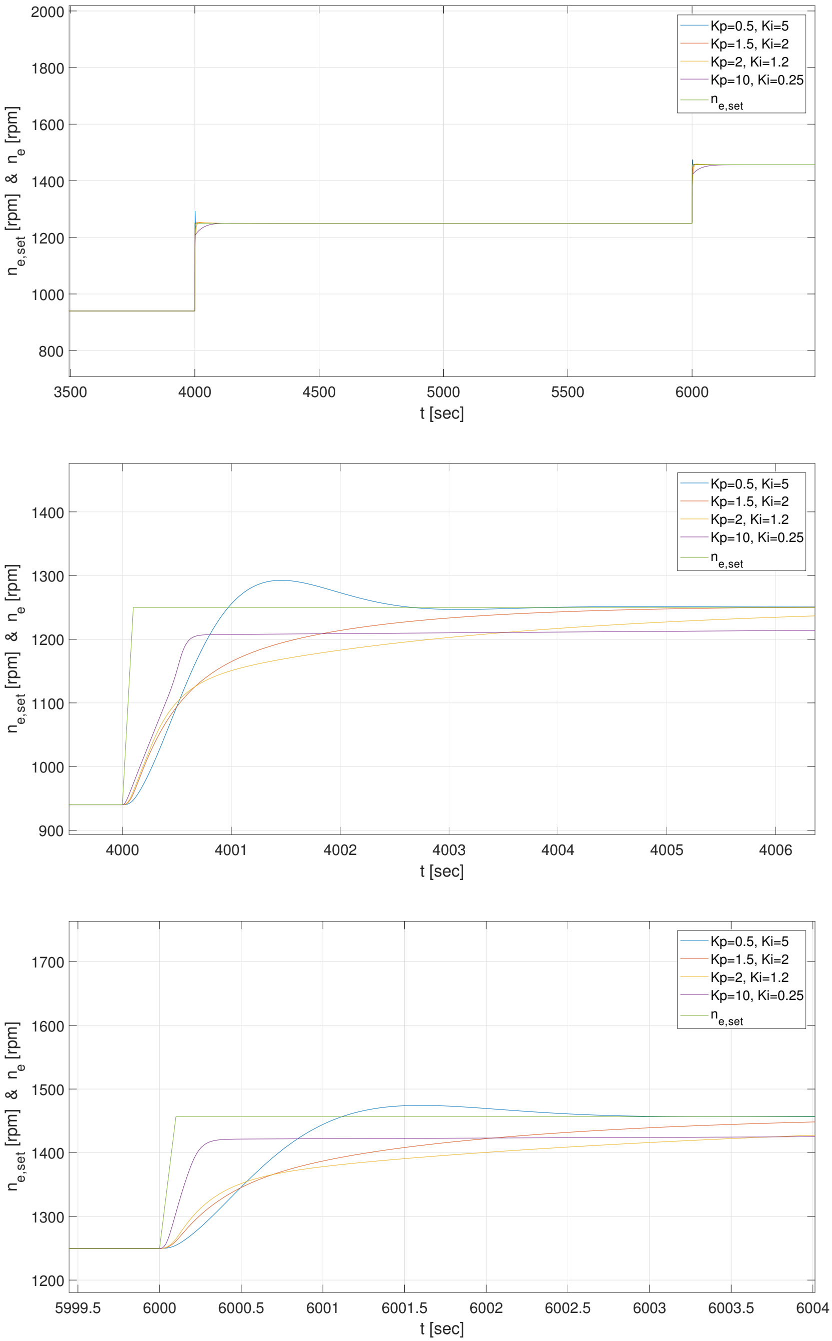


Figure 3.21: Response of actual engine speed, $n_e$, to two-step increase of governor engine speed setpoint, $n_{e,set}$.

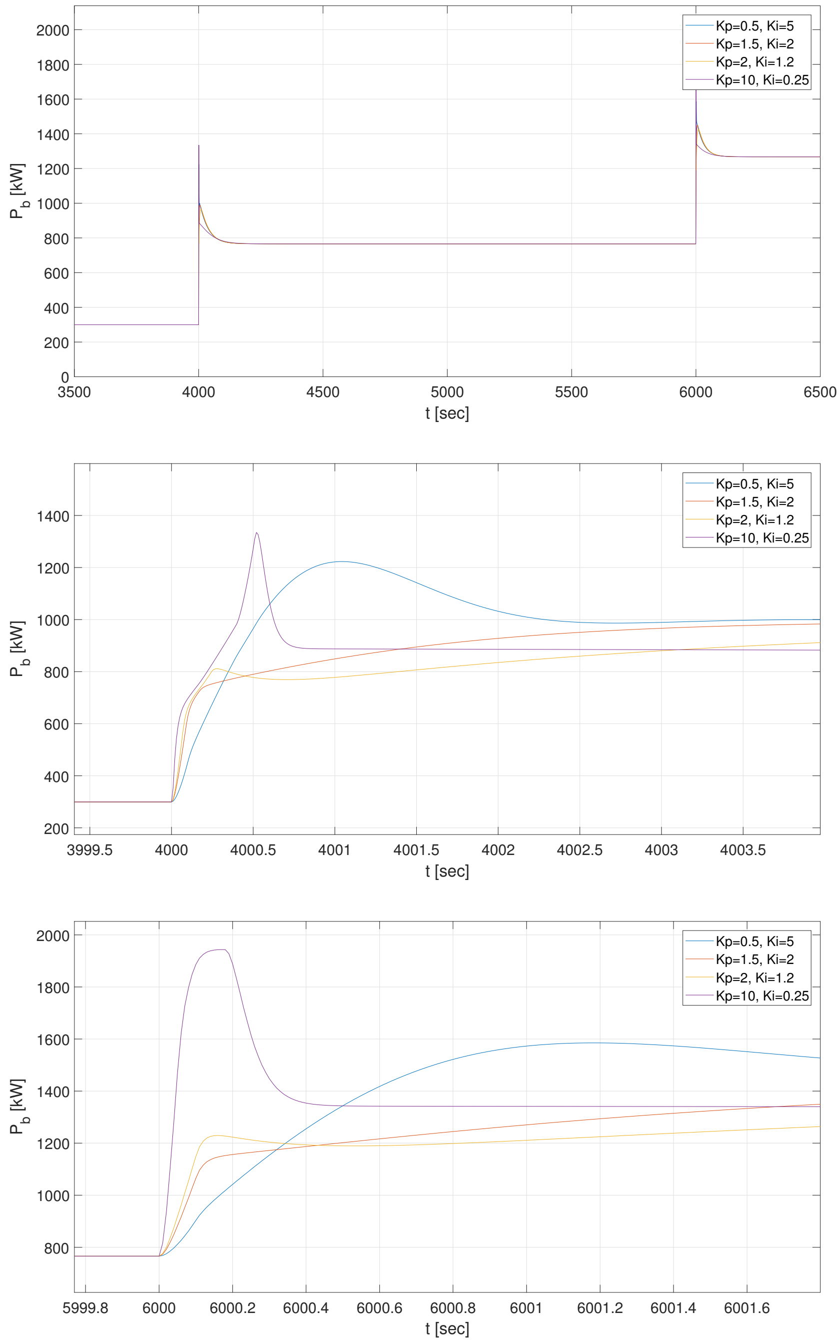


Figure 3.22: Response of brake engine power, $P_B$, to two-step increase of engine speed, $n_e$.

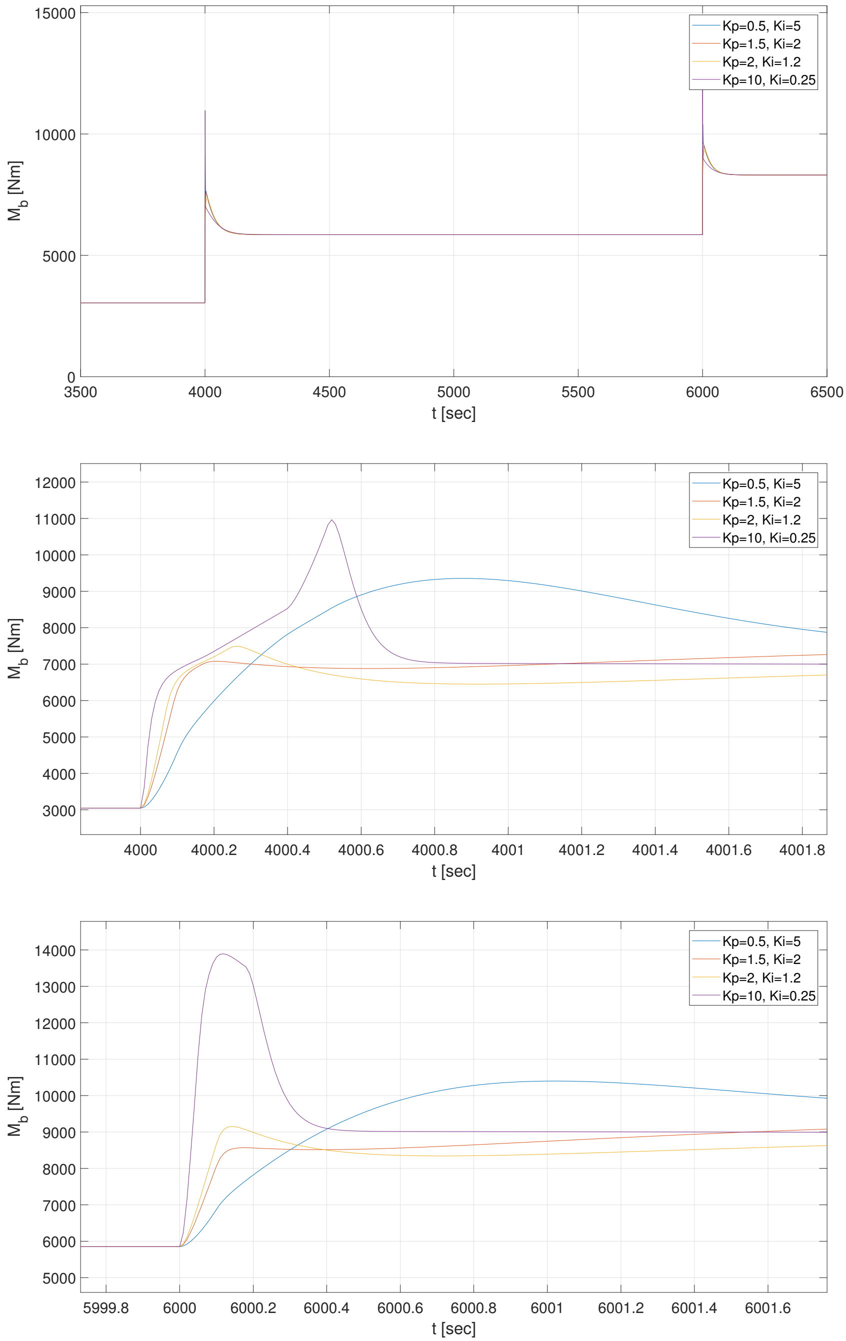


Figure 3.23: Response of brake engine torque, $M_B$, to two-step increase of engine speed, $n_e$.

3

As for the Figure 3.21, it shows the ability of the engine speed to follow the governor setpoint. Given the theoretical background on PID controllers, [Franklin et al., 1994], the behaviour of each one of the four combinations of $K_p$ and $K_i$ can be interpreted. According to Table 3.4, combination 4 reduces the difference between the actual engine speed and the governor setpoint faster, due to the high value of $K_p$. However, the small value of $K_i$ leads to a significant steady state error. On the other hand, combination 1, which has a small value for $K_p$, reduces the difference between the actual engine speed and the governor setpoint quite slowly, but the steady state error is eliminated quite fast, because of the high value of the $K_i$. With regards to combinations 2 and 3, they both reduce the error between the measured engine speed and the demanded by the controller engine speed at the same time. Their difference though, lies on the steady state error. Combination 2 with higher value of $K_i$ eliminates the steady state error faster than combination 3. These remarks apply exactly the same for both steps of engine speed, $n_e$, increase.

Regarding the similar behaviour of brake engine power and torque, $P_B$ and $M_B$, which are depicted in Figure 3.22 and 3.23 respectively, both are as expected. Combinations 1 and 4 result in a increased overshoot, compared to combinations 2 and 3, due to their significantly higher values of proportional, $K_p$ and integral gain, $K_i$, respectively. Furthermore, combination 1 has a decreased rising time, with respect to the rest combinations, which can be explained by the very high value of $K_p$. On the contrary, combination 4 has the longest rising time, because of the very low value of $K_p$. With regard to the response of brake engine power, $P_B$ and torque, $M_B$, when implementing Combinations 2 and 3, their behaviour is almost similar, with Combination 3 having a slightly shortest rising time compared to Combination 2, as a result of the slightly higher value of $K_p$. These comments, regarding the response of engine power, $P_B$ and engine torque $M_B$, apply the same for the two steps of engine speed increase, which are implemented.

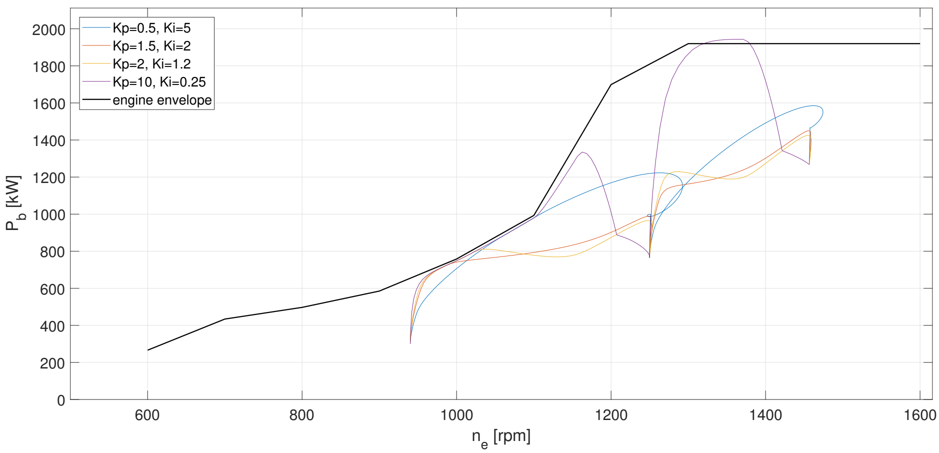


Figure 3.24: Response of load curve in Diesel engine operating envelope, in two-step engine speed increase.

In Figure 3.24, the behaviour of the load curve in the Diesel engine envelope is depicted, when a two-step engine speed increase is applied, using the previously mentioned four different Combinations of the PI controller gains. Additionally, it has to be mentioned that in the plot of Figure 3.24, an extra line can be noticed. This solid line in black colour defines the operating envelope of the Diesel engine, in other words the brake engine power limits, $P_B$, for each value of engine speed, $n_e$. These limits are included in the specifications of the Diesel engine, provided by the engine manufacturer.

Taking this into consideration, it is clearly shown that using Combinations 1 and 4, the behaviour of the load curve is much more aggressive and diverging. This can be attributed to the higher values of $K_p$ and $K_i$, when compared to those of Combinations 2 and 3. The response of the load curves,using Combinations 2 and 3, is smoother, without deviating from what is expected, with Combination 2 having the smoothest behaviour. Taking into account the above-mentioned, Combination 2, with $K_p = 1.5$ and $K_i = 2$ is proved to be the most suitable for the PI controller gains of the simulation model, in case of implementing a two-step engine speed acceleration.



## 3.5. SIMULATION MODEL VALIDATION

According to the definition given by ASME, validation is the process of determining the degree to which a model is an accurate representation of the real world, from the perspective of the intended uses of the model. Following this definition, some available experimental data are going to be used in order to assess the degree of their agreement with the simulation results. By that method, the level of confidence in model predictions is determined. In other words, the level of acceptance of the results, in cases that the simulation model is used to predict real life system behaviour, when experimental data are not available. Furthermore, with a good level of understanding of the underlying physical and mathematical principles, the differences between the experimental data and the simulation results can be explained and the model can be used in a better way, given that a simulation model can never fully capture the real phenomena and the simulation results will never fully agree with the real measurement data.

Regarding the validation process of the model derived in this chapter, the validated system variables are the Diesel engine brake power, $P_B$, the Diesel engine speed, $n_e$, the speed of the shaft driving the propeller $n_{shaft}$ and the vessel speed $v_s$. These variables are validated against measurements taken on board during sea trials of the used reference vessel RGS9316 with respect to static operating points of the ship propulsion plant.

The first system variables presented, regarding the validation of the model, are the brake engine power, $P_b$ plotted with engine speed $n_e$, within the limits of the Diesel engine operating envelope. The left hand side plot in Figure 3.25, presents the load curve derived from measured data, the one with the red dots and the one derived by the results of the simulation model. As it can be seen, in the right hand side plot, the simulated and measured results agree within 15%. The relative error between simulation and real measurements can be attributed to the divergence between the implemented resistance curve and the predicted one.

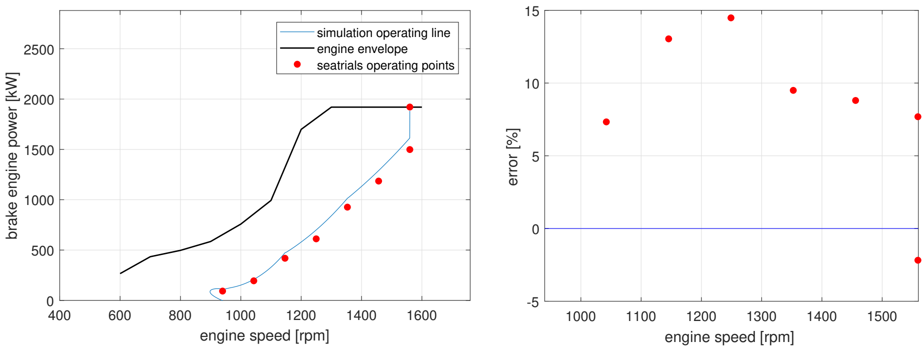


Figure 3.25: LHS: Load curve generated from sea trials data and load curve derived from simulation model. RHS: Divergence between the two load curves.

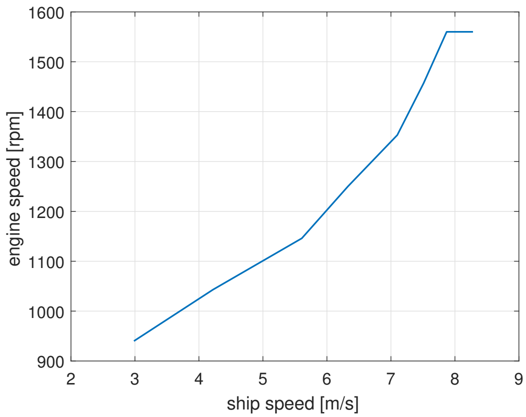


Figure 3.26: Plot of engine speed over vessel speed using measured data.

As it is depicted in Figure 3.15, the range of ship speed for which the implemented resistance curve has higher values than the predicted, corresponds to the range of engine speeds for which the load curve of the simulation model is above the measured load curve, according to Figure 3.26. Additionally, the deviation between the simulation model and the measured load curve can be attributed to differences, regarding the conditions under which the sea trials took place and the conditions, which are assumed in the simulation model (waves, wind speed, draught, trim). Moreover, part of the divergence could be due to the difference between the open water model, which is used in the propeller model of the simulation and is referred to a Fixed Pitch Propeller, whereas the measurement data are referred to the real propeller, which is a Controllable Pitch Propeller. Differences between the settings applied in the simulation model and the reference vessel during the sea trials can also be accused. Finally, another factor causing the deviation between the two load curves could be the power losses along the shaft line for off design operation, which are not captured by the simulation model (efficiency of different components are considered constant throughout the whole range of operating points), nevertheless exist in reality.

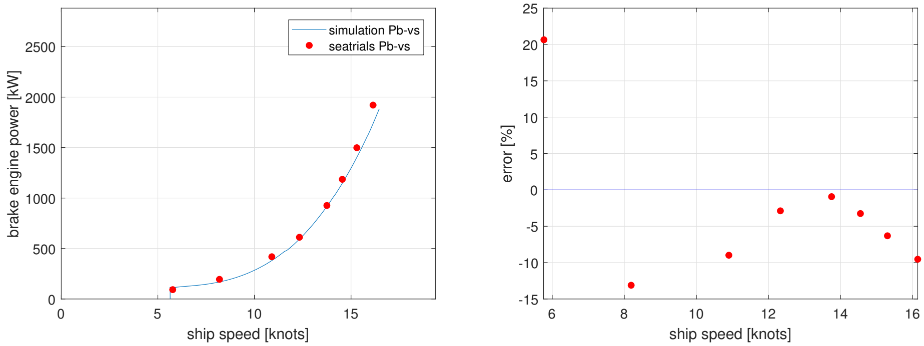


Figure 3.27: LHS: Engine brake power over ship speed plot from sea trials data and simulation data. RHS: Divergence between the two plots of engine brake power over ship speed.

In Figure 3.27, it can be seen that the measured and the simulation results, regarding the plot of engine brake power over the vessel's speed agree within a 13%. Similarly, the measured and simulation results of the plot of the vessel speed over the propeller shaft speed agree within a 9%.

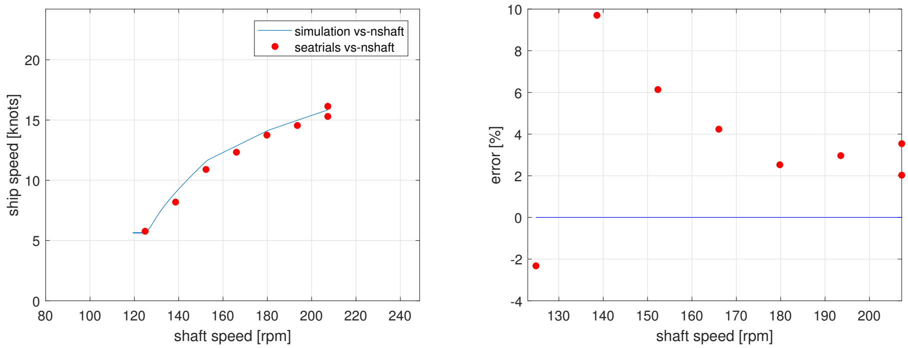


Figure 3.28: LHS: Ship speed over shaft speed plot from sea trials data and simulation data. RHS: Divergence between the two plots of ship speed over shaft speed.

## 3.6. CONCLUSIONS

According to what was presented in this chapter, regarding the simulation model of the propulsion plant of the reference vessel, RGS9316, it is clear that the derived non linear model can adequately capture the real, complex, physical phenomena, which drive the system's behaviour, as regards to engine speed, $n_e$ and engine torque, $M_b$ variations.

As far as the tuning of the model is concerned, the combination of the values of the gains for the engine speed governor were chosen under the perspective of an expected, without abnormalities and significant deviations, response of the system. This response agrees with an expected behaviour, in case of an implemented two steps increase of the engine speed.

With respect to the validation of the static operating points, the agreement of simulation results with measurement data are considered to be within acceptable limits. In the graphs of the load curve in the engine envelope, brake engine power over ship speed and ship speed over propeller shaft speed, simulation and sea trials data follow the same trend line. As for the relative errors, which can be remarked, especially regarding the propeller demand curve in the engine envelope and the graph of ship speed over propeller shaft speed, it can be mainly attributed to three reasons. Firstly, the divergence between the implemented in the model resistance curve and the predictive resistance curve, as it is presented in Figure 3.15. Secondly, the fact that in the propeller simulation model, the open water model used is given by polynomials, which are referred to a Fixed Pitch Propeller (FPP), whereas in reality, the measurements data are referred to a Controllable Pitch Propeller (CPP) with a different open water diagram. Additionally, a difference between the settings applied in the simulation model and the reference vessel during the sea trials, as well as the accuracy of the measurements, taken on board the vessel, can be the reason for the error between measurements and simulation data. Another reason for the deviation between measurements and simulation data could be a difference in the losses for the off design operation, along the shaft line. As it was mentioned in Section 3.1, in the specifications regarding the model goals, the efficiency of different components along the shaft line are considered constant, whereas in reality this is not realistic.

To conclude, despite the small relative error between simulation and measurements data, the outcome of the validation process of the simulation model presented in this chapter ensures that the model can rightfully be used for the investigation of the dynamic behaviour of the propulsion system.

# 4

# LINEARISATION OF SHIP SIMULATION MODEL

*At this chapter, a linear propulsion system model is derived from the non linear model, presented in Chapter 3, in three steps. The derived linear model is verified by means of comparison with the original non linear model in terms of their corresponding dynamic response in the frequency domain. The verification process ensures that the derived linear model can, justifiably, be used as a more simple, handy tool than the non linear model for the propulsion system analysis, controller design and tuning.*

## 4.1. INTRODUCTION AND GENERAL CONSIDERATIONS

A non linear ship propulsion plant model is considered to be a valuable tool, regarding the conceptual propulsion system design and the selection of the most favourable control strategy taking also into account the operational profile of the vessel. In addition, ship propulsion control design and tuning, which require time domain simulations, are achieved using the non linear simulation model of the propulsion plant into consideration.The reason for that is the capability of the non linear simulation models to include the non linear characteristics of each one of the components of the actual propulsion plant and capture the real, complex, physical phenomena, affecting the system's behaviour. Finally, as it was mentioned in Section 3.5, since the non linear model is validated, a high level of confidence, regarding the simulations' results, can be ensured.

On the other hand, the derivation and use of linear ship propulsion plant models seems to be a common practise in marine engineering [Kidd et al., 1985, Van Spronsen and Tousain, 2001, Stapersma and Vrijdag, 2017, Vrijdag and Stapersma, 2017]. Linear ship propulsion models are considered to be an additional tool, when it comes to the analysis of the behaviour of a propulsion system. What is more, linear models offer the possibility for a more clear understanding of the effect of different parameters on the propulsion plant's behaviour and performance, particularly in off design conditions.

Despite the fact that the linear models are usually derived on the grounds that they are more simple than their original non-linear models, requiring less parameters and knowledge of the modelled system, it should be mentioned that a linearised model is only valid in the neighbourhood of equilibrium [Franklin et al., 1994], which means that the linear model is only valid for small perturbations around the steady operation point that is chosen each time. The size of this neighbourhood should always be taken into consideration and, under this perspective, the results, when using a linear model, should be interpreted accordingly. Taking the aforementioned into account, a linear model should always be considered as an auxiliary tool, regarding the systems analysis, and not the replacement of the more complex, non linear model.



In the following Sections, the non linear model of Chapter 3 will be linearised in order to investigate the system behaviour in the frequency domain. The derivation of the linear model will give a clear insight of the influence of the main parameters and variables on the dynamic performance of the propulsion plant. The linearisation will take place in three steps. Each one of the parts of the propulsion plant that are going to be linearised are shown in Figure 4.1. The linearisation of the core propulsion system, excluding the prime mover and the propulsion control system, is considered to be the starting point. The core propulsion system includes the non linear dynamics of ship propulsion plant and is depicted in Figure 4.2. Then, two extensions are added to the linearised model. Firstly, a static Diesel engine model is included to the system. Secondly, the system is extended by the addition of an engine speed governor. Finally, each one of the three linearised parts are verified by comparing the Bode plots of the linear model to the Bode plots of the non linear model respectively.

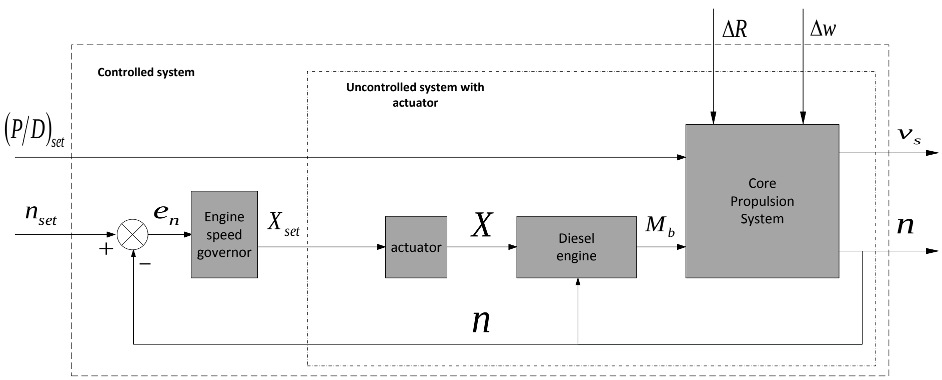


Figure 4.1: Block diagram showing the parts being linearised: a) the core propulsion system, b) the uncontrolled system with actuators, c) the controlled system.

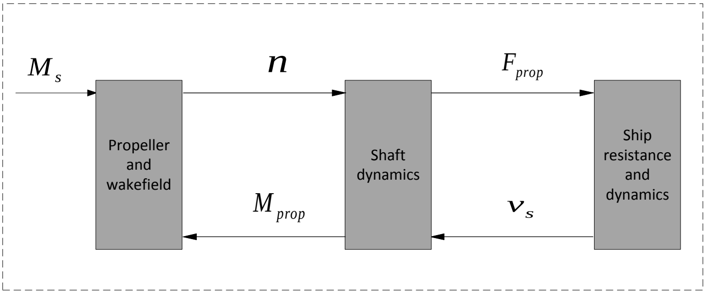


Figure 4.2: Core ship propulsion block diagram.



## 4.2. LINEARISATION PROCESS

At this point, it should be mentioned that, as a result of the linearisation process, the non linear characteristics of the simulation model presented in Chapter 3 will be neglected. The fact of neglecting the non linearities, which will be mentioned below, impose some limitations. The effect of these limitations will be investigated later on in this chapter, by means of comparison of system behaviour between a non linear and linear model, which is derived by the former.

As for the non linearities being disregarded during the linearisation, it is common practise to divide them into categories, [Stapersma and Vrijdag, 2017, Vrijdag and Stapersma, 2017]:

- Non linear characteristics of component models included in the simulation model. The propeller model, included in the core propulsion model has this kind of non linear behaviour, due to the curvature of the lines, which are used in the open water diagram model, in order to calculate the thrust, $K_T$ and the torque, $K_Q$ coefficients.

- Non linearities, as a consequence of multiplications in the underlying mathematical models. Mathematical relations used for the calculation of propeller thrust, $T = \rho \cdot n^2 \cdot D^4 \cdot K_T$ and propeller torque, $Q = \rho \cdot n^2 \cdot D^5 \cdot K_Q$ are two examples of this kind of multiplicative actions. Additionally, non linear characteristics occur due to power operations. An example for this is the resistance curve, $R = a \cdot v_s^e$.

- Non linearities due to limits in the simulation model. The most common example is the saturation of actuators, like the fuel rack actuator, using a mechanical end-stop preventing the engine overspeed and thermal overloading or the limits of a hydraulic system driving the pitch of the propeller blades in case of a controllable pitch propeller.

As it was mentioned before, these neglected non linearities influence the outcome of the comparison of the dynamic response between the non linear and linear model. Consequently, they should be taken into account, during the evaluation of the correct or not derivation of the linear model from the original non linear simulation model. Furthermore, it could be beneficial to take these disregarded non linearities into consideration when using the results of the response of the linear model, when realistic disturbances are applied within the limited neighbourhood of the linearisation point.

## NORMALISATION AND LINEARISATION

The process of normalising and linearising mathematical formulas including multiplicative and power operations is demonstrated in details in [Stapersma and Vrijdag, 2017, Vrijdag and Stapersma, 2017]. This process is then applied to the shaft and ship speed loop as they are shown in the ship propulsion block diagram in Figure 3.6.

The differential equation for the dynamics of the shaft speed loop, as given in Section 3.3.3, is given below, with the assumption of constant shaft inertia, since the change of mass, due to the water entrained by the propeller, is neglected:

4

$$2\pi \cdot I_p \cdot \frac{dn}{dt} = M_s - M_{prop} \tag{4.1}$$

The variation of both shaft and propeller torque around an equilibrium point is:

$$M_s = M_{s,0} + \delta M_s \tag{4.2}$$

$$M_{prop} = M_{prop,0} + \delta M_{prop} \tag{4.3}$$

In case of steady nominal condition, where there is equilibrium between shaft and propeller torque:

$$M_{s,0} = M_{prop,0} \tag{4.4}$$

The substitution of Eq. 4.2 and Eq. 4.3 in Eq. 4.1 and dividing by the value of torque at nominal point results in:

$$\frac{2\pi \cdot I_p}{M_{s,0}} \cdot \frac{n_0}{n_0} \cdot \frac{dn}{dt} = \frac{\delta M_s}{M_{s,0}} - \frac{\delta M_{prop}}{M_{prop,0}} \tag{4.5}$$

Given, that the integration constant of the shaft loop and the normalised shaft speed time derivative are defined as:

$$\tau_n \equiv \frac{2\pi \cdot I_p \cdot n_0}{M_{s,0}} \tag{4.6}$$

$$\frac{1}{n_0} \cdot \frac{dn}{dt} \equiv \frac{dn^*}{dt} \tag{4.7}$$

Then, substitution in Eq. 4.5 leads to:

$$\tau_n \cdot \frac{dn^*}{dt} = \delta M_s^* - \delta M_{prop}^* \tag{4.8}$$

At this point, it has to be pointed out that the division by the nominal torque in Eq. 4.5 is only valid for a chosen nominal point, which is also an equilibrium point for the system that is examined. It goes without saying, that this an important remark, as it dictates that for every different equilibrium point in the system that is under consideration, a different linear model can be derived, regarding the parameters and variables on which the linear model is dependent.

Normalisation of the formula which relates the brake engine torque to the shaft torque (Eq. 3.9), assuming constant total transmission efficiency, results in:

$$\delta M_s^* = \delta M_b^* \tag{4.9}$$

Accepting the relative rotative coefficient as a constant variable, propeller torque and open water torque are equal:

$$\delta M_{prop}^* = \delta Q^* \tag{4.10}$$

According to the linearisation and normalisation method presented in [Stapersma and Vrijdag, 2017], $\delta Q^*$ in equation 4.10 is calculated using the open water torque, $Q = \rho \cdot n^2 \cdot D^5 \cdot K_Q$, which gives:

$$\delta Q^* = 2 \cdot \delta n^* + \delta K_Q^* \tag{4.11}$$



With respect to torque coefficient, $K_Q = g(J, P/D)$, which is a function of advance coefficient, $J$ and pitch over diameter ratio, $P/D$, the linearised formula is:

$$\frac{\delta K_Q}{\delta K_{Q,0}} = b \cdot \frac{\delta J}{J_0} + q \cdot \frac{\delta (P/D)}{(P/D)_0} \tag{4.12}$$

where the normalised propeller derivatives $b$ and $q$ are calculated by:

$$b \equiv \frac{J_0}{K_{Q,0}} \cdot \frac{\delta K_Q}{\delta J}\bigg|_{P/D} \tag{4.13}$$

$$q \equiv \frac{(P/D)_0}{K_{Q,0}} \cdot \frac{\delta K_Q}{\delta (P/D)}\bigg|_{J} \tag{4.14}$$

Consequently, the normalised and linearised Eq. 4.12 becomes:

$$\delta K_Q^* = b \cdot \delta J^* + q \cdot \delta (P/D)^* \tag{4.15}$$

Regarding the rest of the parameters used in the propeller model, linearised advance ratio, $J$, advance velocity, $v_a$ and wake factor, $w$ are given below:

$$J = \frac{v_a}{n \cdot D} \implies \delta J^* = \delta v_a^* - \delta n^* \tag{4.16}$$

$$v_a = (1-w) \cdot v_s \implies \frac{\delta v_a}{v_{a,0}} = \frac{\delta v_s}{v_{s,0}} - \frac{\delta w}{1-w_0} \implies \delta v_a^* = \delta v_s^* - \delta w^* \tag{4.17}$$

Special notation should be done at this point, regarding the change of wake fraction, which is taken into consideration compared to relative rotative efficiency and total transmission losses, which were neglected.

$$\delta w^* = \frac{\delta w}{1-w_0} \tag{4.18}$$

The differential equation for the dynamics of the ship speed loop as given in Section 3.3.4 is given below, with the assumption of constant ship mass, since the change of mass due to the water entrained by the hull is neglected:

$$m_{ship} \cdot \frac{dv_s}{dt} = F_{prop} - F_{ship} \tag{4.19}$$

Small perturbations around both propeller thrust and ship resistance around an equilibrium point, give:

$$F_{prop} = F_{prop,0} + \delta F_{prop} \tag{4.20}$$

$$F_{ship} = F_{ship,0} + \delta F_{ship} \tag{4.21}$$

In case of steady nominal condition, where there is equilibrium between ship resistance and propeller thrust:

$$F_{prop,0} = F_{ship,0} \tag{4.22}$$

Substituting Eq. 4.20-4.22 to Eq. 4.19:

$$m_{ship} \cdot \frac{dv_s}{dt} = \delta F_{prop} - \delta F_{ship} \tag{4.23}$$

Following the same procedure, as for the shaft speed loop, Eq. 4.19 gives:

$$\tau_v \cdot \frac{dv_s^*}{dt} = \delta F_{prop}^* - \delta F_{ship}^* \tag{4.24}$$

The left hand side of Eq. 4.24 is defined, respectively, by:

$$\tau_v \equiv \frac{m_{ship} \cdot v_{s,0}}{F_{ship,0}} \tag{4.25}$$

$$\frac{1}{v_{s,0}} \cdot \frac{dv_s}{dt} \equiv \frac{dv_s^*}{dt} \tag{4.26}$$

In the right hand side of Eq. 4.24, the ship force $F_{ship}$ is equal to resistance $R$ and can be replaced as presented below:

$$\frac{\delta F_{ship}}{F_{ship,0}} = \frac{R}{R_0} \implies \delta F_{ship}^* = \delta R^* \tag{4.27}$$

Given that the resistance can be represented as a polynomial curve:

$$R = \alpha \cdot v_s^e \implies \frac{\delta R}{R_0} = \frac{\delta \alpha}{\alpha_0} + e \cdot \frac{\delta v_s}{v_{s,0}} \implies \delta R^* = \delta \alpha^* + e \cdot \delta v_s^* \tag{4.28}$$

The power factor $e$ of the resistance curve, which is presented as a multiplication factor, after the normalisation and linearisation process, is called normalised steepness of the resistance curve and is defined by:

$$e \equiv \frac{v_{s,0}}{R_0} \cdot \left.\frac{\delta R}{\delta v_s}\right|_{\alpha} \tag{4.29}$$

The propeller thrust in Eq. 4.24 is derived by the formula relating the propeller thrust to the open water thrust, including the deduction factor:

$$F_{prop} = k_p \cdot (1-t) \cdot T \implies \frac{\delta F_{prop}}{F_{prop,0}} = \frac{\delta T}{T_0} - \frac{\delta t}{1-t_0} \overset{t=const}{\implies} \delta F_{prop}^* = \delta T^* \tag{4.30}$$

Regarding the normalised and linearised open water thrust, it is defined using the open water thrust formula:

$$T = \rho \cdot n^2 \cdot D^4 \cdot K_T \implies \frac{\delta T}{T_0} = 2 \cdot \frac{\delta n}{n_0} + \frac{\delta K_T}{K_{T,0}} \implies \delta T^* = 2 \cdot \delta n^* + \delta K_T^* \tag{4.31}$$

Thrust coefficient, $K_T = f(J, P/D)$, which is a function of advance coefficient, $J$ and pitch over diameter ratio, $P/D$, is linearised and normalised following the same procedure as in Eq. 4.12 and Eq. 4.15 for torque coefficient:

$$\frac{\delta K_T}{K_{T,0}} = \alpha \cdot \frac{\delta J}{J_0} + p \cdot \frac{\delta(P/D)}{(P/D)_0} \implies \delta K_T^* = \alpha \cdot \delta J^* + p \cdot \delta(P/D)^* \tag{4.32}$$



The normalised propeller derivatives $a$ and $p$, presented in Eq. 4.32 are calculated by:

$$\alpha \equiv \frac{J_0}{K_{T,0}} \cdot \frac{\delta K_T}{\delta J}\bigg|_{(P/D)} \tag{4.33}$$

$$p \equiv \frac{(P/D)_0}{K_{T,0}} \cdot \frac{\delta K_T}{\delta(P/D)}\bigg|_{J} \tag{4.34}$$

By substituting Eq. 4.9, 4.10, 4.11, 4.15, 4.16, 4.17 into Eq. 4.8 the linearised mathematical description of the dynamics of the shaft speed loop is given:

$$\tau_n \frac{dn^*}{dt} = \delta M_b^* - (2-b)\delta n^* - b\delta v_s^* + b\delta w^* - q\delta(P/D)^* \tag{4.35}$$

In Eq. 4.35 a clear insight is given, regarding the relation between shaft acceleration $\frac{dn^*}{dt}$, the two state variables, as $\delta n^*$ and $\delta v_s^*$ are called, and the three variables that are considered as inputs for the linearised system, $\delta M_b^*$, $\delta w^*$ and $\delta(P/D)^*$.

Accordingly, the same linearised mathematical description can be derived for the dynamics of the ship speed loop, by substituting Eq. 4.16, 4.17, 4.27, 4.28, 4.30, 4.31, 4.32 into Eq.4.24:

$$\tau_v \frac{dv_s^*}{dt} = (2-a)\delta n^* - (e-\alpha)\delta v_s^* - \delta\alpha^* - \alpha\delta w^* + p\delta(P/D)^* \tag{4.36}$$

Similarly to Eq. 4.35, Eq. 4.36 reveals the relation between ship acceleration $\frac{dv_s^*}{dt}$ the two state variables $\delta n^*$, $\delta v_s^*$ and the inputs of the linearised system presented in this formula $\delta\alpha^*$, $\delta w^*$ and $\delta(P/D)^*$

The derived Eq. 4.35 and Eq. 4.36 are depicted as block diagram in Figure 4.3. In this Figure, the linearised core propulsion system, excluding the prime mover (Diesel engine in the system under consideration) and the propulsion control system (governor), is presented as two first order systems in series, the first one in red colour and the second one in green colour. The inputs of the block diagram of the linearised propulsion plant are clearly shown. In blue colour are $\delta M_b^*$ and $\delta(P/D)^*$, which can be influenced by the operator and in black colour are $\delta\alpha^*$ (resistance perturbation) and $\delta w^*$ (wakefield perturbation), which are defined as disturbances for the system and are environmental dependent. They can, also, be influenced by the operator by changing course, which is not examined in this thesis or by sailing at another speed, in other words changing operating point.

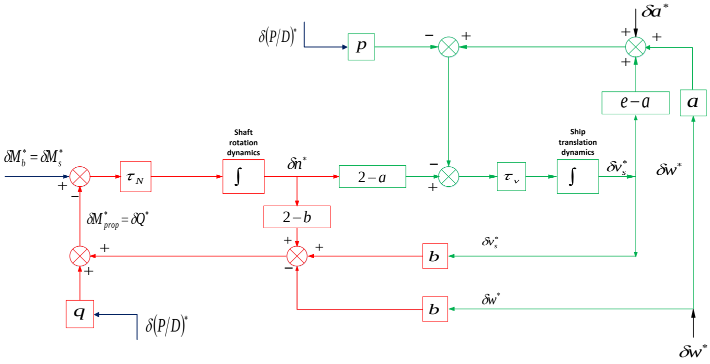


Figure 4.3: Block diagram of linearised core ship propulsion plant.



In order to investigate and elaborate in the system behaviour in the frequency domain, the method used in this thesis is the State-Space notation similarly to the approach followed in [Vrijdag and Stapersma, 2017]. Compared to transfer functions derived using the Laplace transformation as it is done in [Stapersma and Vrijdag, 2017], the State-Space method offers an easier and simpler process to obtain the Bode plots, which will be the tool to examine the response of the system, into consideration, in the frequency domain.

In general, for the State-Space notation, the system equation used, is the one below, [Vrijdag and Stapersma, 2017]:

$$\begin{aligned} \dot{\mathbf{x}} &= A\mathbf{x} + B\mathbf{u} + G\mathbf{w} \\ \mathbf{y} &= C\mathbf{x} + D\mathbf{u} + \mathbf{v} \end{aligned} \tag{4.37}$$

In Eq. 4.37, the first equation is called the *state equation*, while the second one is called the *output equation*. Regarding the coefficients in capital letters presented in Eq. 4.37, $A$ is called *system matrix*, $B$ is known as the *input matrix*, $G$ is called the *gain matrix* for the system disturbances, $C$ is the *output matrix* and $D$ is called the *feedforward matrix*, which couples the input and the output. As for the variables in Eq. 4.37, $\mathbf{x}$ is called *state vector*, $\mathbf{u}$ is the *input vector*, $\mathbf{w}$ is the *disturbance vector* and $\mathbf{y}$ is the *output vector*. The variable $\mathbf{v}$ is called *sensor noise vector*.

At this point it should be mentioned that, for each one of the following steps regarding the linearisation of the propulsion system in this thesis, vectors $\mathbf{u}$ and $\mathbf{w}$ are merged into one input vector $\mathbf{u}$, since both of them are considered as inputs to the linear system. Consequently, the *input matrix*, $B$ and the *gain matrix* for the disturbances, $G$, are merged into one input matrix, $B$. What is more, the above mentioned *sensor noise vector*, $\mathbf{v}$ is not used in this thesis.

## 4.3. Core Propulsion System

### Linear Model

As it was mentioned in Section 4.1, the linearisation of the non linear model, presented in Chapter 3, will be done in three parts. In this Section, the first part will be shown, including only the linearisation of the core propulsion system, as depicted in Figure 4.4, and the verification of the derived linear model, in terms of comparison of the behaviour of the linear model in the frequency domain to the behaviour of the non linear.



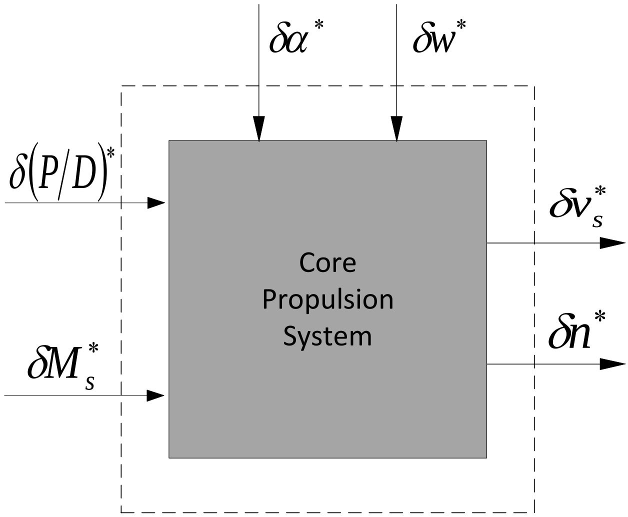


Figure 4.4: Block diagram of linearised core propulsion system.

The linearisation process presented in Section 4.2 is referred to the linearisation of the core propulsion system, as the formulas linearised there represent only the shaft dynamics, the ship dynamics, including the ship's hull resistance, as well as the propeller model and the wakefield, interacting with the propeller blades. The resulting formulas, Eq. 4.35 and Eq. 4.36 can mathematically describe the core propulsion system. Considering the shaft speed, $\delta n^*$ and ship speed, $\delta v_s^*$, as the outputs of the system, the matrices and vectors needed for the State-Space method, as they were presented in the Section before, are given below:

$$
\begin{aligned}
A &= \begin{bmatrix} -\frac{(2-b)}{\tau_n} & -\frac{b}{\tau_n} \\ \frac{(2-\alpha)}{\tau_v} & -\frac{(e-\alpha)}{\tau_v} \end{bmatrix} \\
B &= \begin{bmatrix} \frac{1}{\tau_n} & -\frac{q}{\tau_n} & 0 & \frac{b}{\tau_n} \\ 0 & \frac{p}{\tau_v} & -\frac{1}{\tau_v} & -\frac{\alpha}{\tau_v} \end{bmatrix} \\
C &= \begin{bmatrix} 1 & 0 \\ 0 & 1 \end{bmatrix} \\
D &= \begin{bmatrix} 0 & 0 & 0 & 0 \\ 0 & 0 & 0 & 0 \end{bmatrix} \\
\mathbf{x} = \mathbf{y} &= \begin{bmatrix} \delta n^* \\ \delta v_s^* \end{bmatrix} \\
\mathbf{u} &= \begin{bmatrix} \delta M_b^* \\ \delta (P/D)^* \\ \delta \alpha^* \\ \delta w^* \end{bmatrix}
\end{aligned}
\tag{4.38}
$$

As it was explained in 4.2, the values of the parameters, which are included in the State-Space model, are dependent on the open water propeller diagram, which is used and on the operating point, which is examined each time. The reason for this is that the linearised model is valid only at an equilibrium point and for small perturbations around it. Consequently, different operating-equilibrium point defines different values for the parameters used in the above mentioned system. Consequently, different values for the parameters define different State-Space model.

In this thesis, two different operating points will be used for the three parts of the linearisation process of the non linear simulation model presented in Chapter 3. Taking into account the combination curve, which was presented in Section... and implemented for the validation of the simulation model, the two operating points for which the linear models will be derived, are **operating points 6** and **8**. These two different operating points were chosen aiming to investigate the influence of the operating point on the behaviour of the linear model in the frequency domain.

The values of the necessary variables at the operating points under consideration of the non linear simulation model and the parameters needed to define the State-Space model for the aforementioned operating points, which will be examined, are presented in the two following Tables 4.1.

| System Parameters | Values for **operating point 6** | Values for **operating point 8** | Units of Parameters |
|---|---|---|---|
| $n_0$ | 2.7677 | 3.2257 | $[s^{-1}]$ |
| $M_{b,0}$ | 4.4228E+04 | 7.0014E+04 | [Nm] |
| $I_{p,tot}$ | 3.9526E+03 | 3.9526E+03 | [kg m$^2$] |
| $J_0$ | 0.8012 | 0.7992 | [-] |
| $(P/D)_0$ | 1.1456 | 1.1989 | [-] |
| $v_{s,0}$ | 6.8821 | 8.0003 | $[m/s]$ |
| $F_{ship,0}$ | 1.6948E+05 | 2.6169E+05 | [N] |
| $m_t$ | 3.7449E+06 | 3.7449E+06 | [kg] |
| $K_{T,0}$ | 0.2031 | 0.2308 | [-] |
| $K_{Q,0}$ | 0.0393 | 0.0457 | [-] |
| $a$ | -1.9208 | -1.6760 | [-] |
| b | -1.5884 | -1.4064 | [-] |
| p | 2.8408 | 2.5956 | [-] |
| q | 3.3881 | 3.2164 | [-] |
| e | 2.9348 | 2.8827 | [-] |
| $\tau_n$ | 1.5541 | 1.1442 | $[s]$ |
| $\tau_v$ | 152.0725 | 114.4896 | $[s]$ |

Table 4.1: Variables and parameters of linearised core propulsion system, using the State-Space notation at **operating point 6** and **operating point 8**.

## Verification of Bode plots

The next step, following the derivation of the State-Space model, is the verification of the linear model. This verification will prove whether or not, the linear model was properly derived by the original non linear model, allowing or not, its valid use for perturbations around the examined operating points, within the limits imposed by the linearisation theory. The method followed to verify the linear model in this thesis, is by examining the level of agreement between the Bode plots of the linear and the non linear model.

At this point, it has to be referred that the Bode plots, which are used extensively in electrical engineering and control theory, are graphs of the frequency response of a system. In this case, they relate the response of the output and input variables of the system, by plotting the ratio of the corresponding responses (magnitude) against a horizontal axis proportional to the logarithm of a selected frequency range.

The State-Space model derived for the core propulsion system is implemented in MATLAB, giving to all the necessary variables and parameters the values shown in Table 4.1. Thus, the Bode plots of the linear model are obtained.

As far as the Bode plots of the non linear model are concerned, they are obtained with the use of non linear model simulations, following the method of normalisation and linearisation of the variables involved, which was provided in Section 4.2.

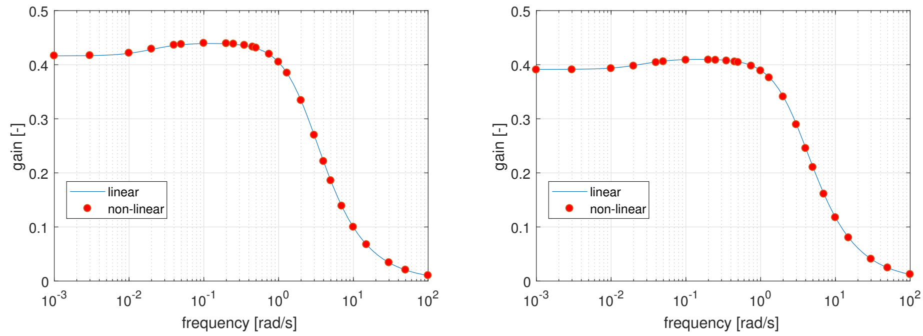


(a) operating point 6 (b) operating point 8



Figure 4.5: Bode plots of shaft speed for wake variation, $\frac{\boldsymbol{\delta n^*}}{\boldsymbol{\delta w^*}}$, of linear (solid line) and non linear (red dots) model of **core propulsion system**.

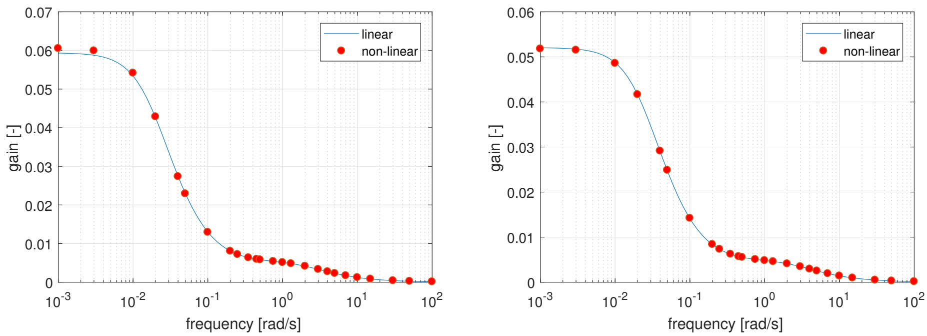


(a) operating point 6 (b) operating point 8

Figure 4.6: Bode plots of ship speed for wake variation, $\frac{\boldsymbol{\delta v_s^*}}{\boldsymbol{\delta w^*}}$, of linear (solid line) and non linear (red dots) model of **core propulsion system**.

The four Bode plots presented in Figure 4.5 and Figure 4.6 are referring to the two operating points, as they were defined in the previous section, with the left plot of each Figure referring to **operating point 6** and the right plot referring to **operating point 8**. These four Bode plots compare the response of the two system states $\delta n^*$ and $\delta v_s^*$, which are considered to be the outputs of the linear system, to a perturbation of the input variable $\delta w^*$. The comparison is made between the Bode plots of the linear (solid line) and non linear model (red dots), with Figure 4.5 demonstrating the response of state variable $\delta n^*$ for the two aforementioned operating points, whereas Figure 4.6 shows the response of state variable $\delta v_s^*$.

As far as the comparison done in Figure 4.5 and 4.6 is concerned, it can be noticed that the response of shaft speed and ship speed to wake variation, $\frac{\delta n^*}{\delta w^*}$ and $\frac{\delta v_s^*}{\delta w^*}$ of the linear system fully agrees to the correspondent one of the non linear system for the whole range of examined frequencies. This remark applies for both the examined operating points.

## 4.4. UNCONTROLLED SYSTEM WITH ACTUATORS

### LINEAR MODEL

In this Section, the second step of linearisation of the propulsion plant is presented, regarding the uncontrolled system including the actuators, as it is depicted in Figure 4.7. What is more, the verification of the derived linear model will take place, comparing the behaviour of the linear model in the frequency domain to the behaviour of the non linear.

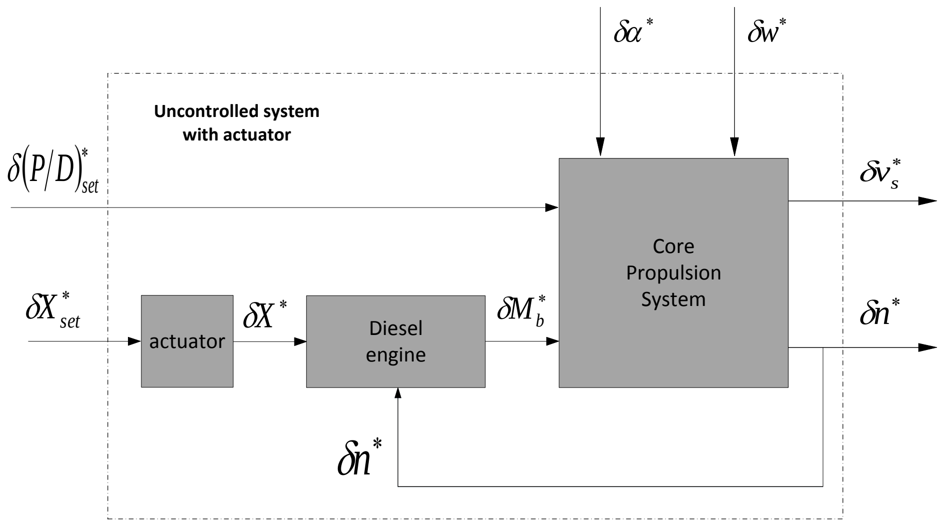


Figure 4.7: Block diagram of linearised uncontrolled propulsion system with actuators.

Following the process of linearisation presented in Section 4.2, two components are added, as shown in Figure 4.7. These two components are the Diesel engine, which, according to the non linear simulation model, drives the propeller shaft and its fuel rack actuator. As it was referred in Section 3.3.2, the Diesel engine of the non linear simulation model, is simply modelled, using the fuel rack map of the Diesel engine under consideration. Such a fuel rack map relates the engine torque, which is the desired output of the model, with the fuel rack position, $X$, and the engine speed, $n_e$. Linearisation and normalisation of Eq. (equation of diesel model presented in chapter 3), which describes mathematically the model described before, leads to the following linear formula:

$$\frac{\delta M_b}{M_{b,0}} = g \cdot \frac{\delta n}{n_0} + v \cdot \frac{\delta X}{X_0} \tag{4.39}$$

The normalised derivatives, $g$ and $v$, which are introduced in Eq. 4.39 are defined below:

$$g \equiv \frac{n_0}{M_{b,0}} \cdot \frac{\delta M_b}{\delta n}\bigg|_X \tag{4.40}$$

$$v \equiv \frac{X_0}{M_{b,0}} \cdot \frac{\delta M_b}{\delta X}\bigg|_n \tag{4.41}$$

These normalised derivatives can be calculated using the Diesel engine's fuel rack map, as it was referred in Section 3.3.2 and shown in Figure 3.12. Thus Eq. 4.39 can be written as below:

$$\delta M_b^* = g \cdot \delta n^* + v \cdot \delta X^* \tag{4.42}$$

4

Since the fuel map of the used diesel engine is not available as well as the factory acceptance acceptance test, from which the fuel map can be derived according to Section 3.3.2, typical values for the normalised derivatives, $g$ and $v$ of Eq. 4.39 and Eq. 4.42 will be used. A range of typical values for normalised derivative $g$ is between -1 and -0.5, [Vrijdag and Stapersma, 2017]. This range of values causes a slightly negative slope of the constant fuel rack lines, as depicted in Figure 3.12. As far as the normalised derivative $v$ is concerned, a range of typical values usually, lies between 0.75 and 1.25. Taking into account the lack of available fuel map or data coming from the Factory Acceptance Test(FAT) of the Diesel engine under consideration, the most simplified assumption is going to be used, regarding the relation between the torque output of the engine, $M_b$ and the engine speed, $n_e$ and fuel rack position, $X$, as inputs. This means that, the Diesel engine is considered to be a constant torque machine. In other words, the normalised derivative $g$ gets the value $g = 0$. What is more, the value of the second normalised derivative $v$ gets the value $v = 1$.

As for the fuel rack actuation mechanism, which is also added in this step of the linearisation process, its dynamics are very fast compared to the ship and shaft speed loop dynamics. This is due to the very low mass of the mechanism when this is compared to the available displacement forces of the fuel injection pump. As a result, the dynamics of the fuel rack actuation mechanism is neglected:

$$\delta X^* = \delta X^*_{set} \tag{4.43}$$

The addition and substitution of the linearised mathematical formulas, representing the sub models, which were added in this second step of the linearisation process, will be added and substituted in the mathematical formulas describing the shaft and ship speed loop, which were presented in Eq. 4.35 and 4.36. Furthermore, for completeness reasons, a differential equation is added describing the propeller pitch control system and its actuating mechanism. In this thesis, the propeller pitch control system is absent in the non linear simulation model, so it is its actuating mechanism. For this reason, the values of all the variables presented in this differential equation are set to zero.

$$\begin{aligned}
\tau_n \frac{dn^*}{dt} &= v\delta X^*_{set} - (2-b-g)\delta n^* - b\delta v_s^* + b\delta w^* - q\delta(P/D)^* \\
\tau_v \frac{dv_s^*}{dt} &= (2-\alpha)\delta n^* - (e-\alpha)\delta v_s^* - \delta\alpha^* - \alpha\delta w^* + p\delta(P/D)^* \\
\tau_{(P/D)} \frac{d(P/D)^*}{dt} &= \delta(P/D)^*_{set} - \delta(P/D)^*
\end{aligned} \tag{4.44}$$

Following the State-Space notation, the matrices and vectors representing the linearised model of the uncontrolled system with actuators are given below:

$$
\begin{aligned}
A &= \begin{bmatrix} -\frac{(2-b-g)}{\tau_n} & -\frac{b}{\tau_n} & -\frac{q}{\tau_n} \\ \frac{(2-\alpha)}{\tau_v} & -\frac{(e-\alpha)}{\tau_v} & \frac{p}{\tau_v} \\ 0 & 0 & -\frac{1}{\tau_{(P/D)}} \end{bmatrix} \\
B &= \begin{bmatrix} \frac{v}{\tau_n} & 0 & 0 & \frac{b}{\tau_n} \\ 0 & 0 & -\frac{1}{\tau_v} & -\frac{\alpha}{\tau_v} \\ 0 & \frac{1}{\tau_{(P/D)}} & 0 & 0 \end{bmatrix} \\
C &= \begin{bmatrix} 1 & 0 & 0 \\ 0 & 1 & 0 \\ 0 & 0 & 1 \end{bmatrix} \\
D &= \begin{bmatrix} 0 & 0 & 0 & 0 \\ 0 & 0 & 0 & 0 \\ 0 & 0 & 0 & 0 \end{bmatrix} \\
\mathbf{x} = \mathbf{y} &= \begin{bmatrix} \delta n^* \\ \delta v_s^* \\ \delta (P/D)^* \end{bmatrix} \\
\mathbf{u} &= \begin{bmatrix} \delta X_{set}^* \\ \delta (P/D)_{set}^* \\ \delta \alpha^* \\ \delta w^* \end{bmatrix}
\end{aligned}
\tag{4.45}
$$

## VERIFICATION OF BODE PLOTS

After the derivation of the linear model and the matrices of the State-Space notation for the uncontrolled system with actuators, the Bode plots are going to be derived, by implementing the model in MATLAB. The values needed for the variables and parameters, which consist the matrices in the State-Space notation of the linear system, are given in Table 4.2 for operating point 6 and operating point 8.

| System Parameters | Values for **operating point 6** | Values for **operating point 8** | Units of Parameters |
|---|---|---|---|
| $n_0$ | 2.7677 | 3.2257 | $[s^{-1}]$ |
| $M_{b,0}$ | 4.4228E+04 | 7.0014E+04 | [Nm] |
| $I_{p,tot}$ | 3.9526E+03 | 3.9526E+03 | [kg m$^2$] |
| $J_0$ | 0.8012 | 0.7992 | [-] |
| $(P/D)_0$ | 1.1456 | 1.1989 | [-] |
| $v_{s,0}$ | 6.8821 | 8.0003 | $[m/s]$ |
| $F_{ship,0}$ | 1.6948E+05 | 2.6169E+05 | [N] |
| $m_t$ | 3.7449E+06 | 3.7449E+06 | [kg] |
| $K_{T,0}$ | 0.2031 | 0.2308 | [-] |
| $K_{Q,0}$ | 0.0393 | 0.0457 | [-] |
| $a$ | -1.9208 | -1.6760 | [-] |
| b | -1.5884 | -1.4064 | [-] |
| p | 2.8408 | 2.5956 | [-] |
| q | 3.3881 | 3.2164 | [-] |
| e | 2.9348 | 2.8827 | [-] |
| g | 0 | 0 | [-] |
| v | 1 | 1 | [-] |
| $\tau_n$ | 1.5541 | 1.1442 | [s] |
| $\tau_v$ | 152.0725 | 114.4896 | [s] |

Table 4.2: Variables and parameters of linearised uncontrolled system with actuators, using the State-Space notation at **operating point 6** and **operating point 8**.

By obtaining the Bode plots, the linear model of the system depicted in Figure 4.7 is verified, in the same way, as it was done for the linearised model of core propulsion model in Section 4.3. The Bode plots of shaft speed, $\delta n^*$ and ship speed, $\delta v_s^*$, for wake variation, $\delta w^*$, for the two different operating points, **operating point 6** and **operating point 8** and for the two different models, linear and non linear are derived and compared in the plots of Figures 4.8 and 4.9 below.

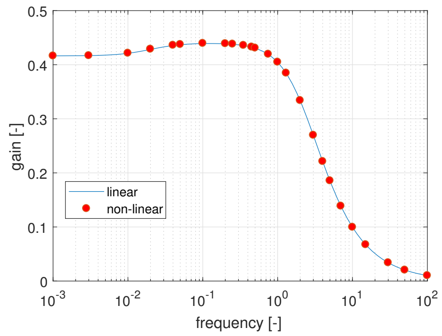


(a) operating point 6

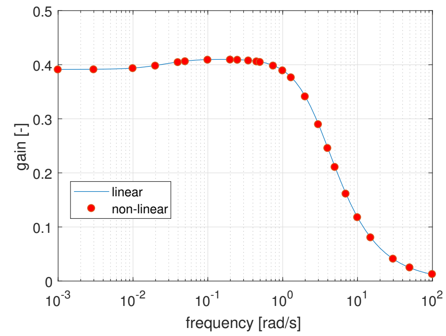


(b) operating point 8

Figure 4.8: Bode plots of shaft speed for wake variation, $\frac{\boldsymbol{\delta n^*}}{\boldsymbol{\delta w^*}}$, of linear (solid line) and non linear (red dots) model of **uncontrolled system with actuators**.

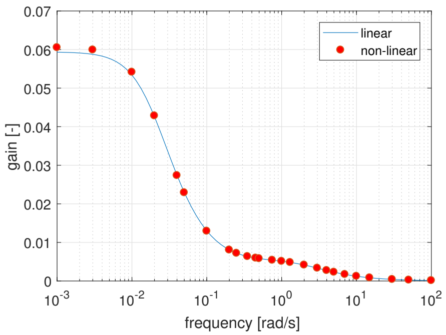


(a) operating point 6

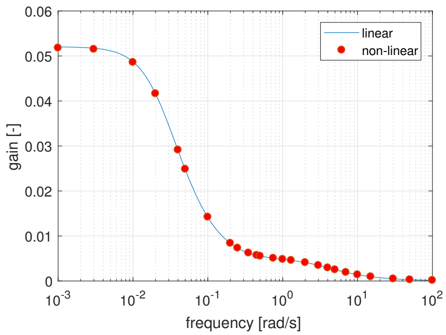


(b) operating point 8

Figure 4.9: Bode plots of ship speed for wake variation, $\frac{\boldsymbol{\delta v_s^*}}{\boldsymbol{\delta w^*}}$, of linear (solid line) and non linear (red dots) model of **uncontrolled system with actuators**.

Regarding the outcome of this comparison of the response of shaft and ship speed to the wake variation, $\frac{\delta n^*}{\delta w^*}$ and $\frac{\delta v_s^*}{\delta w^*}$, between the linear and the non linear system, it can be noticed that they completely agree, for both the operating points, which were chosen to be examined.

## 4.5. CONTROLLED SYSTEM

### LINEAR MODEL

In this Section, the third step of the linearisation process of the propulsion plant is presented, with regard to the controlled system, as it is depicted in Figure 4.10. Additionally, the derived linear model is verified by means of comparison of the Bode plots of the linear and the non linear model.

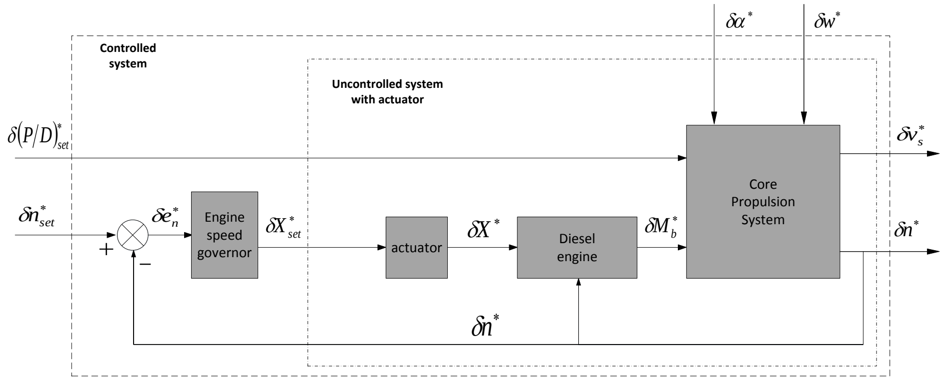




Figure 4.10: Block diagram of linearised controlled propulsion system.

The controlled system, which is linearised in this Section, is the actual propulsion system, including the engine speed controller. This additional component can be seen in the block diagram of Figure 4.10, where it is referred as engine speed governor. This engine speed governor is considered to be a linear PI controller.

Regarding the engine speed controller of the original non linear simulation model, from which the linear one is derived, there are some limitations that are implemented in the controller, which are meant to protect the Diesel engine by preventing phenomena like the overloading of the engine. These limitations, which are including in type 3 non linearities, as they were presented in Section 4.2, can not be captured by the derived linear model. The reason for this, is that these kinds of limiting functions are activated in off design conditions and more specifically, during accelerations and decelerations or during operation near the engine's envelope limits. However, in this thesis the linearisation of the non linear model is referred only to very small perturbations around two operating points, from which none of the two is on the engine's limits. Consequently, as both of the operating points presented before, have sufficient margin from the engine's envelope and the fluctuations, which are implemented around them, remain small, as it is also dictated by the linearisation theory, it is reasonable to consider that additional non linear features in the governor, such as engine's torque limitations, remain inactive. As a result, the governor, as a total, has a linear behaviour.

The addition of the speed controller in this third part of linearisation, will cause some differences to the linear model, compared to the one derived in Section 4.4. Firstly, the PI controller needs as input the error in rotational speed, which is defined as:

$$\delta e_n^* = \delta n_{set}^* - \delta n^* \tag{4.46}$$

The integral of this error, which is calculated in the PI controller, will be one extra element of the state vector **x**:

$$\delta E_n^* = \int_0^t \delta e_n^* dt \Longrightarrow \frac{dE_n^*}{dt} = \delta e_n^* \tag{4.47}$$

Taking into consideration the above mentioned, the output of the PI controller for the linear model is:

$$\delta X_{set}^{*} = K_p \delta e_n^{*} + K_i \delta E_n^{*} \tag{4.48}$$



Substitution of Eq. 4.46 and Eq. 4.48 in Eq. 4.44, results in the new mathematical description of the linear model:

$$\begin{aligned}
\tau_n \frac{dn^*}{dt} &= (-2+b+g-vK_p)\delta n^* - b\delta v_s^* + vK_i\delta E_n^* - q\delta(P/D)^* + vK_p\delta n_{set}^* + b\delta w^* \\
\tau_v \frac{dv_s^*}{dt} &= (2-\alpha)\delta n^* - (e-\alpha)\delta v_s^* + p\delta(P/D)^* - \delta\alpha^* - \alpha\delta w^* \\
\tau_{(P/D)} \frac{d(P/D)^*}{dt} &= \delta(P/D)_{set}^* - \delta(P/D)^*
\end{aligned} \tag{4.49}$$

The variable engine brake $\delta M_b^*$ is linearly related to the system states $\delta n^*$, $\delta E_n^*$ and to the input $\delta n_{set}^*$:

$$\delta M_b^* = (g - vK_p)\delta n^* + vK_i \delta E_n^* + vK_p \delta n_{set}^* \tag{4.50}$$

As a result, by considering the variable engine brake torque $\delta M_b^*$ as an output of the linear model, the State-Space notation of the linearised controlled system becomes:

$$
\begin{aligned}
A &= \begin{bmatrix} \frac{-2+b+g-vK_p}{\tau_n} & -\frac{b}{\tau_n} & -\frac{q}{\tau_n} & \frac{vK_i}{\tau_n} \\ \frac{(2-\alpha)}{\tau_v} & -\frac{(e-\alpha)}{\tau_v} & \frac{p}{\tau_v} & 0 \\ 0 & 0 & -\frac{1}{\tau_{(P/D)}} & 0 \\ -1 & 0 & 0 & 0 \end{bmatrix} \\
B &= \begin{bmatrix} 0 & \frac{vK_p}{\tau_n} & 0 & \frac{b}{\tau_n} \\ 0 & 0 & -\frac{1}{\tau_v} & -\frac{\alpha}{\tau_v} \\ \frac{1}{\tau_{(P/D)}} & 0 & 0 & 0 \\ 0 & 1 & 0 & 0 \end{bmatrix} \\
C &= \begin{bmatrix} 1 & 0 & 0 & 0 \\ 0 & 1 & 0 & 0 \\ 0 & 0 & 1 & 0 \\ g-vK_p & 0 & 0 & vK_i \end{bmatrix} \\
D &= \begin{bmatrix} 0 & 0 & 0 & 0 \\ 0 & 0 & 0 & 0 \\ 0 & vK_p & 0 & 0 \end{bmatrix} \\
\mathbf{x} &= \begin{bmatrix} \delta n^* \\ \delta v_s^* \\ \delta (P/D)^* \\ \delta E_n^* \end{bmatrix} \\
\mathbf{y} &= \begin{bmatrix} \delta n^* \\ \delta v_s^* \\ \delta (P/D)^* \\ \delta M_b^* \end{bmatrix} \\
\mathbf{u} &= \begin{bmatrix} \delta (P/D)_{set}^* \\ \delta n_{set}^* \\ \delta \alpha^* \\ \delta w^* \end{bmatrix}
\end{aligned}
\tag{4.51}
$$

## VERIFICATION OF BODE PLOTS

By implementing in MATLAB the State-Space notation of the linearised controlled system, the Bode plots of the linear model for a specific range of frequencies are derived, demonstrating the response of the output variables of the linear system to small disturbances of the input variables of the system. Following the same method as in the previous Sections, the linearised controlled system is verified, in terms of comparison of the Bode plots of the linear and non linear model. This comparison is shown in Figures 4.11, 4.12 and 4.13

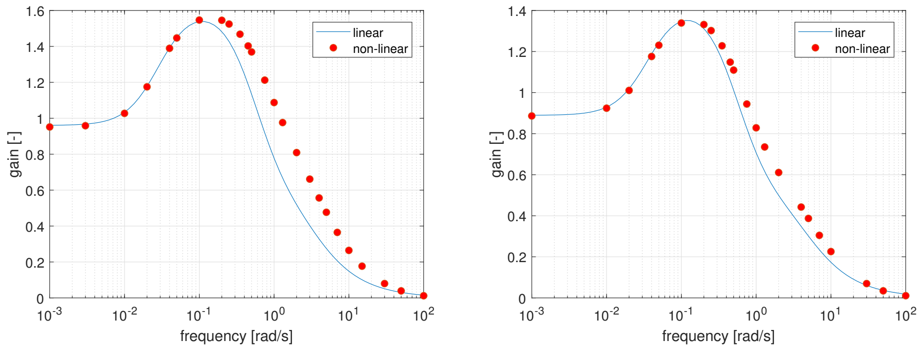


(a) operating point 6 (b) operating point 8



Figure 4.11: Bode plots of brake engine torque for wake variation, $\frac{\boldsymbol{\delta M_b^*}}{\boldsymbol{\delta w^*}}$, of linear (solid line) and non linear (red dots) model of **controlled system**.

As far as Figure 4.11 is concerned, it shows that for part of the frequency range, the Bode plot of brake engine torque, $\delta M_b^*$ to the wake variation $\delta w^*$ of the linear model does not agree completely with the corresponding Bode plot of the non linear model. More specifically, between the values of frequency $\omega = 10^{-3} rad/s$ and $\omega = 10^{-1} rad/s$, the Bode plots of the linear and non linear system completely agree, whereas in the range of frequencies between $\omega = 2 \cdot 10^{-1} rad/s$ and $\omega = 10 rad/s$, a divergence can be noticed between the two Bode plots, with the response of brake engine torque, $\delta M_b^*$ to the wake variation, $\delta w^*$ of the non linear model being higher than the corresponding of the linear model. In the last part of the examined range of frequencies, between $\omega = 2 \cdot 10 rad/s$ and $\omega = 10^2 rad/s$, the bode plots of the linear and non linear model completely agree.

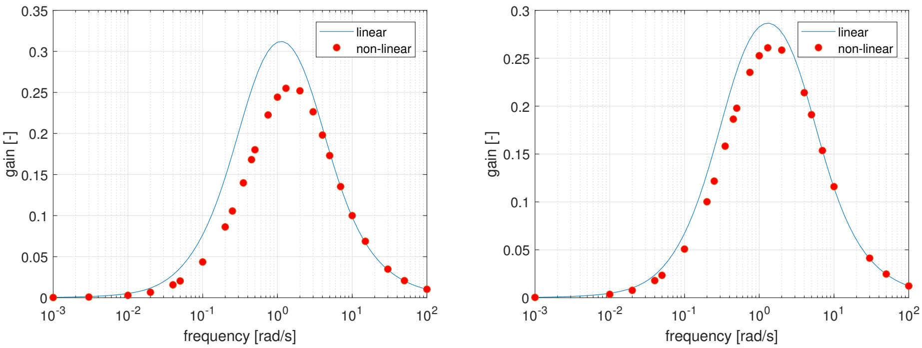


(a) operating point 6 (b) operating point 8

Figure 4.12: Bode plots of shaft speed for wake variation, $\frac{\boldsymbol{\delta n^*}}{\boldsymbol{\delta w^*}}$, of linear (solid line) and non linear (red dots) model of **controlled system**.

Similarly to Figure 4.11, in Figure 4.12 it can be noticed that the Bode plots of linear and non linear systems do not fully agree for the whole range of the frequencies, which is under consideration. More specifically, the Bode plots of linear and non linear system agree in the range of frequencies between $\omega = 10^{-3} rad/s$ and $\omega = 5 \cdot 10^{-2} rad/s$, with the deviation between the Bode plots of the two models lying between $\omega = 10^{-1} rad/s$ and $\omega = 2 rad/s$. In that range of frequencies, it is remarked, that the response of the shaft speed $\delta n^*$ to the wake variation $\delta w^*$ of the non linear system is lower than the correspondent of the linear system. What is more, in the last part of the examined range of frequencies, that means between $\omega = 3 rad/s$ and $\omega = 10^2 rad/s$, a perfect agreement between the two Bode plots can be noted.

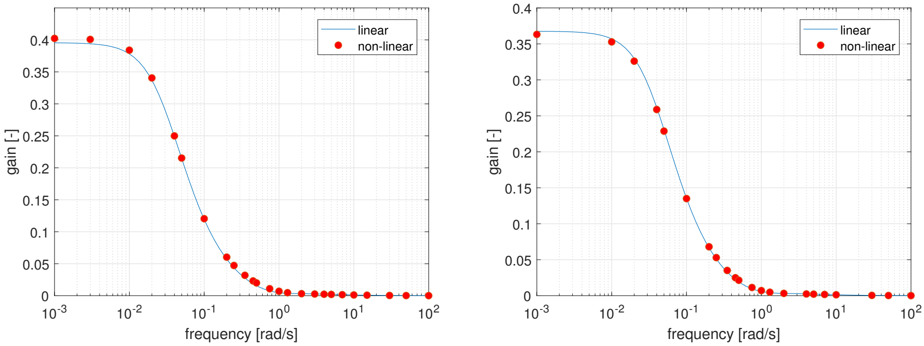


(a) operating point 6 (b) operating point 8

Figure 4.13: Bode plots of ship speed for wake variation, $\frac{\delta v_s^*}{\delta w^*}$, of linear (solid line) and non linear (red dots) model of **controlled system**.

Figure 4.13 shows that the response of ship speed, $\delta v_s^*$ to wake variation $\delta w^*$ of the linear model agrees absolutely with the corresponding one of the non linear model, throughout the whole range of frequencies under consideration.

Additionally, a remark referring to Figures 4.11, 4.12, 4.13 is that, regardless the absolute or not agreement between the Bode plots of the linear and the non linear system, the Bode plots of both linear and non linear system follow exactly the same trend line throughout the whole range of frequencies. This means that both the Bode plots of linear and non linear system have their peaks and dips for exactly the same values of frequency. For example, in Figure 4.12, for operating point 8, it can be noticed that for both linear and non linear system, the response of shaft speed $\delta n^*$ to wake variation $\delta w^*$ has a peak at exactly the same value of frequency, $\omega = 1.5 rad/s$, even if this peak is lower for the non linear system compared to that for the linear system. For lower and higher values of frequency, the response of shaft speed, $\delta n^*$ to wake variation $\delta w^*$ is gradually reduced, until it reaches the upper and lower bound of the examined range of frequencies, for both linear and non linear system, having the same slope. The same remark applies for the rest of the Bode plots, $\frac{\delta M_b^*}{\delta w^*}$ and $\frac{\delta v_s^*}{\delta w^*}$, as well as for both operating points under consideration.

## 4.6. CONCLUSIONS

Taking into account the aforementioned, the conclusion regarding the rightful use or not of the linear model for fluctuations around an operating-equilibrium point, for which the non linear simulation model has been linearised, can be finally drawn.

In regard to the first two parts of linearisation process, as they were presented in Section 4.3 and 4.4, the verification process showed that there is absolute agreement of the Bode plots of shaft and ship speed to wake variation, $\frac{\delta n^*}{\delta w^*}$ and $\frac{\delta v_s^*}{\delta w^*}$, for both the linear and the non linear model and for both the examined operating points.

Regarding the last part of the linearisation process, the linearisation of the controlled system, which is the realistic one, as it contains all the components of an actual propulsion system, including the engine speed controller compared to the previous two, the verification process showed that the introduction of the controller resulted in some deviations between the Bode plots of the linear and non linear model, with regard to the response of brake engine torque and shaft speed to wake variation, $\frac{\delta M_b^*}{\delta w^*}$ and $\frac{\delta n^*}{\delta w^*}$. However, this deviation is considered to be within the acceptable limits for the purpose of this thesis. Despite this offset, which can be noticed only in part of the examined range of frequencies, the Bode plots of these two variables for both the linear and non linear system behave in the same way, following the same trend line throughout the whole examined range of frequencies. As for the Bode plot of ship speed, $\frac{\delta v_s^*}{\delta w^*}$, there is no impact on its behaviour after the introduction of the controller to the propulsion plant in the last part of the linearisation process. This means that the response of ship speed, $\delta v_s^*$, to wake variation, $\delta w^*$ of the linear system agrees completely to the correspondent one of the non linear system.

According to the above mentioned, the conclusion, which is drawn, is that the linear model of the controlled system, of the actual propulsion system, can be correctly used as a simpler and additional tool, compared to the non linear model, in order to examine the behaviour of the propulsion plant in case of relatively small but realistic disturbances around a certain operating point. Such case can be a ship sailing in waves. Additionally, the linear model can be used as a simple tool, for the design and tuning of the engine speed controller of the propulsion plant, since it can capture the realistic, dynamic behaviour of the propulsion plant at a sufficient level of accuracy.

# 5

# Load Variations: Ship Direction, System Operating Point and Sea State

*The effect of different factors causing load (torque) fluctuations on the Diesel engine's operating point, when a vessel sails in waves, are investigated, using the linear model of the ship's propulsion system derived in Chapter 4. More specifically, the impact of the Sea State and the heading of the vessel with respect to the waves, are examined. Furthermore, the effect of parameters related to the system's operating point are going to be inspected. Finally, the outcome of the examination of the above mentioned causes of engine's operating point load fluctuations are going to be analysed.*

## 5.1. Introduction

Having proved, in Chapter 4, the rightfulness of the use of the linear model of a ship's propulsion system in case of fluctuations around an operating/equilibrium point of the system, the derived linear model for the reference vessel RGS9316, is employed in order to investigate the impact of three different factors on the dynamic response of the operating point of a Diesel engine, which is used as the prime mover in the propulsion plant of a ship, when the ship sails in waves. One of the major outcomes outlined in Chapter 4, regarding the linear ship propulsion system model derived, is that linear models are much more simple and engage less parameters, when they are used as tools for the examination of the dynamic behaviour of vessel's propulsion system, compared to more complex non-linear models. Taking into account these significant advantages, the derived linear model is used to inspect the effect of the heading, the system's operating point and the Sea State on the dynamic response of the Diesel engine's operating point, in terms of torque and speed fluctuations, within the limits of the engine's operating envelope. More precisely, regarding the Sea State, the impact of different wave amplitudes on the dynamic behaviour of the propulsion system will be examined, in terms of brake engine torque and engine speed variations. As for the ship direction with respect to the waves, the influence of following and head waves on the ship's propulsion system, regarding engine torque and speed variations is investigated. Similarly, Diesel engine's torque and engine's speed variations dependency on different operating points of the vessel's propulsion system is inspected, in case of a vessel sailing in wave field. The demonstration of the impact of the above mentioned factors on the engine's torque and speed variations are analysed. In that way, a clear, concrete and useful insight is attempted to be given, with respect to the influence of a wide range of external disturbances on the dynamic behaviour of the propulsion system of a ship sailing in waves.

## 5.2. General Considerations

At this point, it would be useful to give some details, regarding the inspection of the impact of the previously mentioned factors on ship's propulsion system model dynamic behaviour.

5

As far as the concept of sailing in waves, which is the focus of this work, is concerned, waves cause both resistance and wakefield perturbations for the vessel's propulsion system model. These disturbances are clearly depicted in Figure 3.6, where the block diagram of the whole propulsion system model is shown, as well as in Figure 3.8 and Figure 3.17, where wakefield and resistance variation models are illustrated, respectively.

Despite the fact that sailing in wave field causes both wakefield and ship resistance variations, which are considered to be the disturbance inputs of the propulsion system model, in this thesis, only the wakefield input and its influence on the dynamic behaviour of the system operating point will be investigated. The reasons for that are extensively presented in Section 2.6.2 and briefly summarised below:

- The impact of wakefield variations on the behaviour of the rotating shaft system and the engine's operating point is more direct in comparison to the impact of ship resistance variations.

- high level of difficulty in order to model the ship resistance variations. Following the most commonly used methods, the determination of added resistance in waves requires accurate data regarding vessel's motions in waves, like pitch, heave and relative phase difference between these motions. This kind of calculations lies out of the scope of this work.

With respect to the examination of the dynamic response of the engine operating point in case of external disturbances, it is, mainly, accomplished by studying the elliptic trajectory of the engine operating point, being either within the limits of the engine envelope or being demonstrated alone, outside the engine envelope limits. Additionally, the derivation of the elliptic trajectory will be based on the Bode plots of engine torque and engine speed variation over wakefield variation. The Bode plots will be obtained by using the linear controlled system model derived in Section 4.5. If the Bode plots are obtained, then the values of the gains, $\left|\frac{\delta n^*}{\delta w^*}\right|$ and $\left|\frac{\delta M_b^*}{\delta w^*}\right|$ and phase angles $\angle\frac{\delta n^*}{\delta w^*}$ and $\angle\frac{\delta M_b^*}{\delta w^*}$ can be read and used in the correspondent formulas for the required plots of the elliptic trajectory of the engine's operating point. The mathematical formulas relating the values obtained from the Bode plots of the linearised propulsion system model and the geometric properties of the ellipse of the operating point are presented below:

### 5.2.1. ELLIPSE GEOMETRIC PROPERTIES

The geometric properties of the engine operating point, in case of regular waves are defined by the values of the Bode plots $\frac{\delta n^*}{\delta w^*}$ and $\frac{\delta M_b^*}{\delta w^*}$ of the linear propulsion system model. The external sinusoidal wakefield variation which acts on the system model results in the harmonic oscillating signal of engine speed and brake engine torque variation at a certain frequency $\omega$:

$$\begin{aligned} \delta n^* &= \delta w^* \left| \frac{\delta n^*}{\delta w^*} \right| \cos\left(\omega t + \phi_{n,w}\right) \\ \delta M_b^* &= \delta w^* \left| \frac{\delta M_b^*}{\delta w^*} \right| \cos\left(\omega t + \phi_{M_b,w}\right) \end{aligned} \tag{5.1}$$

It has to be mentioned that the phase of these two signals with respect to the wake-disturbance signal, the second term of the cosine argument, $\phi_{n,w}$ and $\phi_{M_b,w}$ in the formulas of Eq. (5.1) is not important. What is important and affects the plot of the elliptic operating point is the relation of the phase of the two harmonic oscillating signals of engine speed $\delta n^*$ and brake engine torque $\delta M_b^*$. Thus the phase angle $\phi_{n,w}$ is subtracted from both signals and Eq. (5.1) becomes:

$$\begin{aligned} \delta n^* &= \left|\delta n^*\right| \cos\left(\omega t\right) \\ \delta M_b^* &= \left|\delta M_b^*\right| \cos\left(\omega t + \phi_{M_b,n}\right) \end{aligned} \tag{5.2}$$

where $\phi_{M_b,n} = \phi_{M_b,w} - \phi_{n,w}$.

Using the trigonometric identity $\cos\left(\omega t + \phi\right) = \cos\left(\omega t\right)\cos\left(\phi\right) - \sin\left(\omega t\right)\sin\left(\phi\right)$, and noting $\phi_{M_b,n}$ as $\phi$ from now on, the second formula of Eq.(5.2) can be re-written:

$$\frac{\delta M_b^*}{|\delta M_b^*|} = \cos\left(\omega t\right)\cos\left(\phi\right) - \sin\left(\omega t\right)\sin\left(\phi\right) \tag{5.3}$$

Combining the first part of Eq. (5.2) with the trigonometric identity $\sin^2\left(\phi\right) + \cos^2\left(\phi\right) = 1$, it is extracted that:

$$\begin{aligned} \cos\left(\omega t\right) &= \frac{\delta n^*}{|\delta n^*|} \\ \sin\left(\omega t\right) &= \sqrt{1 - \left(\frac{\delta n^*}{|\delta n^*|}\right)^2} \end{aligned} \tag{5.4}$$

Substitution of Eq. (5.4) in Eq. (5.3) leads to:

$$\frac{\delta M_b^*}{|\delta M_b^*|} = \frac{\delta n^*}{|\delta n^*|}\cos\left(\phi\right) - \sqrt{1 - \left(\frac{\delta n^*}{|\delta n^*|}\right)^2}\sin\left(\phi\right) \tag{5.5}$$

Re-arranging and squaring both sides of the equality results in:

$$\left(\frac{\delta M_b^*}{|\delta M_b^*|} - \frac{\delta n^*}{|\delta n^*|}\cos\left(\phi\right)\right)^2 = \left(-\sqrt{1 - \left(\frac{\delta n^*}{|\delta n^*|}\right)^2}\sin\left(\phi\right)\right)^2 \tag{5.6}$$

5

Combination of $\cos^2(\phi) + \sin^2(\phi)$ and Eq. (5.6) gives:

$$\left(\frac{1}{|\delta n^*|}\right)^2 \delta n^{*2} - \frac{2\cos(\phi)}{|\delta n^*||\delta M_b^*|} \cdot \delta n^* \delta M_b^* + \left(\frac{1}{|\delta M_b^*|}\right)^2 \delta M_b^{*2} - \sin^2(\phi) = 0 \tag{5.7}$$

It can be noticed that Eq. (5.7) can be matched to the general form of the quadratic equation in the Cartesian coordinate system:

$$Ax^2 + Bxy + Cy^2 + Dx + Ey + F = 0 \tag{5.8}$$

where:

$$\begin{aligned} A &= \left(\frac{1}{|\delta n^*|}\right)^2 \\ B &= -\frac{2\cos(\phi)}{|\delta n^*||\delta M_b^*|} \\ C &= \left(\frac{1}{|\delta M_b^*|}\right)^2 \\ D &= 0 \\ E &= 0 \\ F &= -\sin^2(\phi) \end{aligned} \tag{5.9}$$

Geometrically, an **ellipse** can be defined as a set of points (locus of points) in the Euclidean plane such that for any point $P$ of the set, the sum of the distances $|PF_1|$, $|PF_2|$ to two fixed points $F_1$, $F_2$, the *foci*, is constant and usually denoted by $2\alpha$, $\alpha > 0$. Aiming to avoid the special case of a line segment, it is assumed that $2\alpha > |F_1|F_2$. Consequently, the definition of the set of points of an ellipse is given by the following mathematical expression and it is graphed in Figure 5.1:

$$E = \{P \in \Re^2 || PF_2| + |PF_1| = 2\alpha\} \tag{5.10}$$

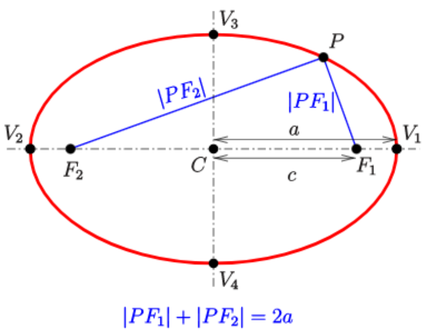


Figure 5.1: Definition of an ellipse as a locus of points.

According to analytic geometry, the **ellipse** is defined as a quadratic: the set of points $(X, Y)$ of the Cartesian plane that satisfy Eq. (5.8), provided that $B^2 - 4AC < 0$. In this case, since for Eq. (5.7) the expression $B^2 - 4AC$ is always negative, then Eq. (5.7) describes an ellipse. As for Eq. (5.8), the described ellipse is defined in the $x - y$ coordinate system. It has to be noted that in order to reveal the properties of the ellipse, it is beneficial to rotate the Cartesian coordinate system $x - y$ over an angle $\alpha$, in that way that the resulting coordinating system after the rotation, $x' - y'$, is aligned with the major and the minor axes of the ellipse as shown in Figure 5.2. The mathematical expression that relates the original and the rotated coordinate system is given by:

$$\begin{aligned} x' &= x\cos(\alpha) + y\sin(\alpha) \\ y' &= -x\sin(\alpha) + y\cos(\alpha) \end{aligned} \tag{5.11}$$

and

$$\begin{aligned} x &= x'\cos(\alpha) - y'\sin(\alpha) \\ y &= x'\sin(\alpha) + y'\cos(\alpha) \end{aligned} \tag{5.12}$$

The substitution of Eq. (5.12) into the general form of the quadratic equation of Eq. (5.8) will result in the ellipse equation written in the $x' - y'$ rotated coordinated system:

$$A'x'^2 + B'x'y' + C'y'^2 + D'x' + E'y' + F' = 0 \tag{5.13}$$

where the coefficients are given by:

$$\begin{aligned} A' &= A\cos^2(\alpha) + B\cos(\alpha)\sin(\alpha) + C\sin^2(\alpha) \\ B' &= B\cos(2\alpha) + (C - A)\sin(2\alpha) \\ C' &= C\cos^2(\alpha) - B\cos(\alpha)\sin(\alpha) + A\sin^2(\alpha) \\ D' &= D\cos(\alpha) + E\sin(\alpha) = 0 \\ E' &= E\cos(\alpha) - D\sin(\alpha) = 0 \\ F' &= F \end{aligned} \tag{5.14}$$

5

Setting term $B'$ equal to zero:

$$B' = B\cos(2\alpha) + (C - A)\sin(2\alpha) = 0 \tag{5.15}$$

the angle of rotation of the coordinate system, $\alpha$ can be determined:

$$\alpha = \frac{1}{2}\cot^{-1}\left(\frac{A - C}{B}\right) \tag{5.16}$$

The outcome of Eq. (5.16) is, also, the angle of rotation of the ellipse. Additionally, simplification of Eq. (5.13) gives the form of the equation presented below:

$$A'x'^2 + C'y'^2 + F' = 0 \tag{5.17}$$

Re-arranging Eq. (5.17) leads to the following, widely known, form of the ellipse equation:

$$\frac{-A'}{F'}x'^2 + \frac{-C'}{F'}y'^2 = 1 \tag{5.18}$$

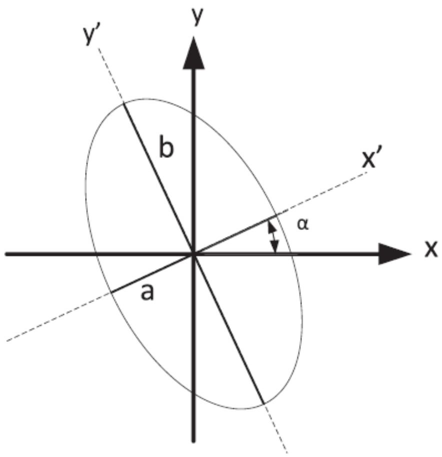


Figure 5.2: Ellipse on a rotated coordinate system, [Vrijdag and Stapersma, 2017].

From this form of the ellipse equation the shape parameters, the semi-major and semi-minor axes can be obtained. Since depending on the orientation of the ellipse, varying from vertical or horizontal, the position of the semi-major and semi-minor axes can be switched, the two axes of the ellipse defined in Eq. (5.18) are called first and second axis respectively. Consequently, the size of the *first axis* is defined by:

$$a = \sqrt{\frac{-F'}{A'}} \tag{5.19}$$

and the size of the *second axis* is given by:

$$b = \sqrt{\frac{-F'}{C'}} \tag{5.20}$$

## 5.3. SHIP DIRECTION

5

In this section, the first of the three aforementioned factors influencing the engine's torque variation, $\delta M_b$ will be investigated. This factor is the *ship direction*, which means the sailing direction of the ship, with respect to the incoming waves. Particularly, two specific ship headings relative to the wave direction are examined in this thesis:

- *following* waves
- *head* waves

The ship's heading with respect to the incoming waves is defined by the angle $\mu$ which is graphed in Figure 5.3. In case of this thesis and according to Figure 5.3 the angle $\mu$ gets two values:

- $\mu = 0°$, for following waves
- $\mu = 180°$, for head waves

As far as the range of frequencies of the waves that are examined, it has to be noted that, when a ship is sailing, it will generally "meet "the incoming waves with a different apparent frequency, the frequency of encounter $\omega_e$, which is different from the wave frequency. The relation between the wave frequency, and the frequency of encounter, in deep water is given by:

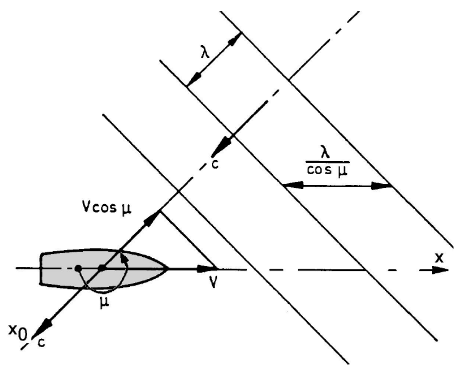


Figure 5.3: Frequency of encounter, [Journée and Massie, 2000].

$$\begin{aligned} \omega_e &= \omega - \frac{\omega^2}{g} V \cdot \cos(\mu) \\ &= \omega \cdot \left(1 - \frac{V}{c} \cdot \cos(\mu)\right), \qquad \text{by using:} \quad c = \frac{g}{\omega} \end{aligned} \tag{5.21}$$

where:

| | |
|---|---|
| $\omega$ | :wave frequency in a fixed reference $[rad/s]$ |
| $\omega_e$ | :frequency of encounter in a moving reference $[rad/s]$ |
| $V$ | :forward ship speed $[m/s]$ |
| $c$ | :wave speed $[m/s]$ |
| $g$ | :gravitational acceleration $[m/s^2]$ |
| $\mu$ | :ship heading relative to wave direction [rad] |

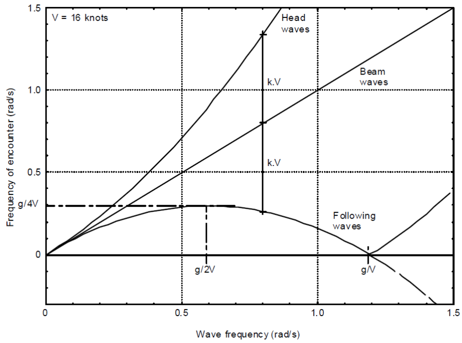


Figure 5.4: Relation between $\omega_e$ and $\omega$, [Journée and Massie, 2000].



More specifically, for the examination of the impact of the direction of the ship with respect to the waves the linear model of the ship propulsion system will be used, as it was derived in Section 4.5. By implementing the matrices of the State-Space notation in MATLAB, the Bode plots are derived. Then, as it was presented in Section 5.2.1, the values of gains $\left|\frac{\delta M_b^*}{\delta w^*}\right|$ and $\left|\frac{\delta n^*}{\delta w^*}\right|$ and phase angles $\angle\frac{\delta n^*}{\delta w^*}$ and $\angle\frac{\delta M_b^*}{\delta w^*}$ are used for the derivation of the elliptic trajectory of the engine's operating point. Moreover, as it was mentioned in Section 3.2, the linearisation of the propulsion system model, in this thesis, is applied for **operating point 6** and **8**. However, since in this Section, only the impact of the heading of the vessel with respect to the waves is examined, the derivation of the linear model and the corresponding Bode plots will be done only for one operating point. The selected operating point for this Section is **operating point 8**. Besides this, it is worth noting that, for this Section, the gain values, Proportional and Integral, of the ship propulsion system's governor are constant. These values are the ones defined in Section 3.4, $K_p = 1.5$ and $K_i = 2$.

As far as the wave frequencies that will be investigated are concerned, eight(8) of them are chosen in such way that they are considered representative of the entire range of frequencies. For each one of the selected wave frequencies, $\omega$, the encounter frequency, $\omega_e$, is calculated for both concepts under consideration, following and head waves. According to Eq. (5.21), the encounter frequency for each one of the two cases gets a different value, since the angle $\mu$ gets two values, 0° and 180° for following and head waves, respectively. This is depicted in Figure 5.4. Besides the selected wave frequencies that are chosen to be examined, a ship speed has to be chosen, as it is required in Eq. (5.21) for the calculation of the frequencies of encounter, $\omega_e$. The ship speed, $V$ is determined by the operating point that is selected to be examined. As it was previously mentioned, the selected operating point for this Section is **operating point 8**. Accordingly, all the related values to **operating point 8** can be found in Table 4.2. The corresponding **ship speed** is $\mathbf{V_s = 8.0003m/s}$.
The chosen wave frequencies as well as the rest of the variables and parameters of the

linearised ship propulsion system model and the corresponding, derived Bode plots and engine operating point trajectories are presented in the following tables and Figures for the following and head waves, respectively.

**$\omega = 0.01$ rad/s**

Regarding the first chosen wave frequency $\omega = 0.01$ [rad/s], it can be noticed on Table 5.1 that the frequency of encounter $\omega_e$ for following and head waves respectively has the same value. This means that the values of gains $\left|\frac{\delta n^*}{\delta w^*}\right|$ and $\left|\frac{\delta M_b^*}{\delta w^*}\right|$ and phase angles $\angle\frac{\delta n^*}{\delta w^*}$ and $\angle\frac{\delta M_b^*}{\delta w^*}$, similarly, have the same values for following and stern waves for this wave frequency. As a result, the engine's operating point trajectories are exactly the same for both cases under consideration, stern and head waves, as it is graphed in Figures 5.6a and 5.6b. According to the Bode plots of $\frac{\delta n^*}{\delta w^*}$ and $\frac{\delta M_b^*}{\delta w^*}$, for this very low frequency the dynamic response of the engine's torque over the wake variation is high, whereas the response of the engine's speed over the wake variation is negligible. These responses explain the shape of the engine's operating ellipse, which has collapsed to a line, with only engine's torque variations, $\delta M_b^*$. Additionally, the orientation of the line is vertical, for the specific values of gains and phase angles.

5

**$\omega = 0.05$ rad/s**

As for the second wave frequency that is used, $\omega = 0.05$ rad/s, observing Table 5.2, it can be noticed that it is almost the same case as the one with $\omega = 0.01$ [rad/s]. The frequency of encounter, $\omega_e$, has approximately the same value for both cases under consideration, following and head waves. Consequently, the values of gains $\left|\frac{\delta n^*}{\delta w^*}\right|$ and $\left|\frac{\delta M_b^*}{\delta w^*}\right|$ and phase angles $\angle\frac{\delta n^*}{\delta w^*}$ and $\angle\frac{\delta M_b^*}{\delta w^*}$, similarly, are the same for following and head waves for this wave frequency. This contributes to the fact that the engine's operating point has the same dynamic behaviour for following and head waves, as illustrated in Figure 5.7a and Figure 5.7b. More specifically, the formed operating ellipse has the same shape and orientation. This means that the case of following and head waves result in the same fluctuations in engine's torque and engine's speed, when a ship sails in waves with wave frequency of $\omega = 0.05$ [rad/s]. Compared to the previous case of wave frequency, $\omega = 0.01$ [rad/s], the values of gains in Bode plots of $\frac{\delta n^*}{\delta w^*}$ and $\frac{\delta M_b^*}{\delta w^*}$ for this one $\omega = 0.05$ [rad/s] are a little bit higher. This leads to the fact that the engine's operating trajectory is not a line anymore, but an ellipse which has the major axis, the one related to the engine's torque variation $\delta M_b^*$, much longer than the minor axis, which is the one related to the engine's speed variation, $\delta n^*$.

**$\omega = 0.1$ rad/s**

Observing the values of the parameters for the third examined wave frequency, $\omega = 0.1$ rad/s in Table 5.3, it can be noted that the frequency of encounter $\omega_e$ has approximately the same value for following and head waves. It follows that, similarly, the values of gains $\left|\frac{\delta n^*}{\delta w^*}\right|$ and $\left|\frac{\delta M_b^*}{\delta w^*}\right|$ and phase angles $\angle\frac{\delta n^*}{\delta w^*}$ and $\angle\frac{\delta M_b^*}{\delta w^*}$ are the same for following and head waves occurring for $\omega = 0.1$ rad/s. As a consequence of this, the engine's operating point elliptic trajectories are identical in case of following and head waves. This is clearly graphed in Figure 5.8a and Figure 5.8b, where it can be seen that following and head waves result in the same engine's torque and the engine's speed fluctuations for waves with frequency equal to $\omega = 0.1$ rad/s. Compared to the previously examined wave frequency of $\omega = 0.05$ rad/s, the values of gains in Bode plots of $\frac{\delta n^*}{\delta w^*}$ and $\frac{\delta M_b^*}{\delta w^*}$ are slightly higher leading to slightly longer major axis and almost double minor axis.

**$\omega = 0.5$ rad/s**

For the case of wave frequency $\omega = 0.5$ rad/s, the frequency of encounter for the cases under consideration, following and head waves does not have the same value anymore. The values are different and this can be confirmed by the data provided in Table 5.4. Consequently, the values of gains $\left|\frac{\delta n^*}{\delta w^*}\right|$ and $\left|\frac{\delta M_b^*}{\delta w^*}\right|$ and phase angles $\angle\frac{\delta n^*}{\delta w^*}$ and $\angle\frac{\delta M_b^*}{\delta w^*}$ will be different for following and head waves, leading to different engine's operating ellipses. This is demonstrated in Figure 5.9a and in Figure 5.9b, where it can be noticed that for the case of stern waves the dynamic response of the engine results in an approximately vertical operating ellipse, with higher engine's torque fluctuations compared to the case of head waves for which the dynamic response of the engine results in an operating ellipse with higher value for the angle of rotation compared to the stern waves. This means that for the case of head waves the engine's speed fluctuations are higher compared to the those in case of stern waves. What is more, observing Figures 5.9c and 5.9d and Table 5.4, the differences between the major and minor axis of the elliptic trajectories can be explained, since the value of $\left|\frac{\delta M_b^*}{\delta w^*}\right|$ is higher for the case of stern waves than the case of head waves. On the contrary, the value of $\left|\frac{\delta n^*}{\delta w^*}\right|$ is higher for the case of head waves than the case of stern waves.

**$\omega = 1$ rad/s**

For the case of wave frequency $\omega = 1$ rad/s, the values of the frequency of encounter for following and head waves are quite different. This is stated in Table 5.5. Therefore, the engine's point elliptic trajectories are quite different for following and head waves. On the one hand, the elliptic trajectory for stern waves is nearly vertical with a very small angle of rotation. This means that for the case of stern waves high engine's torque fluctuations and negligible engine's speed fluctuations can be remarked. On the other hand, the elliptic trajectory for head waves has significantly larger angle of rotation compared to the one for stern waves. This means that for the case of head waves the engine's speed fluctuations are higher compared to the case of stern waves, whereas the engine's torque fluctuations are less for the case of head waves compared to the case of stern waves. This is clearly graphed in Figure 5.10a and Figure 5.10b. Additionally, the differences regarding the dimensions of the major and minor axis of the elliptic trajectories for stern and head waves can be explained by the values of the gains of the Bode plots, according to Figure 5.10c and Figure 5.10d. More specifically, the value of $\left|\frac{\delta M_b^*}{\delta w^*}\right|$ is much higher for the case of stern waves compared to the case of head waves. On the contrary, the value of $\left|\frac{\delta n^*}{\delta w^*}\right|$ is much higher for the case of head waves than it is in case of stern waves.

**$\omega = 2$ rad/s**

With respect to the case of wave frequency $\omega = 2$ rad/s, the values of the frequency of encounter for the two cases under consideration, following and head waves, are quite different. This is confirmed by the values demonstrated in Table 5.6. Observing these values, the shape of the elliptic trajectories for the engine's operating point for the two cases, following and head waves, can be justified. For the case of wave frequency under consideration, both elliptic trajectories for stern and head waves have an inclination, with the value of the angle rotation being higher for the case of head waves. Moreover, what is special for this case of wave frequency, is that regarding the case of stern waves, both the engine's torque and speed fluctuations are higher compared to those in case of head waves, which is shown in Figure 5.11a and Figure 5.11b. This can be seen by observing the values of gains of the Bode plots in Figure 5.11c and Figure 5.11d. More specifically, the values of $\left|\frac{\delta M_b^*}{\delta w^*}\right|$ and $\left|\frac{\delta n^*}{\delta w^*}\right|$ are higher for the case of following waves. This contributes to the fact that the operating ellipse for the stern waves has longer major and minor axis, resulting in higher torque and speed fluctuations as it was previously mentioned.

5

**$\omega = 5$ rad/s**

For the case of wave frequency $\omega = 5$ rad/s, there is a significant difference regarding the values of frequency of encounter for the two cases under consideration, following and head waves. This is demonstrated in Table 5.7. The values shown there explain the elliptic trajectories, illustrated in Figure 5.12a and in Figure 5.12b. The resulting operating ellipses for both examined cases, following and head waves, are almost identical. They have the same angle of rotation with the only difference between the two being the length of the major axis of the elliptic trajectories, the one related to the engine's torque variations, $\delta M_b^*$, which is longer for the case of stern waves. That means that the engine's torque fluctuations are higher in case of stern waves compared to the engine's torque fluctuations in case of head waves. As far as the minor axis is concerned, it is nearly the same for both cases of following and head waves. Additionally, the above mentioned can be confirmed by the values of the gains, $\left|\frac{\delta M_b^*}{\delta w^*}\right|$ and $\left|\frac{\delta n^*}{\delta w^*}\right|$, which are depicted on the Bode plots in Figure 5.12c and in Figure 5.12d, respectively. At this point it is worth noting the really small dimensions of both elliptic trajectories in following and head waves. This is better highlighted in Figure 5.12a, where the size of both operating ellipses can be compared to the Diesel engine's operating envelope. Observing Figure 5.12a, combined with the Bode plots of Figure 5.12c and Figure 5.12d it follows that for such high values of wave frequencies and frequencies of encounter, the dynamic response of the engine, meaning torque and speed fluctuation, is almost negligible with the elliptic trajectory of the engine's operating point collapsing to a point. This can be justified by examining Figure 5.5, where the ship's propulsion block diagram is graphed.

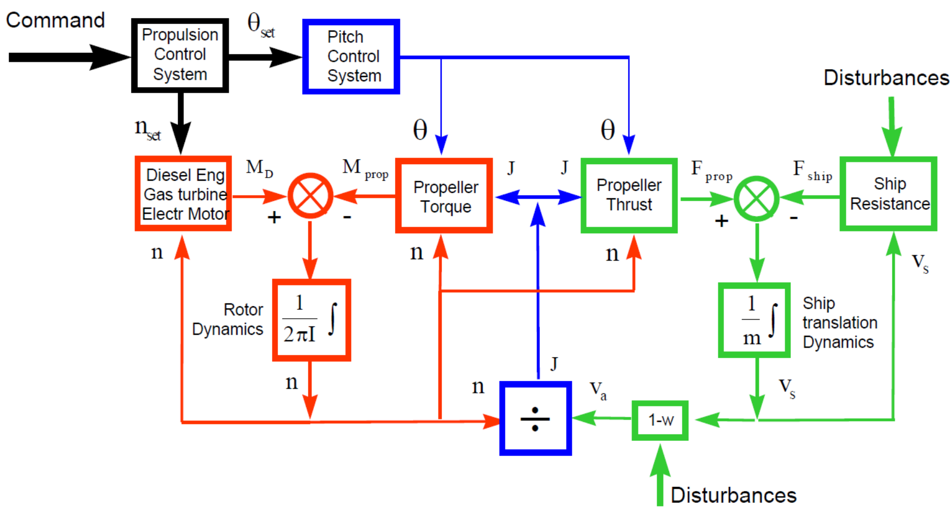


Figure 5.5: Ship propulsion block diagram.



According to literature [Stapersma and de Heer, 2000] and as it was mentioned in Section 2.6.2, the block of the shaft's inertia and its associated integrator acts as "low pass"filter between the wake disturbance and its effect on the Diesel engine dynamic response. In other words, this "low pass"filter only passes low frequency amplitudes, effectively blocking higher frequencies of disturbance.

**$\omega$ = 10 rad/s**

As for the wave frequency $\omega$ = 10 rad/s, the frequencies of encounter occurring for following and head waves are quite different. This is demonstrated in Table 5.8. According to Figure 5.13a and Figure 5.13b, it can be noticed that the dynamic behaviour of the engine's operating point is almost the same. The angle of rotation is the same for both elliptic trajectories, as well as the dimensions of the major and minor axis of the two operating ellipses. This means that the resulting fluctuations in terms of engine's torque and engine's speed are the same. Furthermore, the above mentioned can be confirmed by the values of gains in Bode plots in Figure 5.13c and in Figure 5.13d. Similarly to the case of wave frequency $\omega$ = 5 rad/s, in Figure 5.13a, it is highlighted that the size of the elliptic trajectory for both following and head waves is small, with the operating ellipse collapsing to an operating point in both cases. The same justification, as in case of wave frequency $\omega$ = 5 rad/s, can be also applied here, using the ship propulsion block diagram in Figure 5.5.

| Wave Frequency $\boldsymbol{\omega} = \mathbf{0.01}$ **[rad/s]** | | |
|---|---|---|
| Parameters | Following Wave $\mu = 0°$ | Head Wave $\mu = 180°$ |
| $\omega_e$ [rad/s] | 0.0099 | 0.0101 |
| $\delta w^*$ [-] | 0.15 | 0.15 |
| $\left\lvert \frac{\delta n^*}{\delta w^*} \right\rvert$ [-] | 0.0046 | 0.0046 |
| $\angle \frac{\delta n^*}{\delta w^*}$ [deg] | 276.4616 | 276.4616 |
| $\left\lvert \frac{\delta M_b^*}{\delta w^*} \right\rvert$ [-] | 0.9293 | 0.9293 |
| $\angle \frac{\delta M_b^*}{\delta w^*}$ [deg] | 6.8913 | 6.8913 |
| a [-] | 6.969e-4 | 6.969e-4 |
| b [-] | 0.1394 | 0.1394 |
| $\alpha$ [deg] | 0.0021 | 0.0021 |

Table 5.1: Variables and parameters of following and head waves for $\omega = 0.01$ rad/s at **operating point 8**.

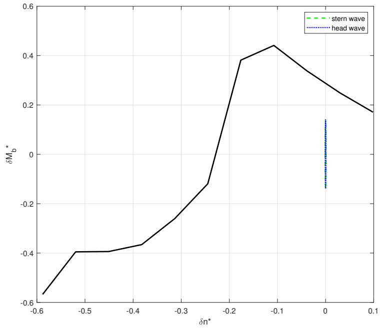


(a) Operating ellipse in engine operating envelope

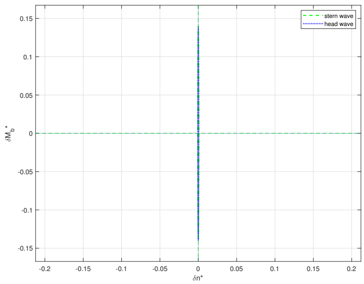


(b) Operating ellipse

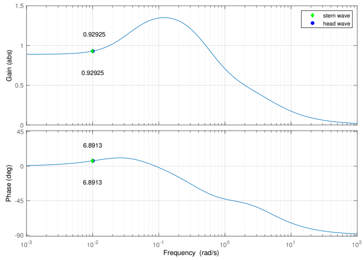


(c) $\frac{\delta M_b^*}{\delta w^*}$ in head and stern waves

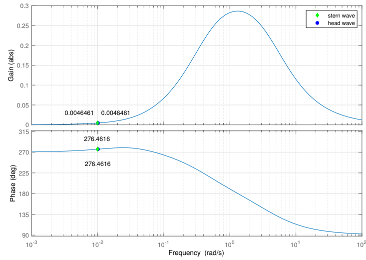


(d) $\frac{\delta n^*}{\delta w^*}$ in head and stern waves

Figure 5.6: Operating ellipse and Bode plots in stern and head waves for $\boldsymbol{\omega} = \mathbf{0.01}$ **rad/s**.

| Wave Frequency $\boldsymbol{\omega} = \mathbf{0.05}$ **[rad/s]** | | |
|---|---|---|
| Parameters | Following Wave $\mu = 0°$ | Head Wave $\mu = 180°$ |
| $\omega_e$ [rad/s] | 0.048 | 0.052 |
| $\delta w^*$ [-] | 0.15 | 0.15 |
| $\left\lvert \frac{\delta n^*}{\delta w^*} \right\rvert$ [-] | 0.0329 | 0.0329 |
| $\angle \frac{\delta n^*}{\delta w^*}$ [deg] | 274.7413 | 274.7413 |
| $\left\lvert \frac{\delta M_b^*}{\delta w^*} \right\rvert$ [-] | 1.2546 | 1.2546 |
| $\angle \frac{\delta M_b^*}{\delta w^*}$ [deg] | 6.9929 | 6.9929 |
| a [-] | 0.0049 | 0.0049 |
| b [-] | 0.1882 | 0.1882 |
| $\alpha$ [deg] | 0.059 | 0.059 |

Table 5.2: Variables and parameters of following and head waves for $\omega = 0.05$ rad/s at **operating point 8**.

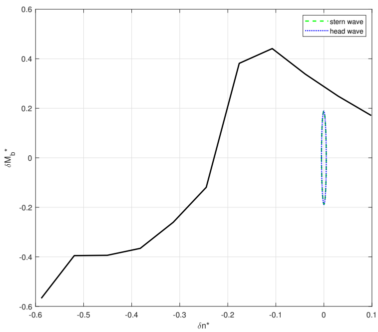


(a) Operating ellipse in engine operating envelope

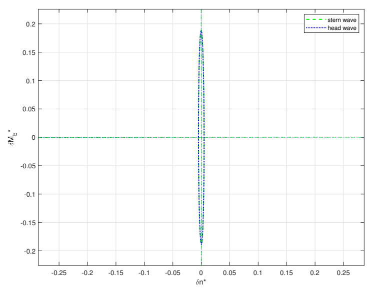


(b) Operating ellipse

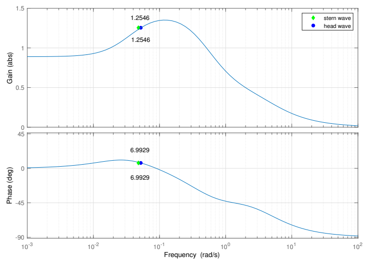


(c) $\frac{\delta M_b^*}{\delta w^*}$ in head and stern waves

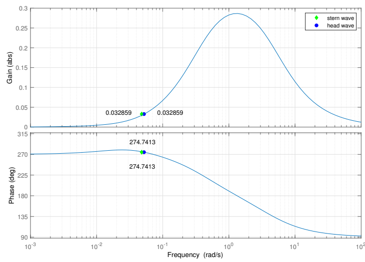


(d) $\frac{\delta n^*}{\delta w^*}$ in head and stern waves

Figure 5.7: Operating ellipse and Bode plots in stern and head waves for $\boldsymbol{\omega} = \mathbf{0.05}$ **rad/s**.

| Wave Frequency $\boldsymbol{\omega} = \mathbf{0.1}$ **[rad/s]** | | |
|---|---|---|
| Parameters | Following Wave $\mu = 0°$ | Head Wave $\mu = 180°$ |
| $\omega_e$ [rad/s] | 0.0918 | 0.1082 |
| $\delta w^*$ [-] | 0.15 | 0.15 |
| $\left\lvert \frac{\delta n^*}{\delta w^*} \right\rvert$ [-] | 0.0653 | 0.0765 |
| $\angle \frac{\delta n^*}{\delta w^*}$ [deg] | 264.4147 | 261.1933 |
| $\left\lvert \frac{\delta M_b^*}{\delta w^*} \right\rvert$ [-] | 1.3452 | 1.3512 |
| $\angle \frac{\delta M_b^*}{\delta w^*}$ [deg] | -1.4076 | -3.9324 |
| a [-] | 0.0098 | 0.0114 |
| b [-] | 0.2018 | 0.2027 |
| $\alpha$ [deg] | 0.2032 | 0.2767 |

Table 5.3: Variables and parameters of following and head waves for $\omega$ = 0.1 rad/s at **operating point 8**.

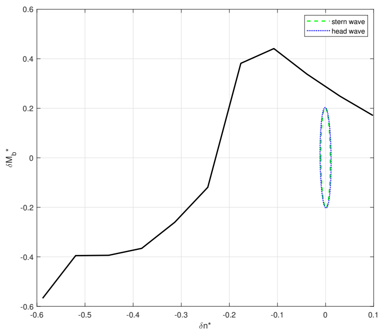


(a) Operating ellipse in engine operating envelope

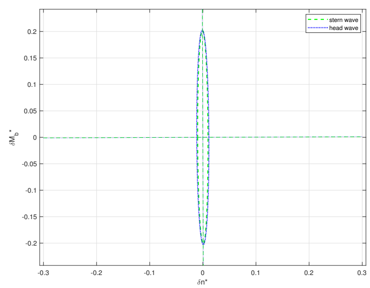


(b) Operating ellipse

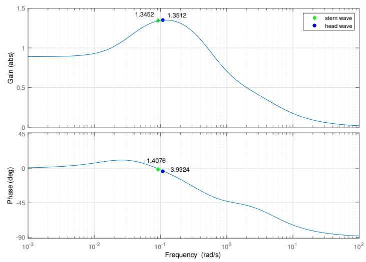


(c) $\frac{\delta M_b^*}{\delta w^*}$ in head and stern waves

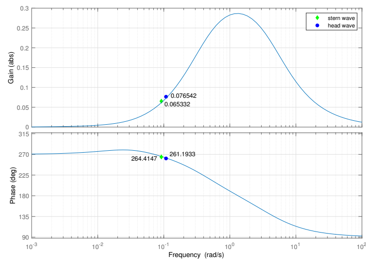


(d) $\frac{\delta n^*}{\delta w^*}$ in head and stern waves

Figure 5.8: Operating ellipse and Bode plots in stern and head waves for $\boldsymbol{\omega} = \mathbf{0.1}$ **rad/s**.

| Wave Frequency $\boldsymbol{\omega} = \mathbf{0.5}$ **[rad/s]** | | |
|---|---|---|
| Parameters | Following Wave $\mu = 0°$ | Head Wave $\mu = 180°$ |
| $\omega_e$ [rad/s] | 0.2961 | 0.7039 |
| $\delta w^*$ [-] | 0.15 | 0.15 |
| $\left\lvert \frac{\delta n^*}{\delta w^*} \right\rvert$ [-] | 0.1726 | 0.2682 |
| $\angle \frac{\delta n^*}{\delta w^*}$ [deg] | 235.7925 | 201.7935 |
| $\left\lvert \frac{\delta M_b^*}{\delta w^*} \right\rvert$ [-] | 1.2267 | 0.8385 |
| $\angle \frac{\delta M_b^*}{\delta w^*}$ [deg] | -22.0224 | -39.5373 |
| a [-] | 0.0253 | 0.0349 |
| b [-] | 0.1841 | 0.1274 |
| $\alpha$ [deg] | 1.7340 | 9.4365 |

Table 5.4: Variables and parameters of following and head waves for $\omega$ = 0.5 rad/s at **operating point 8**.

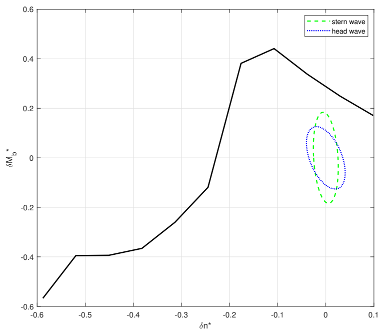


(a) Operating ellipse in engine operating envelope

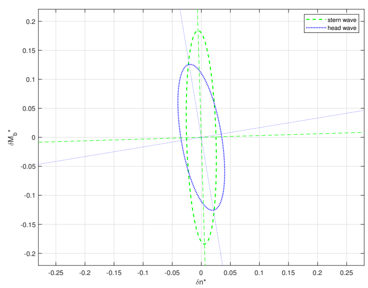


(b) Operating ellipse

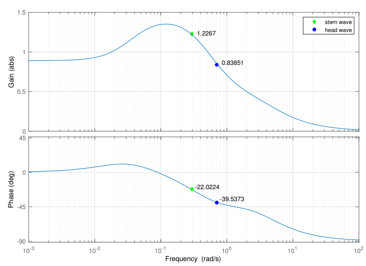


(c) $\frac{\delta M_b^*}{\delta w^*}$ in head and stern waves

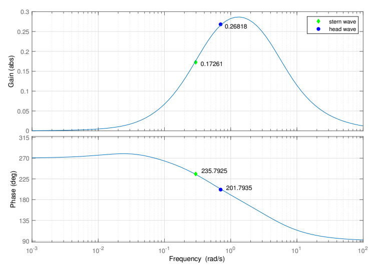


(d) $\frac{\delta n^*}{\delta w^*}$ in head and stern waves

Figure 5.9: Operating ellipse and Bode plots in stern and head waves for $\boldsymbol{\omega} = \mathbf{0.5}$ **rad/s**.

5

| Wave Frequency $\boldsymbol{\omega} = \mathbf{1}$ [rad/s] | | |
|---|---|---|
| Parameters | Following Wave $\mu = 0°$ | Head Wave $\mu = 180°$ |
| $\omega_e$ [rad/s] | 0.1845 | 1.8155 |
| $\delta w^*$ [-] | 0.15 | 0.15 |
| $\left\lvert \frac{\delta n^*}{\delta w^*} \right\rvert$ [-] | 0.1189 | 0.2803 |
| $\angle \frac{\delta n^*}{\delta w^*}$ [deg] | 249.9023 | 168.3358 |
| $\left\lvert \frac{\delta M_b^*}{\delta w^*} \right\rvert$ [-] | 1.3260 | 0.5186 |
| $\angle \frac{\delta M_b^*}{\delta w^*}$ [deg] | -12.3699 | -47.5031 |
| a [-] | 0.0177 | 0.0224 |
| b [-] | 0.1989 | 0.0855 |
| $\alpha$ [deg] | 0.6961 | 25.5325 |

Table 5.5: Variables and parameters of following and head waves for $\omega = 1$ rad/s at **operating point 8**.

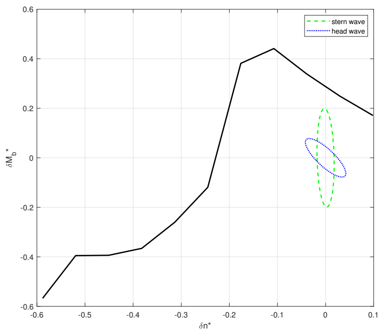


(a) Operating ellipse in engine operating envelope

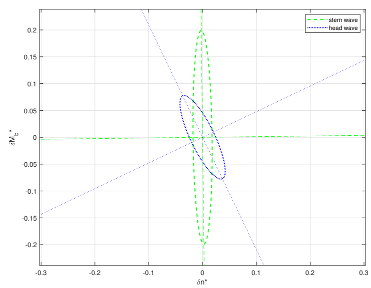


(b) Operating ellipse

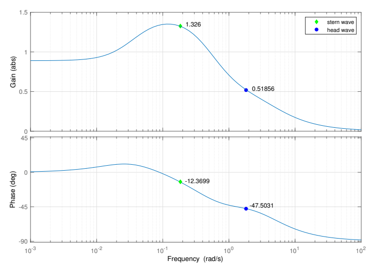


(c) $\frac{\delta M_b^*}{\delta w^*}$ in head and stern waves

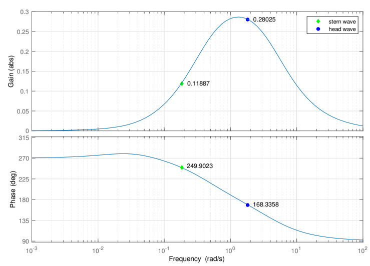


(d) $\frac{\delta n^*}{\delta w^*}$ in head and stern waves

Figure 5.10: Operating ellipse and Bode plots in stern and head waves for $\boldsymbol{\omega} = \mathbf{1}$ **rad/s**.

| Wave Frequency $\boldsymbol{\omega} = \mathbf{2}$ **[rad/s]** | | |
|---|---|---|
| Parameters | Following Wave $\mu = 0°$ | Head Wave $\mu = 180°$ |
| $\omega_e$ [rad/s] | 1.2621 | 5.2621 |
| $\delta w^*$ [-] | 0.15 | 0.15 |
| $\left\lvert \frac{\delta n^*}{\delta w^*} \right\rvert$ [-] | 0.2866 | 0.1835 |
| $\angle \frac{\delta n^*}{\delta w^*}$ [deg] | 179.3763 | 129.9655 |
| $\left\lvert \frac{\delta M_b^*}{\delta w^*} \right\rvert$ [-] | 0.6032 | 0.2834 |
| $\angle \frac{\delta M_b^*}{\delta w^*}$ [deg] | -45.1744 | -63.7638 |
| a [-] | 0.0284 | 0.0055 |
| b [-] | 0.0961 | 0.0503 |
| $\alpha$ [deg] | 20.5849 | 32.6149 |

Table 5.6: Variables and parameters of following and head waves for $\omega = 2$ rad/s at **operating point 8**.

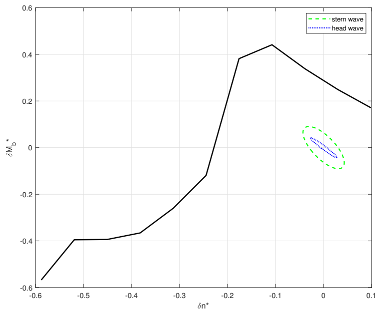


(a) Operating ellipse in engine operating envelope

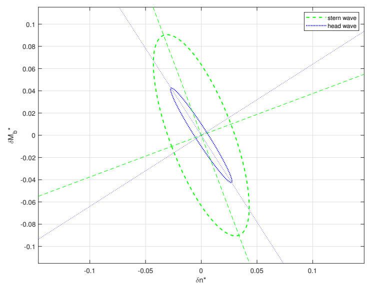


(b) Operating ellipse

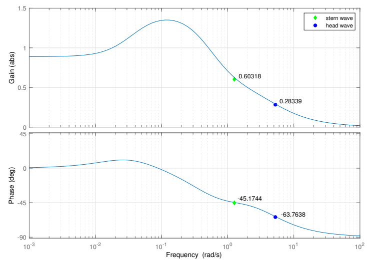


(c) $\frac{\delta M_b^*}{\delta w^*}$ in head and stern waves

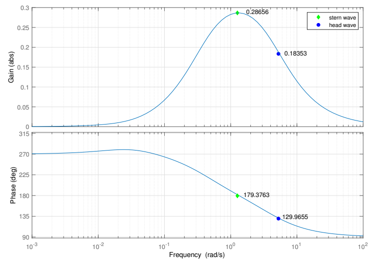


(d) $\frac{\delta n^*}{\delta w^*}$ in head and stern waves

Figure 5.11: Operating ellipse and Bode plots in stern and head waves for $\boldsymbol{\omega} = \mathbf{2}$ **rad/s**.

| Wave Frequency $\boldsymbol{\omega} = \mathbf{5}$ [rad/s] | | |
|---|---|---|
| Parameters | Following Wave $\mu = 0°$ | Head Wave $\mu = 180°$ |
| $\omega_e$ [rad/s] | 15.3881 | 25.3881 |
| $\delta w^*$ [-] | 0.15 | 0.15 |
| $\left\lvert \frac{\delta n^*}{\delta w^*} \right\rvert$ [-] | 0.0741 | 0.0473 |
| $\angle \frac{\delta n^*}{\delta w^*}$ [deg] | 105.0299 | 99.5391 |
| $\left\lvert \frac{\delta M_b^*}{\delta w^*} \right\rvert$ [-] | 0.1115 | 0.0711 |
| $\angle \frac{\delta M_b^*}{\delta w^*}$ [deg] | -79.6945 | -83.4339 |
| a [-] | 7.6289e-04 | 3.0667e-04 |
| b [-] | 0.0201 | 0.0128 |
| $\alpha$ [deg] | 33.5653 | 33.6407 |

Table 5.7: Variables and parameters of following and head waves for $\omega = 5$ rad/s at **operating point 8**.

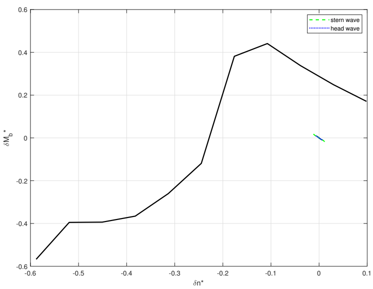


(a) Operating ellipse in engine operating envelope

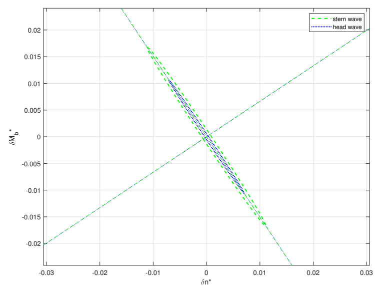


(b) Operating ellipse

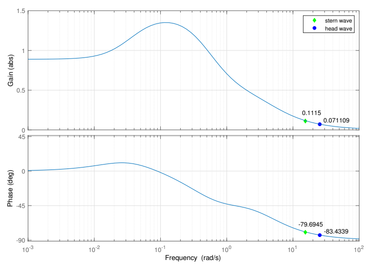


(c) $\frac{\delta M_b^*}{\delta w^*}$ in head and stern waves

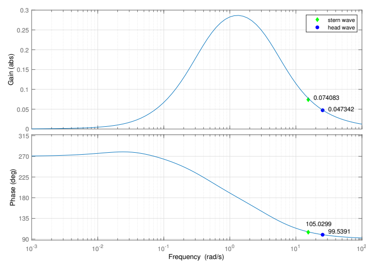


(d) $\frac{\delta n^*}{\delta w^*}$ in head and stern waves

Figure 5.12: Operating ellipse and Bode plots in stern and head waves for $\boldsymbol{\omega} = \mathbf{5}$ **rad/s**.

| Wave Frequency $\omega = \mathbf{10}$ **[rad/s]** | | |
|---|---|---|
| Parameters | Following Wave $\mu = 0°$ | Head Wave $\mu = 180°$ |
| $\omega_e$ [rad/s] | 71.5526 | 91.5526 |
| $\delta w^*$ [-] | 0.15 | 0.15 |
| $\left\lvert \frac{\delta n^*}{\delta w^*} \right\rvert$ [-] | 0.0162 | 0.0139 |
| $\angle \frac{\delta n^*}{\delta w^*}$ [deg] | 93.2457 | 92.7807 |
| $\left\lvert \frac{\delta M_b^*}{\delta w^*} \right\rvert$ [-] | 0.0243 | 0.0208 |
| $\angle \frac{\delta M_b^*}{\delta w^*}$ [deg] | -87.7608 | -88.0815 |
| a [-] | 3.5461e-05 | 2.6026e-05 |
| b [-] | 0.0044 | 0.0037 |
| $\alpha$ [deg] | 33.6844 | 33.6859 |

Table 5.8: Variables and parameters of following and head waves for $\omega$ = 10 rad/s at **operating point 8**.

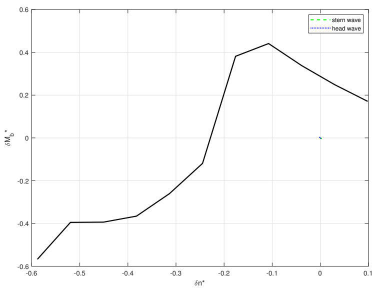


(a) Operating ellipse in engine operating envelope

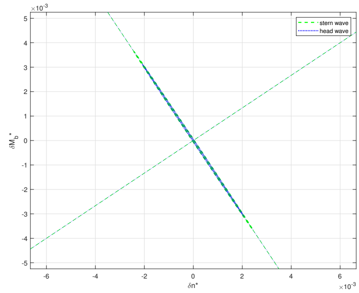


(b) Operating ellipse

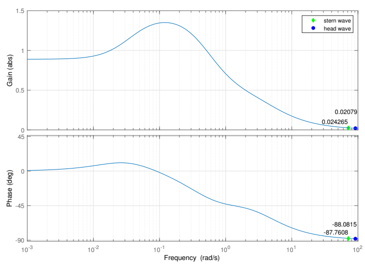


(c) $\frac{\delta M_b^*}{\delta w^*}$ in head and stern waves

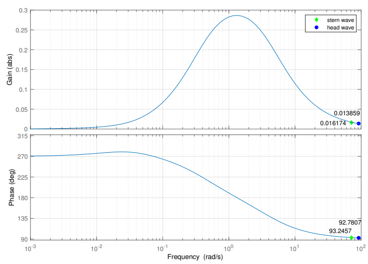


(d) $\frac{\delta n^*}{\delta w^*}$ in head and stern waves

Figure 5.13: Operating ellipse and Bode plots in stern and head waves for $\boldsymbol{\omega} = \mathbf{10}$ **rad/s**.

## 5.4. Operating Point

In this section, the second of the three previously mentioned factors affecting the dynamic response of the engine's operating point in terms of torque and speed fluctuations in the engine operating envelope, will be investigated. This factor is the system operating point, meaning that the impact of different system operating points on the engine's dynamic behaviour, when the vessels sails in a wave field, is examined. As it was described in Section 4.3, the linear model of non-linear ship propulsion model is only derived for two operating points, since according to theory, linear models are only valid for specific equilibrium points and small perturbations around them. In this work these equilibrium points are the two static operating points that are chosen to be investigated. The description of these two operating points is given in Section 4.3 and their position within the engine operating envelope can be noticed in Figure 5.14.



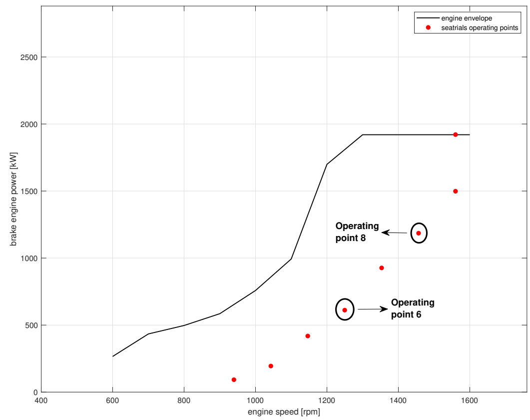


Figure 5.14: Examined Operating point 6 and Operating point 8 on the engine's operating line.

Regarding the impact of the system operating point on the engine's operating point dynamic behaviour, with all the rest of the factors being constant, the influence of the two chosen system operating points, 6 and 8, is examined. Besides the derived Bode plot diagrams that are required in order to plot the elliptic trajectory of the engine's operating point, the system's operating point influences the wake disturbance modelling, which is dependent on the ship speed that is defined by the selected operating point. More specifically, as it is described in Section A.3, the variation of the wake fraction due to the orbital motion of water particles in waves depends on the ship speed $v_s$ for a given wave disturbance with known wave amplitude $\zeta_a$ and wave frequency $\omega$. The wake fraction variation is calculated in Eq. (A.9) which is given below:

$$w = 1 - \frac{v_a}{v_s} + \frac{\zeta_a \omega e^{kz}}{v_s} \sin\left(\omega_e t - kx\right)$$

Consequently, the normalised change of wake fraction, $\delta w^*$, is also dependent on the ship speed and thus on the system operating point, as it is shown in Eq. (A.10), (A.11) and (A.12). For that reason and given that all the rest factors have to stay unchanged (Sea State & ship direction with respect to waves), one Sea State is selected between those presented in Figure A.1. For the chosen Sea State >8, as presented in Figure A.1, four(4) different wave frequencies are examined. Each one of them gives a different wave amplitude. With the wave amplitude $\zeta_a$ and wave frequency $\omega$ known, the normalised change of wake fraction can be calculated for the two examined operating points following the process presented in Section A.3. The wave amplitude spectrum of Sea State >8 is demonstrated below:

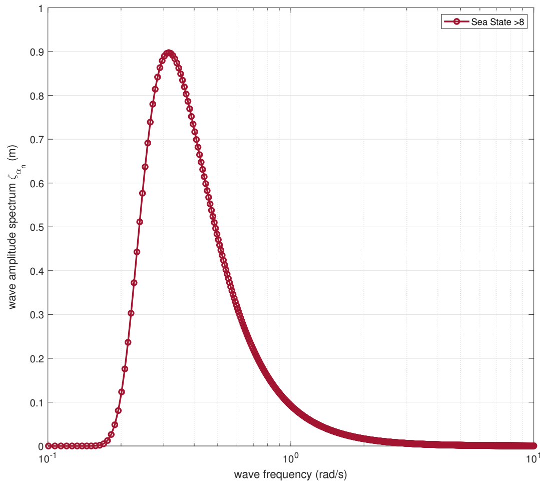


Figure 5.15: Wave amplitude spectrum, $\zeta_{a_n}$ for Sea State >8 as presented in Figure A.1.

Furthermore, for the examined wave frequencies of the Sea State >8 the frequency of encounter, $\omega_e$, is defined according to Eq. (5.21) for the two system operating points under consideration. The input to Eq. (5.21) that changes with respect to the system operating point is the speed, $V$, at which the vessel sails. The value of ship speed for both operating points under consideration can be found in Table 4.2. As far as the direction of the ship in respect to the incoming waves is concerned, it is constant. It has to be mentioned that, for this Section the following waves, $\mu = 0°$, is the chosen ship direction. Finally, it has to be mentioned that regarding the values of the gains of the governor, $K_p$ and $K_i$, that are used for the derivation of the linear model are constant and the same as the ones used in the previous Section 5.3.

As for the plotted results of the dynamic response of the engine's operating point with respect to different operating points, what has to be mentioned is that the system operating point influences only the size of the elliptic trajectory of the engine's operating point. On the other hand, the system operating point has no effect on the angle of rotation of the operating ellipse. More specifically, what can be remarked regarding the elliptic trajectories of operating point 6 and 8 throughout the whole range of examined wave frequencies, $\omega$, is that the angle of rotation is nearly the same for both. The only case that it can be considered that there is a slight difference with respect to the angle of rotation of the two operating ellipses between operating point 6 and 8 is wave frequency $\omega = 2$ rad/s. Moreover, it can be noticed that the operating ellipse for operating point 6 has larger engine's torque fluctuations, $\delta M_b^*$ and engine's speed fluctuations, $\delta n^*$ compared to the corresponding operating point 8 throughout the whole range of frequencies.



The reason that the elliptic trajectory of the engine's operating point for operating point 6 is larger in terms of both axes compared to the corresponding elliptic trajectory for operating point 8 can only be attributed to the difference in the value of the normalised change of wake fraction, $\delta w^*$ and not to the derived Bode plots of $\frac{\delta n^*}{\delta w^*}$ and $\frac{\delta M_b^*}{\delta w^*}$ for the two operating points.

Observing Figures 5.16 - 5.23, it can be noticed that the derived Bode plots are almost identical for operating points 6 and 8. Furthermore, it should be pointed out that the values of frequencies of encounter, $\omega_e$, for the two operating points are quite close to each other for all the examined wave frequencies, $\omega$, since the only difference is because of the different vessel speed, $\mathbf{V_6 = 6.8821}$ **m/s** and $\mathbf{V_8 = 8.0003}$ **m/s**. Consequently, that results in values quite close to each other for the gains $\left|\frac{\delta n^*}{\delta w^*}\right|$ and $\left|\frac{\delta M_b^*}{\delta w^*}\right|$ and phase angles $\angle\frac{\delta n^*}{\delta w^*}$ and $\angle\frac{\delta M_b^*}{\delta w^*}$. According to Section 5.2.1, these values multiplied by the normalised change of wake fraction, $\delta w^*$, determine the dimensions of the elliptic trajectories. Given that the values of gains $\left|\frac{\delta n^*}{\delta w^*}\right|$ and $\left|\frac{\delta M_b^*}{\delta w^*}\right|$ are quite close to each other for both operating point 6 and 8, the differences that can be noticed in size of the operating ellipses for operating points 6 and 8 can only be attributed to the difference in the values of the normalised change of wake fraction. This also explained according to the theory presented in Section A.3, where it is documented that the value of the normalised change of wake fraction, $\delta w^*$, depends on the ship speed $v_s$ and as a consequence on the system's operating point. The difference of the value of the normalised change of wake fraction for operating point 6 and 8 can be detected in Tables 5.9 - 5.16, where the values of all the relevant parameters are listed.

| Wave Frequency $\omega$ = **0.3 rad/s** Wave Amplitude $\zeta_a$ = **0.89 m** | | |
|---|---|---|
| Parameters | Operating Point 6 | Operating Point 8 |
| $\omega_e$ [rad/s] | 0.2369 | 0.2266 |
| $\delta w^*$ [-] | 0.0455 | 0.0392 |
| $\left\lvert \frac{\delta n^*}{\delta w^*} \right\rvert$ [-] | 0.1767 | 0.1358 |
| $\angle \frac{\delta n^*}{\delta w^*}$ [deg] | 238.3307 | 245.5247 |
| $\left\lvert \frac{\delta M_b^*}{\delta w^*} \right\rvert$ [-] | 1.4247 | 1.3018 |
| $\angle \frac{\delta M_b^*}{\delta w^*}$ [deg] | -20.9505 | -15.4730 |
| a [-] | 0.0079 | 0.0053 |
| b [-] | 0.0649 | 0.0510 |
| $\alpha$ [deg] | 1.3410 | 0.9452 |

Table 5.9: Variables and parameters at operating point 6 and 8 for $\omega$ = 0.3 rad/s in **following waves**.

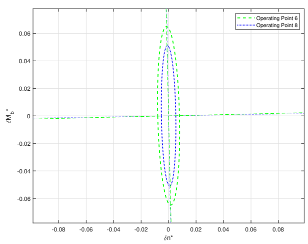


(a) Elliptic trajectory of operating point 6 and 8

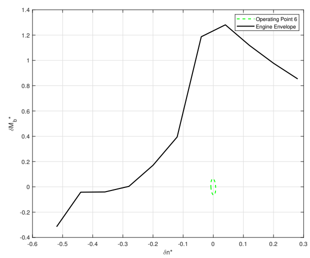


(b) Operating point 6 in engine's operating envelope

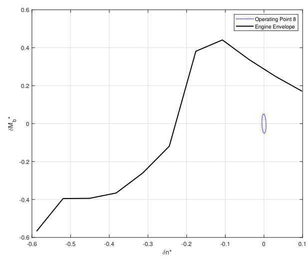


(c) Operating point 8 in engine's operating envelope

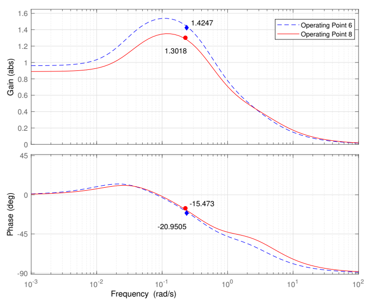


(d) $\frac{\delta M_b^*}{\delta w^*}$ for operating point 6 and 8

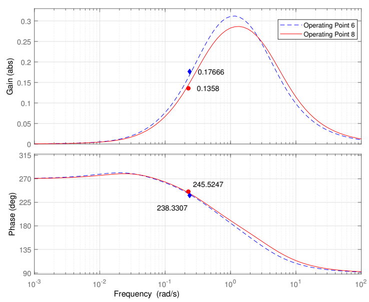


(e) $\frac{\delta n^*}{\delta w^*}$ for operating point 6 and 8

Figure 5.16: Operating ellipse and Bode plots for operating point 6 and operating point 8, in following waves, for $\boldsymbol{\omega}$ = **0.3 rad/s**.

| Wave Frequency $\boldsymbol{\omega} = \mathbf{0.4\ rad/s}$ <br> Wave Amplitude $\boldsymbol{\zeta_a} = \mathbf{0.71\ m}$ | | |
|---|---|---|
| Parameters | Operating Point 6 | Operating Point 8 |
| $\omega_e$ [rad/s] | 0.2878 | 0.2695 |
| $\delta w^*$ [-] | 0.0492 | 0.0423 |
| $\left\lvert \frac{\delta n^*}{\delta w^*} \right\rvert$ [-] | 0.1976 | 0.1726 |
| $\angle \frac{\delta n^*}{\delta w^*}$ [deg] | 233.1254 | 235.7925 |
| $\left\lvert \frac{\delta M_b^*}{\delta w^*} \right\rvert$ [-] | 1.3743 | 1.2267 |
| $\angle \frac{\delta M_b^*}{\delta w^*}$ [deg] | -24.4188 | -22.0224 |
| a [-] | 0.0095 | 0.0071 |
| b [-] | 0.0677 | 0.0519 |
| $\alpha$ [deg] | 1.8121 | 1.7340 |

Table 5.10: Variables and parameters at operating point 6 and 8 for $\omega = 0.4$ rad/s in **following waves**.

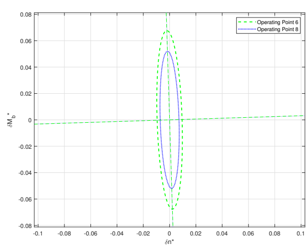


(a) Elliptic trajectory of operating point 6 and 8

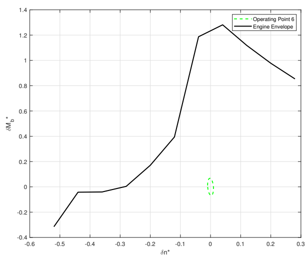


(b) Operating point 6 in engine's operating envelope

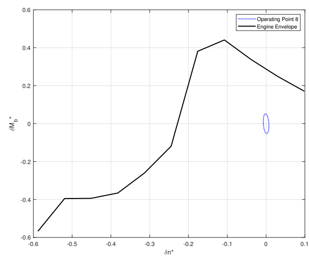


(c) Operating point 8 in engine's operating envelope

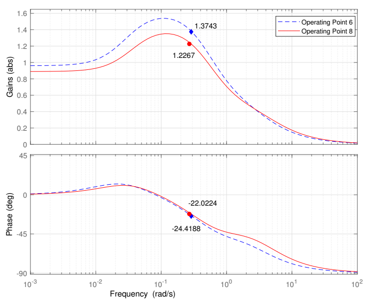


(d) $\frac{\delta M_b^*}{\delta w^*}$ for operating point 6 and 8

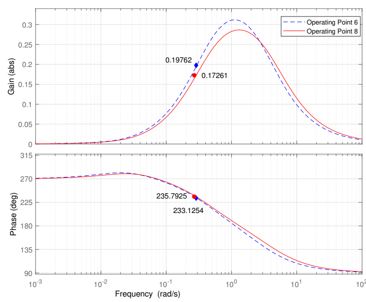


(e) $\frac{\delta n^*}{\delta w^*}$ for operating point 6 and 8

Figure 5.17: Operating ellipse and Bode plots for operating point 6 and operating point 8, in following waves, for $\boldsymbol{\omega} = \mathbf{0.4\ rad/s}$.

| Wave Frequency $\boldsymbol{\omega} = \mathbf{0.5\ rad/s}$<br>Wave Amplitude $\boldsymbol{\zeta_a} = \mathbf{0.47\ m}$ | | |
|---|---|---|
| Parameters | Operating Point 6 | Operating Point 8 |
| $\omega_e$ [rad/s] | 0.3246 | 0.2961 |
| $\delta w^*$ [-] | 0.0416 | 0.0358 |
| $\left\lvert \frac{\delta n^*}{\delta w^*} \right\rvert$ [-] | 0.2187 | 0.1726 |
| $\angle \frac{\delta n^*}{\delta w^*}$ [deg] | 227.5966 | 235.7925 |
| $\left\lvert \frac{\delta M_b^*}{\delta w^*} \right\rvert$ [-] | 1.3141 | 1.2267 |
| $\angle \frac{\delta M_b^*}{\delta w^*}$ [deg] | -27.9499 | -22.0224 |
| a [-] | 0.0088 | 0.0060 |
| b [-] | 0.0547 | 0.0439 |
| $\alpha$ [deg] | 2.4414 | 1.7340 |

Table 5.11: Variables and parameters at operating point 6 and 8 for $\omega = 0.5$ rad/s in **following waves**.

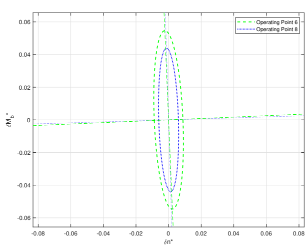


(a) Elliptic trajectory of operating point 6 and 8

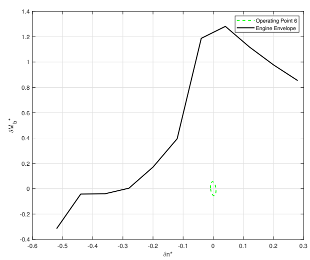


(b) Operating point 6 in engine's operating envelope

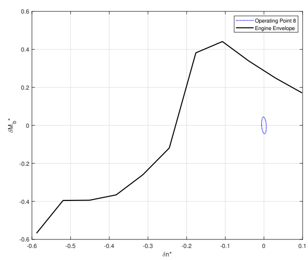


(c) Operating point 8 in engine's operating envelope

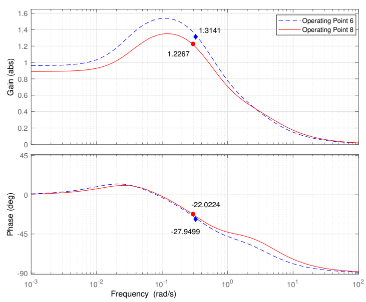


(d) $\frac{\delta M_b^*}{\delta w^*}$ for operating point 6 and 8

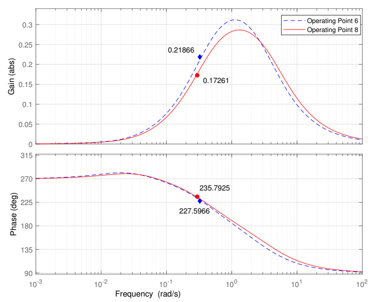


(e) $\frac{\delta n^*}{\delta w^*}$ for operating point 6 and 8

Figure 5.18: Operating ellipse and Bode plots for operating point 6 and operating point 8, in following waves, for $\boldsymbol{\omega} = \mathbf{0.5\ rad/s}$.

| Wave Frequency $\boldsymbol{\omega} = \mathbf{0.6}$ **rad/s**<br>Wave Amplitude $\boldsymbol{\zeta_a} = \mathbf{0.31}$ **m** | | |
|---|---|---|
| Parameters | Operating Point 6 | Operating Point 8 |
| $\omega_e$ [rad/s] | 0.3474 | 0.3064 |
| $\delta w^*$ [-] | 0.0337 | 0.0290 |
| $\left\lvert \frac{\delta n^*}{\delta w^*} \right\rvert$ [-] | 0.2187 | 0.1726 |
| $\angle \frac{\delta n^*}{\delta w^*}$ [deg] | 227.5966 | 235.7925 |
| $\left\lvert \frac{\delta M_b^*}{\delta w^*} \right\rvert$ [-] | 1.3141 | 1.2267 |
| $\angle \frac{\delta M_b^*}{\delta w^*}$ [deg] | -27.9499 | -22.0224 |
| a [-] | 0.0071 | 0.0049 |
| b [-] | 0.0444 | 0.0356 |
| $\alpha$ [deg] | 2.4414 | 1.7340 |

Table 5.12: Variables and parameters at operating point 6 and operating point 8 for $\omega$ = 0.6 rad/s in **following waves**.

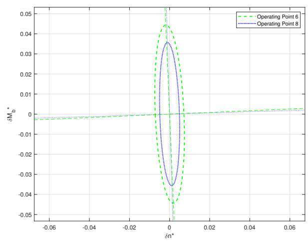


(a) Elliptic trajectory of operating point 6 and 8

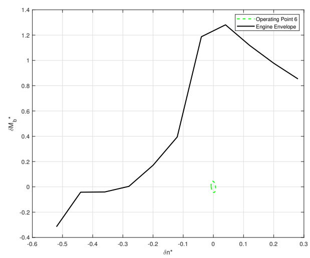


(b) Operating point 6 in engine's operating envelope

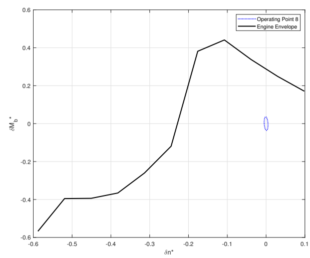


(c) Operating point 8 in engine's operating envelope

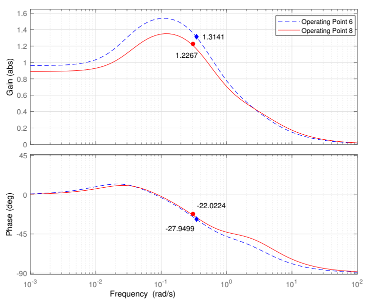


(d) $\frac{\delta M_b^*}{\delta w^*}$ for operating point 6 and 8

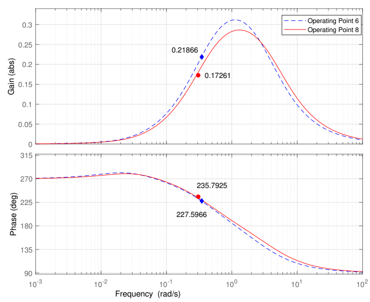


(e) $\frac{\delta n^*}{\delta w^*}$ for operating point 6 and 8

Figure 5.19: Operating ellipse and Bode plots for operating point 6 and operating point 8, in following waves, for $\boldsymbol{\omega} = \mathbf{0.6}$ **rad/s**.

| Wave Frequency $\omega = \mathbf{0.7\ rad/s}$ Wave Amplitude $\zeta_a = \mathbf{0.22\ m}$ | | |
|---|---|---|
| Parameters | Operating Point 6 | Operating Point 8 |
| $\omega_e$ [rad/s] | 0.3562 | 0.3004 |
| $\delta w^*$ [-] | 0.0288 | 0.0248 |
| $\left\lvert \frac{\delta n^*}{\delta w^*} \right\rvert$ [-] | 0.2187 | 0.1726 |
| $\angle \frac{\delta n^*}{\delta w^*}$ [deg] | 227.5966 | 235.7925 |
| $\left\lvert \frac{\delta M_b^*}{\delta w^*} \right\rvert$ [-] | 1.3141 | 1.2267 |
| $\angle \frac{\delta M_b^*}{\delta w^*}$ [deg] | -27.9499 | -22.0224 |
| a [-] | 0.0061 | 0.0042 |
| b [-] | 0.0379 | 0.0304 |
| $\alpha$ [deg] | 2.4414 | 1.7340 |

Table 5.13: Variables and parameters at operating point 6 and operating point 8 for $\omega$ = 0.7 rad/s in **following waves**.

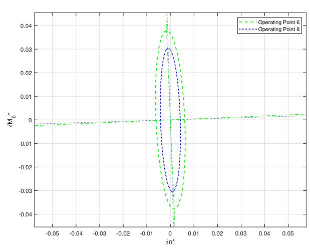


(a) Elliptic trajectory of operating point 6 and 8

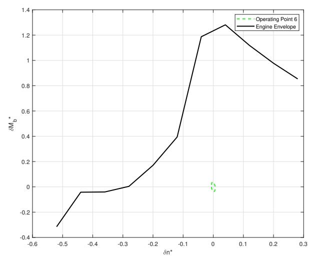


(b) Operating point 6 in engine's operating envelope

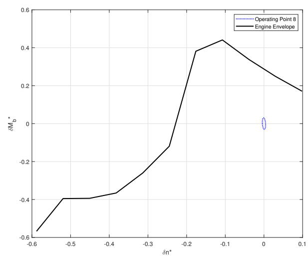


(c) Operating point 8 in engine's operating envelope

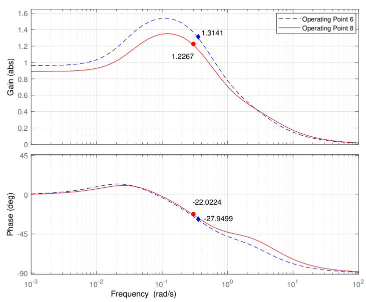


(d) $\frac{\delta M_b^*}{\delta w^*}$ for operating point 6 and 8

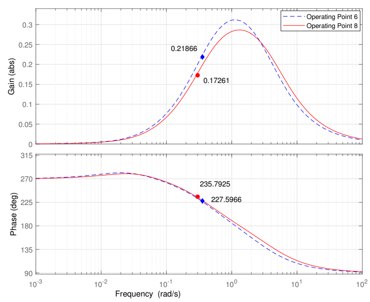


(e) $\frac{\delta n^*}{\delta w^*}$ for operating point 6 and 8

Figure 5.20: Operating ellipse and Bode plots for operating point 6 and operating point 8, in following waves, for $\omega = \mathbf{0.7\ rad/s}$.

| Wave Frequency $\boldsymbol{\omega} = \mathbf{0.8\ rad/s}$ Wave Amplitude $\boldsymbol{\zeta_a} = \mathbf{0.16\ m}$ | | |
|---|---|---|
| Parameters | Operating Point 6 | Operating Point 8 |
| $\omega_e$ [rad/s] | 0.3510 | 0.2781 |
| $\delta w^*$ [-] | 0.0248 | 0.0213 |
| $\left\lvert\frac{\delta n^*}{\delta w^*}\right\rvert$ [-] | 0.2187 | 0.1726 |
| $\angle\frac{\delta n^*}{\delta w^*}$ [deg] | 227.5966 | 235.7925 |
| $\left\lvert\frac{\delta M_b^*}{\delta w^*}\right\rvert$ [-] | 1.3141 | 1.2267 |
| $\angle\frac{\delta M_b^*}{\delta w^*}$ [deg] | -27.9499 | -22.0224 |
| a [-] | 0.0052 | 0.0036 |
| b [-] | 0.0326 | 0.0261 |
| $\alpha$ [deg] | 2.4414 | 1.7340 |

Table 5.14: Variables and parameters at operating point 6 and operating point 8 for $\omega$ = 0.8 rad/s in **following waves**.

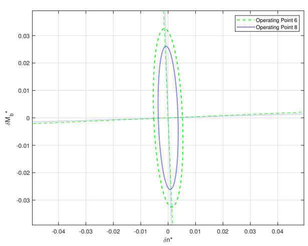


(a) Elliptic trajectory of operating point 6 and 8

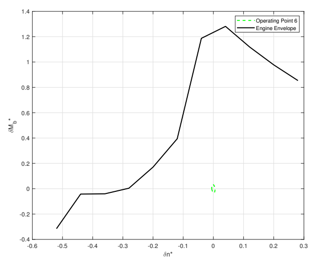


(b) Operating point 6 in engine's operating envelope

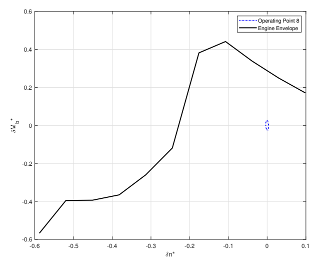


(c) Operating point 8 in engine's operating envelope

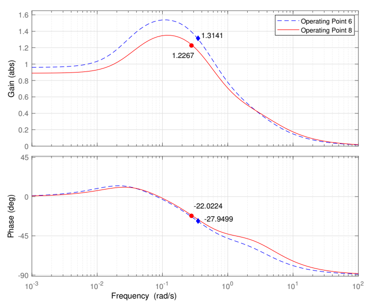


(d) $\frac{\delta M_b^*}{\delta w^*}$ for operating point 6 and 8

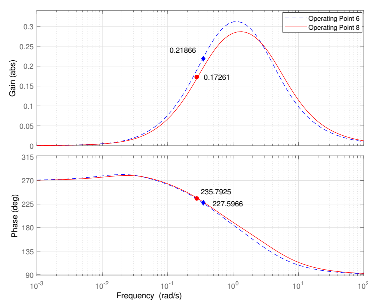


(e) $\frac{\delta n^*}{\delta w^*}$ for operating point 6 and 8

Figure 5.21: Operating ellipse and Bode plots for operating point 6 and operating point 8, in following waves, for $\boldsymbol{\omega} = \mathbf{0.8\ rad/s}$.

| Wave Frequency $\boldsymbol{\omega}$ = **1 rad/s** Wave Amplitude $\boldsymbol{\zeta_a}$ = **0.092 m** | | |
|---|---|---|
| Parameters | Operating Point 6 | Operating Point 8 |
| $\omega_e$ [rad/s] | 0.2985 | 0.1845 |
| $\delta w^*$ [-] | 0.0193 | 0.0166 |
| $\left\lvert \frac{\delta n^*}{\delta w^*} \right\rvert$ [-] | 0.1976 | 0.1189 |
| $\angle \frac{\delta n^*}{\delta w^*}$ [deg] | 233.1254 | 249.9023 |
| $\left\lvert \frac{\delta M_b^*}{\delta w^*} \right\rvert$ [-] | 1.3743 | 1.3260 |
| $\angle \frac{\delta M_b^*}{\delta w^*}$ [deg] | -24.4188 | -12.3699 |
| a [-] | 0.0037 | 0.0020 |
| b [-] | 0.0266 | 0.0220 |
| $\alpha$ [deg] | 1.8121 | 0.6961 |

Table 5.15: Variables and parameters at operating point 6 and operating point 8 for $\omega = 1$ rad/s in **following waves**.

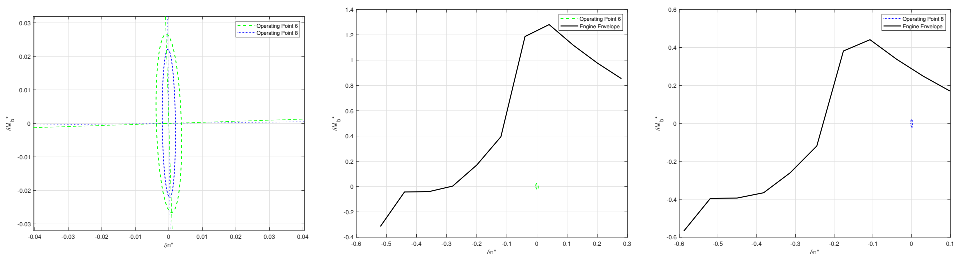


(a) Elliptic trajectory of operating point 6 and 8 (b) Operating point 6 in engine's operating envelope (c) Operating point 8 in engine's operating envelope

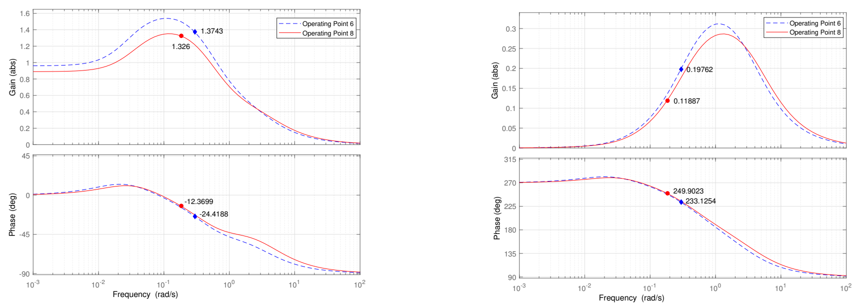


(d) $\frac{\delta M_b^*}{\delta w^*}$ for operating point 6 and 8 (e) $\frac{\delta n^*}{\delta w^*}$ for operating point 6 and 8

Figure 5.22: Operating ellipse and Bode plots for operating point 6 and operating point 8, in following waves, for $\boldsymbol{\omega}$ = **1 rad/s**.

| Wave Frequency $\boldsymbol{\omega} = \mathbf{2}$ **rad/s** Wave Amplitude $\boldsymbol{\zeta_a} = \mathbf{0.016}$ **m** | | |
|---|---|---|
| Parameters | Operating Point 6 | Operating Point 8 |
| $\omega_e$ [rad/s] | 0.8062 | 1.2621 |
| $\delta w^*$ [-] | 0.0134 | 0.0115 |
| $\left\lvert \frac{\delta n^*}{\delta w^*} \right\rvert$ [-] | 0.3073 | 0.2866 |
| $\angle \frac{\delta n^*}{\delta w^*}$ [deg] | 190.9698 | 179.3763 |
| $\left\lvert \frac{\delta M_b^*}{\delta w^*} \right\rvert$ [-] | 0.8450 | 0.6032 |
| $\angle \frac{\delta M_b^*}{\delta w^*}$ [deg] | -45.9759 | -45.1744 |
| a [-] | 0.0034 | 0.0022 |
| b [-] | 0.0115 | 0.0074 |
| $\alpha$ [deg] | 12.2826 | 20.5849 |

Table 5.16: Variables and parameters at operating point 6 and operating point 8 for $\omega = 2$ rad/s in **following waves**.

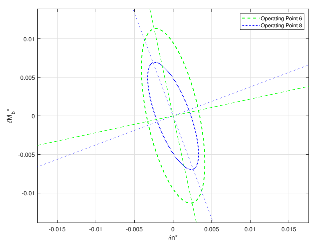


(a) Elliptic trajectory of operating point 6 and 8

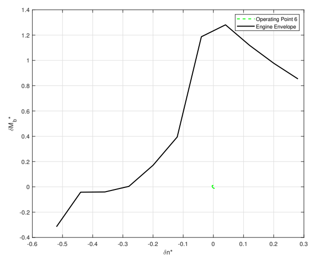


(b) Operating point 6 in engine's operating envelope

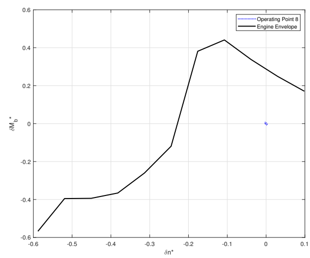


(c) Operating point 8 in engine's operating envelope

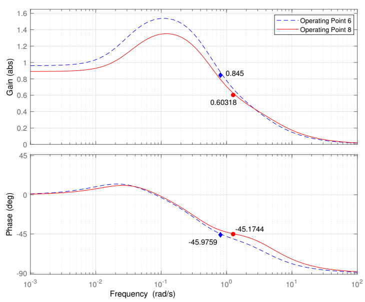


(d) $\frac{\delta M_b^*}{\delta w^*}$ for operating point 6 and 8

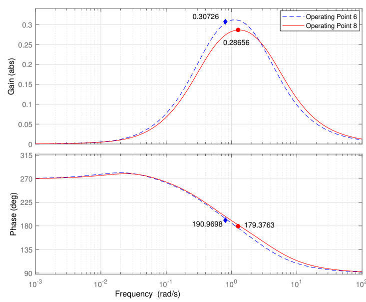


(e) $\frac{\delta n^*}{\delta w^*}$ for operating point 6 and 8

Figure 5.23: Operating ellipse and Bode plots for operating point 6 and operating point 8, in following waves, for $\boldsymbol{\omega} = \mathbf{2}$ **rad/s**.

## 5.5. SEA STATE

In this section the impact of different *Sea States*, on the torque variations, $\delta M_b^*$, of the engine's operating point is examined. In order to investigate the impact of different Sea States on the engine's dynamic response, these Sea States have to be translated into wake disturbance, caused by the waves that are generated in each specific Sea State that is selected to be examined.

According to literature, [Holthuijsen, 2007, Journée and Massie, 2000], each Sea State can be described by a wave frequency spectrum, as shown in Figure 5.24. The mathematical formulations of these normalised uni-directional wave energy spectra are based on two parameters:

- the significant wave height, $H_{1/3}$
- the average wave periods $\overline{T}$, defined by $T_1$, $T_2$ or $T_p$

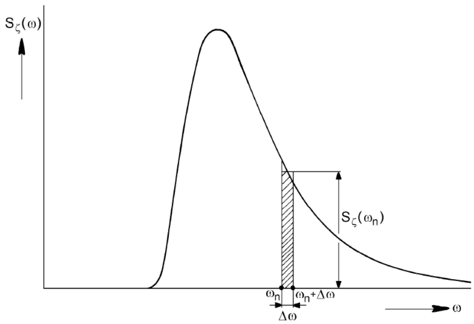


Figure 5.24: Wave energy spectrum, [Journée and Massie, 2000].

As a result, the general mathematical expression of wave energy spectra is:

$$S_\zeta(\omega) = H_{1/3}^2 \cdot f(\omega, \overline{T})$$

from which it follows that the spectral values are proportional to the significant wave height squared, $H_{1/3}^2$ and to a function of $\omega$ and $\overline{T}$. These mathematical expressions can be readily found in literature, as well as the required data, significant wave height $H_{1/3}$ and modal wave period $T_p$, for these mathematical expressions, in order to calculate the wave frequency spectrum for each Sea State. In this thesis the used data, which are shown in Figure 5.25, are found in [Journée and Massie, 2000], describing the open ocean annual Sea State occurrences for the North Atlantic.

Applying the above mentioned spectral mathematical formulations, one can derive the wave amplitude spectrum for each one of the Sea States that are presented in Figure 5.25, respectively. At this point it has to be stressed out that the investigation of the impact of the Sea State on the dynamic behaviour of the Diesel engine operating point in the engine's operating envelope is done only in terms of the maximum wave amplitude that each one of the considered Sea States cab cause. For that reason only the peak wave amplitude $\zeta_{\alpha_n}$ of each Sea State is chosen with its corresponding wave frequency, $\omega_n$, in order to calculate the wake variation, caused by the orbital motion of water particles, as it is extensively explained in Section 2.5.1. This wake variation is a sinusoidal signal, which is linearised and normalised according to Eq. (4.18). At that point, the linearised and normalised change of wake fraction, $\delta w^*$, is used for the derivation of the engine's operating point elliptic trajectory, according to the procedure presented in Section 5.2.1. In this Section, the derived wave amplitude spectra for the Sea States which are given in Figure 5.25 are presented together with their peak wave amplitudes $\zeta_{\alpha_n}$, their corresponding wave frequencies $\omega_n$ and the derived normalised changes of wake fraction.

The procedure followed in order to derive all the above mentioned and the mathematical equations involved in this procedure are clearly stated in Appendix A. In the following Figure 5.26 the wave amplitude spectra of the Sea States shown in Figure 5.25, are depicted:

| Sea State Number (−) | Significant Wave Height $H_{1/3}$ (m) | | Sustained Wind Speed 1) (kn) | | Probability of Sea State (%) | Modal Wave Period $T_p$ (s) | |
|---|---|---|---|---|---|---|---|
| | Range | Mean | Range | Mean | | Range 2) | Most 3) Probable |
| North Atlantic | | | | | | | |
| 0 - 1 | 0.0 - 0.1 | 0.05 | 0 - 6 | 3 | 0 | - | - |
| 2 | 0.1 - 0.5 | 0.3 | 7 - 10 | 8.5 | 7.2 | 3.3 - 12.8 | 7.5 |
| 3 | 0.50 - 1.25 | 0.88 | 11 - 16 | 13.5 | 22.4 | 5.0 - 14.8 | 7.5 |
| 4 | 1.25 - 2.50 | 1.88 | 17 - 21 | 19 | 28.7 | 6.1 - 15.2 | 8.8 |
| 5 | 2.5 - 4.0 | 3.25 | 22 - 27 | 24.5 | 15.5 | 8.3 - 15.5 | 9.7 |
| 6 | 4 - 6 | 5.0 | 28 - 47 | 37.5 | 18.7 | 9.8 - 16.2 | 12.4 |
| 7 | 6 - 9 | 7.5 | 48 - 55 | 51.5 | 6.1 | 11.8 - 18.5 | 15.0 |
| 8 | 9 - 14 | 11.5 | 56 - 63 | 59.5 | 1.2 | 14.2 - 18.6 | 16.4 |
| >8 | >14 | >14 | >63 | >63 | <0.05 | 18.0 - 23.7 | 20.0 |

Figure 5.25: North Atlantic Annual Sea State Occurrences, [Journée and Massie, 2000].

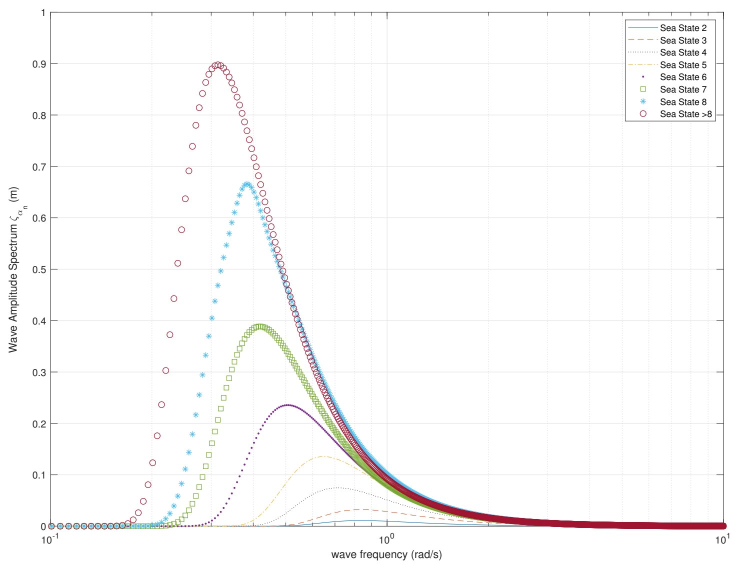


Figure 5.26: Derived Wave Amplitude Spectrum, $\zeta_{\alpha_n}$.

For each one of the Wave Amplitude Spectra graphed in Figure 5.26, the peak wave amplitude and its corresponding wave frequency are provided in Table 5.17.

For the wave frequencies, $\omega_n$, shown in Figure 5.17, the corresponding frequencies of encounter, $\omega_e$, are determined for the case of *following waves*, at *operating point 8* according to Eq. (5.21) with the ship speed being $V_s = 8.0003$ m/s and $\mu = 0°$. Consequently, by using the Bode plots derived for the linear system at this specific operating point, the elliptic trajectories of the engine's operating point, under the impact of the aforementioned Sea States, are derived. This derivation, combined with the system's response, described by the Bode plots due to the wake disturbance $\delta w^*$, offers the possibility to examine the Sea States impact on the engine's operating point dynamic response. What is more, it should be mentioned that for the derivation of the Bode plots of the linear ship model the governor's gains that are used are the same with those referred in Section 5.3, which means $K_p = 1.5$ and $K_i = 2$.

In Figure 5.27a and Figure 5.27b it is indicated that the elliptic trajectories, as a result of the dynamic response of the engine's operating point, due to the influence of different Sea States, are mainly influenced in terms of torque variation, $\delta M_b^*$ and much less in terms of engine speed variation $\delta n^*$. This can be easily explained by observing the Bode plots of $\frac{\delta M_b^*}{\delta w^*}$ and $\frac{\delta n^*}{\delta w^*}$ as they are presented in Figure 5.27c and Figure 5.27d, respectively, as well as the definition of the ellipse geometric properties, which are demonstrated in Section 5.2.1. The major axis of the operating ellipse, as it is defined in Eq. (5.20), is dependent, on the one hand, on the relation of the phase angles of the two Bode plots, $\angle\frac{\delta M_b^*}{\delta w^*}$ and $\angle\frac{\delta n^*}{\delta w^*}$ and on the other hand, on the amplitude of the torque variation, $\delta M_b^*$. Regarding the phase angles, their relation for the eight different Sea States is the same since, as it can be noticed from the Bode plots their values are almost the same for both Bode plots $\frac{\delta M_b^*}{\delta w^*}$ and $\frac{\delta n^*}{\delta w^*}$. Despite the fact that the values of the gains $\left|\frac{\delta M_b^*}{\delta w^*}\right|$ are almost the same, similarly to those of phase angles, it has to be mentioned that in order to calculate the amplitude of the torque variation, $\delta M_b^*$, the gain $\left|\frac{\delta M_b^*}{\delta w^*}\right|$ has to be multiplied by the normalised change of wake fraction, $\delta w^*$. As it can be noticed in Table 5.18, the amplitude of the wake variation $\delta w^*$ increases as the Sea State increases, resulting in higher values of the amplitude of the torque variation, $\delta M_b^*$, each time and consequently in higher torque fluctuations regarding the dynamic response of the engine's operating point. As far as the engine speed fluctuation is concerned, it seems that the impact of different Sea States seems to be less, compared to torque fluctuations, due to quite low values of gains $\left|\frac{\delta n^*}{\delta w^*}\right|$, as it can be noticed in Figure 5.27d.

| Wave Amplitude Spectra $\zeta_{\alpha_n}$ | |
|---|---|
| Peak Wave Amplitude, $\zeta_{\alpha_n}$ [m] | Wave frequency, $\omega_n$ [rad/s] |
| 0.011 | 0.8357 |
| 0.0322 | 0.8357 |
| 0.0746 | 0.7163 |
| 0.1354 | 0.6472 |
| 0.2356 | 0.5089 |
| 0.3887 | 0.4210 |
| 0.6660 | 0.3833 |
| 0.8977 | 0.3142 |

Table 5.17: Values of maximum wave amplitudes for each one Sea State included in Figure 5.26 with the corresponding wave frequencies.

| Sea State | $\omega_e$ [rad/s] | $\delta w^*$ [-] | $\left\lvert\frac{\delta n^*}{\delta w^*}\right\rvert$ [-] | $\angle\frac{\delta n^*}{\delta w^*}$ [deg] | $\left\lvert\frac{\delta M_b^*}{\delta w^*}\right\rvert$ [-] | $\angle\frac{\delta M_b^*}{\delta w^*}$ [deg] | a [-] | b [-] | $\alpha$ [deg] |
|---|---|---|---|---|---|---|---|---|---|
| 2 | 0.2662 | 0.0015 | 0.1538 | 240.8183 | 1.2688 | -18.7028 | 2.3430e-04 | 0.0020 | 1.2815 |
| 3 | 0.2662 | 0.0045 | 0.1538 | 240.8183 | 1.2688 | -18.7028 | 6.8727e-04 | 0.0058 | 1.2815 |
| 4 | 0.2979 | 0.0086 | 0.1726 | 235.7925 | 1.2267 | -22.0224 | 0.0015 | 0.0106 | 1.734 |
| 5 | 0.3056 | 0.0139 | 0.1726 | 235.7925 | 1.2267 | -22.0224 | 0.0023 | 0.0170 | 1.734 |
| 6 | 0.2977 | 0.0183 | 0.1726 | 235.7925 | 1.2267 | -22.0224 | 0.0031 | 0.0224 | 1.7340 |
| 7 | 0.2764 | 0.0245 | 0.1726 | 235.7925 | 1.2267 | -22.0224 | 0.0041 | 0.0300 | 1.7340 |
| 8 | 0.2635 | 0.0379 | 0.1538 | 240.8183 | 1.2688 | -18.7028 | 0.0057 | 0.0481 | 1.2815 |
| >8 | 0.2337 | 0.0414 | 0.1538 | 240.8183 | 1.2688 | -18.7028 | 0.0063 | 0.0526 | 1.2815 |

Table 5.18: Variables and parameters for following waves, at operating point 8 for 8 different Sea States.

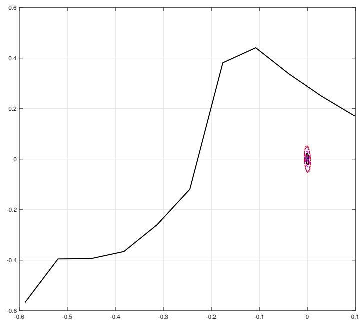

(a) Operating ellipses in engine operating envelope

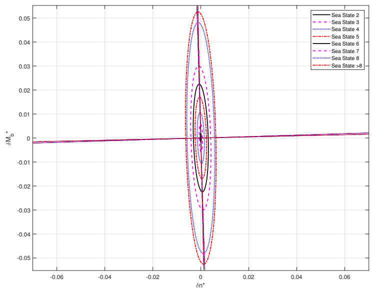


(b) Operating ellipses

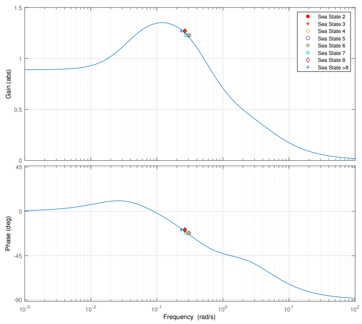


(c) $\frac{\delta M_b^*}{\delta w^*}$ in stern waves at operating point 8

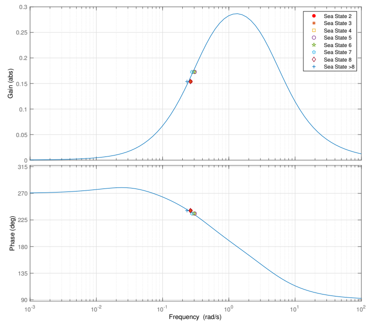


(d) $\frac{\delta n^*}{\delta w^*}$ in stern waves at operating point 8

Figure 5.27: Operating ellipses and Bode plots in stern waves at operating point 8 for Sea States as presented in Figure 5.25.

## 5.6. CONCLUSIONS

Taking into account all the above mentioned in the previous Sections regarding the ship direction with respect to the waves, the system operating point and the Sea State, their impact on the engine's operating point dynamic response is highly divergent.

As far as the impact of the two ship directions with respect to the incoming waves is concerned, the dynamic response of the engine's operating point is different between the two examined directions, following and head waves for the majority of wave frequencies, $\omega$, examined. The main difference caused by the ship direction with respect to the waves is that the operating ellipse resulting in case of head direction is more anticlockwise rotated compared to the operating ellipse resulting in case of following waves. This means that head direction leads to less fluctuations in the torque axis and more fluctuations in the speed axis compared to the corresponding fluctuations resulting from stern direction. Additionally, for a specific wave frequency under study the head direction results in a higher value of the encounter frequency compared to the encounter frequency resulting for the following direction. That means that for relatively higher wave frequencies, the operating ellipses resulting for head direction have smaller area (smaller size for both axis) compared to the operating ellipses resulting for following direction. This is explained by the low pass filter role that the shaft inertia has in the ship propulsion system, reducing the impact of high frequencies on the Diesel engine dynamic response.

As for the impact of the two different operating points, the derived Bode plots for the two operating points 6 and 8 are almost the same with values of the corresponding gains being also quite close to each other for the two examined operating points. Nevertheless, the operating ellipses resulting for operating point 6 are larger in terms of the size of both axes major and minor compared to the corresponding operating ellipses resulting for operating point 8. This means that operating point 6 leads to more fluctuations in both brake engine torque and engine speed direction compared to operating point 8. The difference of the size of the operating ellipses between operating point 6 and 8 can only be attributed to the higher value of normalised change of wake fraction, $\delta w^*$, in case of operating point 6 compared to operating point 8, since according to theory reported in Section A.3, the value of normalised change of wake fraction depends on the operating point and more specifically on the ship speed, which is dependent on the operating point. On the other hand, the operating point has no impact on the angle of rotation of the elliptic trajectories of the two different operating points for the whole range of frequencies examined.

As for the impact of different Sea States, the engine's operating point dynamic response is different, regarding the size of the operating ellipse for each different Sea State. mainly regarding the engine's torque fluctuations, $\delta M_b^*$. The elliptic trajectories of the engine's operating point, occurring due to different Sea States have different major and minor axes. More specifically, the major and minor axes of each elliptic trajectory increases as the Sea State is increased as a consequence of the increase of the wake disturbance amplitude, $\delta w^*$. This means that for higher Sea States the fluctuations become larger both in engine speed and brake engine torque direction.

Finally, according to the conclusion of the diverse impact of ship direction, system operating point and Sea States on the engine's dynamic behaviour it can be rightfully considered that there might be beneficial to schedule the governor gains according to each case under consideration each time. In other words, it might be useful to set the gains of the engine controller dependent on the three factors which were examined in this chapter, the ship direction with respect to the waves, the system operating point and the Sea States.

# 6

# Governor Gain Scheduling: Refinement of Diesel Engine's Dynamic Behaviour

*The possibility of any benefits lying in refining the existing governor's settings will be investigated in this Chapter. Taking into account the outcome of the previous chapter, the potential profit of making the gains of the engine's controller dependent on the system operating point, the Sea State and the direction of the ship with respect to the waves will be assessed. The governor gain scheduling, directly related to the wave induced disturbance and the operating point, will be attempted by developing a gains scheduling algorithm. The developed algorithm makes use of the linear model of the ship propulsion plant combined with an optimisation algorithm which employs a metaheuristic technique well-known for each effectiveness in dealing with hard optimisation.*

## 6.1. Introduction & General Considerations

In this Chapter the refinement of the Diesel engine's controller, used in the vessel under consideration, is attempted. According to the problem definition and the research questions, as they were defined in Section 1.2 and Section 1.4 respectively, the ultimate goal of this work is to examine the possibilities of influencing the size and the orientation of the elliptic trajectory of the engine operating point, aiming to prevent the activation of the propeller pitch control, when the ship sails in waves. The avoidance of activation of the propeller pitch control maintains the average delivered power and as a result the maximum average ship speed, which is particularly valuable in case of speed trials, as it is extensively explained in Chapter 1. The refinement of the existing propulsion controller settings consists in regulating the values of gains of the PID controller of the Diesel engine's governor, whose structure and function was clearly described in Section 3.3.2, according to the disturbance acting on the propulsion system.

As far as the avoidance of activation of propeller pitch control is concerned, it will be attempted by re-sizing and re-orientating the elliptic trajectory of the engine operating point by means of governor gains scheduling. The followed approach is given below:

1. Derivation of contour plots which will confirm the potential improvement of the dynamic behaviour of the operating ellipse in the engine envelope, in terms of preventing the propeller pitch control activation.

2. Development of gain scheduling algorithm aiming at the prevention of the propeller pitch control activation.

The structure of this Chapter, following the above mentioned approach in order to achieve the refinement of the Diesel engine's dynamic response in the engine envelope is presented below:



- Formulation of the engineering problem into a mathematical problem. This step involves quantifying the problem, by expressing the main goal of the thesis in mathematical terms. This requires the selection of suitable mathematical function, which has to be optimised;minimised or maximised. This mathematical function is called *objective function*.

- Derivation of contour plots in MATLAB. They demonstrate the potential improvement regarding the selected objective function.

  – Verification of the results of derived contour plots by applying them in the non-linear ship propulsion model, which was derived in Chapter 3.

- Initialise the gains scheduling algorithm. Given that the engineering problem has been put in a mathematical framework, the properties of the established optimisation problem are studied. Then, a proper metaheuristic method is selected to provide solution to the problem within acceptable time limits. Initialisation addresses the selection of the values of control parameters for the chosen metaheuristic method.

- Evaluation of gains scheduling algorithm in:

  – Regular waves.

  – Irregular waves.

## 6.2. PROBLEM FORMULATION

This thesis addresses the issue of the decrease of the average maximum ship speed, which has to be attained especially in case of speed trials, due to the activation of propeller pitch control, when the vessel sails in waves. As it was stated in Section 1.4, this work deals with this problem by investigating the possibilities to re-size and re-orientate the elliptic trajectory of the engine operating point, in such way that **the operating ellipse does not touch the limits of the engine operating envelope** and thus, **the propeller pitch control remains deactivated**. The re-sizing and re-orientating of the operating ellipse is attempted by means of tuning the Diesel engine governor gains.

Regarding the approach of tuning the governor gains, aiming to re-size and re-orientate the elliptic trajectory of the engine operating point, this follows from the linear model and its Bode plots derived in Chapter 4. The State-Space system given by Eq. (4.51) depends on the values of the gains of the PID controller, $K_p$ and $K_i$, as it is described in Section 4.5. As a consequence of the dependence of the State-Space model on $K_p$ and $K_i$, the Bode plots, which are derived based on the State-Space system, will similarly be dependent on gain settings $K_p$ and $K_i$. In other words, different combination of values of the PID gains lead to different Bode plots. Furthermore, according to the formulas derived in Section 5.2.1, the Bode plots govern the geometric properties of the elliptic trajectory of the engine operating point in the engine envelope due to a sinusoidal wake disturbance. Consequently, the geometric properties are affected by the governor settings, $K_p$ and $K_i$.



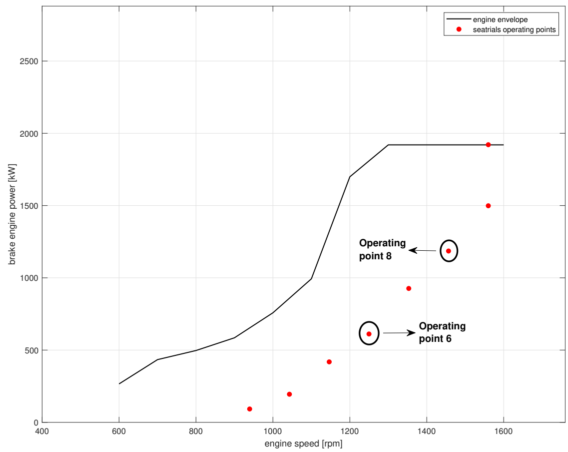


Figure 6.1: Operating point 6 and Operating point 8 under examination on the engine's operating line.

In Chapter 4, the linear ship propulsion system model was derived and verified. In Chapter 5, it was demonstrated that based on the linear ship propulsion model and on the Bode plots, the elliptic trajectory of the engine operating point, due to a sinusoidal wakefield disturbance, can be determined. More specifically, as it was shown in Section 5.2.1, starting from the Bode plots the geometric properties of the operating ellipse like the orientation, Eq. 5.16, and the size of its semi minor axis, Eq. 5.19 and semi major axis, Eq. 5.20, can be determined. Provided that these fundamental geometric properties as well as the canonical form of the ellipse formula, Eq. (5.18), are known, further geometric properties, which are related to the limits of the engine operating envelope, can be defined.

Taking into account all the above mentioned, there are several geometric properties that could be defined as the objective function of an algorithm, aiming to re-size and re-orientate the operating ellipse avoiding its contact with the engine envelope. The following three which are presented below are the ones which were examined within this thesis. However, only the third one proved to be able to meet the requirements and thus, it is used as the objective function of the metaheuristic algorithm in the gains scheduling algorithm. At this point it should be mentioned that the attempt to re-size and re-orientate the elliptic trajectory refers to two engine operating points, which are clearly illustrated in Figure 6.1. Apparently the limits for each one of the two points under examination are different in terms of their position with respect to the engine operating envelope limits. Consequently, this fact leads to diversity in the way that the geometric properties have to be defined and used, in order to achieve the goal which is the prevention of any contact between the operating ellipse and the engine envelope lines.

6

### 6.2.1. Angle of Rotation

As far as the **angle of rotation** criterion is concerned, the formula calculating the angle of rotation of the semi-major axis the elliptic trajectory is given by Eq.(5.16) and is depicted in Figure 6.2. Given the formula calculating the angle of rotation of the semi-major axis, one could seek the combination of controller settings which results in an angle of rotation whose value would be the same as the slope of the engine envelope line, which is closest to the ellipse and as a result the ellipse has the highest possibility to touch. In that way it is attempted to make the major axis of the ellipse parallel to the straight line under study. Therefore, the contact of the operating ellipse with the line of the engine envelope can be avoided, as depicted in

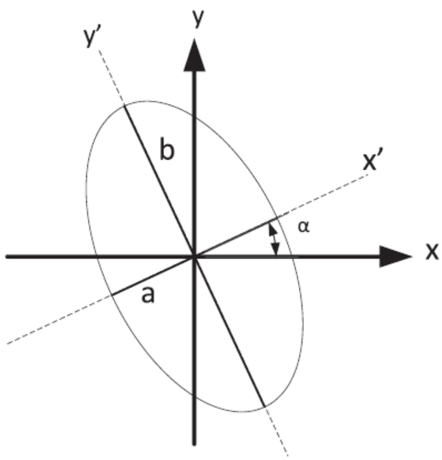


Figure 6.2: Operating ellipse angle of rotation.

Figure 6.3 . An objective function based on this criterion could be formulated as below:

$$Z = \quad \text{minimize}\left\{\text{Difference = slope of line - angle of rotation of ellipse semi-major axis}\right\} \tag{6.1}$$

Obviously, as it was mentioned before, depending on the operating point under study each time, the line of the engine envelope that needs to be avoided changes. This means that the slope of the line that has to be compared to the angle of rotation of the ellipse semi-major axis, similarly, changes. Despite the fact that according to Figure 6.3 the approach of minimising the difference between the slope of the line of the engine envelope and the angle of rotation of the ellipse semi-major axis could lead to the desired result, the possibility of getting results like those shown in Figure 6.4, points out the inadequacy of this criterion to prevent any contact between the operating ellipse and the engine envelope limits. In this case, regardless the minimisation of the difference between the slope of the line of the engine envelope and the angle of rotation of the ellipse semi-major axis, the operating ellipse with the dashed line still touches the limits of the engine operating envelope. This is because of the fact that the size of both the major and minor axis of the ellipse increases. Thus, the use of this geometric property as the objective function is rejected.



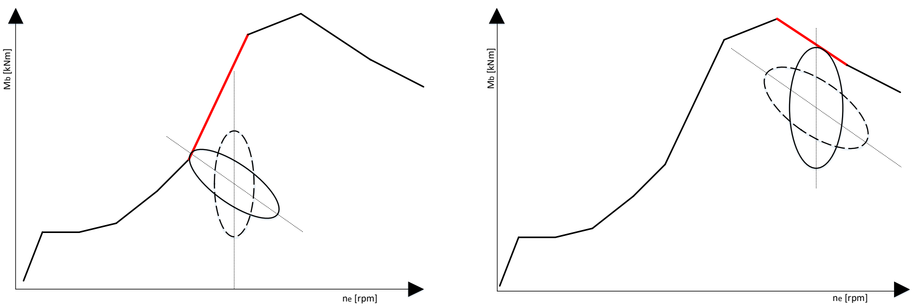


(a) Operating point 6 (b) Operating point 8

Figure 6.3: Angle of rotation criterion in engine envelope with the ellipse not touching the limits.

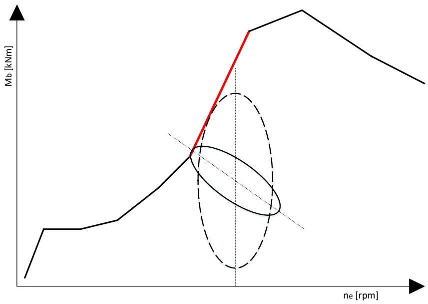


(a) Operating point 6

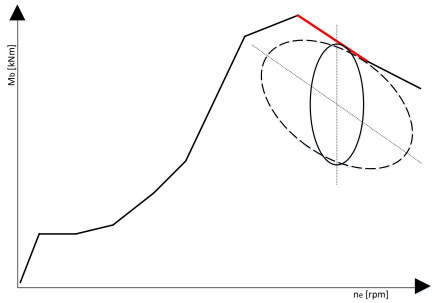


(b) Operating point 8

Figure 6.4: Angle of rotation criterion in engine envelope, with the ellipse touching the limits.

### 6.2.2. Area of Ellipse

As far as the **area of an ellipse** criterion is concerned, the formula calculating this geometric property is given below:

$$A = \pi ab \tag{6.2}$$



where:

$a$ :size of the first semi axis [m]
$b$ :size of the second semi axis [m]

The size of the first and second semi axes are given in Eq. (5.19) and Eq. (5.20) respectively. Given the formula calculating the area of the elliptic trajectory of the operating point, one could seek the combination of governor gains which results in the minimum possible area of the elliptic trajectory of the engine operating point. In that way it is attempted to prevent any contact between the operating ellipse and the limits of the engine operating envelope as illustrated in Figure 6.5. An objective function based on this criterion could be the one formulated below:

$$Z = \quad \text{minimize}\{A = \pi ab\} \tag{6.3}$$

Despite the fact that according to Figure 6.5 the approach of minimising the area of the elliptic trajectory of the engine operating point could be beneficial in terms of avoiding any contact between the ellipse and the limits of the engine operating envelope, a possible occasion like the one illustrated in Figure 6.6 highlights the existing possibility for this criterion to fail preventing any contact between the operating ellipse and the limits of the engine envelope. As it is shown in Figure 6.6, the area of the operating ellipse with the dashed line is smaller than the area of the operating ellipse with solid line. Nevertheless, the combination of settings of the controller results in an operating ellipse with smaller area but with long enough major axis with the ellipse still touching the lines of the engine envelope. Consequently, the criterion of the area of the operating ellipse is considered insufficient to prevent any contact between the operating ellipse and the lines of the engine envelope.

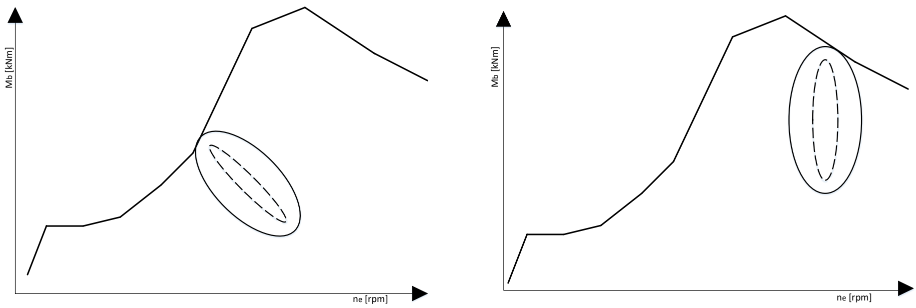


(a) Operating point 6 (b) Operating point 8

Figure 6.5: Area of ellipse criterion in engine envelope, with the ellipse not touching the limits.

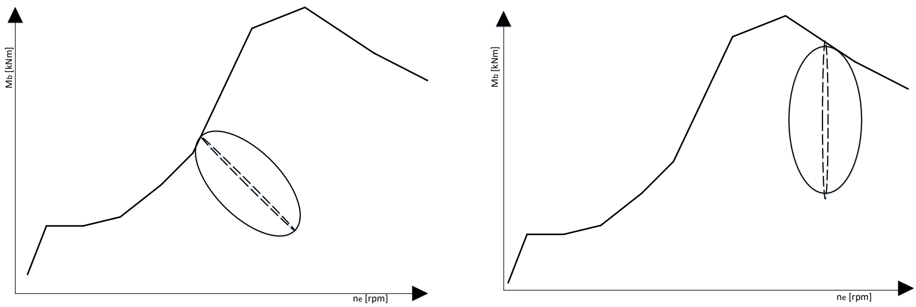


(a) Operating point 6 (b) Operating point 8

Figure 6.6: Area of ellipse criterion in engine envelope, with the ellipse touching the limits.

### 6.2.3. SHORTEST DISTANCE BETWEEN AN ELLIPSE AND A STRAIGHT LINE

As far as the **shortest distance between an ellipse and a straight line** criterion is concerned, the procedure in order to calculate this geometric property, when the mathematical formulas of the ellipse and the straight line are known, is extensively presented in Appendix B. Since the shortest distance between an ellipse and a straight line is determined, one could seek the combination of gains of the Diesel engine's governor which maximises the shortest distance between the elliptic trajectory of the engine operating point and the line of the engine envelope under consideration and thus prevents the contact between the ellipse and the engine envelope. The line with which the contact needs to be avoided, depends on the examined operating point each time and it is the one which is closer to the operating ellipse under study. This is clearly depicted in Figure 6.7. An objective function based on this criterion could be formulated as below:

$$Z = \text{mazimize}\left\{\text{Shortest Distance between operating ellipse and engine envelope line}\right\} \tag{6.4}$$

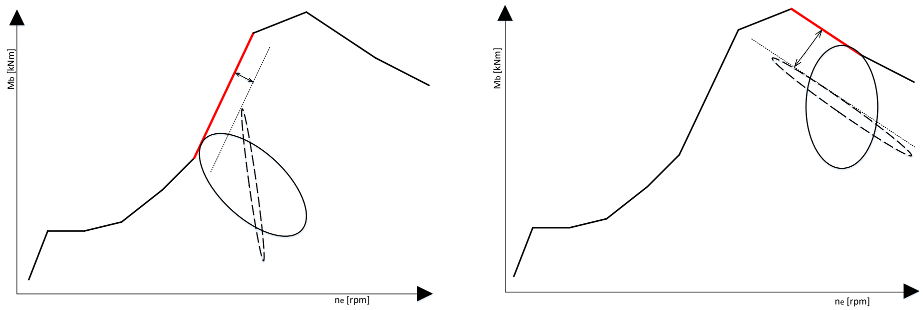


(a) Operating point 6 (b) Operating point 8

Figure 6.7: Shortest distance between ellipse and line criterion in engine envelope.



Compared to the two above mentioned criteria, the ellipse angle of rotation and the area of ellipse, the shortest distance between an ellipse and a straight line ensures that the elliptic trajectory does not touch the limits of the engine envelope in any case. This is provided by the geometric property itself, since at its definition it is assumed that there is a minimum distance between the elliptic trajectory of the engine operating point and the line of the engine envelope which is closer to the ellipse. By attempting the maximisation of the shortest distance between the operating ellipse and the line, the optimum combination of $K_p$ and $K_i$ is attempted to be found, assuring the fact that the ellipse lies as far away as possible from the line of the engine envelope.

*For this reason, the geometric property of the shortest distance between an ellipse and a straight line is selected as the suitable criterion in order to prevent any contact between the operating ellipse and the engine operating envelope limits and consequently the activation of the propeller pitch control.*

At this point, it should be stressed out that most likely the implementation of multiobjective optimisation will lead to an even better results with respect to the ultimate goal which is the prevention of any contact between the elliptic trajectory of the engine's operating point and the engine envelope line. More specifically, the implementation of two geometric criteria could ensure that there will be no contact between the operating ellipse and the engine envelope lines, leading at the same time to an improved dynamic behaviour of the operating ellipse in the engine envelope in terms of less excursions in the direction of engine speed and engine torque. This could happen by employing for instance the criterion of shortest distance between an ellipse and a straight line and the criterion of area of an ellipse. However, this would come at the cost of a more complicated optimisation problem. This case is not investigated in this thesis as it lies out of its scope.

### OPERATING POINT 6

As it was previously mentioned, the geometric property of the shortest distance between an ellipse and a straight line is the criterion which is applied in order to determine the combination of governor gains for which the elliptic trajectory of the engine operating point does not touch the limits of the engine envelope. The mathematical formulas calculating the shortest distance between an ellipse and a straight line are extensively described in Appendix B. In this section only the determination of the straight line, as the limit which has to be avoided, is presented.

In the direction of applying the criterion, it should to be taken into account that there are two examined operating points, operating point 6 and 8, as shown on the engine operating line in Figure 6.1. In terms of that, the line which needs to be avoided has to be separately and specifically defined for each operating point.



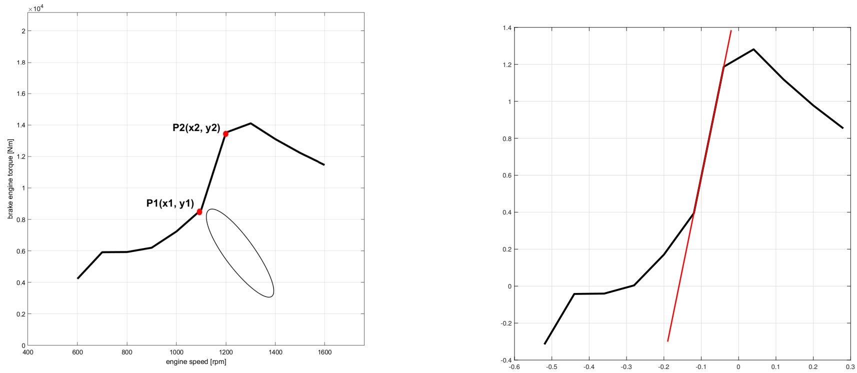


(a) Two points passing through the line that needs to be avoided.

(b) Highlighted straight line to be avoided.

Figure 6.8: Determination of the line to avoid in engine envelope for operating point 6.

As far as Operating point 6 is concerned, the limits of the engine envelope that has to be avoided is the part of the engine envelope that is closer to the elliptic trajectory of the engine operating point and consequently has the highest possibilities to touch the operating ellipse. By plotting the elliptic trajectory of the engine operating point 6 caused by a sinusoidal wake disturbance, as shown in Figure 6.8, the part of the engine envelope curve that has to be avoided can be determined. The straight line that has to be avoided is illustrated in Figure 6.8b. Given two points of the engine envelope curve, as depicted in Figure 6.8a, the equation of the of straight line is given by the following equation:

$$\left.\begin{array}{l} P_1(x_1, y_1) \\ P_2(x_2, y_2) \end{array}\right\} \implies \frac{y - y_1}{y_2 - y_1} = \frac{x - x_1}{x_2 - x_1} \tag{6.5}$$

In that way, the parameters of the general equation of a straight line, as given in literature, $Ax + By + C = 0$, can be determined. Once they are defined, the procedure described in Appendix B can be followed to calculate the shortest distance between the operating ellipse and the line of the engine envelope.

## OPERATING POINT 8

As far as Operating point 8 is concerned, the limits of the engine envelope that has to be avoided is the part of the engine envelope curve that is closer to the elliptic trajectory of the engine operating point and therefore has the highest possibilities to touch the operating ellipse. By plotting the elliptic trajectory of the engine operating point 8 caused by a sinusoidal wake disturbance, as depicted in Figure 6.9, the part of the engine envelope curve that has to be avoided can be determined. By locating the necessary points on this part of the curve, the straight line that will be used in the shortest distance between an ellipse and a line criterion can be defined using methods that fit linear polynomial curve to given points in Matlab.

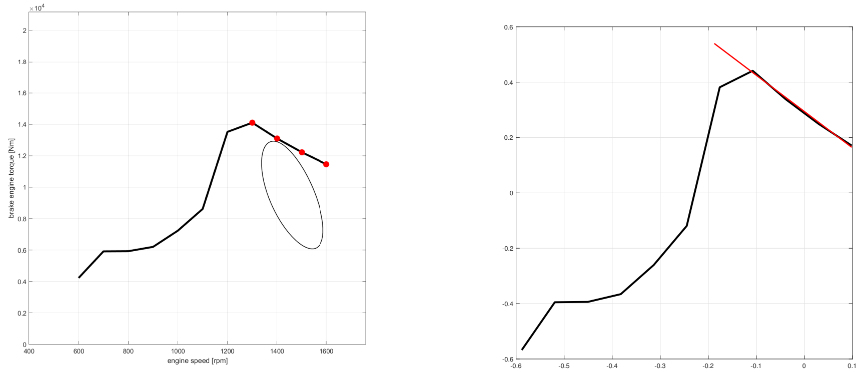


(a) Points passing through the line that needs to be avoided.

(b) Highlighted straight line to be avoided

Figure 6.9: Determination of the line to be avoided in engine envelope for operating point 8.

Following that the method the parameters of the general equation of a straight line as given in literature, $Ax + By + C = 0$, can be determined. Once these parameters are determined, the process described in Appendix B can be followed in order to calculate the shortest distance between the elliptic trajectory of the engine operating point and the straight line approximating the curve of the engine envelope.

### 6.2.4. INFEASIBLE SOLUTIONS

At this point it should be mentioned that there is a special group of results regarding of the solutions of the gains scheduling algorithm, the maximum shortest distance between the operating ellipse and the straight line of the engine operating envelope for both Operating point 6 and 8 which are considered infeasible and should be rejected. In some cases the gains scheduling algorithm, attempting to determine the maximum shortest distance between the elliptic trajectory of the engine operating point and the engine envelope, comes up with solutions in which the resulting operating ellipse intersects the engine envelope due to the fact that the algorithm is not able to realise that the operating ellipse is already in contact with the engine envelope (intersection points). In that case the algorithm assumes that the tangents on the ellipse, which are parallel to the engine envelope, still have a distance from it which can be determined. A typical case like this is illustrated in Figure 6.10.

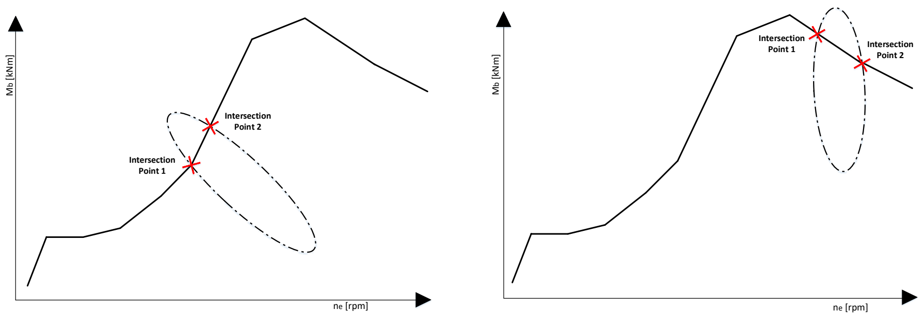


(a) Example for operating point 6.

(b) Example for operating point 8.

Figure 6.10: Examples of rejected solutions in case of intersection between operating ellipse and engine envelope line.

This phenomenon is attributed to the properties of the linear model. As it was mentioned in Section 4.2, during the linearisation process of the original non-linear ship propulsion model some of the non-linearities are neglected. These non-linearities are presented in Section 4.2. The third non-linearity presented in Section 4.2 refers to hard limits that exist in the non-linear model but they are neglected in the linear model. Such kind of limitation is the engine envelope, operating as protective feature in the engine governor(detailed description of engine's governor structure in Section 3.3.2). The limitation of the engine envelope is neglected in the linear model, leading the gains scheduling algorithm to solutions in which the resulting operating ellipse intersects the engine envelope lines. More specifically, when the combination of controller settings, which is the solution of the algorithm, is applied back to the non-linear model, the occurred elliptic trajectory of the engine operating point touches the line of the engine envelope, instead of lying in distance from the engine's limit as it should be (gains scheduling algorithm objective). This kind of solutions can not be accepted and consequently have to be filtered and rejected by the algorithm itself. The methodology integrated in the gains scheduling algorithm in order to force it reject such kind of solutions is described in details in Section B.3 in the Appendix B.

## 6.3. Contour Plots

According to the followed approach, which aims to achieve the refinement of the Diesel engine dynamic response, as it is presented in Section 6.1, as a first step contour plots derived in Matlab will be used in order to confirm the potential improvement of the dynamic behaviour of the engine operating point.

Contour plots of the shortest distance between the operating ellipse and the engine envelope limits, using as independent variables the PID controller gains $K_p$ and $K_i$, are derived in Matlab. These contour plots demonstrate the opportunities for further enhancement of the shortest distance between the operating ellipse and the limits of the engine envelope by employing different combinations of controller settings from those currently used.



The input acting on the linear model causing the elliptic trajectory of the engine operating point is sinusoidal wakefield disturbance (regular wave). A range of different wave frequencies for the wake disturbance is applied. Based on the results of [Vrijdag and Stapersma, 2017] for several combinations of PID gains, it is confirmed that low wave frequencies, ($\omega \simeq 0.1$rad/s), lead to more vertically oriented operating ellipses, whereas higher wave frequencies, ($\omega \simeq 5$rad/s), result in anticlockwise rotated operating ellipses. Following these findings and taking into account the shape of the engine envelope and the location of the engine operating points under study in the engine envelope, Figure 6.1, it can be concluded that low wave frequencies are more critical for Operating point 8. On the other hand, higher wave frequencies are more critical for Operating point 6. Therefore, a range of five different wave frequencies of the sinusoidal wake disturbance is examined, with the amplitude of the disturbance being constant. In that way, the level of improvement that can be achieved, compared to the currently used controller settings, will be illustrated.

### Operating Point 6

As mentioned before, the contour plots for the shortest distance between the operating ellipse and the limits of the engine operating envelope are derived in MATLAB. In this Section Operating point 6 is under study. Five wave frequencies of the wakefield disturbance acting on the linearised ship propulsion system are investigated, with the amplitude of the wakefield disturbance being constant. The derived contour plot for each wave frequency is presented. The value of the shortest distance for the current values of the governor settings together with the new gains leading to higher values of the shortest distance between the operating ellipse and the limits of the engine envelope are given in tables, as Table 6.1, where:

| | |
|---|---|
| $K_{p_c}$ | :currently used proportional gain |
| $K_{i_c}$ | :currently used integral gain |
| $s.d._c$ | :shortest distance between the operating ellipse and the engine envelope limits for currently used gains |
| $K_{p_n}$ | :new proportional gain |
| $K_{i_n}$ | :new integral gain |
| $s.d._n$ | :shortest distance between the operating ellipse and the engine envelope limits for new gains |
| $\delta s.d.$ | :percentage change of s.d. given by $\delta s.d. = [(s.d._n - s.d._c)\,/\,s.d._c] \cdot 100$ |

Additionally, the values of the currently used governor gains as well as the values of gains leading to the maximum shortest distance according to the derived contour plots, are applied to the non-linear ship propulsion system model which is presented in Chapter 3. The elliptic trajectories of the engine operating point in the engine envelope resulting from the two different combinations of governor settings, applied in the non-linear model, are presented below. In that way, it is confirmed that the conclusions drawn from the contour plots derived by employing the linear model can be applied in the non-linear model, giving the expected results. This step is significant in terms of verifying the conclusions drawn by the use of the linear model since, as it was previously mentioned, the linear model is considered as an additional tool to the non-linear model which is the only one capable of capturing the real phenomena taking place in a propulsion plant in operation.

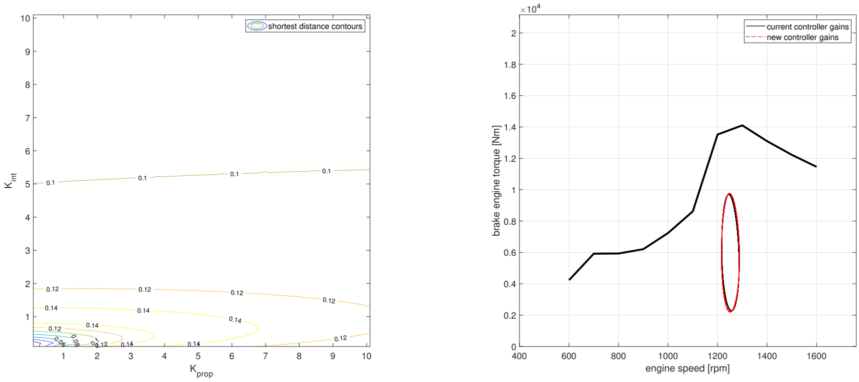

(a) Shortest distance contour plot (b) Elliptic trajectories of engine operating point

Figure 6.11: Contour plot and operating ellipses for current and new governor gains for $\omega = 0.1$ rad/s at operating point 6.

| $\omega = 0.1$ [rad/s], $\delta w^* = 0.4$, operating point 6 | | | | | | |
|---|---|---|---|---|---|---|
| $Kp_c$ | $Ki_c$ | $s.d._c$ | $Kp_n$ | $Ki_n$ | $s.d._n$ | $\delta s.d.$ [%] |
| 2 | 1.2 | 0.143 | 0.5 | 1.2 | 0.1437 | 0.5 |



Table 6.1: Current, new governor settings and corresponding shortest distances for $\omega =$ 0.1 rad/s at **operating point 6**.

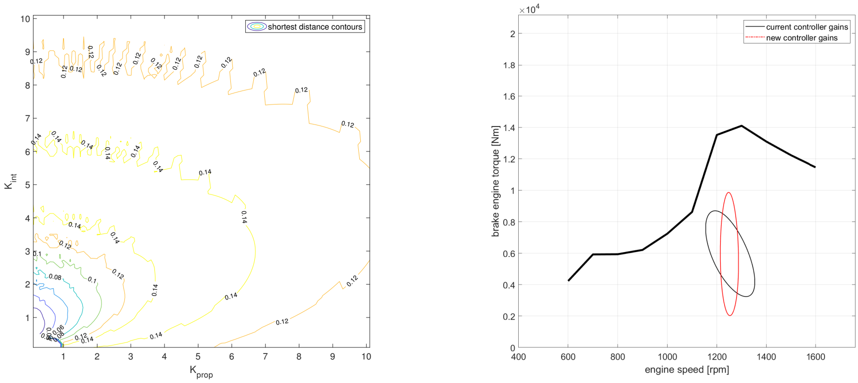

(a) Shortest distance contour plot (b) Elliptic trajectories of engine operating point

Figure 6.12: Contour plot and operating ellipses for current and new governor gains for $\omega = 0.5$ rad/s at operating point 6.

| $\omega = 0.5$ [rad/s], $\delta w^* = 0.4$, operating point 6 | | | | | | |
|---|---|---|---|---|---|---|
| $Kp_c$ | $Ki_c$ | $s.d._c$ | $Kp_n$ | $Ki_n$ | $s.d._n$ | $\delta s.d.$ [%] |
| 2 | 1.2 | 0.1005 | 1 | 6.1 | 0.1369 | 36.2 |

Table 6.2: Current, new governor settings and corresponding shortest distances for $\omega =$ 0.5 rad/s at **operating point 6**.

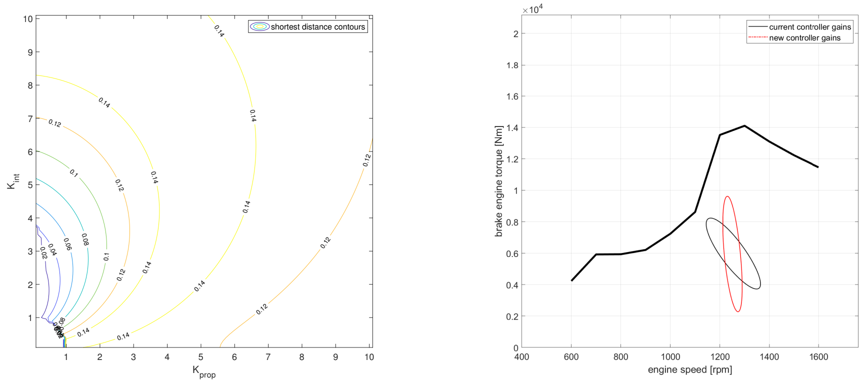


(a) Shortest distance contour plot (b) Elliptic trajectories of engine operating point

Figure 6.13: Contour plot and operating ellipses for current and new governor gains for $\omega = 1$ rad/s at operating point 6.

| $\omega = 1$ [rad/s], $\delta w^* = 0.4$, operating point 6 | | | | | | |
|---|---|---|---|---|---|---|
| $K_{p_c}$ | $K_{i_c}$ | $s.d._c$ | $K_{p_n}$ | $K_{i_n}$ | $s.d._n$ | $\delta s.d.$ [%] |
| 2 | 1.2 | 0.1238 | 6.1 | 8.8 | 0.1396 | 12.76 |



Table 6.3: Current, new governor settings and corresponding shortest distances for $\omega = 1$ rad/s at **operating point 6**.

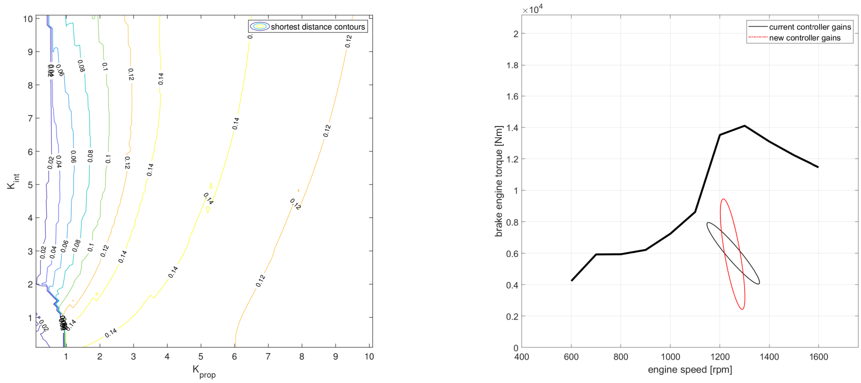


(a) Shortest distance contour plot (b) Elliptic trajectories of engine operating point

Figure 6.14: Contour plot and operating ellipses for current and new governor gains for $\omega = 2$ rad/s at operating point 6.

| $\omega = 2$ [rad/s], $\delta w^* = 0.4$, operating point 6 | | | | | | |
|---|---|---|---|---|---|---|
| $K_{p_c}$ | $K_{i_c}$ | $s.d._c$ | $K_{p_n}$ | $K_{i_n}$ | $s.d._n$ | $\delta s.d.$ [%] |
| 2 | 1.2 | 0.14 | 6.4 | 9.8 | 0.1409 | 0.64 |

Table 6.4: Current, new governor settings and corresponding shortest distances for $\omega = 2$ rad/s at **operating point 6**.

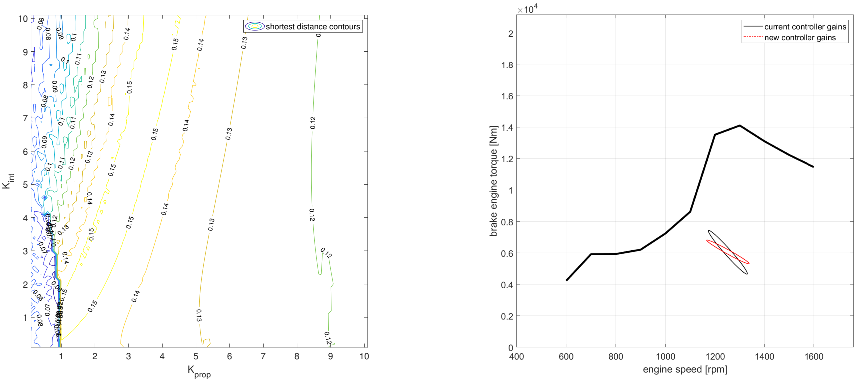


(a) Shortest distance contour plot

(b) Elliptic trajectories of engine operating point

Figure 6.15: Contour plot and operating ellipses for current and new governor gains for $\omega = 5$ rad/s at operating point 6.

| $\omega = 5$ [rad/s], $\delta w^* = 0.4$, operating point 6 | | | | | | |
|---|---|---|---|---|---|---|
| $K_{p_c}$ | $K_{i_c}$ | $s.d._c$ | $K_{p_n}$ | $K_{i_n}$ | $s.d._n$ | $\delta s.d.$ [%] |
| 2 | 1.2 | 0.1493 | 1 | 0.5 | 0.152 | 1.8 |

Table 6.5: Current, new governor settings and corresponding shortest distances for $\omega = 5$ rad/s at **operating point 6**.

Closer inspection of the above presented in Figures 6.11 - 6.15 and Tables 6.1 - 6.5 confirms that:

- multiple combinations of controller settings can lead to larger shortest distance between the operating ellipse and the engine envelope compared to the currently used governor settings.
- for the wave frequency of $\omega = 0.1$ rad/s, the margin for improvement is negligible since the operating ellipse for the currently used governor gains is already vertical and the line of the engine envelope lies on the left hand side of the ellipse.
- for the wave frequency of $\omega = 0.5$ rad/s, there is a significant margin of improvement, since the operating ellipse of the currently used gains is anticlockwise rotated (towards the engine envelope line) with larger size, compared to the operating ellipse of the new gains which is more vertically oriented with remarkably less excursions in speed direction and slightly more in torque direction. This is aligned with the findings of [Vrijdag and Stapersma, 2017], which suggest that for wave frequency of $\omega \simeq 0.5$ rad/s and high value of $K_p$ and $K_i \simeq 0$ the generated operating ellipse tends to get a more vertical orientation being almost collapsed to an operating line.
- for the following two wave frequencies, there is some margin of improvement which is less compared to the previously examined wave frequency. This margin of im-

provement is gradually reduced as the wave frequency of the disturbance increases. Despite the fact that the operating ellipse generated by the currently used gains remains to be anticlockwise rotated, the size is reduced due to the "low pass"filter action of the shaft inertia and its associated integrator between the wake disturbance and its effect on the Diesel engine. Consequently, high frequency disturbances do not affect the engine that much, resulting in small fluctuations of engine speed and brake engine torque.

## OPERATING POINT 8

Similarly to operating point 6, contour plots of the shortest distance as well as the resulting elliptic trajectories of the engine operating point of currently used and new governor gains are presented for operating point 8.

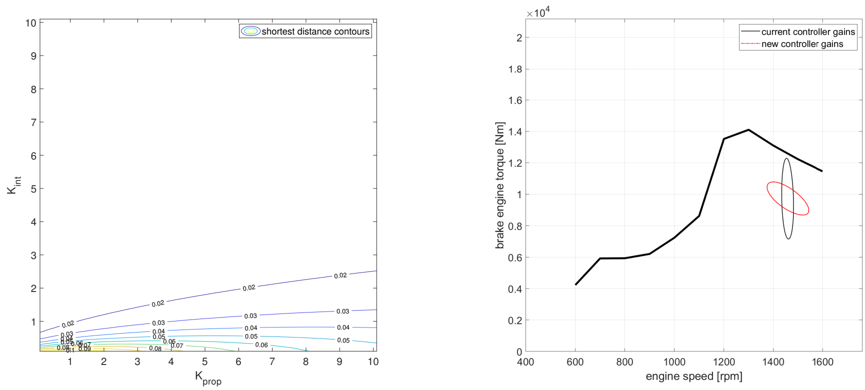


(a) Shortest distance contour plot (b) Elliptic trajectories of engine operating point

Figure 6.16: Contour plot and operating ellipses for current and new governor gains for $\omega = 0.1$ rad/s at operating point 8.

| $\omega = 0.1$ [rad/s], $\delta w^* = 0.2$, operating point 8 | | | | | | |
|---|---|---|---|---|---|---|
| $K_{p_c}$ | $K_{i_c}$ | $s.d._c$ | $K_{p_n}$ | $K_{i_n}$ | $s.d._n$ | $\delta s.d.$ [%] |
| 2 | 1.2 | 0.02001 | 1 | 0.1 | 0.1093 | 446.23 |

Table 6.6: Current, new governor settings and corresponding shortest distances for $\omega$ = 0.1 rad/s at **operating point 8**.

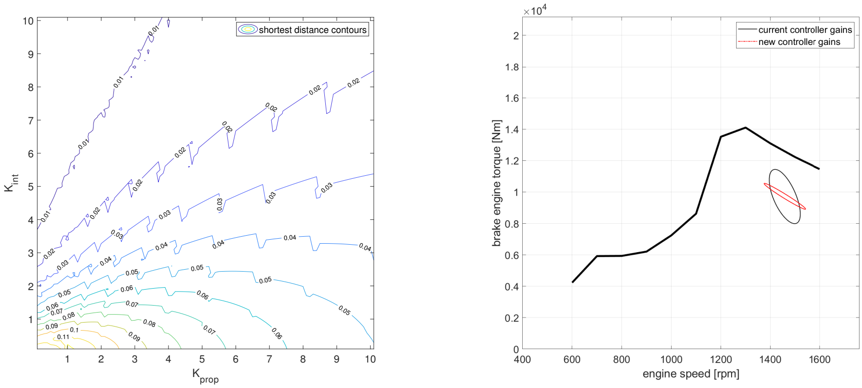


(a) Shortest distance contour plot (b) Elliptic trajectories of engine operating point

Figure 6.17: Contour plot and operating ellipses for current and new governor gains for $\omega = 0.5$ rad/s at operating point 8.

| $\omega = 0.5$ [rad/s], $\delta w^* = 0.2$, operating point 8 | | | | | | |
|---|---|---|---|---|---|---|
| $Kp_c$ | $Ki_c$ | $s.d._c$ | $Kp_n$ | $Ki_n$ | $s.d._n$ | $\delta s.d.$ [%] |
| 2 | 1.2 | 0.08046 | 1.1 | 0.1 | 0.1215 | 51 |



Table 6.7: Current, new governor settings and corresponding shortest distances for $\omega =$ 0.5 rad/s at **operating point 8**.

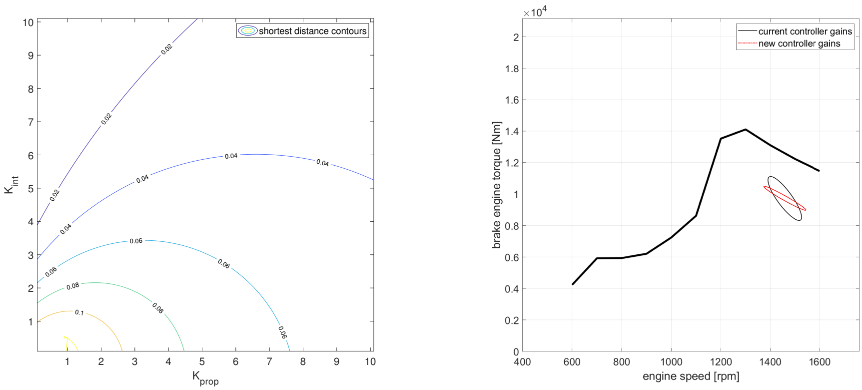


(a) Shortest distance contour plot (b) Elliptic trajectories of engine operating point

Figure 6.18: Contour plot and operating ellipses for current and new governor gains for $\omega = 1$ rad/s at operating point 8.

| $\omega = 1$ [rad/s], $\delta w^* = 0.2$, operating point 8 | | | | | | |
|---|---|---|---|---|---|---|
| $Kp_c$ | $Ki_c$ | $s.d._c$ | $Kp_n$ | $Ki_n$ | $s.d._n$ | $\delta s.d.$ [%] |
| 2 | 1.2 | 0.09872 | 1 | 0.2 | 0.1241 | 25.71 |

Table 6.8: Current, new governor settings and corresponding shortest distances for $\omega = 1$ rad/s at **operating point 8**.

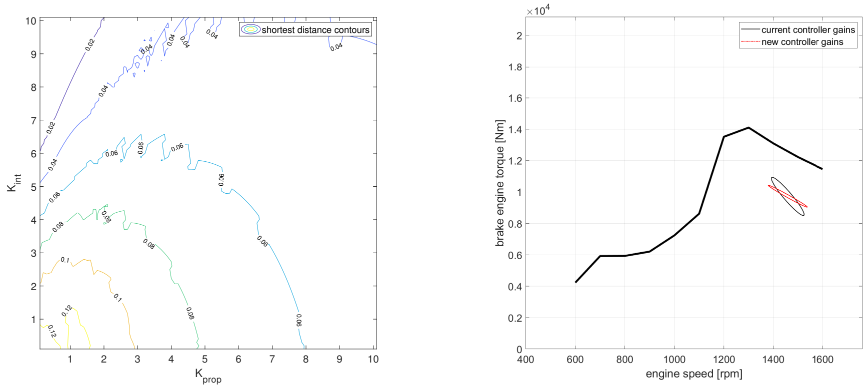


(a) Shortest distance contour plot (b) Elliptic trajectories of engine operating point

Figure 6.19: Contour plot and operating ellipses for current and new governor gains for $\omega = 2$ rad/s at operating point 8.

| $\omega = 2$ [rad/s], $\delta w^* = 0.2$, operating point 8 | | | | | | |
|---|---|---|---|---|---|---|
| $Kp_c$ | $Ki_c$ | $s.d._c$ | $Kp_n$ | $Ki_n$ | $s.d._n$ | $\delta s.d.$ [%] |
| 2 | 1.2 | (0.1, 0.12) | 1 | 0.2 | 0.1299 | (29.9, 8.25) |



Table 6.9: Current, new governor settings and corresponding shortest distances for $\omega = 2$ rad/s at **operating point 8**.

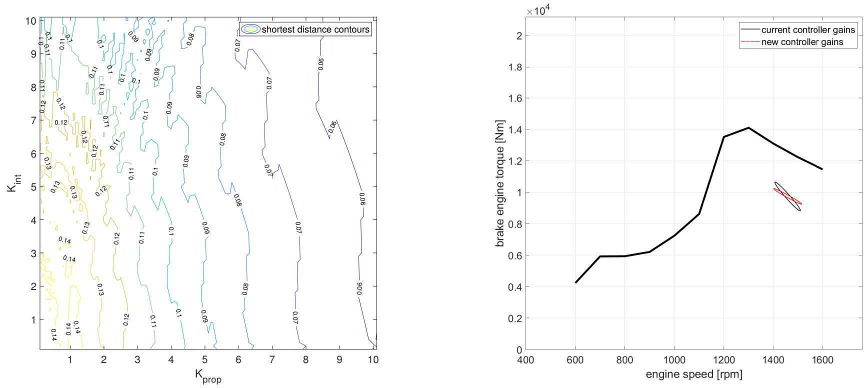


(a) Shortest distance contour plot (b) Elliptic trajectories of engine operating point

Figure 6.20: Contour plot and operating ellipses for current and new governor gains for $\omega = 5$ rad/s at operating point 8.

| $\omega = 5$ [rad/s], $\delta w^* = 0.2$, operating point 8 | | | | | | |
|---|---|---|---|---|---|---|
| $Kp_c$ | $Ki_c$ | $s.d._c$ | $Kp_n$ | $Ki_n$ | $s.d._n$ | $\delta s.d.$ [%] |
| 2 | 1.2 | 0.1277 | 1 | 0.4 | 0.1461 | 14.4 |

Table 6.10: Current, new governor settings and corresponding shortest distances for $\omega = 5$ rad/s at **operating point 8**.

Closer observation of Figures 6.16 - 6.20 and Tables 6.6 - 6.10 leads to the following findings:

- multiple combinations of controller settings can lead to better results in terms of the shortest distance between the operating ellipse and the engine envelope line compared to the currently used controller settings.
- taking into account the position of the examined operating point in the engine envelope, larger distance between the operating ellipse and the engine envelope line results in anticlockwise rotated operating ellipses. Apparently this means that the new operating ellipse has less engine torque fluctuations and more engine speed fluctuations compared to the operating ellipse of the currently used gains.
- for the majority of the wave frequencies examined here, it seems that the a value of the proportional gain around $K_p \simeq 1$ and the integral gain around $K_i \simeq 0.2$ seems to be suitable in order to increase the shortest distance between the operating ellipse and the engine limits. This is reasonable and in line with the findings in [Vrijdag and Stapersma, 2017] where it is illustrated that for a wide range of frequencies, gain values of $K_p \simeq 1$ and $K_i \simeq 0$ result in an anticlockwise rotated operating ellipse with a small-size first axis (Eq. (5.19)), which tends to collapse into a line. This has to be always considered in combination with the position of the examined operating point in the engine envelope. This position defines the desired orientation and size for the operating ellipse.
- the margin of improvement is remarkably high for the first examined wave frequency $\omega = 0.1$ rad/s but it is gradually decreased for the rest of the investigated frequencies. This is in line with the findings in [Vrijdag and Stapersma, 2017], where it is documented that in higher frequencies, $\omega > 0.1$ rad/s, the operating ellipse is anticlockwise rotated for a wide range of $K_p$ and $K_i$ used. Taking into account that at operating point 8, the objective is to rotate the ellipse anticlockwise as well as to reduce its size, it is expected that the opportunity to increase the shortest distance between the operating ellipse and the engine envelope limits, by using other values of $K_p$ and $K_i$, is significantly reduced as the frequency of the disturbance increases.

Taking into consideration both the derived contour plots as well as the implementation of their results in the non-linear ship propulsion system and the resulting elliptic trajectories of the engine operating point it is confirmed that there is the opportunity to increase the shortest distance between the operating ellipse and the engine envelope limits for a wide range of wave frequencies of the wakefield disturbance. The margin of improvement varies for each specific case in terms of the examined operating point and the wave frequency. Consequently, one could rightfully seek a different combination of governor settings to the one currently used, in order to prevent any contact between the elliptic trajectory of the engine operating point and the engine envelope limits in every different case regarding the operating point, the wave frequency and the amplitude of the wakefield disturbance. An attempt to dynamically schedule the gains of the governor according to the disturbance each time is presented in the following sections.

## 6.4. GOVERNOR GAINS SCHEDULING ALGORITHM

Taking into account the conclusion outlined in the previous section, in this Section the establishment of a process, which will give the governor of the non-linear ship propulsion system model the ability to schedule its gains according to the operating point and the wakefield disturbance acting on the model each time, is attempted.

The issue of increasing the shortest distance between the elliptic trajectory of the engine operating point and the engine envelope limits, aiming to prevent any contact between them is addressed by the development of a simple gains scheduling algorithm. This gains scheduling algorithm is capable of finding the combination of governor gains $K_p$ and $K_i$ (optimum combination or near to optimum combination) which increases (maximises or nearly maximises) the shortest distance between the operating ellipse and the engine envelope line, ensuring that there will not be any contact between these two. The gain scheduling depends on the operating point as well as the parameters of the wakefield disturbance acting on the model. This means that the values of the controller settings are not constant and predefined, the selection of which is for instance based on contour plots, like those presented in the previous Section. The gains vary according to the operating point and the disturbance input (wakefield disturbance) and they are each time rescheduled, seeking the combination of $K_p$ and $K_i$ which results in an operating ellipse with the maximum shortest distance from the engine envelope line. The search of the optimum or close-to-optimum combination of governor gains to achieve this, is attempted by employing a metaheuristic method for hard optimisation problems.

Due to an impressive research on the topic of difficult optimisation problems, a significant number of developed techniques, capable of finding the optimum or quite-close-to-optimum solutions to this kind of problems, can be found in literature [Dréo et al., 2006, Hillier, 2012]. The four most widely known metaheuristics are:

- the simulated annealing method
- the tabu search
- the genetic and evolutionary algorithms
- the ant colony algorithms

The one applied in the gains scheduling algorithm developed in this work is the **simulated annealing**. A detailed presentation of the simulated annealing method is given in Appendix C.

The starting point of this gains scheduling algorithm is the linearised ship propulsion system model as it was presented in Section 4.5 in its State-Space form. The linear model as described in Eq. (4.51) together with the corresponding Bode plots of $\delta n^* / \delta w^*$ and $\delta M_b^* / \delta w^*$ are derived. Based on these necessary tools and taking into consideration the sinusoidal wakefield disturbance under study in each case (different amplitude and wave frequency of the disturbance), the elliptic trajectory of the engine operating point in the engine envelope is determined (Section 5.2.1). Using the equation of the operating ellipse and the equation of the engine envelope line, the shortest distance between these two is calculated following the process described in Section B.2. Applying the simulated annealing method, the above described procedure is executed iteratively for numerous combinations of governor gains,$K_p$ and $K_i$ of which the set of values is predefined, aiming to find the one which leads to the maximum shortest distance between the elliptic trajectory of the engine operating point and the corresponding engine envelope line. In that way it is guaranteed that the operating ellipse lies in a distance from the engine envelope limits preventing any contact between these and consequently avoiding the activation of the propeller pitch controller. It goes without saying that solutions like these presented in Section 6.2.4 are rejected in the algorithm following the procedure presented in Section B.3. The objective of the gains scheduling algorithm, as a mathematical optimisation problem, $\mathscr{P}$, can be formulated as below:

$$\mathscr{P} = \begin{cases} \underset{K_p, K_i}{\text{maximize}} \quad s.d.\left(K_p, K_i\right) = \min\left(d_1 = \dfrac{\left|Ax_1 + By_1 + C\right|}{\sqrt{A^2+B^2}}, d_2 = \dfrac{\left|Ax_2 + By_2 + C\right|}{\sqrt{A^2+B^2}}\right) \\ \text{subject to:} \quad x_{i.p.} = \left[x_{i.p._1}\left(K_p, K_i\right), x_{i.p._2}\left(K_p, K_i\right)\right] \notin \mathbb{R}, \\ \qquad\qquad\quad K_p, K_i \in [0.1 : 0.1 : 10]. \end{cases} \tag{6.6}$$

where:

| | |
|---|---|
| $K_p, K_i$ | :proportional and integral gain of engine governor |
| $s.d.$ | :shortest distance between operating ellipse and engine envelope line for $\left(K_p, K_i\right)$ |
| $d_1, d_2$ | :the distances of two points, $P\left(x_1, y_1\right)$ & $P\left(x_2, y_2\right)$, lying on the ellipse, from the given engine envelope line. The tangents at these two points are parallel to the given line. The minimum of these two values is the distance to be maximised. |
| $x_{i.p._1}\left(K_p, K_i\right), x_{i.p._2}\left(K_p, K_i\right)$ | :intersection points between generated operating ellipse and engine envelope line |

Regarding the variables that are presented in the mathematical formulation of the optimisation problem solved by the gains scheduling algorithm, details with respect to the calculation of the two distances $d_1, d_2$, as well as the shortest distance between the generated operating ellipse and the engine envelope line, $s.d.$, are given in Section B.2. Moreover, the calculation of the two possible intersection points between the generated operating ellipse and the engine envelope line, $x_{i.p._1}\left(K_p, K_i\right), x_{i.p._2}\left(K_p, K_i\right)$, as well as the determination of the feasibility of the generated solution for each combination of governor gains, in terms of intersecting the engine envelope line or not, are extensively documented in Section B.3.

The flow chart and the structure of the general simulated annealing algorithm are presented in Section C.2. Additionally, the way that the involved control parameter, temperature T, is calculated is demonstrated in Section C.2. In this Section, the flow chart of the simulated annealing algorithm, adjusted to the specific problem, is presented below in Figure 6.21. At this point, it should be mentioned that parameter $N$ included in the flowchart below indicates the number of degrees of freedom of the problem under study. In this case, the governor gains are considered to be the degrees of freedom of the examined problem. Since the governor gains are two, $K_p$ & $K_i$, this means that $N$=2.

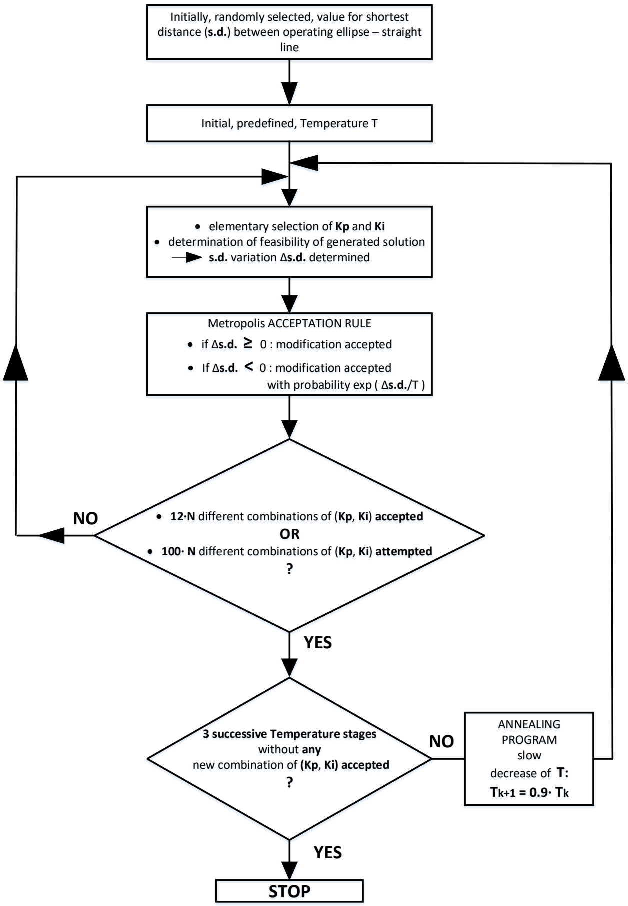


Figure 6.21: Flow chart of simulated annealing algorithm, adjusted to shortest distance between operating ellipse - line problem.

The developed gains scheduling algorithm is integrated in the governor block of the ship propulsion system simulation model as it is described in the scheme of Figure 6.22.

This Figure indicates that one of the essential input, required for the gains scheduling algorithm, is the parameters of the wakefield disturbance, acting on the propulsion system model, caused by the waves. These parameters have to be defined and provided in advance by the user as input data in case of the simulation model. On the other hand, in case of a real-time software tool, capable of dynamically determining the optimum (or close to optimum) combination of gains, $K_p$ & $K_i$, of the PID controller, the parameters of the wakefield disturbance should be defined after deterministically predicting the future encountering wave. This can be done by using for instance forward looking wave sensors, [Naaijen, 2017]. Thereafter, the calculated wakefield disturbance parameters, amplitude $\delta w^*$ and wave frequency $\omega$, have to be provided as input to the gain scheduling algorithm of the Diesel engine's algorithm.

### 6.4.1. Regular Waves

In this Section, the effectiveness of the algorithm in refining the dynamic behaviour of the elliptic trajectory of the engine operating point in the engine envelope is evaluated in case of regular waves.

Given that the gains scheduling algorithm is integrated in the non -linear model of the ship propulsion system, as depicted in Figure 6.22, it attempts to prevent any contact between the elliptic trajectory of the engine operating point and the engine envelope line by maximising its distance from the engine envelope limits. For the sinusoidal wakefield disturbances acting on the non-linear simulation model, three different wave frequencies are examined at both operating points 6 & 8 with the amplitude of the disturbance being $\delta w^* = 0.6$ and $\delta w^* = 0.25$ for the two operating points respectively.

In the following Figures, the elliptic trajectory of the engine operating point in the engine envelope is shown together with the time trace of wake disturbance, engine torque and engine speed signals. The compared results are generated for the currently used and the new combination of governor gains with the latter being determined by the gains scheduling algorithm. Additionally, the Bode plots of the shortest distance between the operating ellipse and the engine envelope line are generated based on the linear ship propulsion system model derived for the currently used and the combination of governor gains determined by the algorithm. Moreover, the reader should notice the different time scale between the different wave frequencies examined in the Figures below.

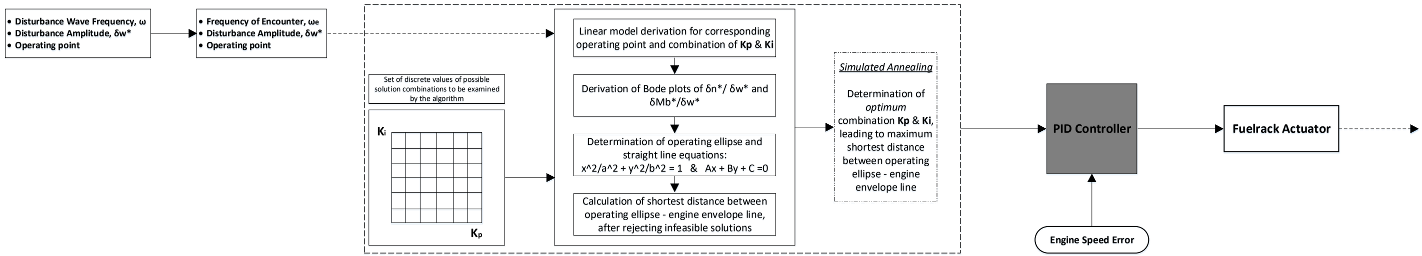


Figure 6.22: Governor layout with gains scheduling algorithm integrated in non-linear simulation model

6

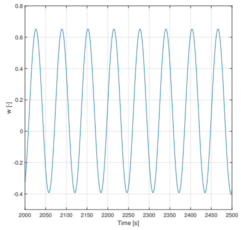


(a) Wake at operating point 6

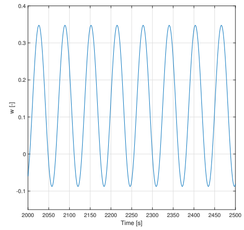


(b) Wake at operating point 8

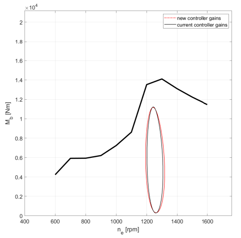


(c) Operating ellipse at operating point 6

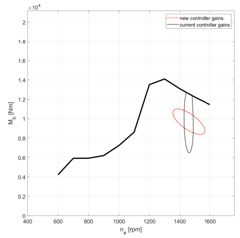


(d) Operating ellipse at operating point 8

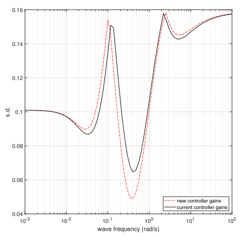


(e) Shortest distance in frequency domain at operating point 6

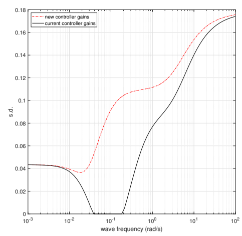


(f) Shortest distance in frequency domain at operating point 8

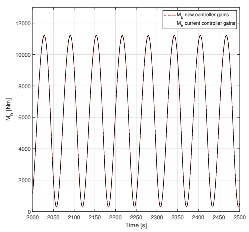


(g) Brake engine torque at operating point 6

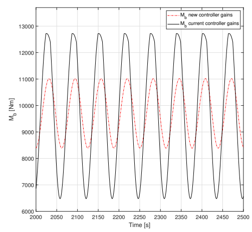


(h) Brake engine torque at operating point 8

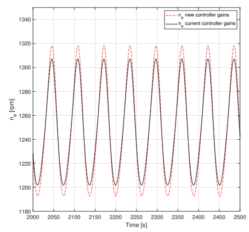


(i) Engine speed at operating point 6

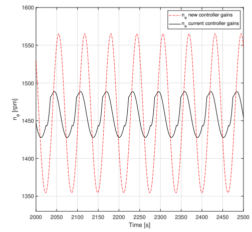


(j) Engine speed at operating point 8

Figure 6.23: Results of gains scheduling algorithm for $\boldsymbol{\omega} = \mathbf{0.1}$ **rad/s** at operating point 6 & 8.

6

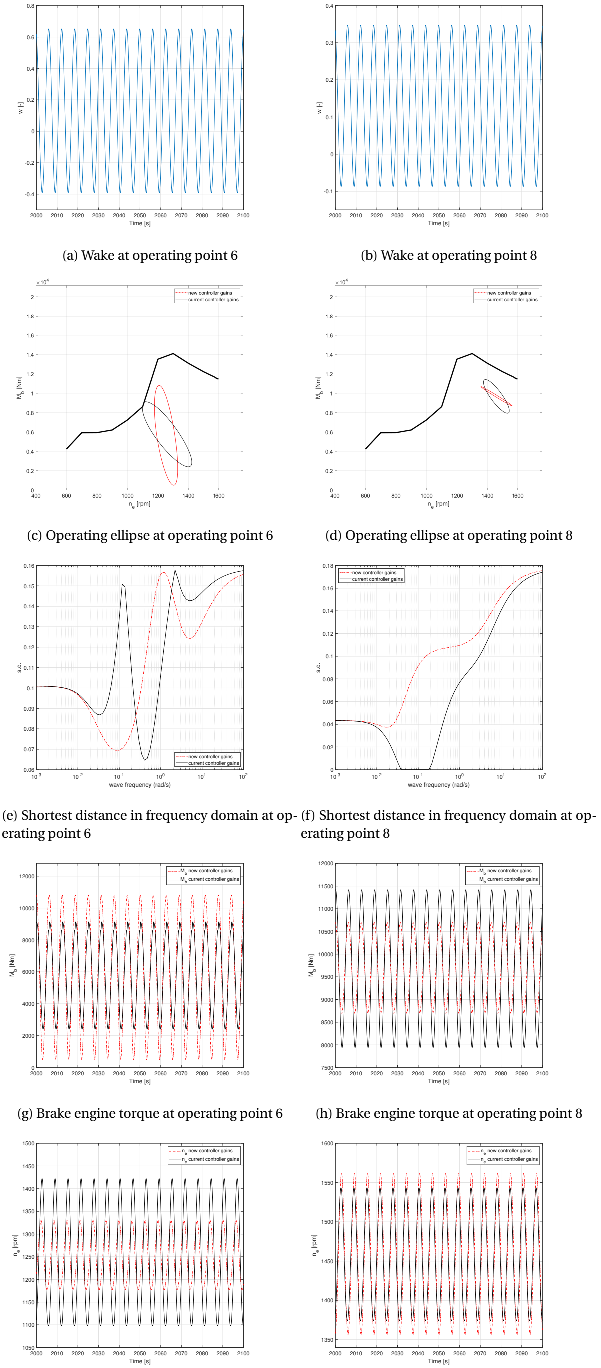


(a) Wake at operating point 6

(b) Wake at operating point 8

(c) Operating ellipse at operating point 6

(d) Operating ellipse at operating point 8

(e) Shortest distance in frequency domain at operating point 6

(f) Shortest distance in frequency domain at operating point 8

(g) Brake engine torque at operating point 6

(h) Brake engine torque at operating point 8

(i) Engine speed at operating point 6

(j) Engine speed at operating point 8

Figure 6.24: Results of gains scheduling algorithm for $\boldsymbol{\omega} = \mathbf{1}$ **rad/s** at operating point 6 & 8.

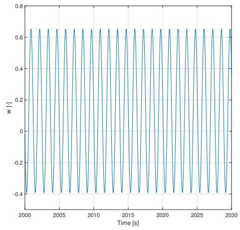


(a) Wake at operating point 6

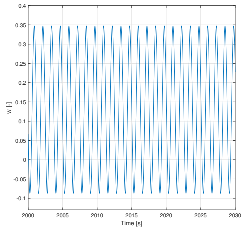


(b) Wake at operating point 8

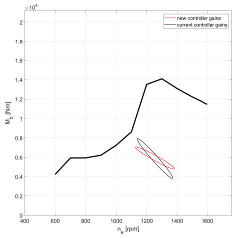


(c) Operating ellipse at operating point 6

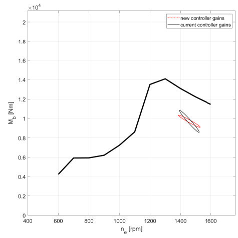


(d) Operating ellipse at operating point 8

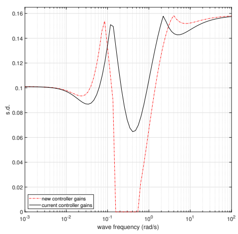


(e) Shortest distance in frequency domain at operating point 6

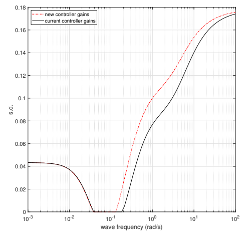


(f) Shortest distance in frequency domain at operating point 8

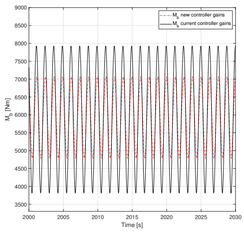


(g) Brake engine torque at operating point 6

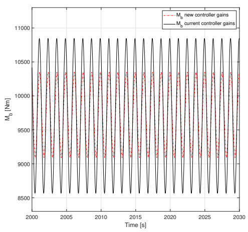


(h) Brake engine torque at operating point 8

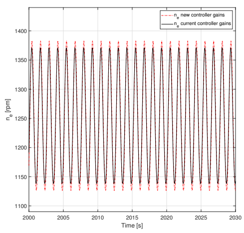


(i) Engine speed at operating point 6

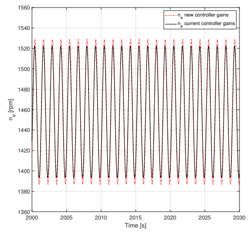


(j) Engine speed at operating point 8

Figure 6.25: Results of gains scheduling algorithm for $\boldsymbol{\omega} = \mathbf{5\ rad/s}$ at operating point 6 & 8.

6

As it can be noticed, the results achieved by the gains scheduling algorithm are aligned with what is suggested by the derived contour plots in the previous section:

**Operating point 6:** The gains scheduling algorithm achieved to determine the suitable combination of gains for the three sinusoidal wakefield disturbances examined. For all three cases the dynamic behaviour of the engine operating point for the new combination of gains was improved, compared to the behaviour resulting from the currently used gains. This improvement is defined as the increase of the shortest distance between the operating ellipse and the engine envelope line, with the operating ellipse avoiding any contact with the engine envelope limits. The improvement potential is quite high for the medium wave frequency and significantly lower for high and low wave frequencies. This is in line with what was presented in previous Section.

**Operating point 8:** The gains scheduling algorithm achieved to determine the suitable combination of gains for the three sinusoidal wakefield disturbances examined. For all three cases the dynamic behaviour of the engine operating point for the new combination of gains was improved, compared to the behaviour resulting from the currently used gains. This means that the shortest distance between the operating ellipse and the engine envelope line is increased for the three examined wave frequencies, with the operating ellipse avoiding any contact with the engine envelope limits. The opportunity of improvement seems to be reduced as the wave frequency of the disturbance increases. This is in line with the outcome of the previous section, Section 6.3, where the contour plots were derived.



### 6.4.2. IRREGULAR WAVES

In case of irregular waves the examined cases involve two Sea States, Sea State 5 and Sea State 7 as they are defined in Figure A.1, two sailing directions of the vessel with respect to the waves, head and following waves and two operating points, operating point 6 and 8. Using the parameters of the selected Sea State, the vessel direction and the operating point under study and following the assumptions and simplifications as they are presented in Section A.3, the time trace of the wakefield disturbance signal is generated. The procedure followed to generate the wakefield disturbance signal is presented in details in Section A.4.

At this point it should be mentioned how the gains scheduling algorithm is designed to operate in case of wakefield disturbance acting on the propulsion system model caused by irregular waves. As it is illustrated in Figure 6.22, the gains scheduling algorithm requires the wave frequency $\omega$ of the wakefield disturbance as input data. Then, based on the wave frequency $\omega$, the frequency of encounter $\omega_e$ is calculated, following Eq. (5.21), and the gains scheduling algorithm determines the optimum or close to optimum combination of governor gains for this specific frequency of encounter $\omega_e$. The wave frequency $\omega$ for which the frequency of encounter $\omega_e$ is calculated, is selected based on the wave amplitude spectrum, $\zeta_{\alpha_n}$, which is derived by the wave energy spectrum $S_\zeta(\omega)$, of the Sea State under study. More specifically, the selected wave frequency $\omega$ is the one corresponding to the maximum wave amplitude $\zeta_{\alpha_n}$, as it is indicated in Figure 6.26. For this wave frequency $\omega$, the frequency of encounter $\omega_e$, is calculated and the gains scheduling algorithm determines the optimum governor gains for this frequency of encounter, $\omega_e$. The derivation process of the wave energy spectrum $S_\zeta(\omega)$ and wave amplitude spectrum $\zeta_{\alpha_n}$ is presented in Section A.2.

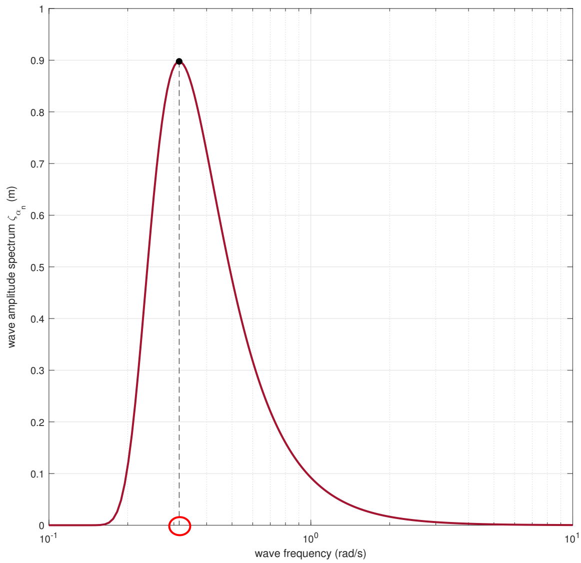


Figure 6.26: Maximum value of wave amplitude spectrum in wave frequency domain.

In the Figures below, the results of the simulation employing the gains scheduling algorithm are compared to the results of the simulation by using the currently used governor gains $K_p$ and $K_i$. The time trace of the wake disturbance signal is presented together with the elliptic trajectory of the engine operating point in the Diesel engine envelope, the brake engine torque and the engine speed time signal. Additionally, the reader should notice the different time scale between the head and following waves in the Figures below.

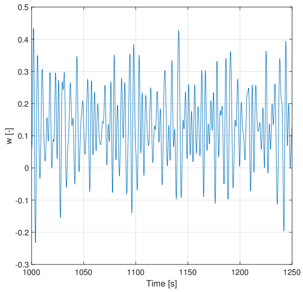


(a) Wake in head waves.

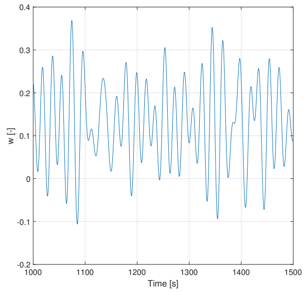


(b) Wake in following waves.

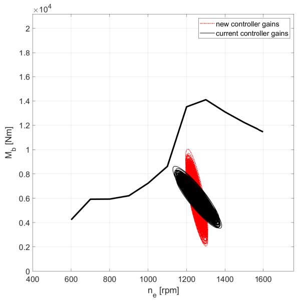


(c) Operating cloud in head waves.

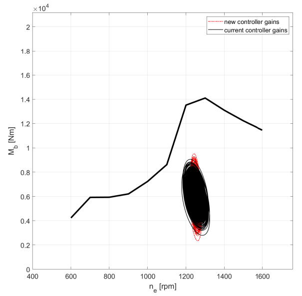


(d) Operating cloud in following waves.

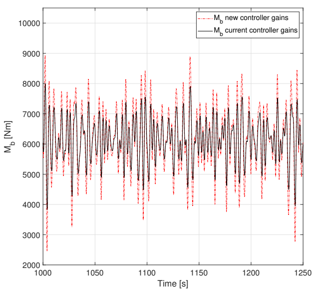


(e) Brake engine torque in head waves.

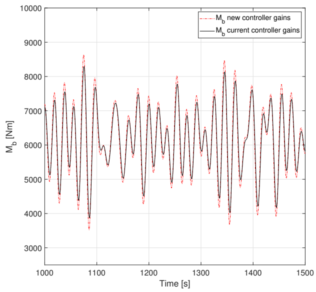


(f) Brake engine torque in following waves.

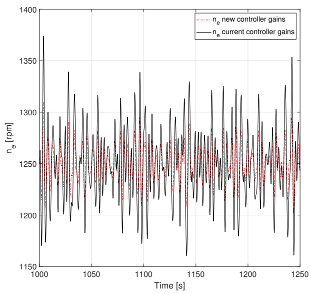


(g) Engine speed in head waves.

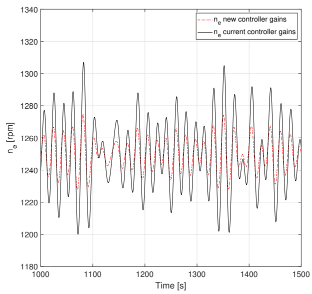


(h) Engine speed in following waves.

Figure 6.27: Results of gains scheduling algorithm in head and following waves for Sea State 5 at operating point 6.

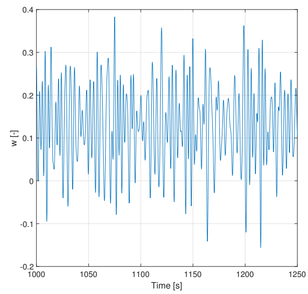


(a) Wake in head waves.

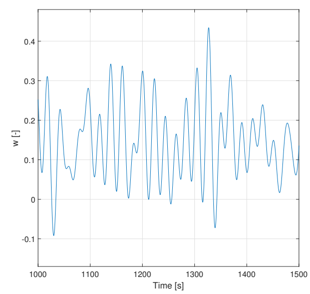


(b) Wake in following waves.

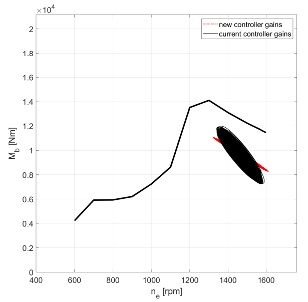


(c) Operating cloud in head waves.

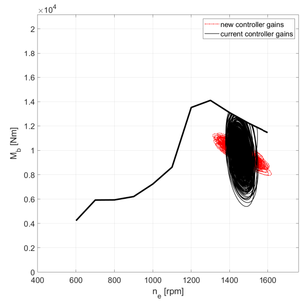


(d) Operating cloud in following waves.

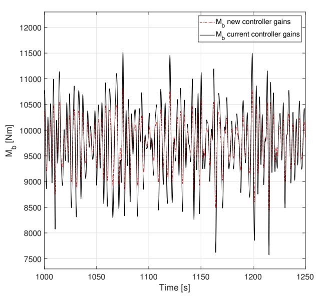


(e) Brake engine torque in head waves.

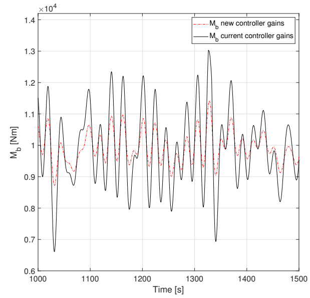


(f) Brake engine torque in following waves.

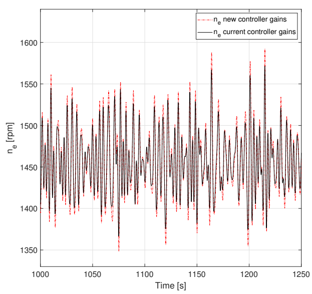


(g) Engine speed in head waves.

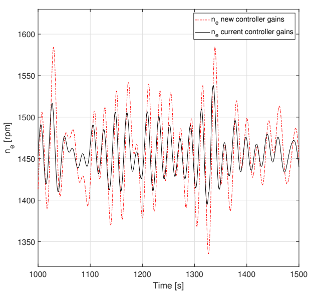


(h) Engine speed in following waves.

Figure 6.28: Results of gains scheduling algorithm in head and following waves for Sea State 5 at operating point 8.

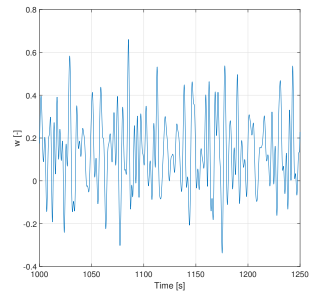


(a) Wake in head waves.

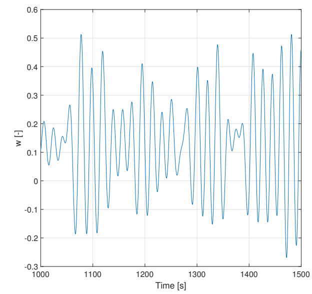


(b) Wake in following waves.

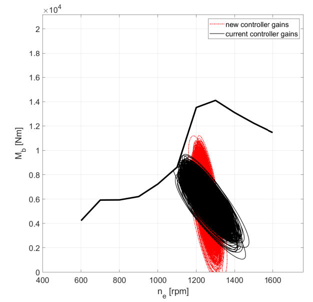


(c) Operating cloud in head waves.

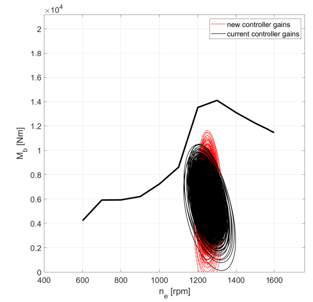


(d) Operating cloud in following waves.

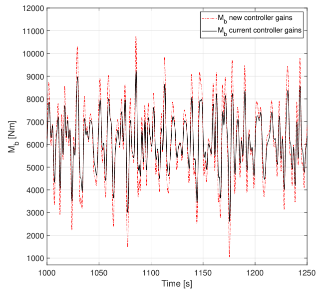


(e) Brake engine torque in head waves.

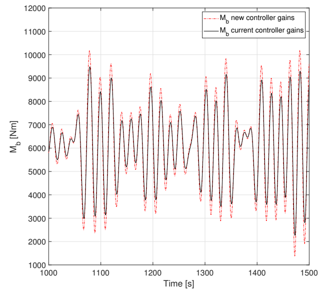


(f) Brake engine torque in following waves.

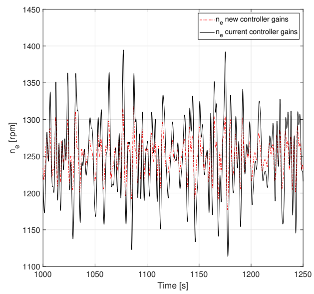


(g) Engine speed in head waves.

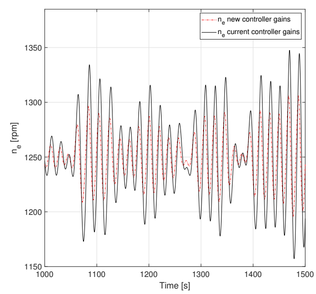


(h) Engine speed in following waves.

Figure 6.29: Results of gains scheduling algorithm in head and following waves for Sea State 7 at operating point 6.

6

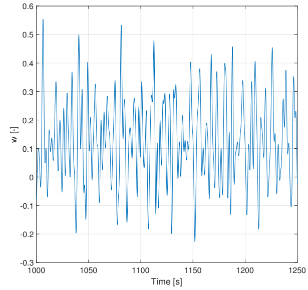


(a) Wake in head waves.

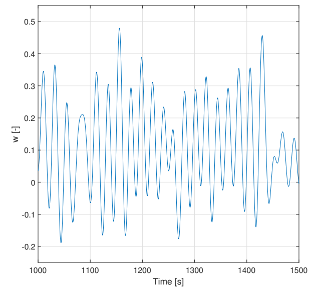


(b) Wake in following waves.

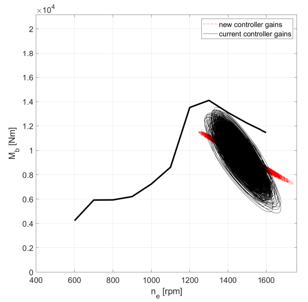


(c) Operating cloud in head waves.

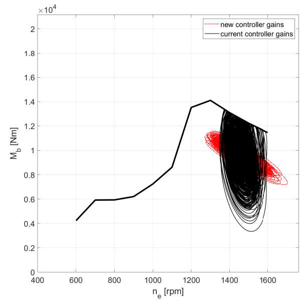


(d) Operating cloud in following waves.

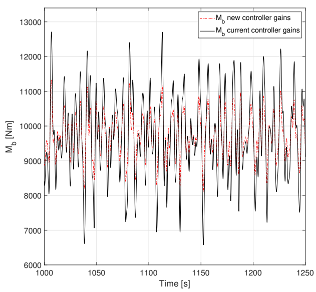


(e) Brake engine torque in head waves.

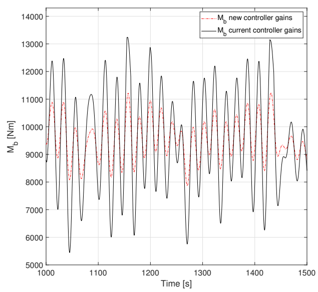


(f) Brake engine torque in following waves.

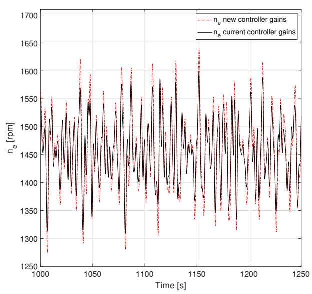


(g) Engine speed in head waves.

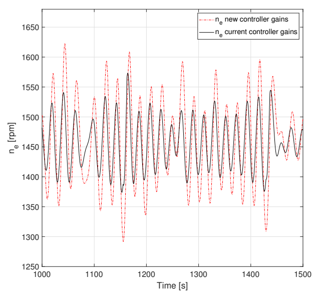


(h) Engine speed in following waves.

Figure 6.30: Results of gains scheduling algorithm in head and following waves for Sea State 7 at operating point 8.

As it can be noticed in the results reported in Figures 6.27 - 6.30 the gains scheduling algorithm achieves to improve the dynamic behaviour of the Diesel engine operating cloud in all cases; both Sea States 5 & 7, both vessel directions with respect to the waves, head and following waves as well as the two examined operating points 6 & 8. The accomplished improvement deals with the possibility of the operating cloud touching the engine envelope limits. In that sense, the gains scheduling algorithm gives as solution a combination of governor gains, $K_p$ and $K_i$, which generates an operating cloud with increased shortest distance from the engine operating envelope limits compared to the shortest distance of the operating cloud generated by the currently used governor gains. By generating an engine operating cloud which lies in the maximum or close to the maximum distance from the engine operating envelope line, it is ensured that the propeller pitch controller will remain deactivated.

## 6.5. CONCLUSIONS

According to the results reported in this Chapter, it is confirmed that by employing the suitable geometric criterion as the objective function in the mathematically formulated problem, it is possible to achieve the refinement of the dynamic response of the Diesel engine operating point in the engine envelope. This refinement is accomplished by means of making the controller gains dependent on the system operating point and the wave induced disturbance, which is directly related to the Sea State and the direction of the ship with respect to the waves.



Following the structure of this Chapter, as a first step the contour plots defining the shortest distance between the operating ellipse and the engine operating envelope limits were derived with independent variables the governor gains $K_p$ & $K_i$. These contour plots suggest that an improved dynamic behaviour of the operating ellipse in the engine envelope can be obtained by means of governor gains scheduling. The shortest distance between the operating ellipse and the engine envelope line can be increased, compared to the corresponding shortest distance resulting from the currently used governor gains, by making the gains scheduling dependent on the operating point and the wave induced disturbance acting on the ship propulsion model.

The second step involves the development of the gains scheduling algorithm. The developed algorithm makes use of the linear model of the ship propulsion system to mathematically formulate the engineering problem. This mentioned engineering issue is defined as the effort to keep the fluctuations of the Diesel engine operating point as far away as possible from the limits of the engine operating envelope and thus, retain the propeller pitch control deactivated during a vessel's operation in waves. The gains scheduling algorithm combines the linear model with an employed metaheuristic algorithm to achieve the optimum of the objective function, which is the maximisation of the shortest distance between the elliptic trajectory of the engine operating point and the engine operating envelope limits. The algorithm is evaluated in case of regular and irregular waves. In both cases it is proved capable of improving the dynamic behaviour of the elliptic trajectory of the engine operating point in the engine envelope by automatically determining the combination of governor gains which generates an operating ellipse with increased shortest distance from the engine envelope limits compared to the operating ellipse generated by the currently used gains. In that way it is confirmed that the gains scheduling algorithm is able to dynamically maximise or nearly maximise the shortest distance between the generated operating ellipse and the engine envelope limits in every studied case preventing any contact between those two.

Therefore, it can be argued that for the cases, regular and irregular waves studied in this Chapter, the developed gains scheduling algorithm achieves the main objective of this work, which is to keep the propeller pitch control deactivated and in that way retain the average delivered power and the average maximum ship speed when the vessel sails in waves. Additionally, it should be mentioned that despite the fact of sustaining the average delivered power and the average maximum ship speed, the achievement of keeping the operating ellipse as far away as possible from the limits of the engine operating envelope is beneficial regarding the issue of thermal overloading of the engine [Grimmelius and Stapersma, 2001].

# 7

# CONCLUSIONS & RECOMMENDATIONS

*This work focuses on influencing the size and the orientation of the elliptic trajectory of the engine operating point in the engine operating envelope, aiming to prevent the activation of the propeller pitch controller, when the vessel sails in waves. This is attempted by refining the existing propulsion control system by means of governor gains scheduling. The Diesel engine controller settings are determined by a developed gains scheduling algorithm, which relies on the linearised ship propulsion system model combined with a metaheuristic method for hard optimisation problems. The potential and limitations of this work are presented in this Chapter, as well as the author's general recommendations for future, further research on the topic.*

## 7.1. CONCLUSIONS

Taking into account the research objectives as they are presented in Section 1.4, the following conclusions can be drawn:

1. Before investigating the possibilities to influence the size and the orientation of the elliptic trajectory of the engine operating point by making the governor's gain scheduling dependent on the system operating point, on the Sea State and the direction of the vessel with respect to the waves, the impact of those three factors on the dynamic response and load fluctuations of the Diesel engine in a seaway were investigated.

   *With respect to the Diesel engine load fluctuations in a seaway:*

- *What is the impact of the different Sea States?*

  As far as the the impact of the different Sea States is concerned, seven different Sea States were investigated in terms of the effect of their maximum wave amplitude on the amplitude of the wakefield disturbance acting on the ship propulsion system model. For that reason the energy spectra of these seven Sea States were used in order to derive the corresponding wave amplitude spectra. The maximum wave amplitude of each one of the wave amplitude spectra was selected together with the corresponding wave frequency and were used for the calculation of the wakefield disturbance amplitude. The reported results demonstrate that the increasing Sea State results in the increase of the wakefield disturbance amplitude. As a consequence of the increasing wakefield disturbance amplitude, the excursions in both speed and torque direction become larger. In other words, as the Sea State increases, the size of the elliptic trajectory of the engine operating point regarding both axis increases as well. Finally, it has to be mentioned that the different Sea States have an insignificant effect on the angle of rotation of the operating ellipse, with the operating ellipses derived for the different Sea States having almost the same orientation.

- *What is the impact of head and stern waves?*

  Regarding the impact of the vessel direction with respect to waves, two directions were investigated; head and following waves. It seems that for the head direction the resulting operating ellipse is more anticlockwise rotated compared to the one resulting from the following waves. This means that head direction leads to less excursions in the torque direction and more excursions in the speed direction compared to the corresponding fluctuations resulting from stern direction. Additionally, for a specific wave frequency under study the head direction results in a higher value of the encounter frequency compared to the encounter frequency resulting for the following direction. That means that for relatively higher wave frequencies, the operating ellipses resulting for head direction have smaller area (smaller size for both axis) compared to the operating ellipses resulting for following direction. This is explained by the low pass filter role that the shaft inertia has in the ship propulsion system, reducing the impact of high frequencies on the Diesel engine dynamic response.

- *What is the impact of the propulsion system operating point?*

  With regard to the impact of the system operating point, two operating points were investigated. The outcome of this investigation suggests that the system operating point has insignificant influence on the angle of rotation of the elliptic trajectory of the engine operating point in the engine operating envelope. Nevertheless, the system operating point affects the size of the operating ellipse. More specifically, the size of both axes of the operating ellipse decreases as the system operating point increases. This means that for lower operating point the fluctuations in both directions of brake engine torque and engine speed are larger. Given that the gain values from the Bode plots are quite close to each other for both operating points examined, the difference in the size of the operating ellipses can only be attributed to the higher value of the normalised change of wake fraction for lower system operating point. Following the theory presented in Section A.3, the value of the normalised change of wake fraction depends on the ship speed and consequently to the system operating point.

The variation of the impact of the three previously mentioned factors on the Diesel engine load fluctuations, resulting in different dynamic behaviour of the engine operating ellipse in the engine envelope, suggested that it would make sense to make the gain scheduling of the governor dependent on the system operating point, on the Sea State and the direction of the vessel with respect to the waves. The factor of the system operating point is also included and the reason for this is that despite the fact that this factor makes almost no difference on the engine's dynamic behaviour for the two examined operating points, the position of these two operating points with respect to the engine envelope limits requires different resizing and re-orientation, aiming at avoiding any contact between the elliptic trajectory of the engine operating point and the engine envelope limits. This means that different gain scheduling is required, which should depend on the operating point.



2. *Is it possible to influence the size and the orientation of the Diesel engine operating ellipse, by trying to refine the existing propulsion control system and making the gain scheduling of the governor dependent on the system operating point, on the Sea State and/or on the heading of the vessel regarding the waves?*

   This constitutes the main goal of this thesis. As it is documented in Chapter 6, this was achieved in two steps:

   - Firstly, the generation of contour plots in MATLAB with independent variables the governor gains, $K_p$ & $K_i$, clearly proved the opportunity of enhancement of the dynamic response of the elliptic trajectory of the Diesel engine operating point in the engine envelope. More specifically, the operating ellipse was re-sized and re-orientated with the objective being the increase of the shortest distance between the elliptic trajectory of the engine operating point and the limits of the engine envelope, with the latter being mathematically formulated as straight lines. The contour plots were derived for two operating points due to sinusoidal wakefield disturbances of which the amplitude was constant. On the other hand, regarding the wave frequencies of those disturbances acting on the linear model, a number frequencies was examined covering a wide range of the possible disturbance frequencies. The results, regarding the shortest distance between the operating ellipse and the engine envelope limits, using the combinations of governor gains, $K_p$ & $K_i$, from the derived contour plots were compared to those generated by the already used combination of gains at the particular propulsion plant which is modelled. The results of this comparison is visualised and quantified in Section 6.3.

- Secondly, the development of a gains scheduling algorithm based on the State-Space notation of the linear ship propulsion system model. By using this particular notation, the mathematical equation of the elliptic trajectory of the engine operating point caused by sinusoidal wakefield disturbances can be determined, together with the mathematical formulation of the lines of the engine envelope. By employing a metaheuristic algorithm and using as objective function the maximisation of the shortest distance between the operating ellipse and the engine envelope lines, the re-sizing and the re-orientation of the operating ellipse is achieved based on the acting wakefield disturbance on the ship propulsion system each time. The potential of the gains scheduling algorithm is examined in case of regular and irregular waves. Regarding the regular waves, two operating points were examined for a low, medium and high wave frequency of the wakefield disturbance acting on the system each time with the amplitude of the disturbance being constant. The combination of governor gains, $K_p$ & $K_i$, as generated solution of the gains scheduling algorithm was applied on the simulation model of the ship propulsion plant and the resulting operating ellipses are compared to those resulting from the already used governor gains in Section 6.4.1. The outcome of the comparison is that the algorithm is capable of re-sizing and re-orientating the operating ellipse by increasing the shortest distance between the operating ellipse and the engine envelope limits for each one of the examined wakefield disturbances, with the room of improvement depending on the combination of the examined operating point and the wave frequency of the wakefield disturbance. Finally, the potential of the gains scheduling algorithm was investigated in case of irregular waves. More specifically, two Sea States were examined for two operating points and for two directions of the ship with respect to the waves, following and head waves. The solutions generated by the gains scheduling algorithm were compared to those of the already used governor gains and the results are visualised in Section 6.4.2. The outcome of this comparison is that the gains scheduling algorithm is capable of increasing the shortest distance between the operating ellipse and the engine envelope line for the examined operating points, Sea States and headings of the vessel with respect to the waves. Therefore, it is proved that the Diesel engine operating ellipse can be re-sized and re-orientated by means of refining the already existing propulsion control system and making the gain scheduling of the governor dependent on the system operating point, on the Sea State and on the heading of the vessel regarding the waves.

3. *Is it possible to maintain the maximum average ship speed during speed trials by means of tuning governor gains?*

As it was previously mentioned, the Diesel engine operating ellipse is re-sized and re-orientated by refining the already existing propulsion control system. This refinement is achieved by using a gains scheduling algorithm which employs a metaheuristic algorithm. The objective function of this metaheuristic algorithm is the maximisation of the shortest distance between the operating ellipse and the engine envelope limits. In that way it is ensured that the re-sizing and the re-orientation of the operating ellipse prevents any contact between the operating ellipse and the engine envelope lines. Consequently, the propeller pitch control remains deactivated during vessel's operation, such as the speed trials. As a result, the average delivered power is retained as well as the maximum average speed.

## 7.2. RECOMMENDATIONS FOR FUTURE WORK

The main focus of this work was to investigate the possibilities of re-sizing and re-orientating the elliptic trajectory of the engine operating point in the engine envelope, when the vessel sails in waves, by means of gain scheduling the existing speed governor. The ultimate goal of influencing the dynamic behaviour of the engine operating point in off-design conditions, is to avoid any contact between the operating ellipse and the engine envelope. Consequently, the activation of the propeller pitch control is prevented, allowing the vessel operating in wave field to retain the maximum average speed, by retaining the average delivered engine power. Despite the fact that the preliminary results seem to be quite promising, several recommendations can be given which might be used as the starting point for further research in the future:



### SIMULATION MODEL

1. It goes without saying that the linear model of the ship propulsion system is considered to be the essential tool, regarding the research objectives of this thesis. The derived linear model provides the opportunity to investigate the dynamic behaviour of the propulsion plant when sailing in waves at different encounter frequencies. Taking this to the next level, in this work the derived linear model of the propulsion system is used to schedule the speed governor gains. However, in order to confirm that the linearised model can, rightfully, be employed for the controller settings tuning, it is verified by means of comparing the Bode plots derived from the linear and the non-linear model, respectively. Despite the fact that the results of the verification are quite satisfying, there are still some deviations between the Bode plots derived from the two models, as shown in Section 4.5. Given that the developed gains scheduling algorithm is based on the Bode plots derived from the linear model, this could lead to wrong decisions regarding the selected combination of governor gains. For instance, a combination of gains that generates an operating ellipse which does not touch the envelope limits according to the calculations based on the Bode plots of linear model, could result in an operating ellipse that touches the engine envelope line when applied in the non-linear

model. Consequently, in order to improve the reliability of the linearised model, establishing it as a trustworthy tool for the governor gains scheduling, it would be valuable to eliminate these deviations between the Bode plots derived from the two models, leading to an identical dynamic response of both models in the frequency domain. In that way, it could be confirmed that any conclusions drawn using the linear model, with regard to the engine's controller tuning for example, can be applied on the non-linear ship propulsion model ensuring the alignment between the results of linear and non-linear model. As it is illustrated in Chapter 4, these deviations between the Bode plots of the two propulsion system models can be noticed only after the addition of the governor's block diagram, which apparently affects significantly the behaviour of the whole system. Taking into account the structure of the governor's block diagram as it is presented in Figure 3.10, it includes two blocks which are responsible for the linearisation of the engine speed signals (actual value coming from the integration of the shaft speed loop and reference value coming from the vessel operator), one block determining the engine's torque limitations, as a function of the engine speed, and the PID controller block. Given that the engine's torque limitations are provided by the engine manufacturer and that the PID controller block is, correctly, built according to theory, special attention should be given in the two blocks linearising the values of actual and reference speed in order to deal with the issue of deviations between the Bode plots of non-linear and linear model. Taking the previously mentioned into account, it is considered that the deviations could, possibly, be attributed to the scaling used for the linearisation process in these two blocks.



2. If the prediction of the true dynamic behaviour of then a complete ship propulsion system model is needed, which should involve the two main disturbances acting acting on the system. In that sense, the resistance disturbance has to be added to the existing propulsion system. A adequate resistance disturbance model should be developed, establishing the propulsion system model as totally valid. Such an advanced model of the added ship resistance due to wave field requires the calculation of ship motions due to waves. A relevant discussion on the subject can be found in Section 2.5.2, along with useful references.

3. Regarding the wakefield disturbance, an extended, enriched model of this specific disturbance would serve the purpose of obtaining a more accurate and realistic simulation model of the ship propulsion system. Thus, the engine's controller could be more properly tuned, leading to an even more valid simulation model for the study of the dynamic response of the ship propulsion plant. The wakefield disturbance model could be extended by taking into account components of the unsteady wake velocities which are neglected in this work, such as velocity components due to wave reflection on the hull, components of radiated wave velocity due to ship motions as well as velocity components due to relative motion of the vessel, like surge, heave and pitch. Moreover, additional extensions would involve the effects of propeller submergence, due to heave and pitch motions, as well as occasional propeller emergence on wake and engine load fluctuations. An extensive presentation of methods to implement the required extensions of the wakefield

disturbance model along with useful references are given in Section 2.5.1.

4. As far as the prime mover is concerned, this thesis focuses only on Diesel engines. It would be considered useful to extend the existing model by including other prime movers, such as gas turbines or electric motors, with the latter becoming quite common lately due to the increasing development of hybrid propulsion systems. In that case, the opportunity of enhancement of the dynamic response of the above mentioned prime movers, using the gains scheduling algorithm could be examined. Moreover, regarding the existing prime mover, a simplified Diesel engine model was applied, relating the fuel rack position, the engine speed as inputs and the engine speed as output. Taking into account the lack of fuel rack map and factory acceptance test report, typical values were used for the formula relating the previously mentioned variables. Therefore, the use of a fuel rack map or a factory acceptance test for the derivation of the fuel rack map would lead to a more realistic Diesel engine model. Additionally, an engine model of higher level of detail could be applied, for instance an advance Seilinger model, including also the dynamics of a turbocharger. In this case the impact of the gains scheduling algorithm on additional variables could be studied like the Diesel engine fuel consumption, engine emissions or even the thermal loading of the engine.

5. What is more, another extension which could be made is to investigate the gains scheduling algorithm effectiveness during acceleration/deceleration and manoeuvring. This would require a more sophisticated wakefield disturbance as well as the addition an advanced resistance disturbance model, capable of capturing the real phenomena occurring during these operational modes.



### Gains Scheduling Algorithm

6. With respect to the developed gains scheduling algorithm, further improvements could be achieved leading to higher quality results by implementing extensions of the metaheuristic method. Such a suggested extension, which could possibly result in more effective gains scheduling algorithm, is the implementation of a hybrid metaheuristic method combined with multiobjective optimisation, [Dréo et al., 2006]. Hybridisation quite often involves the co-operation of two metaheuristics or the combination of an efficient metaheuristic and a simple local search algorithm. The second metaheuristic or the local search algorithm employed could have different objective, compared to the main metaheuristic, introducing in this way the principles of multiobjective optimisation. As far as the gains scheduling algorithm is concerned, it could be hybridised by implementing another metaheuristic technique, tabu search, genetic and evolutionary algorithms, ant colony algorithms or a simple local search algorithm, which would consider an objective contradictory or not completely aligned with the objective of the main metaheuristic, the Simulated Annealing. This objective could be for instance the geometric criterion of the area of the operating ellipse as presented in Section 6.2.2 whose results are not always to the same direction as the results of the shortest distance between the operating ellipse and envelope line criterion in terms of avoid-

ing the activation of propeller pitch control. However, simultaneous consideration of both, could refine the results regarding the ultimate goal, which is the prevention of any contact between the operating ellipse and the engine envelope line. In such case, Simulated Annealing could ensure the maximisation of shortest distance between the operating ellipse and the envelope line and the employment of a local search algorithm, which would simply take the form of the passage of the relay between the metaheuristic and the local technique, could optimise the solutions found by Simulated Annealing, in terms of minimising excursions in speed and torque direction and at the same time increasing even more the distance between the operating ellipse and the engine envelope line.

7. Moreover, refinements on the design of an efficient metaheuristic method can lead to further reduction of the computational time of the developed gains scheduling algorithm.

   - Such a refinement could be the suitable choice of the neighbourhood of the metaheuristic algorithm. The neighbourhood in a metaheuristic method is defined as the set of neighbours or in other words the set of accessible configurations of the problem. A smart choice of the neighbourhood could lead to reduction of the computational time of gains scheduling algorithm. For instance, in case of the gains scheduling algorithm, if it is known in advance, by using the contour plots, that the desired solutions are only possible for a subset of neighbours for example for high values of both governor gains $K_p$ & $K_i$, then the neighbourhood can be chosen in that way that only this specific range of values of $K_p$ & $K_i$ will be allowed as accessible configurations.
   - Another refinement, which could result in decrease of the computational time, has to do with the control parameters used in metaheuristic methods. These parameters in case of Simulated Annealing are the control parameter of Temperature, T, as well as the parameters involved in the stopping criteria of the method. The optimal adjustment of these parameters, based either on theory or on experience of the user, will lead to less computational time for the gains scheduling algorithm, [Dréo et al., 2006]. However, it is possible that the reduction in computational time will come at the cost of lower quality solutions, which means that the solutions might not be that close to the global optimal.
   - Additionally, the choice of the programming language which is used for the development of the gains scheduling algorithm can make a difference in terms of computational time.

### FULL SCALE VALIDATION

8. Finally, there is no doubt that in order to prove the validity of the developed gains scheduling algorithm and the results reported in this thesis, a quite interesting and significant step would be the model-scale and full-scale validation. Obtaining data from model-scale and full-scale tests could impose new directions regarding the

research for the improvement of the existing work and contribute to the development of an actual governor optimisation software. A requirement for that would be the addition of an advanced model for both wakefield and resistance disturbance in the ship propulsion model, as well as further refinement of the existing algorithm, decreasing even more the required computational time by following the previously mentioned suggestions. In that way a real-time gains scheduling software could be implemented on the existing Diesel engine speed governor, improving its behaviour. This would require the prediction of the future incoming wave by using forward looking wave sensors. The use of such kind of device tend to become quite common in the near future, following recent studies which have identified the possibility of deterministic prediction of waves by using the already existing nautical radars as remote wave sensors, [Naaijen, 2017]. In any case, the previously mentioned recommendations suggest that theoretical enhancement of the existing work should be attempted in parallel to further practical development.

# A

# WAKE DISTURBANCE MODELLING

*In the following, a demonstration of the method followed to derive the disturbance of the wake velocity due to waves, using data from wave spectra is given.*

## A.1. INTRODUCTION

As extensively discussed, earlier in Section 2.6.2, the disturbance of the wake velocity by waves has the most direct dynamic impact on the propulsion plant at sea, always compared to the effect of the other disturbance that acts on a ship's propulsion plant, the ship resistance disturbance. Again, the reasons for that are sufficiently explained in Section 2.6.2. However, in this Section a step further will be taken, by showing how to derive the wake variations, caused by a wave field, acting on the propeller and consequently, on the propulsion plant. This is achieved by using data provided by wave spectra.

## A.2. STANDARD WAVE SPECTRA

A lot of effort has been done by researchers trying to describe a wave frequency spectrum in standard forms. Some of the mathematical formulations that researchers have come up with, can be found in the literature. One of these mathematical formulations, which can be readily found in literature [Holthuijsen, 2007, Journée and Massie, 2000, Branlard, 2010], is the *JONSWAP spectrum*, which is the result of an extensive wave measurement program, known as the Joint North Sea Wave Project (JONSWAP), that took place in the North Sea. Analysis of the data provided by this wave measurement program led to the

A

definition of a **mean JONSWAP** wave spectrum:

$$S_{JS}(f) = 0.3125 \cdot H_s^2 \cdot T_P \cdot \left(\frac{f}{f_p}\right)^{-5} \cdot \exp\left[-1.25 \cdot \left(\frac{f}{f_p}\right)^{-4}\right] \cdot (1 - 0.287 \log\gamma) \cdot \gamma^{\exp\left[-0.5\left(\frac{\frac{f}{f_p}-1}{-\sigma}\right)^2\right]} \tag{A.1}$$

where:

$$f_p = \frac{1}{T_p} \quad \text{(peak frequency)}$$
$$\gamma = 3.3 \quad \text{(peak-shape parameter)}$$

and $\sigma$:

$$\sigma = \begin{cases} 0.07, & \text{for } f < f_p = \frac{1}{T_p} \\ 0.09, & \text{for } f > f_p = \frac{1}{T_p} \end{cases} \tag{A.2}$$

Besides JONSWAP, another mathematical formulation of these normalised wave energy spectra, commonly found in the literature, is Bretschneider Wave Spectra. However, this one is not applied in this thesis. The required input for this mathematical formulation, as described in Eq. (A.1) are the wave peak period, $T_p$ and the significant wave height, $H_s$. The values for these variables can be obtained by measurements. In this thesis, the statistical data that will be used in order to generate the wave spectra are found in [Journée and Massie, 2000] and presented in Figure A.1.

| Sea State Number (–) | Significant Wave Height $H_{1/3}$ (m) | | Sustained Wind Speed 1) (kn) | | Probability of Sea State (%) | Modal Wave Period $T_p$ (s) | |
|---|---|---|---|---|---|---|---|
| | Range | Mean | Range | Mean | | Range 2) | Most 3) Probable |
| North Atlantic | | | | | | | |
| 0 - 1 | 0.0 - 0.1 | 0.05 | 0 - 6 | 3 | 0 | - | - |
| 2 | 0.1 - 0.5 | 0.3 | 7 - 10 | 8.5 | 7.2 | 3.3 - 12.8 | 7.5 |
| 3 | 0.50 - 1.25 | 0.88 | 11 - 16 | 13.5 | 22.4 | 5.0 - 14.8 | 7.5 |
| 4 | 1.25 - 2.50 | 1.88 | 17 - 21 | 19 | 28.7 | 6.1 - 15.2 | 8.8 |
| 5 | 2.5 - 4.0 | 3.25 | 22 - 27 | 24.5 | 15.5 | 8.3 - 15.5 | 9.7 |
| 6 | 4 - 6 | 5.0 | 28 - 47 | 37.5 | 18.7 | 9.8 - 16.2 | 12.4 |
| 7 | 6 - 9 | 7.5 | 48 - 55 | 51.5 | 6.1 | 11.8 - 18.5 | 15.0 |
| 8 | 9 - 14 | 11.5 | 56 - 63 | 59.5 | 1.2 | 14.2 - 18.6 | 16.4 |
| >8 | >14 | >14 | >63 | >63 | <0.05 | 18.0 - 23.7 | 20.0 |

Figure A.1: North Atlantic Annual Sea State Occurrences, [Journée and Massie, 2000].

Since the ultimate goal is to model the wake disturbance that is caused as a consequence of the wave field, the water particle velocity, at a specified distance from the water surface, has to be calculated. Therefore, the wave amplitude, $\zeta_{a_n}$, corresponding to each wave frequency, $\omega_n$, for the whole range of the wave energy spectrum has to be determined. Given that the wave energy spectrum, $S_\zeta(\omega_n)$, can be derived by Eq. (A.1), then the wave amplitude, $\zeta_{a_n}$, can be calculated by:

$$S_\zeta(\omega_n)\cdot d\omega = \frac{1}{2}\zeta_{a_n}^2 \implies \\ \zeta_{a_n} = \sqrt{2S_\zeta(\omega_n)\cdot d\omega} \tag{A.3}$$

where $d\omega$ is the constant difference between two successive frequencies, as it is illustrated in Figure A.2.

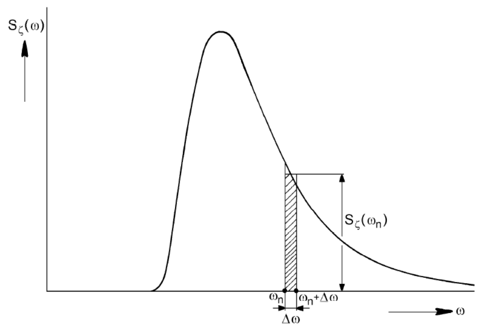


Figure A.2: Wave energy spectrum over a range of wave frequencies, $\omega$, [Journée and Massie, 2000].

At this point, it should be mentioned that when the wave spectra are given as a function of frequency in Hertz, like it is done in this thesis, $(f = 1/T)$, instead of $\omega$, in $[rad/s]$, they have to be transformed. The spectral value for the waves based on $\omega$, $S_\zeta(\omega)$, is not equal to the spectral value, $S_\zeta(f)$, based on $f$. Nevertheless, in case of calculating the wave amplitude, $\zeta_{a_n}$, the needed value is that of the product of the spectral value, $S_\zeta(f)$, times the corresponding frequency interval, $df$. The value of this product is the same for the spectral values, based either on frequency $f$ or on wave frequency $\omega$:

$$S_\zeta(\omega)\cdot d\omega = S_\zeta(f)\cdot df \tag{A.4}$$

This follows from the requirement that an equal amount of energy must be contained in the corresponding frequency intervals $d\omega$ or $df$. This means that as long as the value of $S_\zeta(f)\cdot df$ is calculated, it is the same like having the value of $S_\zeta(\omega)\cdot d\omega$. Then according to Eq. (A.3) the wave amplitude spectrum can be determined and plotted over a range of wave frequencies. In Figure A.3, the wave amplitude spectrum has been calculated for all the Sea States, for which there are available the required data from Figure A.1

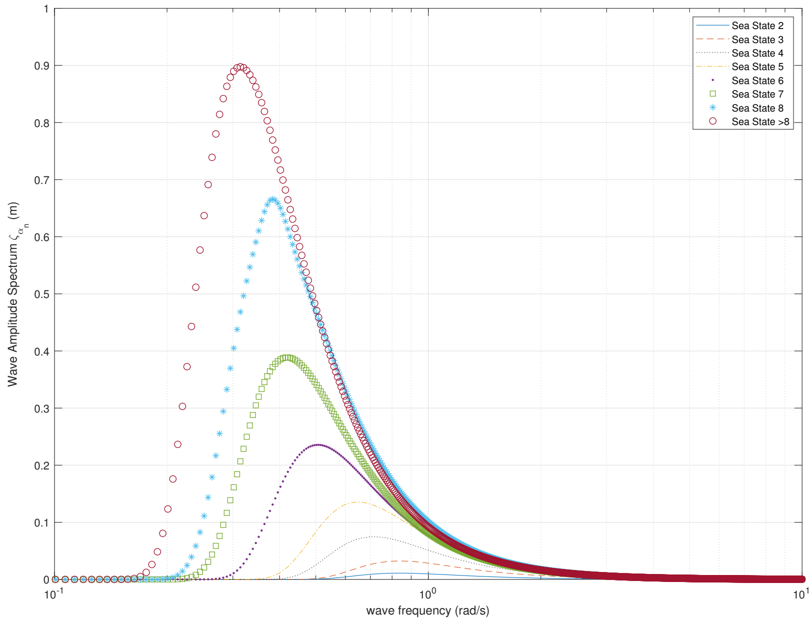


Figure A.3: Derived Wave Amplitude Spectra, $\zeta_{\alpha_n}$ for the Sea States presented in Figure A.1.

## A.3. WAKE DISTURBANCE DUE TO WAVE ORBITAL MOTION

In Section 2.5.1, the reasons causing disturbances to the inflow velocities to propeller in waves were extensively presented. According to literature, one of the main reasons these disturbances is the orbital motion of the water particles in waves. Before presenting the proper equations, which describe the orbital motions of water particles in waves and how they attribute to the wake variations, it is worth noting, as in Section 2.6.2, the assumptions that are applied in order to model the unsteady wake velocities due to waves:

1. Only the undisturbed incoming waves are modelled, without taking into account the rest of the contributing factors. Such contributing factors are the radiated and diffracted waves as well as the relative water velocity due to ship motions. More details regarding the contribution of these factors are given in Section 2.5.1.
2. Only the axial component of the velocity, $u_x$, through the propeller disc is modelled.
3. The radial distribution of the disturbance over the propeller disc is not taken into

account. The wake disturbance over the whole radius is assumed equal to the disturbance at the centre of the propeller hub.

4. The speed and heading of the ship are considered constant in the unsteady wake-field model.

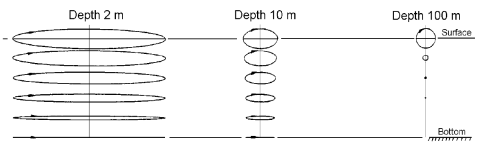


Figure A.4: Water particles orbital motion due to waves for three different depths, [Journée and Massie, 2000].

Taking into consideration the above mentioned simplifications and assumptions with the respect to the wake disturbance modelling, the method of calculating the water particle motions due to undisturbed waves will be discussed. More specifically, following the 2nd of the aforementioned key assumptions and considering only the case of **deep water**, only the axial component of the water particle velocities is given by the following equation, [Holthuijsen, 2007, Journée and Massie, 2000, Krogstad and Arntsen, 2000]:

$$u_x = \zeta_a \omega e^{kz} \sin\left(\omega_e t - kx\right) \tag{A.5}$$

where:

| | |
|---|---|
| $\zeta_a$ | :amplitude of the corresponding wave |
| $\omega_e$ | :frequency of encounter for the corresponding wave |
| $k$ | :wave number given by $k = \omega^2/g$ |
| $z$ | :distance from the water surface |

Regarding the frequency of encounter, it is given by the following equation:

$$\begin{aligned} \omega_e &= \omega - \frac{\omega^2}{g} V \cdot \cos\left(\mu\right) \\ &= \omega \cdot \left(1 - \frac{V}{c} \cdot \cos\left(\mu\right)\right), \qquad \text{by using:} \quad c = \frac{g}{\omega} \end{aligned} \tag{A.6}$$

where:

| | |
|---|---|
| $\omega$ | :wave frequency in a fixed reference [rad/s] |
| $\omega_e$ | :frequency of encounter in a moving reference [rad/s] |
| $V$ | :forward ship speed [m/s] |
| $c$ | :wave speed [m/s] |
| $g$ | :gravitational acceleration [$m/s^2$] |
| $\mu$ | :ship heading relative to wave direction [rad] |

As far as the determination of the distance from the water surface at which the wake disturbance and the water particle velocities are going to be calculated is concerned, the

A

3rd of the above mentioned assumptions has to be taken into account. Since the wake disturbance distribution is ignored and its value is only calculated at the centre of the propeller hub, then it follows that the distance from the water surface $z$ is the distance of the centre of the propeller hub from the water surface. Regarding the reference model, RGS9316, which is under consideration in this thesis, data from the vessel's particulars as well as data extracted from the drawing of propulsion plant arrangement will be used. Provided that the design draught of the RGS9316 is given in Table 3.1, then the distance of the vessel's propeller hub centre from the baseline is required in order to calculate the distance of the centre of the propeller hub from the water surface. This dimension can be obtained by observing the drawing of the propeller shaft arrangement, as illustrated in Figure A.5.

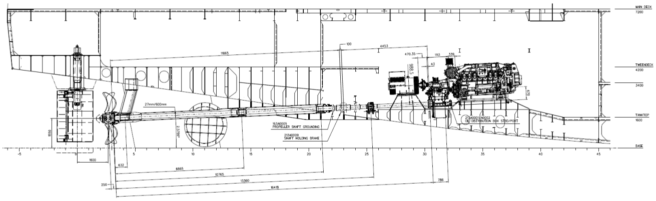

(a) Propeller shaft arrangement

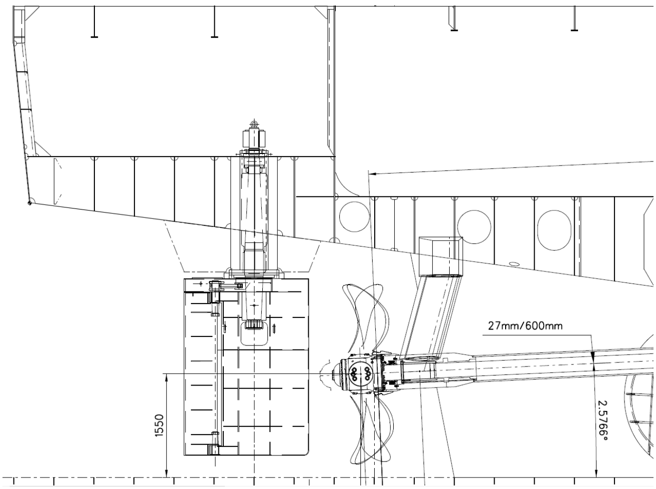


(b) Distance of propeller hub centre from the vessel's baseline.

Figure A.5: Distance of propeller hub centre from the vessel's baseline, based on propeller shaft arrangement.

Consequently and according to Figure A.5, the distance, $z$, of the centre of the propeller hub from the water surface is given below:

$$z = T - \text{distance of the centre of propeller hub from vessel's baseline} \tag{A.7}$$

where $T$ is the design draught and is given as the vessel's particulars. Since the value of $z$ is calculated for a specific propeller, then the axial component, $u_x$, of the water particle velocity due to a specified wave with known amplitude, $\zeta_a$ and frequency, $\omega$, can be determined. From that point on, taking into account the above mentioned key assumptions for the wake disturbance, the unsteady wake velocities (advance velocities), due to waves can be determined as shown below:

$$\begin{aligned} v_a &= (1-w)\cdot v_s + u_x \implies \\ v_a &= (1-w)\cdot v_s + \zeta_a \omega e^{kz} \sin(\omega_e t - kx) \end{aligned} \tag{A.8}$$

According to Eq. (A.8), it follows that the variation of the wake fraction, $w$, due to waves can be calculated by:

$$w = 1 - \frac{v_a}{v_s} + \frac{\zeta_a \omega e^{kz}}{v_s} \sin(\omega_e t - kx) \tag{A.9}$$

**Normalised Change of Wake Fraction** In case that the normalised change of the wake fraction, $\delta w^*$, has to be derived, as required input to the State-Space model of the linearised propulsion system, then from Eq. (A.9) only the amplitude (maximum value) of the wake disturbance signal is needed:

$$w_{max} = 1 - \frac{v_a}{v_s} + \frac{\zeta_a \omega e^{kz}}{v_s} \tag{A.10}$$

The normalisation process of the change of the wake fraction is done as it was presented in Eq. (4.18). In Eq. (4.18), $w_0$ is called the nominal value of the wake fraction, in other words the value of the wake fraction when there is no disturbance (calm water) and is defined by:

$$w_0 = 1 - \frac{v_a}{v_s} \tag{A.11}$$

Consequently, according to Eq. (4.18), the normalised change of wake fraction is given by:

$$\begin{aligned} \delta w^* &= \frac{\delta w}{1-w_0} \implies \\ \delta w^* &= \frac{w_{max} - w_0}{1-w_0} \implies \\ \delta w^* &= \frac{\left(1 - \frac{v_a}{v_s} + \frac{\zeta_a \omega e^{kz}}{v_s}\right) - \left(1 - \frac{v_a}{v_s}\right)}{1 - \left(1 - \frac{v_a}{v_s}\right)} \implies \\ \delta w^* &= \frac{\frac{\zeta_a \omega e^{kz}}{v_s}}{\frac{v_a}{v_s}} \implies \\ \delta w^* &= \frac{\zeta_a \omega e^{kz}}{v_a} \end{aligned} \tag{A.12}$$

A

## A.4. WAKE DISTURBANCE IN IRREGULAR WAVES

Based on the wave spectra used for the generation of waves in time domain, wake disturbance signal in time domain can, similarly, be generated. Starting by selecting the Sea State under consideration, as they are presented in Figure A.1, the wave peak period, $T_p$ and the significant wave height, $H_s$, are defined. Consequently, from Eq. (A.1) and Eq. (A.2) the wave energy spectrum, $S_\zeta(\omega_n)$, for the Sea State under consideration, is calculated. Then, from the JONSWAP spectrum the wave amplitude spectrum can be derived based on Eq. (A.3). Wave amplitude spectra for several Sea States are demonstrated in Figure A.3. Using the calculated wave amplitude spectrum and Eq. (A.9), the wake disturbance in irregular waves can be determined. As it is referred in Eq. (A.11), the first part of Eq. (A.9) is the nominal value of wake fraction, $w_0$. The rest of Eq. (A.9) is the part that is defined as wake disturbance due to waves. In case of irregular waves the wake disturbance due to wavefield is given by:

$$w_{disturbance} = \frac{1}{v_s} \sum_{n=1}^{N} \zeta_{a_n} \omega_n e^{k_n z} \sin\left(\omega_{e_n} t + \epsilon_n\right) \tag{A.13}$$

where:

| | |
|---|---|
| $N$ | :number of intervals, $\Delta\omega$,that the axis of wave frequencies, $\omega$, of the wave energy spectrum, $S_\zeta(\omega_n)$, is divided [-] |
| $\zeta_{a_n}$ | :vector of calculated wave amplitudes, $\zeta_a$ [m], corresponding to each wave frequency , $\omega_n$, as presented in the wave amplitude spectrum |
| $\omega_n$ | :vector of wave frequencies of the wave energy spectrum [rad/s] |
| $k_n$ | :vector of wave numbers, corresponding to each wave frequency, $\omega_n$, of the wave energy spectrum, given by $k_n = \omega_n^2/g$ |
| $g$ | :gravitational acceleration $[m/s^2]$ |
| $z$ | :distance from the water surface [m] |
| $\omega_{e_n}$ | :vector of frequencies of encounter corresponding to each one of the wave frequencies of the wave energy spectrum [rad/s] |
| $\epsilon_n$ | :vector of phase angles selected from a set of uniformly distributed random numbers in the range of $0 \le \epsilon_n < 2\pi$ [rad] |

The wake disturbance due to irregular waves, $w_{disturbance}$, as it is calculated in Eq. (A.13), is then added to the nominal value of wake fraction, $w_0$. The summation of these two values for each time step of a time domain simulation define the total wake disturbance of a ship propulsion system. In Figure A.6, a simulated time series of wake disturbance in irregular waves is illustrated.

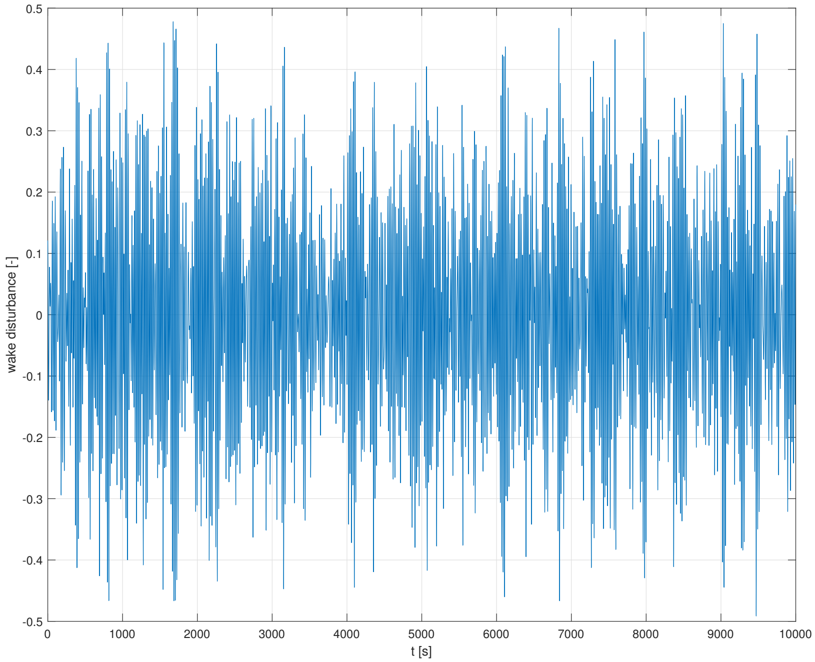


Figure A.6: Simulated time series for wake disturbance for the Sea State 7, as Sea States are given in Figure A.1.

## REQUIRED INPUTS FOR SIMULATED ANNEALING METAHEURISTIC ALGORITHM

The metaheuristic algorithm, called Simulated Annealing, that is applied in this thesis in order to refine the gain scheduling of the governor according to the wake disturbance under consideration is also implemented in the case of irregular waves. The required inputs for the metaheuristic algorithm are referred below:

- Operating point of the system
- Normalised Change of Wake Fraction, $\delta w^*$, of the disturbance under consideration
- Frequency of encounter, $\omega_e$, of the of the disturbance under consideration

In case of irregular waves the operating point of the system is known and defined. In regard to the normalised change of wake fraction, $\delta w^*$, the maximum value of the sim-

A

ulated time series of wake disturbance for the Sea State under consideration is needed to be determined. This means that for a simulated time series of wake disturbance for a Sea State, as the one shown in Figure A.6, the maximum value, $w_{disturbance_{max}}$, has to be defined. Given the maximum value of a time series wake disturbance, following Eq. (A.12) the normalised change of wake fraction in case of irregular waves is calculated as follows:

$$\begin{aligned} \delta w^* &= \frac{\delta w}{1-w_0} \implies \\ \delta w^* &= \frac{w_{max}-w_0}{1-w_0} \implies \\ \delta w^* &= \frac{\left(w_{disturbance_{max}}+w_0\right)-w_0}{1-w_0} \implies \\ \delta w^* &= \frac{w_{disturbance_{max}}}{1-w_0} \end{aligned} \tag{A.14}$$

Regarding the frequency of encounter used as input for the algorithm, in case of of irregular waves a Sea State has to be selected beforehand. For the Sea State under consideration, as it was described before, the wave amplitude spectrum has to be derived as it is shown in Figure A.3. Based on this, the wave frequency, $\omega$, for which the spectrum has the maximum value of wave amplitude, $\zeta_{a_{max}}$, has to be determined. Given this wave frequency, the corresponding frequency of encounter, $\omega_e$, following Eq. (A.6) has to be calculated, dependent on the ship speed, $V$ and the direction of the vessel with respect to the waves, $\mu$. This calculated frequency of encounter is used as the necessary frequency input for the metaheuristic algorithm, which is integrated in the ship propulsion system model.

# B

# Shortest Distance Between an Ellipse & a Straight Line

*In the following, a demonstration of the mathematical method followed to calculate the shortest distance between an ellipse and a line is given.*

## B.1. Introduction

The mathematical approach aiming to calculate the shortest distance between an ellipse and a line is presented in this Appendix. A requirement in order to proceed with the mathematical calculations is that the mathematical equations of both the ellipse and the line under consideration are known.

## B.2. Calculation Process

As far as the calculation of the shortest distance of an ellipse from a line is concerned, this is defined as the problem of the of the calculation of the extremum distance, either maximum or minimum, of a point of an ellipse from the line. The points on the ellipse, where the extrema are located, are points at which the tangent to the ellipse is parallel to the line. This means that the slope of the tangent to the ellipse at these points has to be equal to the slope of the line. In order to proceed with the calculation process the mathematical formulas of an ellipse and a line, used as examples in this section, will be

B

given.

$$\begin{aligned} Ax + By + C = 0 & \quad \text{Line equation} \\ \frac{x^2}{m} + \frac{y^2}{n} = 1 & \quad \text{Ellipse equation} \end{aligned} \tag{B.1}$$

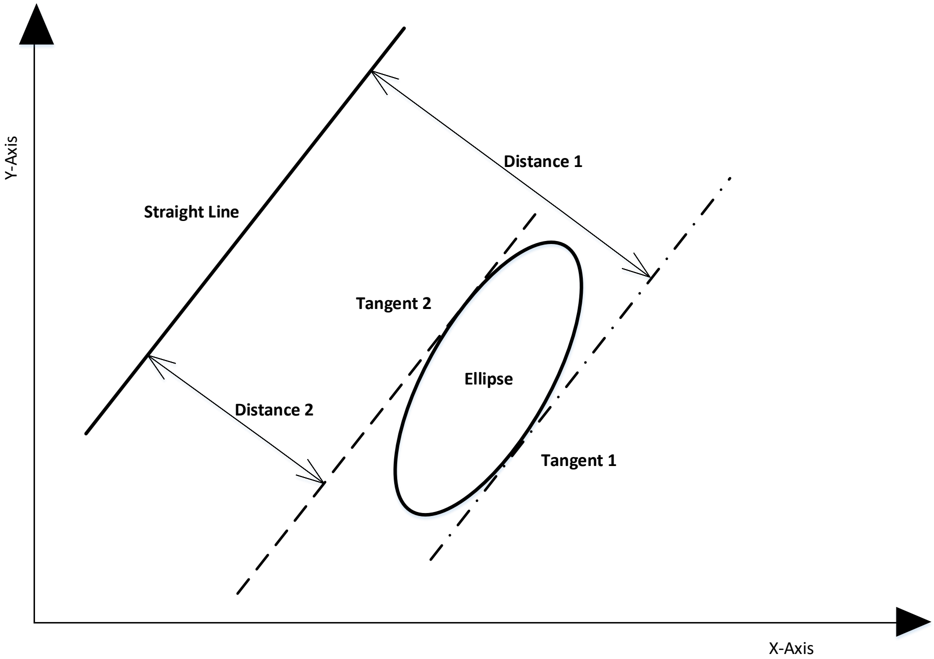


Figure B.1: Calculation of minimum and maximum distance of a line from an ellipse.

The first step in this procedure will be to determine the points of the ellipse at which the tangent to the ellipse is parallel to the given line. This requires the differentiation of the known ellipse equation, as given in Eq. (B.1), with respect to $x$:

$$\begin{aligned} 2\frac{x}{m} + 2\frac{y}{n}\frac{dy}{dx} = 0 \implies \\ \frac{dy}{dx} = \frac{-nx}{my} \end{aligned} \tag{B.2}$$

Rearranging Eq. (B.1) results in the following:

$$\begin{aligned}
&\frac{x^2}{m}+\frac{y^2}{n}=1 \implies \\
&\frac{y^2}{n}=1-\frac{x^2}{m} \implies \\
&y^2=n-n\frac{x^2}{m} \implies \\
&y=\pm\sqrt{n-n\frac{x^2}{m}}
\end{aligned} \tag{B.3}$$

Combination of Eq. (B.2) and Eq. (B.3) leads to:

$$\frac{dy}{dx}=\frac{-nx}{m\sqrt{n-n\frac{x^2}{m}}} \tag{B.4}$$

Using Eq. (B.4), the slope of the tangent at any point on the ellipse can be determined, requiring only the $x$ co-ordinate.

Following the original hypothesis, that the points on the ellipse, where the extrema are located, are points at which the tangent to the ellipse is parallel to the given line, the slope of the line is calculated by differentiating the line's equation, as it is given in Eq. (B.1), with respect to x:

$$\begin{aligned}
&Ax+By+C=0 \implies \\
&By=-Ax-C \implies \\
&y=-\frac{A}{B}x-\frac{C}{B} \implies \\
&\frac{dy}{dx}=-\frac{A}{B}
\end{aligned} \tag{B.5}$$

According to the original hypothesis, Eq. (B.5), which represents the line's slope, must be

B

equal to the right hand side of Eq. (B.4):

$$
\begin{aligned}
\frac{-nx}{m\sqrt{n-n\frac{x^2}{m}}} &= -\frac{A}{B} \implies \\
-xn &= -\frac{A}{B}m\sqrt{n-n\frac{x^2}{m}} \implies \\
(-xn)^2 &= \left(-\frac{A}{B}m\sqrt{n-n\frac{x^2}{m}}\right)^2 \implies \\
x^2n^2 &= \left(\frac{A}{B}\right)^2 m^2\left(n-n\frac{x^2}{m}\right) \implies \\
x^2n^2 &= \left(\frac{A}{B}\right)^2 m^2 n-\left(\frac{A}{B}\right)^2 mnx^2 \implies \\
x^2n &= \left(\frac{A}{B}\right)^2 m^2-\left(\frac{A}{B}\right)^2 mx^2 \implies \\
\left(n+\left(\frac{A}{B}\right)^2 m\right)x^2 &= \left(\frac{A}{B}\right)^2 m^2 \implies \\
x &= \pm\sqrt{\frac{\left(\frac{A}{B}\right)^2 m^2}{n+\left(\frac{A}{B}\right)^2 m}}
\end{aligned}
\tag{B.6}
$$

In Eq. (B.6) the $x$ co-ordinates of the points on the ellipse, where the extrema are located, are determined. Substituting Eq. (B.6) in Eq. (B.3), the $y$ co-ordinates of these points are determined:

$$
\begin{aligned}
y &= \pm\sqrt{n-\frac{n}{m}\frac{\left(\frac{A}{B}\right)^2 m^2}{n+\left(\frac{A}{B}\right)^2 m}} \implies \\
y &= \pm\sqrt{n-n\frac{\left(\frac{A}{B}\right)^2 m}{n+\left(\frac{A}{B}\right)^2 m}} \implies \\
y &= \pm\sqrt{n\left[1-\frac{\left(\frac{A}{B}\right)^2 m}{n+\left(\frac{A}{B}\right)^2 m}\right]}
\end{aligned}
\tag{B.7}
$$

The outcome of Eq. (B.6) and Eq. (B.7), is the co-ordinates of the points on the ellipse where the extrema are located are determined. By combining these co-ordinates in any way, two points, $P_1$ and $P_2$, can be defined:

$$
\begin{aligned}
P_1(x_1, y_1) &\implies P_1\left(\sqrt{\frac{\left(\frac{A}{B}\right)^2 m^2}{n+\left(\frac{A}{B}\right)^2 m}}, \quad \sqrt{n\left[1-\frac{\left(\frac{A}{B}\right)^2 m}{n+\left(\frac{A}{B}\right)^2 m}\right]}\right) \\
P_2(x_2, y_2) &\implies P_2\left(-\sqrt{\frac{\left(\frac{A}{B}\right)^2 m^2}{n+\left(\frac{A}{B}\right)^2 m}}, \quad -\sqrt{n\left[1-\frac{\left(\frac{A}{B}\right)^2 m}{n+\left(\frac{A}{B}\right)^2 m}\right]}\right)
\end{aligned}
\tag{B.8}
$$

Having defined the extrema lying on the ellipse, $P_1$ and $P_2$, the distance of each one of these two points from the given line in Eq. (B.1) has to be calculated. Due to the fact that it is not known in advance which of the two determined points has the minimum or maximum distance from the given line, the distance from the line has to be calculated for both points. The minimum of this calculation is the desired shortest distance between the given ellipse and the line.

The distance of a point $P(x_p, y_p)$ from a given line, as the one given in Eq. (B.1), which is defined as *the length of the line segment which joins the point to the line and is perpendicular to the line* is given by the following equation:

$$
d_p = \frac{|Ax_p + By_p + C|}{\sqrt{A^2+B^2}} \tag{B.9}
$$

The determination of the shortest distance of an ellipse from a line requires the calculation of the distance of both points lying on the ellipse from the given line. The tangents at these two points of the ellipse are parallel to the given line. The minimum of these two values is the desired distance.

$$
\left.
\begin{aligned}
d_1 &= \frac{|Ax_1 + By_1 + C|}{\sqrt{A^2+B^2}} = \frac{\left| A\sqrt{\frac{\left(\frac{A}{B}\right)^2 m^2}{n+\left(\frac{A}{B}\right)^2 m}} + B\sqrt{n\left[1-\frac{\left(\frac{A}{B}\right)^2 m}{n+\left(\frac{A}{B}\right)^2 m}\right]} + C\right|}{\sqrt{A^2+B^2}} \\
d_2 &= \frac{|Ax_2 + By_2 + C|}{\sqrt{A^2+B^2}} = \frac{\left| A\left(-\sqrt{\frac{\left(\frac{A}{B}\right)^2 m^2}{n+\left(\frac{A}{B}\right)^2 m}}\right) + B\left(-\sqrt{n\left[1-\frac{\left(\frac{A}{B}\right)^2 m}{n+\left(\frac{A}{B}\right)^2 m}\right]}\right) + C\right|}{\sqrt{A^2+B^2}}
\end{aligned}
\right\} \implies \min(d_1, d_2)
\tag{B.10}
$$

B

## B.3. SPECIAL CASE: ELLIPSE - LINE INTERSECTION

As far as the calculation of the shortest distance between an ellipse and a line is concerned, this can be, also, calculated in other cases, besides the one previously presented. On the one hand, as it was demonstrated in the previous section, the shortest distance between an ellipse and a line can be calculated when the first is far away from the second and there are no intersection points. On the other hand, the shortest distance between an ellipse and a line exists as a mathematical expression and it is possible to be determined in case that the ellipse intersects the line or vice versa.

As it is clearly shown in Figure B.2 and Figure B.3, an algorithm seeking for the shortest distance between an ellipse and a line following the procedure presented in Section B.2, has to determine the two tangent lines on the ellipse, which are parallel to the given straight line (same slope as the straight line). Despite the fact that the ellipse intersects the line or vice versa, an algorithm which only seeks to determine the two parallel tangent lines and then calculate their distance from the straight line can not realise the fact of intersection. As result, the algorithm will go on with the calculation process of the distance between the points of contact of the tangents on the ellipse and the straight line, as it is described in Eq. (B.1) - Eq. (B.10).

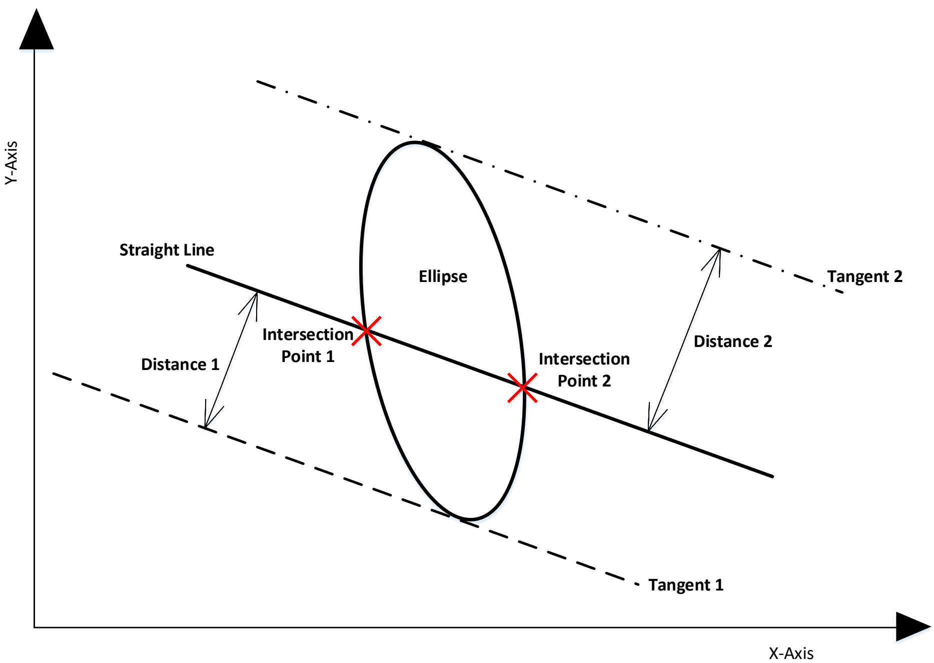


Figure B.2: First case of ellipse - straight line intersection and distances of tangents parallel to straight line.

Taking into account the objective of the metaheuristic algorithm (simulated annealing) employed in Chapter 6, it is undoubtful that the solutions given for cases in which the ellipse intersects the given straight line have to be excluded. As it is stated in Chapter 6, the metaheuristic algorithm is applied, seeking the maximum value of the shortest distance between the elliptic trajectory of the engine operating point and the engine's envelope limits (modelled as straight line). The ultimate goal of this objective is to eliminate the possibilities of the engine's operating ellipse crossing (or touching) the limits of the Diesel engine's operating envelope. The reasons for that are explained extensively in Chapter 6.

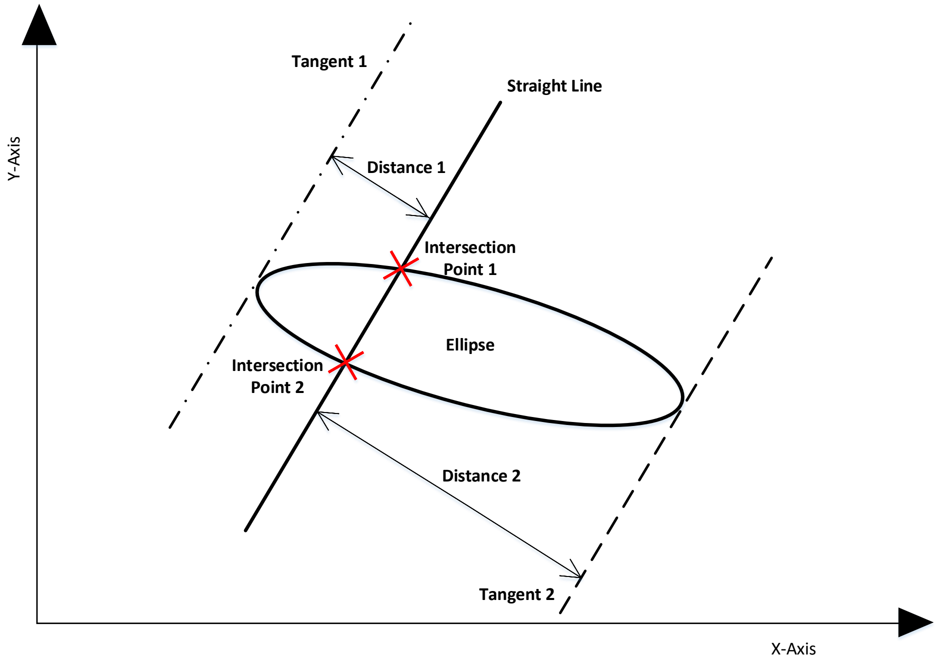


Figure B.3: Second case of ellipse - straight line intersection and distances of tangents parallel to straight line.

At this point the reasons for which such cases like the one depicted in Figure B.2 and Figure B.3 might show up should be mentioned. As it is referred in Section 4.2, during the linearisation process of the ship propulsion model some of the non linearities of the original non linear model are neglected. In Section 4.2 there are three types of non linearities described there that are disregarded. A case as the one depicted in Figure B.2 and Figure B.3 can be attributed to the *third* type of the neglected non linearities. More specifically, according to Section 4.2 there are some limitations in the original non linear simulation model, which are neglected in the derived linear model. Such kind of limitation is the engine's operating envelope, which is neglected allowing the engine operating beyond the boundaries that exit in the real model. As a result, cases like the one depicted in Figure B.4 and Figure B.5 can show up, in which the elliptic trajectory of the engine operating point crosses the limits of the engine's operating envelope, intersecting its boundary line.

According to Section 5.2.1, the shape of the elliptic trajectory of the engine operating point is formed based on the Bode plots of the linearised ship propulsion model. Consequently, as it was demonstrated in Section 4.5 and Eq. (4.51) for different combination of values for proportional gain, $K_p$ and integral gain, $K_i$, used in State-Space form of the linear model, different Bode plots will be derived for a certain engine operating point under consideration. This means that for a specific sinusoidal wake disturbance (given wake amplitude, $|\delta w^*|$, and wave frequency of wake disturbance, $\omega$) different elliptic trajectories will be derived, based on a range of combinations of the engine's governor gains ($K_p$ and $K_i$) values.

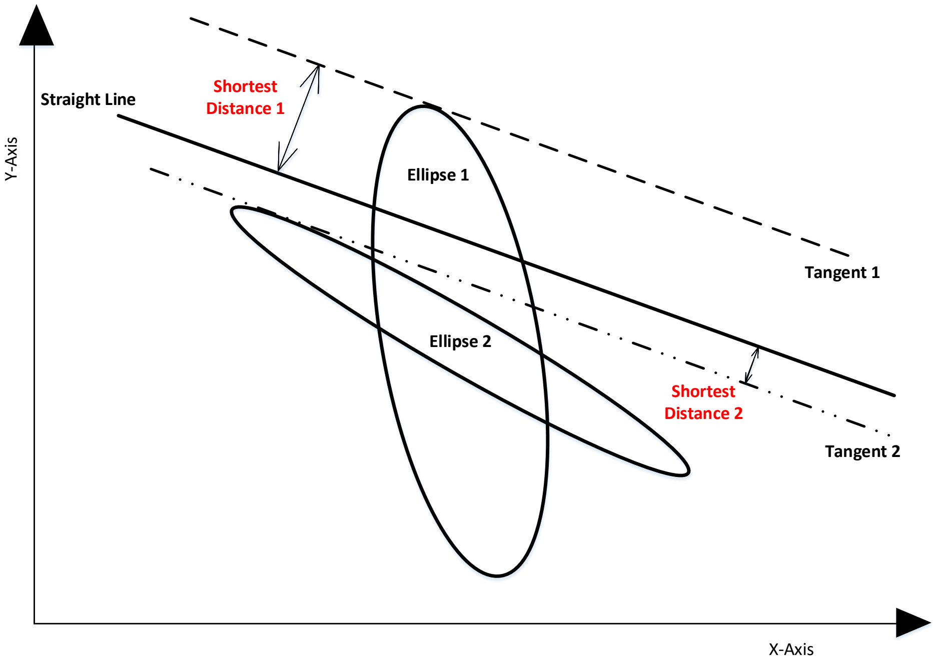


Figure B.4: First case of elliptic trajectories of engine operating point due to different combinations of governor gains $K_p$ and $K_i$.

A typical example of elliptic trajectories of the engine operating point with different dimensions and orientation, with respect to a given straight line, due to different combination of values for $K_p$ and $K_i$ is illustrated in Figure B.4 and Figure B.5. In this Figure only the shortest distance of each ellipse with respect to the line is shown. Additionally, the example shown in Figure B.4 and Figure B.5 is a typical case which needs to be excluded as a possible solution taken into account by the metaheuristic algorithm. In other words, the designer of the metaheuristic algorithm has to set as a constraint for the algorithm that for the selected solution of $K_p$ and $K_i$ values combination, the derived elliptic trajectory should not intersect (or touch) the given straight line. This means that this kind of solutions should be defined as **infeasible** solutions.

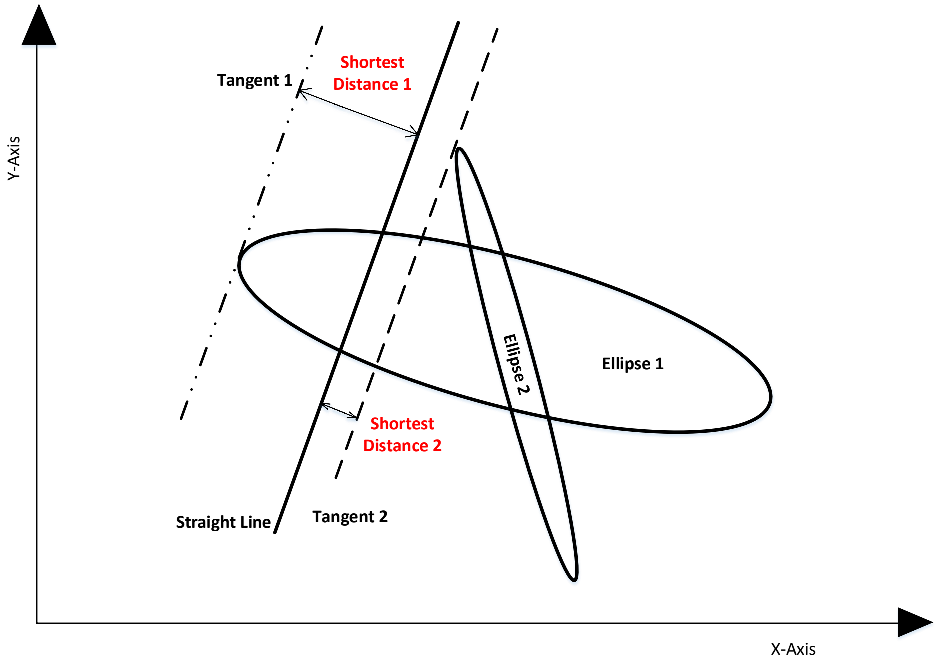


Figure B.5: Second case of elliptic trajectories of engine operating point due to different combinations of governor gains $K_p$ and $K_i$.

More specifically, what is going to happen in a case like the one shown in Figure B.4 and Figure B.5 is that for both ellipses, resulting from two different combinations of $K_p$ and $K_i$ values, the simulated annealing algorithm will determine the tangents on the ellipses which are parallel to the straight line and their corresponding distances from the straight line, based on the above mentioned Eq. (B.9). Then, for each one of the elliptic trajectories of the engine operating point, the tangent with the minimum distance from the straight line will be determined, by applying Eq. (B.10). Given that for both ellipses the tangent with the shortest distance with respect to the straight line is defined, the simulated annealing algorithm, which is employed, will compare the two shortest distances of the tangents of the two ellipses seeking for the largest one, since it is a maximisation algorithm, trying to find the *maximum shortest distance* between all the possibly derived operating ellipses and the given straight line. This means that between the two elliptic trajectories of the engine operating point, Ellipse 1 and Ellipse 2, resulting from two different combinations of values for $K_p$ and $K_i$, the simulated annealing algorithm will choose Ellipse 1, as a result of the fact that the shortest distance of the tangent parallel to the straight line for this Ellipse 1 has the maximum value between the two.

B

In order prevent the selection of a solution like this as the optimum by the algorithm, this solution has to be set as *infeasible*, as it was previously mentioned. To achieve this, one additional function is integrated in the employed algorithm. Every elliptic trajectory of the engine operating point resulting from a specific combination of governor gains $K_p$ and $K_i$ is examined whether it intersects or not the line of the engine envelope under study, before being accepted as a valid solution by the algorithm. This investigation involves the examination of the solutions of the system of equations including the formula of the straight line as well as the formula of the ellipse, as they are given in Eq. (B.1). Rearranging the Line equation given in Eq. (B.1) results in:

$$y = -\frac{A}{B}x - \frac{C}{B} \tag{B.11}$$

Substituting Eq. (B.11) into the ellipse equation leads to:

$$\begin{aligned}
&\frac{x^2}{m} + \frac{\left(-\frac{A}{B}x - \frac{C}{B}\right)^2}{n} = 1 \implies \\
&nx^2 + m\left(\left(\frac{A}{B}\right)^2 x^2 + 2\frac{A}{B}\frac{C}{B}x + \left(\frac{C}{B}\right)^2\right) = mn \implies \\
&nx^2 + \left(\frac{A}{B}\right)^2 mx^2 + 2m\frac{A}{B}\frac{C}{B}x + m\left(\frac{C}{B}\right)^2 - mn = 0 \implies \\
&\left(n + \left(\frac{A}{B}\right)^2 m\right)x^2 + 2m\frac{A}{B}\frac{C}{B}x + m\left(\left(\frac{C}{B}\right)^2 - n\right) = 0
\end{aligned} \tag{B.12}$$

The roots of a quadratic equation are given by:

$$\begin{aligned}
&ax^2 + bx + c = 0 \implies \\
&x_1 = \frac{-b + \sqrt{b^2 - 4ac}}{2a} \quad \text{and} \quad x_2 = \frac{-b - \sqrt{b^2 - 4ac}}{2a}
\end{aligned} \tag{B.13}$$

From Eq. (B.13) follows that the roots of Eq. (B.12):

$$\left.\begin{aligned}
x_{i.p._1} &= \frac{-\left(2m\frac{A}{B}\frac{C}{B}\right) + \sqrt{\left(2m\frac{A}{B}\frac{C}{B}\right)^2 - 4\left(n + \left(\frac{A}{B}\right)^2 m\right) m \left(\left(\frac{C}{B}\right)^2 - n\right)}}{2\left(n + \left(\frac{A}{B}\right)^2 m\right)} \\
x_{i.p._2} &= \frac{-\left(2m\frac{A}{B}\frac{C}{B}\right) - \sqrt{\left(2m\frac{A}{B}\frac{C}{B}\right)^2 - 4\left(n + \left(\frac{A}{B}\right)^2 m\right) m \left(\left(\frac{C}{B}\right)^2 - n\right)}}{2\left(n + \left(\frac{A}{B}\right)^2 m\right)}
\end{aligned}\right\} \implies x_{i.p.} = \left[x_{i.p._1}, x_{i.p._2}\right] \tag{B.14}$$

where i.p. stands for *intersection point*. Taking into consideration Eq. (B.14), the algorithm has to determine the feasibility of its generated solution by examining which of the following conditions is satisfied and then act accordingly:

- if Eq. (B.14) has roots which are **real numbers**, $x_{i.p.} \in \mathbb{R}$:

  The ellipse **intersects** the line, thus the combination of PID controller gains $K_p$ and $K_i$, generating as solution the elliptic trajectory of the engine operating point under consideration, should be rejected by the algorithm. The rejection is achieved by giving, for this combination of $K_p$ and $K_i$, a really small value, nearly zero, as the shortest distance between the generated operating ellipse and the engine envelope line. In that way it is ensured that none of these kind of solutions will ever be selected as the optimum by the optimisation algorithm.

- if Eq. (B.14) has roots which are **not real numbers**, $x_{i.p.} \notin \mathbb{R}$:

  The ellipse **does not intersect** the line, thus the combination of PID controller gains $K_p$ and $K_i$, generating as solution the elliptic trajectory of the engine operating point under consideration, should be accepted by the algorithm and compared to the rest accepted combinations, in order to determine whether its shortest distance is the maximum or not.

# C

# Metaheuristics for Hard Optimisation: Simulated Annealing

*In the following, a demonstration of Simulated Annealing, a metaheuristic method followed by researchers who come across new and hard optimisation problems, is given. For the interested reader, the detailed theory, with respect to metaheuristics for hard optimisation, part of which is the Simulated Annealing algorithm, is extensively documented in [Dréo et al., 2006, Hillier, 2012].*

## C.1. Introduction

It goes without saying that engineers, in different technical sectors, have to deal with problems of growing complexity in fields like operations research, design of mechanical systems, image processing, design of electrical circuits, management of industrial production, logistics or improvement of systems performance. This kind of problems are defined as *optimisation problems*. These problems are mathematically formulated with the use of a function which is called *objective function* or *cost function*. The ultimate goal attempting to solve such kind of problems is either the *minimisation* or the *maximisation* of the objective function. Furthermore, the mathematical formulation of optimisation problems may include additional information, which are known as *constraints*. These constraints have to be satisfied by all the parameters of the adopted solutions. In any other case the solutions are not feasible.

As mentioned before, the complexity of optimisation problems is continuously growing, This results in a special kind of problems known as *difficult optimisation* problems. In regard to *difficult optimisation* problems, a group of methods has been developed, which attempt to solve these problems, as well as possible. These methods are called *metaheuristics*. This section emphasises on specifically one type of metaheuristics known as **Simulated Annealing**.

## "DIFFICULT" OPTIMISATION PROBLEMS

C

According to theory, the optimisation problems are distinguished in two groups:

- "discrete" problems
- problems with continuous variables

An abundant research has contributed to the solution of these two types of problems. In respect to problems with continuous variables, traditional methods used for global optimisation are applied. These methods are usually worthless, especially in cases in which the objective function does not seem to follow a particular structural property, like for example convexity. On the other hand, in case of discrete optimisation a significant number of heuristics which give solutions quite close to the optimum is developed. However, these heuristics are formulated for a specific, given problem. The schematic representation of the objective function of a "difficult" optimisation problem is shown in Figure C.1, where the ultimate goal is to minimise the objective function (optimum = minimum). There is no doubt that when the space of the possible configurations of the problem has such a complicated structure, the determination of the global minimum, $c^*$, can become an extremely difficult procedure.

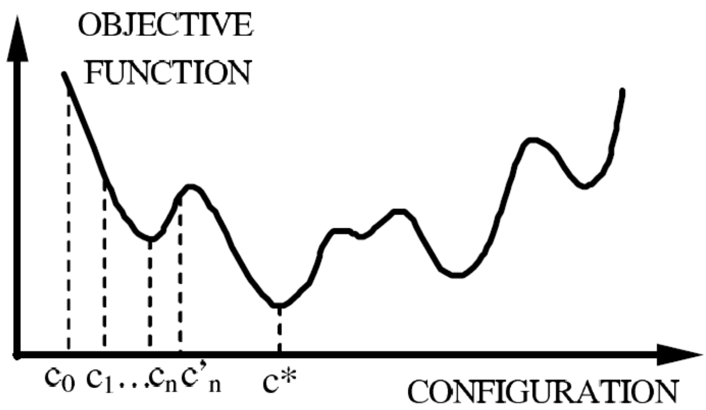


Figure C.1: Shape of the objective function of a difficult optimisation problem, [Dréo et al., 2006].

As far as the “classical”iterative algorithms are concerned, the drawback of their employment compared to the metaheuristics is the high possibility of the algorithm being trapped in a local optimum, staying away from finding the global optimum. The working principles of such a traditional iterative algorithm are presented in a few steps below, based on the objective function of the minimisation problem given in Figure C.1:

- Initial configuration, $c_0$ is chosen as starting point point. It can be selected randomly or can be determined by the designer of the algorithm.
- An elementary modification is applied. The values of the objective function are compared, before and after the applied modification.
- If the change resulted in reduction of the value of the objective function, the modification is accepted. The new configuration $c_1$, which is a “neighbour”of the preceding one, as depicted in Figure C.1, is established as the starting point for the next modification. In the contrary case, the problem returns to the previous configuration, before another modification is attempted.
- The process is made iterative until any modification results in worse value of the objective function.

In Figure C.1, it can be noticed that a classical algorithm of iterative improvement, generally, is not capable of finding the global optimum in an optimisation problem, but only one local optimum, like for example $c_n$ in the objective function in Figure C.1. A traditional algorithm can become more effective by applying it several times, with the initial configurations being arbitrarily selected. However, this choice comes at a price, as the computational time is increased significantly. Additionally there is no guarantee that this process will find the optimal solution.

According to the above mentioned, the major disadvantage of a “classical ”iterative algorithm, is the weakness of escaping from a local optimum, where it might be trapped. This fact will prevent the algorithm from finding the global optimal solution. In order to overcome this limitation another idea was applied in this kind of optimisation problems. This idea is included in metaheuristics, giving them a significant advantage compared to traditional iterative algorithms. This idea consists of the acceptance of the configuration which leads to a temporary degradation of the situation of the problem under consideration. In other words, metaheuristics allow temporarily solutions for the problem, which result in worst value of the objective function (either increase of the value if it is a minimisation problem or decrease of the value if it is a maximisation problem). Moreover, a mechanism for controlling the degradations, specifically designed for each metaheuristic, will prevent the deviation of the solutions from the optimum one. On the other hand, it offers the algorithm the possibility to escape from the trap of a local optimum and explore other “valleys”which might prove to be more beneficial. An example of temporary acceptance of a degradation, is the case of passing from configuration $c_n$ to $c'_n$, as it is shown in Figure C.1, where the optimisation problem under consideration is a minimisation problem. Moreover, in Figure C.2 the different solutions provided by

C

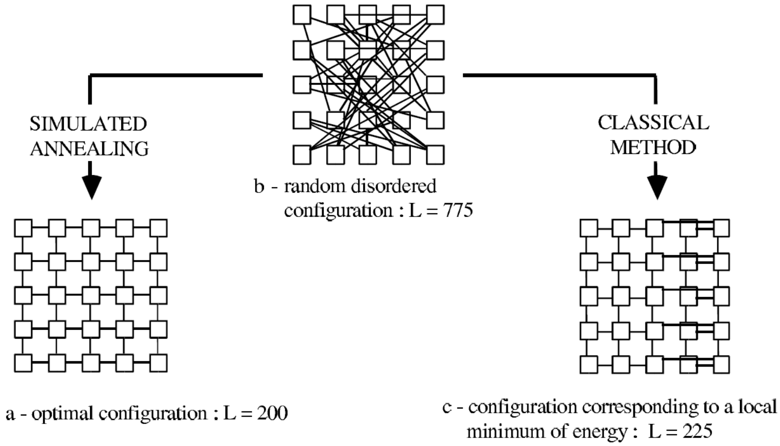


Figure C.2: A traditional method getting trapped in a local minimum of energy in a typical length of connections minimisation problem, [Dréo et al., 2006].

a metaheuristic algorithm (simulated annealing) and a classical iterative method implemented in a random optimisation problem are illustrated.

## C.2. SIMULATED ANNEALING ALGORITHM

One of the metaheuristic methods which was proposed by researchers, in order to solve "difficult"optimisation problems with complicated structure, as the one shown in Figure C.1, is the **simulated annealing** technique. Since the method has been published by researchers, simulated annealing was proved to have the following advantages and disadvantages:

- *effective* in achieving high quality solutions (i.e. absolute optimum or good relative optimum for the objective function)
- *applicable* and *easily implemented* in various optimisation problems, given that the value of the objective function can be rapidly determined after each applied modification
- *easily adjustable*, regarding the implementation of additional constraints in the algorithm
- *includes* several control parameters (initial temperature, rate of temperature reduction, length of temperature stages, stopping criteria of the algorithm) whose values need to be determined
- *greedy* with respect to the computational time required to solve certain types of problems

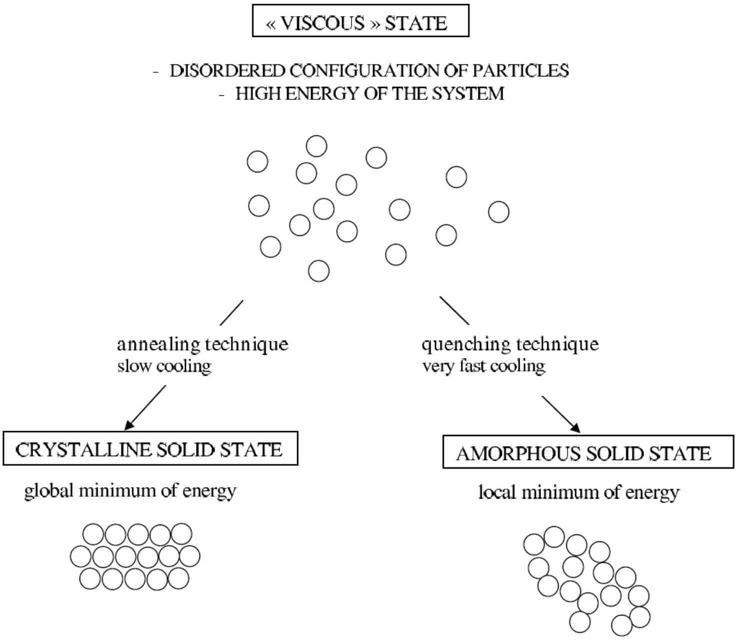


Figure C.3: Comparison of annealing and quenching techniques, [Dréo et al., 2006].

## REAL ANNEALING

Annealing is a strategy which is employed by physicists aiming to approach an optimum state of a material by controlling the temperature. To make the description more clear, the example of the growth of a monocrystal is used. The annealing technique is this example starts by heating a material in advance providing high energy to it. The next step in this process is to cool down the material gradually, by keeping though at each stage a temperature of sufficient duration. This procedure of controlled decrease of the temperature results in a crystallised solid state. This solid state is also considered stable state, corresponding to an absolute minimum of energy. The exactly opposite technique is known as *quenching*. The quenching technique consists in lowering the temperature of the material very fast. Consequently, this may result in an amorphous structure, a metastable state that corresponds to a local minimum of energy. Comparing the two above mentioned opposite methods, in the annealing technique the gradual cooling of a material causes a disorder-order transformation, whereas the quenching method leads to solidification of a disordered state. This comparison is clearly depicted in Figure C.3.

## SIMULATED ANNEALING

The previously mentioned annealing technique inspired some of the researchers working on optimisation algorithms. The idea of using the annealing method to lead a physical system to low energy state resulted in the development of the *Simulated Annealing* technique in order to deal with optimisation problems. The analogy between a physical system and an optimisation problem is shown in Table C.1 and the result of applying simulated annealing in an optimisation problem is demonstrated in Figure C.4. The development of the simulated technique starts by introducing the major control parameter, regarding the optimisation which acts similarly to temperature, when compared to the real annealing. This means that the "temperature"of the system to be optimised should condition the number of accessible states and lead towards the optimal state, if it is lowered gradually in a slow and well controlled way. On the contrary, if the temperature is lowered fiercely it should lead towards a local minimum (function identical to quenching technique).

| *Optimisation problem* | *Physical system* |
|---|---|
| objective function | free energy |
| parameters of the problem | "coordinates"of the particles |
| find a "good"configuration (even optimal configuration) | find the low energy states |

Table C.1: Analogy between an optimisation problem and a physical system, [Dréo et al., 2006].

Attempting to simulate the evolution of a physical system towards its thermodynamic balance at a given temperature, the Metropolis algorithm can be employed. Given the initial configuration the system is subjected to an elementary modification. In case this modification causes a decrease in the objective function (or "energy") of the system (minimisation problem), it is accepted. In case that an increase $\Delta E$ is caused in the value of the objective function, it is also accepted but with a probability of $e^{\frac{-\Delta E}{T}}$.

What actually happens when employing the algorithm is that a real number is generated randomly ranging between 0 and 1. This means that the configuration causing a $\Delta E$ degradation in the objective function is accepted only if the random number generated is lower than or equal to $e^{\frac{-\Delta E}{T}}$. By repeatedly applying the Metropolis rule of acceptance, a sequence of configurations is generated, constituting a Markov chain (details regarding Markov chain in Appendix A in

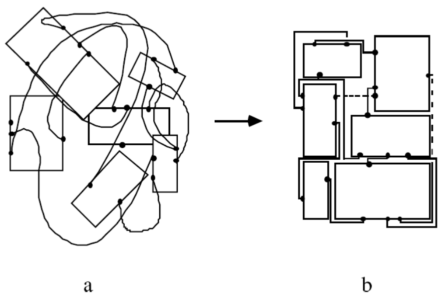


Figure C.4: Disorder-order transformation by applying simulated annealing in a problem of optimum placement of electronic components, [Dréo et al., 2006].

[Dréo et al., 2006]), in that way that each configuration depends on only the immediately previous one. According to the above acceptance rule, at high temperature, $e^{\frac{-\Delta E}{T}}$ is close to 1. As a result, the majority of the modifications are accepted. This allows the algorithm to do a random walk in the configuration space. On the other hand, when the temperature is low $e^{\frac{-\Delta E}{T}}$ is close to 0. Thus, the majority of the modifications leading to a worse value of the objective function is rejected. For temperatures that $e^{\frac{-\Delta E}{T}}$ gets values between 0 and 1, the algorithm may accept degradations of the objective function, which means that the algorithm gives the system the opportunity to escape from a local minimum.

Provided that the thermodynamic balance is reached at a given temperature, the temperature is "slightly"reduced. Then a new Markov chain is applied in this new temperature stage. If the user of the algorithm chooses to reduce the temperature rapidly, the progress towards a new thermodynamic balance is decelerated. Such a process of successive, controlled temperature decrease, employed in an optimisation problem, is shown in Figure C.5.

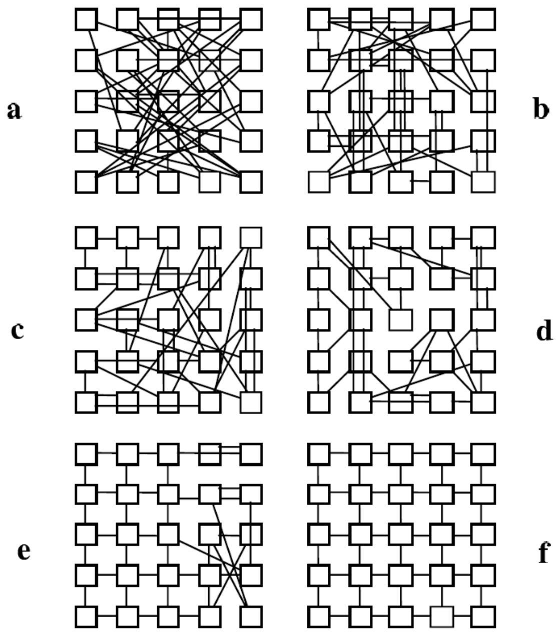


a: $T = 25,\ L = 775$ b: $T = 20,\ L = 525$
c: $T = 13,\ L = 460$ d: $T = 6,\ L = 425$
e: $T = 4,\ L = 260$ f: $T = 3,\ L = 200$

Figure C.5: Evolution of the system at various, successive temperature levels, starting with an arbitrary initial configuration and L indicating the overall length of connections, [Dréo et al., 2006].

According to the theory a correlation between the reduction of the temperature and the minimum duration of the temperature stage is assigned. Finally, by progressing towards very low temperatures (towards zero), the algorithm converges towards the absolute minimum of energy. Relating it to the real annealing process, the procedure is terminated when the system is “solidified”. In other words, either the temperature has reached the zero value (or quite close to this value) or no more modifications of the configuration of the system leading to increase of energy are accepted at the temperature stage under consideration. The structure of simulated annealing algorithm is illustrated in the flow chart in Figure C.6.



## Configuration Space

At this point, the significance of the *configuration space*, which considerably affects the effectiveness of the specific metaheuristic method, should be stressed out. The configuration space is characterised by a “topology”, which is based on the relation between two configurations. The “distance”between two configurations is defined as the minimum number of elementary changes required to pass from one configuration to the other. Additionally, each configuration is related to a specific amount of energy in such a way that a configuration space is represented by an “energy landscape”. The complexity of this “landscape ”defines the level of difficulty of the optimisation problem under study. Moreover, it has to be mentioned that the shape of this landscape is not determined by the nature of the problem under consideration, but it is, mainly, dependent on the formulated objective function and the selection of the elementary modifications, when the algorithm moves from one configuration to the next one.

## Annealing Scheme

Having presented the impact of the form of the configuration space on the effectiveness of the simulated annealing algorithm, there is one more aspect of the algorithm which influences the convergence speed and the determination of the global optimum of the optimisation problem under study. This aspect is called “program annealing”and is related to the definition of the values of the control parameters of the algorithm. The control parameters, whose values need to be predefined, for the algorithm to be applied are listed below:

- the initial temperature
- the length of the homogeneous Markov chains, meaning the criterion of changing temperature stage
- the law of temperature reduction
- the stopping criterion of the algorithm

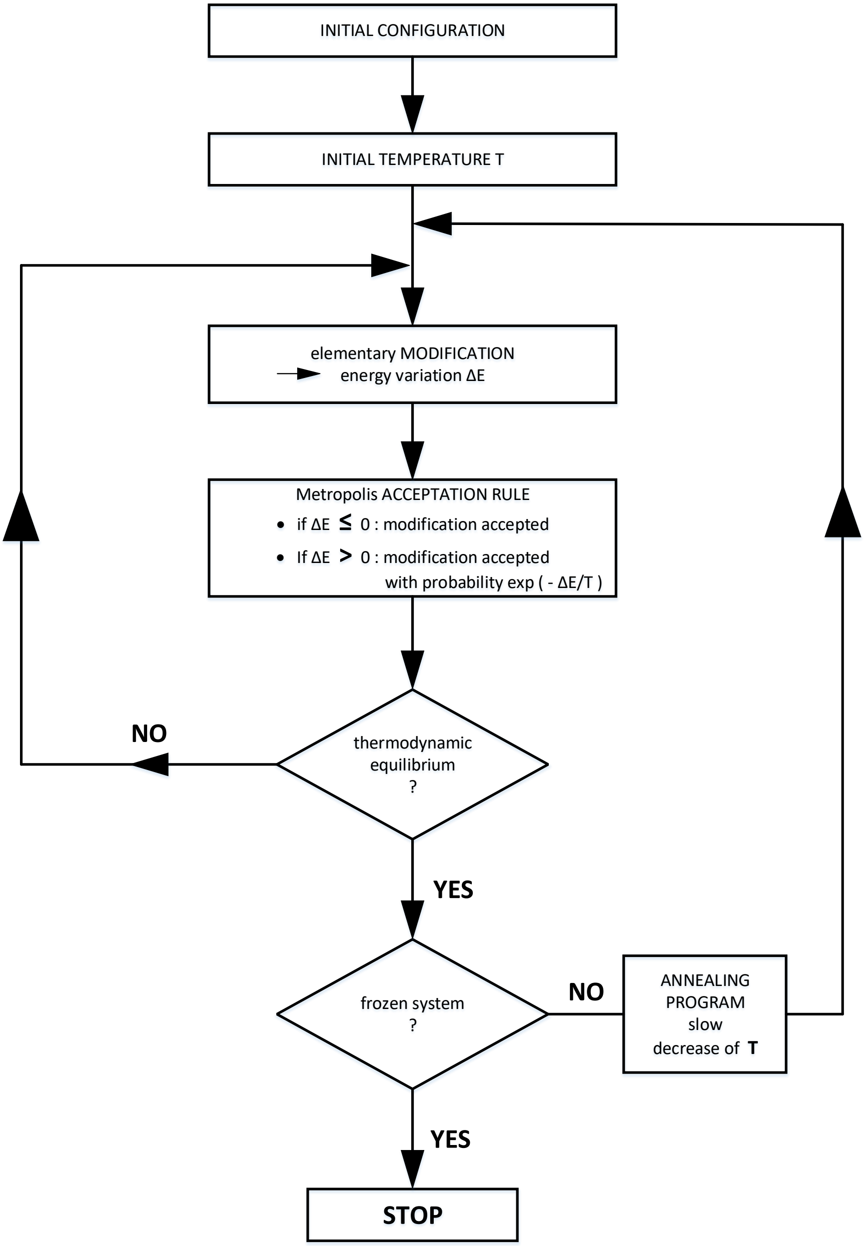


Figure C.6: Simulated Annealing algorithm flow chart.

The definition of the values of the above mentioned control variables of the simulated annealing algorithm, which is considered to be one of the main drawbacks of the specific metaheuristic method, is not based on research results. Their values are usually, adjusted based on empirical results of application of the method. [Dréo et al., 2006] neatly demonstrates some simple, practical rules with respect to the functional structure and the determination of proper values for the above mentioned control variables, used in simulated annealing method:

- *Definition of the objective function.* Constraints of the problem optimisation are established here. Other limitations regarding the nature of the problem are taken into account in the modifications applied during the operation of the algorithm
- *Choice of disturbance mechanisms* for a "current"configuration. The calculation of the corresponding energy change of the objective function, $\Delta E$ has to be **direct** and **quick**, aiming to keep the computational time within reasonable limits.
- *Initial temperature* $T_0$. It is required before the employment of the metaheuristic method. It can be calculated by applying the following algorithm:
    - Initiate 100 disturbances of the problem under study at random. Calculate the average value, $\langle \Delta E \rangle$, of the corresponding $\Delta E$ variations
    - Make the selection for the rate of acceptance $\tau_0$ of the "degrading modifications", according to the assumed "quality"of the initial configuration, for example:
        - "poor"quality: $\tau_0 = 50\%$ (starting at high temperature)
        - "good"quality: $\tau_0 = 20\%$ (starting at low temperature)
    - Calculate $T_0$ based on the following formula: $e^{\frac{-\langle \Delta E \rangle}{T_0}} = \tau_0$
- *Acceptance rule of Metropolis.* It is applied according to the following way: if $\Delta E > 0$, a number r in [0, 1] is randomly generated and the modification under study is accepted if $r < e^{\frac{-\Delta E}{T}}$, where T represents the current temperature
- *Change in temperature stage.* A reduction of the current temperature can take place once one of the 2 following conditions is satisfied during the temperature stages:
    - $12 \cdot N$ perturbations accepted
    - $100 \cdot N$ perturbations attempted

  N representing the number of degrees of freedom (or parameters) of the problem
- *Temperature reduction.* It can be applied by implementing the following geometrical law: $T_{k+1} = 0.9 \cdot T_k$
- *Program termination.* The algorithm can be terminated after 3 successive temperature stages without any perturbation accepted.

- *Essential verifications during the first executions* of the algorithm:
  - the generation of the real random numbers (in [0, 1]) must be well uniform
  - the "quality"of the result should not vary significantly when the algorithm is executed several times:
    - with different "seeds"for the generation of the random numbers
    - with different initial configurations
- *An alternative for the algorithm in order to achieve less computation time.* Provided that simulated annealing is greedy and less effective at low temperature, the use of a "hybrid"metaheuristic algorithm might be beneficial. More specifically, the implemented simulated annealing algorithm can be terminated early, with an algorithm of local type developed for the particular problem applied from that point on, aiming at the refinement of the final solution.

# References


A.B. Aalbers and W. van Gent. Unsteady wake velocities due to waves and motions measured on a ship model in head waves. In *Proceedings of 15th Symposium on Naval Hydrodynamics*, volume 15, pages 69–81, 1984.

Martin Alexandersson. A study of methods to predict added resistance in waves. *Master's thesis, KTH Centre for Naval Architecture*, 2009.

F Perez Arribas. Some methods to obtain the added resistance of a ship advancing in waves. *Ocean Engineering*, 34(7):946–955, 2007.

Emmanuel Branlard. Generation of time series from a spectrum. 2010.

Johann Dréo, Alain Pétrowski, Patrick Siarry, and Eric Taillard. *Metaheuristics for hard optimization: methods and case studies*. Springer Science & Business Media, 2006.

Gene F. Franklin, J. David Powell, Abbas Emami-Naeini, and J. David Powell. *Feedback control of dynamic systems*, volume 3. Addison-Wesley Reading, MA, 1994.

R.D. Geertsma, R.R. Negenborn, K. Visser, and J.J. Hopman. Design and control of hybrid power and propulsion systems for smart ships: A review of developments. *Applied Energy*, 194:30–54, 2017a.

RD Geertsma, RR Negenborn, K Visser, MA Loonstijn, and JJ Hopman. Pitch control for ships with diesel mechanical and hybrid propulsion: Modelling, validation and performance quantification. *Applied Energy*, 206:1609–1631, 2017b.

H.T. Grimmelius and D. Stapersma. Control optimisation and load prediction for marine diesel engines using a mean value simulation model. In *ENSUS 2000, Conference Proceedings*, pages 212–229, 2000.

Hugo T. Grimmelius and Douwe Stapersma. The impact of propulsion plant control on diesel engine thermal loading. In *CIMAC Conference, Hamburg (May 2001)*, 2001.

TH t Havelock. Xlvii. the drifting force on a ship among waves. *The London, Edinburgh, and Dublin Philosophical Magazine and Journal of Science*, 33(221):467–475, 1942.

Frederick S Hillier. *Introduction to operations research*. Tata McGraw-Hill Education, 2012.

Leo H. Holthuijsen. Cambridge University Press, 2007. ISBN 978-0-521-86028-4. URL http://app.knovel.com/hotlink/toc/id:kpWOCW0002/waves-in-oceanic-coastal/waves-in-oceanic-coastal.

Third IMO IMO. Greenhouse gas study 2014, executive summary and final report. *International Maritime Organization, London*, page 280, 2014.

Jin Jiang. Optimal gain scheduling controller for a diesel engine. *IEEE control Systems*, 14(4):42–48, 1994.

J.M.J. Journée and W.W. Massie. *Offshore Hydromechanics*. TU Delft, 2000.

P.T. Kidd, N. Munro, C. Thiruarooran, and D.E. Winterbone. Linear modelling of ship propulsion plants. *Proceedings of the Institution of Mechanical Engineers, Part A: Power and Process Engineering*, 199(1):53–58, 1985.

Harald E. Krogstad and Oivind A. Arntsen. Linear wave theory part a. *Norwegian University of Science and Technology, Trondheim*, 2000.

P Naaijen. Deterministic prediction of waves and wave induced vessel motions: Future telling by using nautical radar as a remote wave sensor. 2017.

Weigang Pan, Yingbing Zhou, and Yaozhen Han. Design of ship main engine speed controller based on optimal active disturbance rejection technique. In *Automation and Logistics (ICAL), 2010 IEEE International Conference on*, pages 528–532. IEEE, 2010.

Stewart Schlesinger. Terminology for model credibility. *Simulation*, 32(3):103–104, 1979.

David L Smith. Linear modeling of a marine gas turbine power plant. In *ASME 1988 International Gas Turbine and Aeroengine Congress and Exposition*, pages V002T03A002–V002T03A002. American Society of Mechanical Engineers, 1988.

D. Stapersma and P. de Heer. Interaction between propulsor and engine. *Proceedings of the 34th WEGEMT School*, pages 1–47, 2000.

D. Stapersma and H.T. Grimmelius. A fresh view on propulsion control ii. In *Proceedings of the 14th international ship control systems symposium. Ottawa, Canada*, 2009.

Douwe Stapersma and Arthur Vrijdag. Linearisation of a ship propulsion system model. *Ocean Engineering*, 142:441–457, 2017.

Douwe Stapersma, P.J.M. Schulten, and H.T. Grimmelius. A fresh view on propulsion control. In *Proceedings of the 7th international naval engineering conference. Amsterdam, The Netherlands*, pages 221–40, 2004.

Jorgen Strom-Tejsen, Hugh Y. H. Yeh, and David D. Moran. Added resistance in waves. *Transactions of the SNAME*, 81:109–143, 1973.

Bhushan Taskar, Kevin Koosup Yum, Sverre Steen, and Eilif Pedersen. The effect of waves on engine-propeller dynamics and propulsion performance of ships. *Ocean Engineering*, 122:262–277, 2016.

Michael S. Triantafyllou and Franz S. Hover. Maneuvering and control of marine vehicles. *Cambridge, Massachusetts, USA: edited by authors*, 2003.

Michio Ueno, Yoshiaki Tsukada, and Katsuji Tanizawa. Estimation and prediction of effective inflow velocity to propeller in waves. *Journal of Marine science and Technology*, 18(3):339–348, 2013.

P.J. Van Spronsen and R.L. Tousain. An optimal control approach to preventing marine diesel engine overloading aboard karel doorman class frigates. *IFAC Proceedings Volumes*, 34(7):493–498, 2001.

T.J.C. van Terwisga, D.J. Noble, R. van't Veer, F. Assenberg, B. McNeice, and P.F. van Terwisga. Effect of operational conditions on the cavitation inception speed of naval propellers. In *Proceedings of the 25th Symposium on Naval Hydrodynamics*, Office of Naval Research, National Academies Pres, St. John's, Newfouland and Labrador, August 8-13 2004.

A. Vrijdag and D. Stapersma. Extension and application of a linearised ship propulsion system model. *Ocean Engineering*, 143:50–65, 2017.

A. Vrijdag, D. Stapersma, and T. van Terwisga. Systematic modelling, verification, calibration and validation of a ship propulsion simulation model. *Journal of Marine Engineering & Technology*, 8(3):3–20, 2009.

Hans Klein Woud and Douwe Stapersma. *Design of propulsion and electric power generation systems*, volume 190253. IMarEST, 2002.

Nikolaos I Xiros. Pid marine engine speed regulation under full load conditions for sensitivity h-norm specifications against propeller disturbance. *Journal of Marine Engineering & Technology*, 3(2):3–11, 2004.